Faraday tomography

of the

Galactic ISM

with the

WSRT

Faraday tomography

of the

Galactic ISM

with the

WSRT

Proefschrift

ter verkrijging van
de graad van Doctor aan de Universiteit Leiden,
op gezag van de Rector Magnificus prof. mr. P.F. van der Heijden,
volgens besluit van het College voor Promoties
te verdedigen op donderdag 15 mei 2008
klokke 16.15 uur

door

Dominic Hubertus Franciscus Maria Schnitzeler

geboren te Heerlen
in 1979

Promotiecommissie

Promotores:	Prof. dr. G. K. Miley	
	Prof. dr. A. G. de Bruyn	(ASTRON, Dwingeloo; Kapteijn Instituut, Groningen)
Co-promotor:	Dr. P. Katgert	
Referent:	Prof. dr. W. N. Brouw	(Kapteijn Instituut, Groningen)
Overige leden:	Dr. T. L. Landecker	(Dominion Radio Astrophysical Observatory, Penticton, Canada)
	Dr. M. Haverkorn	(University of California - Berkeley, USA)
	Prof. dr. V. Icke	
	Prof. dr. K. H. Kuijken	

Vuür d’r pap en de mam.

And so it begins. Magnetic fields make their presence felt by exerting forces on charged particles, which because of this will spiral around the field lines. Highly energetic cosmic rays spiralling around magnetic field lines emit radio waves that we detect with telescopes like the WSRT. In this thesis I study Faraday rotation of these radio waves to learn more about magnetic fields in the Milky Way. [CERN copyright]

Table of contents

Chapter 1

Introduction

On the popular TV series 'Brainiac' one of the presenters asked the question "which direction does a compass point in space?" (Tickle 2006). This thesis is part of an ongoing effort by researchers in different countries to answer that question. But the direction of the field is not only an interesting question for magnetic field aficionados. The magnetic field is important on galactic scales, as its pressure is actually comparable to or larger than the thermal pressure in a galaxy (Beck 2004). The small Larmor radius of charged particles spiralling around the magnetic field lines also produces a strong coupling between the large-scale motion of the ionized plasma and the magnetic field. Because of this coupling, magnetic fields play an important role in the internal dynamics of a Galaxy on many different length scales, from collapsing molecular clouds, to the structure and dynamics of a galaxy as a whole.

In this introduction I will first present the different phases of the interstellar medium (ISM) in galaxies, and discuss their physical properties, heating mechanisms, and observational characteristics. I also include cosmic rays as a separate phase, since the synchrotron radiation they emit plays a fundamental role in my study of the Galactic magnetic field. Then I introduce the magnetic field, and discuss the various ways in which its characteristics can be derived, both in external galaxies, as well as in the Milky Way. Finally, I will briefly describe the contents of the chapters in my thesis, and I discuss my main conclusions.

1.1 The ingredients of the galactic ISM

A magnetic field is both produced by and interacts with charged particles. Since there is a strong coupling between the electrons and ions in the ionized ISM and the magnetic fields, the charged particles cannot move independently from the magnetic field. Collisions between charged and neutral particles also produces a coupling between the ionized and neutral ISM phases, which means that ISM structure in general is intricately connected to structure in the magnetic field, and vice versa. Roughly speaking, the ISM can be thought of as consisting of a few components, or phases. The basis for this classification is formed by the seminal papers by Field, Goldsmith & Habing (FGH; 1969) on the two-phase ISM, and by McKee & Ostriker (MO; 1977) on the 3-phase medium. Observations and numerical modeling have later proven that the ISM is in fact much more diverse, but a classification like this is still helpful. The present overview on the ISM phases is based on papers by Ferrière (2001), Heiles (2001), and on the book by Tielens (2005), unless mentioned otherwise. In Table 1.1 I summarize the properties of the different ISM phases.

Table 1.1 — Temperatures T, densities n and volume filling factors f of the different ISM phases in the Milky Way. I compiled this table from the articles by Ferrière (2001), Heiles (2001), Heiles & Kulkarni (1987) and references therein. Some of these authors claim different values, particularly for the volume filling factors in the Galactic midplane that are known to be highly uncertain (Heiles 2001). This table is meant to give an indication of the relative importance of the different ISM phases and their properties, even though the numbers are at best approximate.

Component		T [K]	n [cm^{-3}]	f
Cold neutral	(CNM)	10 – 100	20 – 50[a]	~ 0.01
Warm neutral	(WNM)	~ 8000	~ 0.2 – 0.4	$\} \sim 0.5$
Warm ionized	(WIM)	~ 8000	0.2 – 0.5	
Hot intercloud	(HIM)	10^5 – 10^6	0.005	~ 0.2 – 0.5

[a] Up to 10^6 cm^{-3} in dense molecular gas.

The cold neutral medium (CNM)
The FGH model predicts that there are two self-regulating ISM phases for a given heating rate and pressure. By self-regulating I mean that a small increase (or decrease) in the heating rate also always leads to a small increase (decrease) in the cooling rate, thereby returning the gas to its initial state. One of these phases is the CNM, that has a temperature of about 10 – 100 K and is efficiently cooled by CII. The CNM is found where the optical depth of clouds and nebulae in the interstellar medium is so high that only very few photons can penetrate. The large optical depths ensure that dust grains can survive, and these very efficiently radiate heat, which keeps temperatures in the cloud low. Also, radiative de-excitation of collisionally excited metals (most importantly the 158 μm CII line) is an effective cooling mechanism in the CNM.The CNM temperatures are low enough for a rich chemistry leading to exotic molecules inside these objects. Because of its low temperature, the CNM is also the phase where the bulk of the star formation takes place. Although the CNM contains a lot of mass ($\sim$ 10^9 $M_\odot$), see Table 1 from Ferrière 2001), it fills only a small volume of the Milky Way, as its density is much higher than average.

The warm neutral medium (WNM)
The other ISM phase predicted by the FGH model is the WNM with a temperature of $\sim$ 8000 K. Lyα emission is an important coolant for regulating the temperature of this phase. The WNM is found both as envelopes of cold CNM clouds that are being warmed by the interstellar radiation field, as well as in between CNM clouds. Heiles (2001) notes that some observations show WNM gas at unstable temperatures, i.e. temperatures at which a small temperature decrease leads to an increase in the cooling rate, which further reduces the temperature etc. However, the FGH model is a thermal equilibrium model for the ISM as a whole, and the ISM gas can locally have properties that are not stable according to the FGH model. Warm (T $\sim$ 6000 – 10000 K) HI gas in the WNM phase produces broad HI emission lines.

The warm ionized medium (WIM)
The WIM is created by ionizing photons, where the CNM and WNM are heated by photons that are not energetic enough to ionize gas. Similar to the WNM, the WIM is found as the more ionized parts of cold CNM/WNM clouds. However, it also occurs as Strömgren spheres close to hot massive stars, and as a more diffuse ionized ISM component. This diffuse component is heated by young massive OB stars, since mechanical heating by hot stars does not produce enough ionization (Tielens 2005). There are two ISM phases with significant quantities of free electrons, the WIM and the HIM (to be discussed next). Snowden et al. (1997) showed from modeling of the diffuse ROSAT X-ray data that in the Galactic midplane the electron density in the HIM is lower than the electron density in the WIM by a factor of 10. Most of the dispersion measure DM[cm^{-3}pc] = $\int_0^\infty n_\mathrm{e}\mathrm{d}l$ (the line-of-sight integral of the electron density n_e), and emission measure EM[cm^{-6}pc] = $\int_0^\infty n_\mathrm{e}^2\mathrm{d}l$ are therefore produced in the WIM.

Heiles (2001) argues that dispersion measure is produced in the more diffuse WIM component, and the emission measure (and Hα intensity) mostly in the clumpy regions surrounding WNM/CNM clouds. However, his results are based on only 4 lines-of-sight, and only some of these support his claim. In this thesis I will therefore assume that both the dispersion measure and the emission measure are produced by the same ISM electrons.

The hot intercloud medium (HIM)
The HIM is created when supernova shock waves heat up the ISM, raising the temperature to 10^5 – 10^6 K. The HIM is located inside cavities blown by supernovae and super bubbles, and also as chimney outbreaks from the Galactic plane into the Galactic halo. It is visible through absorption lines of highly ionized atomic species from e.g. OVI, NV and CIV , and also as a diffuse X-ray background. As it is a very tenuous medium, it gives (for our purpose) negligible contributions to the dispersion measure and emission measure. MO included the HIM as an extension of the FGH model, to account for the energy that supernovae deposit in the ISM.

Cosmic rays
Cosmic rays are highly relativistic particles (mostly protons, nuclei of massive elements, and electrons) that are produced in supernova explosions or ejected in coronal flares of unevolved late-type starts. Several theories exist on how cosmic rays propagate along magnetic field lines, and how they are confined by them. (Cesarsky 1980). Cosmic rays spiral around the field lines, and this continuous acceleration makes them loose energy, that is emitted as synchrotron radiation at radio wavelengths. Important is also that because of their high energy, cosmic rays pervade all other ISM phases.

Heating and cooling play an important role in the ISM dynamics, and they also produce transitions between the ISM phases over (astronomically speaking) small distances. For example, the optical depth is very high inside a molecular cloud that is forming stars, and only cosmic rays can heat the cloud core. Towards the edge of the cloud, photon heating increases, and the temperature of the cloud rises. Even closer to

the edge of the cloud, the temperature becomes so high that dust grains evaporate and molecules are quickly destroyed, producing the WNM phase. At the edge of the cloud, interstellar UV photons ionize atomic hydrogen, and the WNM turns into WIM. At the end of its life a massive star explodes as a supernova, producing a large flux of cosmic rays and ionizing photons, and turning the local ISM into HIM. Material that is swept up by the passing shock waves can cool and form clouds, that can cool even further and form the WNM and CNM phases, thus coming full circle.

1.2 Techniques to study interstellar magnetic fields

There exist several techniques to study magnetic fields in the interstellar medium, and I will discuss a couple of these in this section. Each of them only works for one ISM phase, and each of them can tell you only about either the strength of the magnetic field component along the line-of-sight, $B_{\parallel}$, the strength of the component in the plane of the sky, $B_{\perp}$, or the direction of $B_{\perp}$. The only exception to this is Faraday rotation, that gives you both the strength of $B_{\parallel}$ and the direction of $B_{\perp}$.

First, magnetic fields influence the electron orbitals in atoms and molecules, which leads to splitting of spectral lines, an effect known as Zeeman splitting. This is a very slight effect, and under normal circumstances Doppler broadening and thermal broadening of spectral lines makes Zeeman splitting difficult to detect. The temperatures in the CNM however are so low that Doppler broadening and thermal broadening are only very small, which results in very narrow spectral lines. Under these circumstances Zeeman splitting can be observed. With Zeeman splitting one can derive $B_{\parallel}$. Houde et al. (2002) reconstructed the 3D magnetic field vector in the M17 molecular cloud, using a combination of the Zeeman effect and 350 μm polarimetry with ion-to-neutral molecular line widths.

The CNM is cold enough to harbour dust grains. Elongated dust grains rotate preferentially perpendicular to the magnetic field lines. This produces a net polarization of the radiation passing through the dust cloud, which is known as the Davis-Greenstein effect (Davis & Greenstein 1951). This effect has been used to map the direction of $B_{\perp}$ close to dusty star forming regions. Mathewson & Ford (1970) and Axon & Ellis (1976) mapped the direction of the large-scale Galactic magnetic field over most of the Galaxy, by using starlight that became polarized from the Davis-Greenstein effect.

The volume emissivity of synchrotron radiation is proportional to $B_{\perp}^2$, and to the density of cosmic rays that emit synchrotron radiation. Thus, if the cosmic ray density is known, or if one for example assumes energy equipartition between the cosmic rays and the magnetic fields, it is possible to derive, $B_{\perp}$ from the observed synchrotron brightness temperature. Niklas (1995) used this technique to determine the strength of the total magnetic field (i.e. the vector sum of the large-scale and turbulent magnetic fields) in external galaxies.

When polarized radiation passes through a plasma with an embedded magnetic field, the left- and right hand circular polarizations of the radiation will travel at slightly different phase velocities. This produces a net rotation of the plane of polarization of the incident radiation, an effect that is known as Faraday rotation. If Φ_0 is the position angle of the plane of polarization at which the radiation was emitted, and $\Phi(\lambda)$

the position angle at which the radiation was detected at wavelength λ, after passing through the Faraday-rotating region, then the amount of Faraday rotation is given by

$$\begin{aligned} \Phi(\lambda) - \Phi_0 \,[\mathrm{rad}] &= 0.81 \left[\int_{\mathrm{source}}^{\mathrm{observer}} n_\mathrm{e}\, \vec{B} \cdot \mathrm{d}\vec{l} \right] \lambda^2 \\ &= \mathcal{R}\, \lambda^2 \end{aligned} \tag{1.1}$$

where n_e is the electron density of the plasma [cm^{-3}] , $\vec{B}$ is the magnetic field vector [μG], and $\mathrm{d}\vec{l}$ is an infinitesimal line element in the direction of the observer [pc]. A magnetic field pointing towards the observer is called positive, and it produces a counterclockwise rotation of the plane of polarization. The integral is calculated from the point where the radiation is emitted to the observer. $\mathcal{R}$ is the so-called Faraday depth of the radiation, which measures the amount of Faraday rotation in radians per observing wavelength^2. Note that we distinguish the Faraday depth from the rotation measure of the radiation, RM, which is the derivative of the polarization angle with respect to λ^2. Only when radiation is emitted at one point along the line-of-sight, and subsequently Faraday rotated between the point of emission and the observer, is $\mathcal{R}$ = RM. Observations at multiple wavelengths are required to determine both $\mathcal{R}$ and Φ_0. Since Faraday rotation increases strongly with observing wavelength, it makes sense to observe at long (radio) wavelengths.

We can use the dispersion measure to derive the magnetic field strength from the measured Faraday depths:

$$\langle B_\parallel \rangle \equiv \frac{\int_{\mathrm{source}}^{\mathrm{observer}} n_e \vec{B} \cdot \mathrm{d}\vec{l}}{\int_{\mathrm{line-of-sight}} n_e \mathrm{d}l} = \frac{\mathcal{R}}{0.81\ \mathrm{DM}} \tag{1.2}$$

Since the dispersion measure is an integral along the line-of-sight, we can also only determine the *average* magnetic field strength along the line-of-sight by combining the measured Faraday depths with the dispersion measure. Since the electron density in the WIM ISM phase is much higher than in the HIM, most of the Faraday rotation takes place in the WIM. The magnetic field strengths that we derive from Faraday rotation are therefore magnetic field strengths in the WIM.

Using measured dispersion measures for pulsars at known distances, Cordes & Lazio (2002) constructed a smooth model of the electron density distribution in the Milky Way. With this model one can easily calculate the dispersion measure for an interesting line-of-sight of a given length. Their model is however based on a relatively small number of pulsars, and pulsars are scarce in the second Galactic quadrant and far from the Galactic plane. In chapters 2 – 6 we use an alternative method, where we convert in a number of steps Hα intensities that have been measured in the WHAM survey (Haffner et al. 2003) to dispersion measures. In chapter 9 we compare the results from our method to the dispersion measures that we calculated from the Cordes & Lazio model. This shows that our method works well for Galactic latitudes $|b| > 5^o$.

Synchrotron radiation is an excellent source to study Faraday rotation: at longer wavelengths the synchrotron brightness temperature increases (up to wavelengths of about 1 – 1.5 meters), and also the Faraday effect rotates the plane of polarization over larger angles at longer wavelengths. Synchrotron radiation is also highly polarized, up to 70%, whereas most other types of radiation are at most about 1% polarized. Different types of synchrotron-emitting sources have been used to study the magnetic field of the Milky Way: pulsars, extragalactic radio sources, and the diffuse emission in the ISM. Each of these sources has a couple of advantages and disadvantages, that I will summarize here. As the different types of sources provide complementary information on the Galactic magnetic field, it is useful to combine the information from the different source types.

Pulsars
For pulsars we can directly measure the dispersion measure and Faraday depth, which means that we can use Eqn. 1.2 to accurately determine $\langle B_{\parallel} \rangle$ between us and the pulsar. Also we can get a rough estimate of the physical distance to the pulsar by comparing the measured dispersion measure to models of how the electron densities in the Galaxy are distributed. Distances derived from these models are typically accurate to 25% at best (Taylor et al. 1993). Pulsars have the drawback that they are mostly confined to the Galactic plane, and the surface density of known pulsars is not very high: in chapter 9 we study the area between $80^o \lesssim l \lesssim 200^o$ and $-40^o \lesssim b \lesssim 40^o$, and at the moment only 57 pulsars are known in this region.

Extragalactic radio sources
Many polarized extragalactic radio sources have been catalogued, and especially recent projects like the International Galactic plane survey (Taylor et al. 2003, Haverkorn et al. 2006b) find many more new sources with well-determined rotation measures. Extragalactic sources sample the entire line-of-sight through the Milky Way. By comparing the Faraday depths of pulsars to the Faraday depths of the extragalactic sources, we can derive $\langle B_{\parallel} \rangle$ in the part of the line-of-sight that lies beyond the pulsar. Since the amount of Faraday rotation in intergalactic space is very small compared to the amount of Faraday rotation inside galaxies, this comes down to determining $\langle B_{\parallel} \rangle$ between the pulsar and the rest of the Milky Way. One drawback of extragalactic sources is that there can also be Faraday rotation close to the active galactic nucleus (AGN) that emits the polarized radiation that we study. Since the amount of intrinsic Faraday rotation is not correlated between AGNs, the intrinsic Faraday depths of the AGNs can be averaged out. For this averaging the surface density of extragalactic radio sources must be high enough, otherwise also structure in the Galactic magnetic field will be lost in the averaging process. Another drawback of extragalactic radio sources is that we cannot determine the dispersion measure that we need for deriving $\langle B_{\parallel} \rangle$ from Eqn. 1.2. Therefore one often integrates the Cordes & Lazio model along the entire line-of-sight through the Milky Way, and we also use the WHAM Hα intensities to calculate dispersion measure for extragalactic sources in chapter 9.

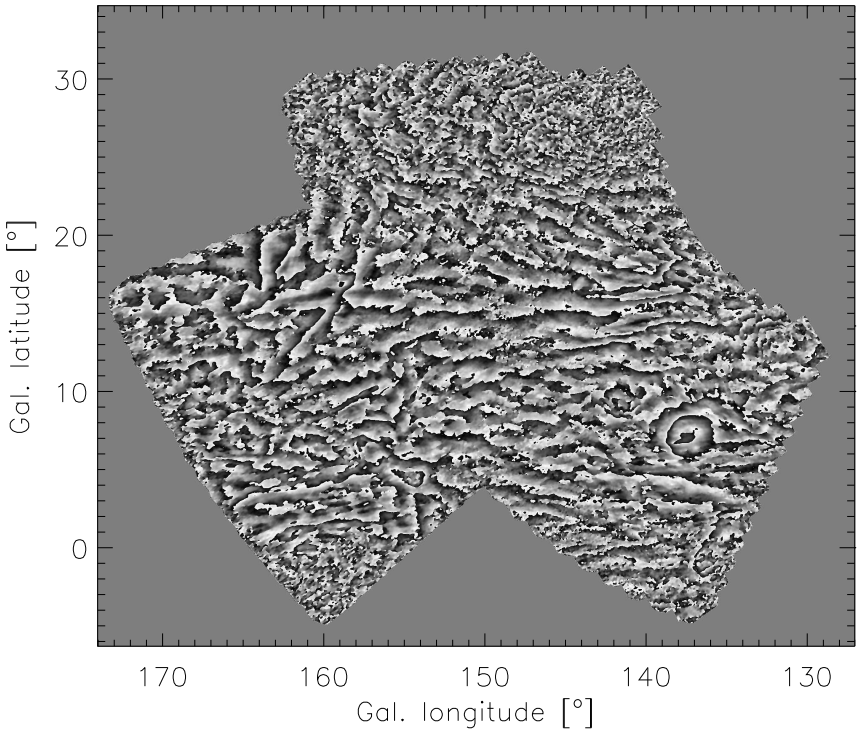

Figure 1.1 — Faraday rotation in action in the Galactic ISM. This figure shows polarization angles from the analysis of the WENSS survey, that we present in chapter 8. The grey scale ranges from -90^o (black) to +90^o (white). The periodicity of the polarization angles makes them wrap around the $\pm$ 90^o boundary, which explains why there are many black/white transitions in this figure. The region above a Galactic latitude of 20^o contains mostly noise.

Diffuse Galactic synchrotron emission

The main advantage of studying Faraday rotation in the diffuse Galactic synchrotron emission is that it is visible in all directions. This allows us to probe the Galactic magnetic field both close to the Galactic plane, and also at high Galactic latitudes. The contiguous lines-of-sight of the diffuse emission also make it possible to study structure in the magnetic field on many different physical scales, ranging from the size of the telescope beam (on the order of arcminutes) to many degrees. Figure 1.1 shows a clear example of Faraday rotation in the Galactic ISM. The diffuse Galactic emission is much more difficult to study than pulsars and extragalactic sources, because there can be multiple regions with Faraday rotation and synchrotron emission along the line-of-sight, and also because variations in synchrotron emissivities and/or Faraday rotation over the telescope beam will reduce the strength of the observed polarized signal. Furthermore it is very difficult to understand where most of the polarized diffuse emission from our Galaxy is coming from. This means that we cannot accurately determine the dispersion measure that we need to calculate $\langle B_{\parallel} \rangle$ from Eqn. 1.2. One solution is to integrate the Cordes & Lazio model over the entire line-of-sight through the Galaxy. This line-of-sight is (often) much longer than the actual line-of-sight to the diffuse emission, which means that the derived average magnetic field strengths will be lower limits to the actual values.

In external galaxies, if you know the strength of the large-scale galactic magnetic field and the inclination of the host galaxy, you can calculate the variation in Faraday depth over the face of the galaxy that is due to the magnetic field geometry. From such modeling, Berkhuijsen et al. (1997) and Fletcher et al. (2004a) determined the strength of the large-scale field in M51 and M31 respectively. In a similar way, Gaensler et al. (2005) used the rotation measures of extragalactic sources to map the large-scale field in the Large Magellanic Cloud.

Instead of using geometrical arguments, Mao et al. determined the strength and orientation of the large-scale field and the strength of the turbulent field in the Small Magellanic Cloud, by combining the $B_{\parallel}$ that they derived from Faraday rotation, with the direction of $B_{\perp}$ from optical starlight polarization, and the strength of $B_{\perp}$ derived using the Chandrasekhar-Fermi method (Mao et al., private communication). In chapter 8 we reconstruct the 3D magnetic field vector by combining information on the strength of $B_{\parallel}$ and direction of $B_{\perp}$ that we derived from Faraday rotation observations with the strength of $B_{\perp}$ that Haverkorn et al. (2004a) modeled from the variation in observed synchrotron intensity in their AURIGA data set.

1.3 The magnetic field of galaxies

In this section and the next I will discuss what we know about magnetic in external galaxies and in the Milky Way. Most of the information in these sections is based on the review by Beck (2007a) and references therein.

Radio polarization observations at short wavelengths ($\lesssim 10$ cm) do not significantly suffer from Faraday rotation, and polarization angle maps at these small wavelengths delineate the magnetic field structure of a galaxy. Magnetic fields have been mapped in this way in many nearby galaxies. Spiral structure in the magnetic field was not only found in spiral galaxies, but also in flocculent galaxies, and even in a number of irregular galaxies[1] (Beck 2005). Magnetic fields have even been observed in dwarf irregular galaxies, and it came as a surprise that the magnetic field strengths in these galaxies are comparable to those found in 'normal' galaxies.

The average total field strength of a sample of 74 spiral galaxies is $\langle B_{\rm tot}\rangle \sim 9$ μG, which was estimated by assuming energy equipartition between the magnetic field and the cosmic rays (Niklas 1995). Radio-faint galaxies like M31 and M33 have slightly weaker fields, $\langle B_{\rm tot}\rangle \sim 6$ μG, and grand-design spirals like M51, M83 and NGC 6964 show stronger fields of $\langle B_{\rm tot}\rangle \sim 15$ μG. The total field in M51's spiral arms is even 30 – 35 μG (Fletcher et al. 2004b). In starburst galaxies $\langle B_{\rm tot}\rangle$ can be as high as 50 μG (M82) – 100μG (NGC 7552). For comparison, the regular (=large-scale) field in typical spiral galaxies $\langle B_{\rm reg}\rangle \sim 1 - 5$ μG. The magnetic field energy density has been thoroughly investigated in NGC 6964, where it is comparable to the energy densities of cosmic rays and of the turbulent interstellar gas. The energy density of the ionized gas is one order of magnitude smaller (but this also depends on the assumed WIM filling factor), and the energy density of the neutral gas is smaller by even almost 2 orders of magnitude. Because they have such a large energy density compared to the other ISM

[1] See also the beautiful maps of magnetic fields in external galaxies on `http://www.mpifr-bonn.mpg.de/staff/wsherwood/mag-fields.html`

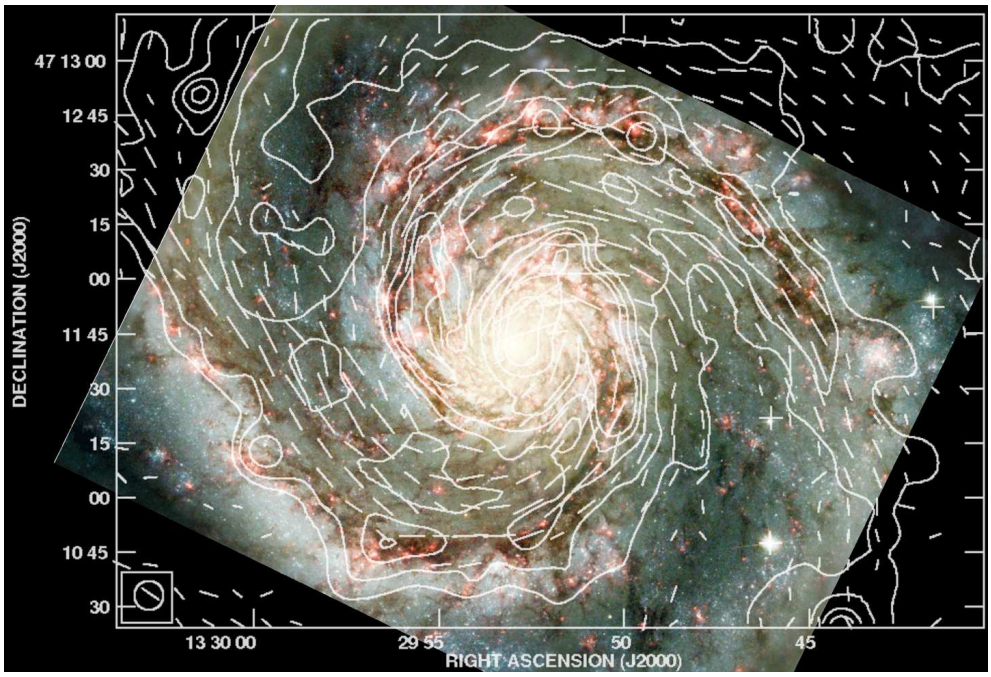

Figure 1.2 — The large-scale magnetic field in the central region of M51, from Fletcher et al. (in prep.). The lines show the direction of the field, and the length of the lines is proportional to the measured polarized intensities. The background shows an optical HST image of M51 (Image courtesy of Andrew Fletcher, NASA, and the Hubble heritage team (STScI/AURA)).

phases, magnetic fields play an important role in the internal dynamics of galaxies.

The large-scale magnetic field in spiral galaxies runs mostly parallel to the optical spiral arms, which can clearly be seen in the central parts of M51 (Fig. 1.2). It is strongest between the optical spiral arms, whereas the total magnetic field is strongest inside the spiral arms. However, Tabataei et al. (2007) found that the large-scale magnetic field is also strong in the spiral arms of M33.

Faraday rotation observations can tell us about the direction of the large-scale magnetic field, but such observations have only been carried out for 20-odd galaxies. In the majority of cases there is no clear dominating axial symmetry mode of the fields. This could hint at strong small-scale variations in the magnetic field (in particular smaller than the telescope beam), or it could mean that the signal/noise ratio of the observations was not high enough.

At this point (early 2008) about 10 edge-on galaxies have been observed to study the structure of the magnetic fields outside the galactic plane and in the galactic halo. The magnetic field in 4 out of the 6 edge-on galaxies observed by Dumke et al. (1995) runs parallel to the galactic plane. In NGC 4631 the magnetic field runs perpendicular to the plane in the inner regions of the galaxy, and parallel to the plane in the outer regions. No significant polarized emission was detected for the remaining galaxy, NGC 5907. Recent observations of NGC 891, NGC 5775, NGC 253 and M104 indicate that the magnetic field turns away from the galactic plane at large distances from the galactic centre and far from the galactic plane, producing an X-shaped field configuration. The opening angles between the legs of the 'X' and the galactic plane can be up to 50^o

(Krause et al. 2006, Heesen et al. 2007). Beck (2007c) argues that in the case of energy equipartition between magnetic fields and cosmic rays, the field should have a scale height of about 4 times the scale height of the synchrotron-emitting thick disk.

1.4 The magnetic field of the Milky Way

A single telescope beam encompasses many tens of parsecs or even kiloparsecs in all but the nearest galaxies, which means that by observing external galaxies we can only determine the properties of magnetic fields on large physical scales. On the other hand, in the Milky Way we can study structure in magnetic fields and the magnetized ISM on many length scales. The downside is that corrections for geometric distortions and for line-of-sight projection effects are more elaborate. Until the LOw Frequency ARray (LOFAR), the Murchison Wide-field Array (MWA) and the Long-Wavelength Array (LWA) come on-line, the Milky Way will be the only astrophysical laboratory where we can study magnetic field structure on small scales.

The strength of the total magnetic field in the solar neighbourhood is about 6 μG, which has been established from radio synchrotron observations, by assuming energy equipartition between the cosmic rays and the magnetic field. Strong et al. (2006) independently confirmed this result by direct measurements of the cosmic ray density in the vicinity of the sun, and by using the variation in cosmic ray density with galactic radius that was established from γ-ray observations. The total magnetic field strength increases to about 11 μG at 4 kpc from the Galactic centre (Berkhuijsen, in Beck 2001). Synchrotron polarization observations in the solar neighbourhood indicate that the ratio of the strength of the large-scale and total magnetic fields $\langle B_{\rm reg}/B_{\rm tot}\rangle \sim 0.6$ (Berkhuijsen 1971; Brouw & Spoelstra 1976; Heiles 1996), which is similar to the $\langle B_{\rm reg}/B_{\rm tot}\rangle \sim 0.6 - 0.7$ that is found for the total radio emission along the local spiral arm (Phillipps et al. 1981). Since $B_{\rm tot} \sim 6$ μG close to the sun, that means that $B_{\rm reg} \sim 4$ μG. This is higher than the $\langle B_{\rm reg}\rangle$ = 1.4 μG that is estimated from pulsar rotation measures and dispersion measures (Rand & Lyne 1994; Han & Qiao 1994; Indrani & Deshpande 1998).

Different observational tools indicate different ranges for the length scales over which the turbulent magnetic field is coherent. Clegg et al. (1992) and Minter & Spangler (1996) estimate, from the rotation measures of extragalactic sources, that the turbulent field is coherent over distances between 0.1 – 100 pc. Pulsar rotation measures and dispersion measures indicate length scales between 10 and 100 pc (Ohno & Shibata 1993), and observations of starlight polarization even length scales between 100 – 1000 pc (Jones et al. 1992). Haverkorn et al. (2004b) reported that there is additional turbulent structure on length scales $\lesssim$ 2 pc. They argued that stellar HII regions can be the source that drives the turbulence on these length scales.

Starlight polarization and pulsar rotation measures show that the pitch angle of the large-scale magnetic field is -8^o, which means that in the solar neighbourhood the large-scale field is pointing towards $l \approx 82^o$. This pitch angle is smaller than the pitch angle of the stellar arms (-18^o) and the pitch angle of the gaseous ISM components (-13^o) (Vallée 1995, 2002). Similar differences of 10^o– 20^o between the magnetic field pitch angle and the spiral arm pitch angle were also found in M51 (Patrikeev et al.

2006). The vertical component of the local field is very small, only about 0.2 μG (Han & Qiao 1994; chapter 8).

Pulsar rotation measures indicate several reversals of the magnetic field direction along Galactic radius. Han (2007) for example argues for a field reversal between each spiral arm and interarm region. Field reversals are on the contrary hardly ever encountered in external galaxies. As Beck (2007a) points out, with the low surface density of known pulsars, it is at the moment not possible to exclude the possibility that the field reversals are local instead of large-scale features. Local variations in rotation measure are known to exist, and have been observed in rotation measure maps of diffuse emission (e.g. Haverkorn et al. 2004c and 2004d). A localized magnetic anomaly was identified by Mitra et al. (2003) in the rotation measures of pulsars whose line-of-sight passes close to or through a star forming region. The errors in pulsar distances are furthermore non-negligible, which makes it difficult to precisely pinpoint pulsar positions with respect to the Galactic spiral arms. Finally, modeling of rotation measures of extragalactic sources close to the Galactic plane (Brown et al. 2003 and 2007) show only reversals between the Scutum-Crux arm and its adjacent interarm regions, and in the molecular ring in the inner Galaxy.

1.5 This thesis

One of the cornerstones of this thesis is the novel technique of Faraday tomography, also known as rotation measure synthesis, with which we can obtain information on the distribution of Faraday-rotating and synchrotron-emitting regions along the line-of-sight. This is a big step forward compared to previous studies, where information on the line-of-sight variation could only be obtained from modeling rotation measures (see e.g. Stepanov et al. 2002, and Brown et al. 2007).

The key to Faraday tomography is that synchrotron emission coming from different parts of the line-of-sight will be Faraday rotated by different amounts, depending on the local electron density and magnetic field strength. The observer sees the sum of the emission coming from different parts along the line-of-sight, that each can have a different amount of Faraday rotation. To obtain information on the distribution of the emitting and rotating regions, one therefore needs to distinguish emission with different Faraday depths. This situation is very similar to when you are listening to an orchestra: your brain automatically picks out the bassoons from the piccolos. Faraday tomography helps us to do just that: separate low frequencies (in this case: small Faraday depths) from high frequencies (large Faraday depths). Furthermore, if there are no reversals in the magnetic field direction, the Faraday depth increases with increasing distance from the observer, which gives us an idea of how the emission regions are ordered along the line-of-sight. Unfortunately, there can be reversals in the magnetic field direction along the line-of-sight. Synchrotron emission coming from beyond a region with a magnetic field reversal will then have the same Faraday depth as an emission region in front of the magnetic field reversal. In this sense it is incorrect to talk about 3D Faraday 'tomography', since contrary to tomography, there is not always a one-to-one correspondence between Faraday depth and physical depth. The term 'tomography' however underlines the potential of this new technique to investigate structure along

the line-of-sight, which previously was not possible.

In my Ph.D. project I have observed 4 regions in the second Galactic quadrant with the Westerbork radio telescope. These 4 data sets have high enough spectral resolution that I can use Faraday tomography, but they cover only small regions on the sky (about $10^o \times 10^o$). Therefore I also used polarization data from the 325 MHz WENSS survey, to study Faraday rotation also over a much larger area of about $40^o \times 30^o$. Unfortunately, WENSS has a bandwidth of only 5 MHz, which means that we cannot use it for Faraday tomography, or to determine rotation measures. However, by interpreting the WENSS polarization angle variations as Faraday depth gradients, we can still derive physical information from WENSS. I worked together with Fabian Heitsch on MHD simulations of the magnetized warm ISM, in particular on what we would see if we apply Faraday tomography to this simulated data set. With these simulations we can better understand how we can interpret our real observations as structure in electron density and magnetic fields. Finally, I combined information from pulsars, extragalactic radio sources and the diffuse Galactic emission to study the properties of the large-scale magnetic field in the second Galactic quadrant.

Main results

Chapter 2 is a short letter where we discuss that synchrotron emission and Faraday rotation not necessarily occur in the same part of the line-of-sight in our GEMINI data set. This seems counter-intuitive, since the cosmic rays that emit synchrotron radiation have very large penetrating power, and we would expect to find them throughout the ISM, also in regions with Faraday rotation.

In **chapter 3** we present a more detailed discussion of our GEMINI data set. Here we explain our observation from chapter 2 in terms of the magnetic field geometry. Synchrotron radiation is emitted perpendicular to the magnetic field lines, which means that we would not detect it when the field is directed along the line-of-sight. This configuration does however produce Faraday rotation, and for such a magnetic field configuration, we would detect no mixing between the synchrotron-emitting and Faraday rotating regions in our Faraday tomography analysis.

Many lines-of-sight in GEMINI show strong synchrotron emission at about the same Faraday depth, with some minor contributions at other Faraday depths. Since GEMINI lies in the direction of the Galactic anti-centre, we are mostly looking perpendicular to the field lines of the large-scale Galactic magnetic field. Faraday rotation is therefore not very strong in this direction, and most of the synchrotron emission along the line-of-sight will have the about same Faraday depth.

The CEPHEUS data set that we present in **chapter 4** is interesting for two important reasons. First, it shows a strong gradient in Faraday depth with Galactic longitude over scales of 5^o– 10^o. GEMINI also shows strong gradients in Faraday depth, but not on such large angular scales. The polarization angle gradients in WENSS that we discuss in chapter 8 and interpret as Faraday depth gradients are strong, but they point away from the Galactic plane, perpendicular to the Faraday depth gradients in CEPHEUS.

It is very remarkable that almost the entire CEPHEUS data set shows negative Faraday depths, while all but one of the extragalactic sources that we detected in CEPHEUS have positive Faraday depths. This implies that at some point along the line-of-sight

the magnetic field changes direction, that this field reversal is present over most of the CEPHEUS data set (an area of $10^o \times 10^o$), and that most of the diffuse emission that we observe, originates between us and the field reversal, otherwise it would have the same Faraday depth as the extragalactic sources.

The Faraday depths of the extragalactic sources in the TRIANGULUM data set (**chapter 5**) are much more negative than the Faraday depths of the diffuse emission. TRIANGULUM lies in a region where the rotation measures of extragalactic sources are known to be very negative. Since the Faraday depths of the extragalactic sources are so much more negative than the Faraday depths of the diffuse emission, not only the electron densities, but also the magnetic field, play a role in creating this special region.

The CAMELOPARDALIS data set that we discuss in **chapter 6** has smaller dispersion measures than the other 3 data sets. We do however find similar Faraday depths as in the other data sets, which must mean that the line-of-sight magnetic field component is stronger in CAMELOPARDALIS than in the other 3 data sets. The Faraday depths of the extragalactic sources and the diffuse emission are very comparable, and in this respect CAMELOPARDALIS is similar to GEMINI.

To better understand how we can interpret the outcome of our Faraday tomography analysis, I worked on how the electron densities and magnetic fields in an MHD simulation by Fabian Heitsch should be scaled to represent the real ISM as well as possible (**chapter 7**). We added relativistic electrons to this simulation, so that the MHD cube also emits synchrotron radiation. I then applied a similar Faraday tomography analysis to this mock data set as to the 4 real WSRT data sets that I analysed in chapters 2 – 6. Since we know in every point of the simulated volume the densities of the thermal and relativistic electrons, and the magnetic field strengths, we can study how the variation in Faraday rotation and synchrotron emission along the line-of-sight creates the structure in Faraday depth that we find in our observations. From these simulations we reached two important conclusions. First, in the largest part of the simulated volume, synchrotron emission does not occur at the same location as Faraday rotation. Second, we find that the large Faraday depths at which we sometimes find strong synchrotron emission, are in more than half of the cases that we studied produced by sharp peaks in the thermal electron density, and not gradually over the line-of-sight. A caveat is that the Mach number of our simulation is about 10, whereas the actual ISM has a Mach number close to 1. Future simulations at lower Mach numbers will show if the conclusions we reach for the highly supersonic simulated ISM are also more generally valid.

In **chapter 8** we present an analysis of the WENSS survey for Galactic longitudes $130^o \lesssim l \lesssim 173^o$, and latitudes -$5^o \lesssim b \lesssim 31^o$. WENSS was originally intended as a survey of extragalactic sources, but it also contains a wealth of diffuse polarization data. What we did not expect to see is the strong stratification of the WENSS polarization angles with Galactic latitude. Models of the large-scale field (see chapter 9), and also our CEPHEUS data set, show a stratification with Galactic longitude. In this chapter we also combine information on the strength of $B_{\parallel}$ and direction of $B_{\perp}$, that we both derive from Faraday rotation, with models of the strength of $B_{\perp}$ by Haverkorn et al. (2004a), to reconstruct the 3D magnetic field vector for a small number of lines-of-sight. We

find that the magnetic field component perpendicular to the Galactic plane is about 0.2 μG – 0.3 μG strong, similar to earlier estimates by Han & Qiao (1994) on the basis of Galactic pulsars.

In **chapter 9** we combine the information from the diffuse Galactic emission and extragalactic sources from our 4 WSRT data sets and WENSS, with literature values on pulsars, extragalactic sources, and diffuse emission, to study the properties of the large-scale magnetic field in the second Galactic quadrant. We compare our method for deriving dispersion measures from Wisconsin Hα Mapper (WHAM) Hα intensities to the dispersion measures from the model by Cordes & Lazio. As it turns out, our method works well at Galactic latitudes $|b| > 5^o$. With all the information that we compiled on Faraday depths and rotation measures, and by using the dispersion measures from WHAM and (at $|b| < 5^o$) the DM calculated from the Cordes & Lazio model, we derive $\langle B_\parallel \rangle$ for all these sources. Pulsars and extragalactic sources often yield the same average magnetic field strength, which is not a trivial result, since the lines-of-sight to these sources have very different length. The diffuse emission shows magnetic field strengths equal to or less than the magnetic field strengths that we derive for pulsars and extragalactic sources. However, since we used the dispersion measures for the entire line-of-sight through the Galaxy to calculate $\langle B_\parallel \rangle$ for the diffuse emission, we can only determine lower limits to the magnetic field strength from the diffuse emission. We compare the $\langle B_\parallel \rangle$ from all these different sources to the best available model of the large-scale magnetic field. The model shows a much stronger gradient with Galactic longitude in $\langle B_\parallel \rangle$ than we observe. This can be explained by a large-scale reversal in the magnetic field direction in the outer Galaxy, but different authors disagree if such a reversal can exist in these regions. The data also show much more correlation on angular scales in between the scales that I modeled, and the smallest scales that I can still address with my data.

Chapter 2

WSRT Faraday tomography of the Galactic ISM at $\lambda \sim 0.86$ m - First results for the GEMINI data set at $(l, b) = (181^\circ, 20^\circ)$

Abstract. We present a Faraday tomography analysis of WSRT data towards the Galactic anti-centre. With Faraday tomography we can study the distribution and properties of Faraday-rotating and synchrotron-emitting regions along the line-of-sight. We developed a new method to calculate a linear fit to periodic data, which we use to determine rotation measures from our polarization angle data. From simulations of a Faraday screen + noise we could determine how compatible the data are with Faraday screens. An unexpectedly large fraction of 14% of the lines-of-sight in our data set show an unresolved main component in the Faraday depth spectrum. For lines-of-sight with a single unresolved component we demonstrate that a Faraday screen in front of a synchrotron emitting region that contains a turbulent magnetic field component can explain the data.

D. H. F. M. Schnitzeler, P. Katgert, and A. G. de Bruyn
Astronomy & Astrophysics, **471**, L21 (2007)

2.1 Introduction

FARADAY tomography is a very powerful tool for studying the relative line-of-sight distribution of regions with synchrotron emission and Faraday rotation. If the thermal plasma does not emit its own synchrotron radiation it simply acts as a Faraday rotating screen for any linearly polarized radiation that illuminates it from the back. However, if the thermal plasma co-exists with relativistic particles which emit (linearly polarized) synchrotron radiation, the situation can be much more complex. This is because the contributions from various parts of the line-of-sight through the plasma combine vectorially, which may even lead to complete cancellation (at certain wavelengths) of the polarized signal emitted in the plasma.

For a simple Faraday screen, the amount of rotation of the plane of linear polarization gives direct information on the Faraday depth $\mathcal{R}$ [rad/m^2] of the screen: $\mathcal{R} = 0.81 \int_{\text{source}}^{\text{observer}} n_e \vec{B} \cdot \mathrm{d}\vec{l}$, the line-of-sight integral of the product of the electron density [cm^{-3}] and the magnetic field component [μG] along the line-of-sight [pc]. In that case, $\mathcal{R}$ and the rotation measure RM = $\partial\,\Phi/\partial\,\lambda^2$ (where Φ is the polarization angle of the radiation) are identical. In the more general case, with a mixture of synchrotron emitting and Faraday rotating layers along the line-of-sight, the relation between RM and $\mathcal{R}$ becomes more complicated. Sokoloff et al. (1998) have calculated the result for various geometries of synchrotron emitting and Faraday rotating layers. When the synchrotron emissivity and Faraday rotation are both constant per unit line-of-sight (a so-called 'Burn slab', Burn 1966), RM = 0.5 $\mathcal{R}_{\text{max}}$, where $\mathcal{R}_{\text{max}}$ is the Faraday depth of the far side of the slab. Sokoloff et al. showed that this is true for any distribution that is mirror-symmetric along the line-of-sight.

We present a first discussion of the use of WSRT observations at $\lambda \sim 0.86$ m, of the linearly polarized component of the diffuse Galactic synchrotron emission towards the Galactic anti-centre. By using Faraday tomography we investigate the properties of the magneto-ionic ISM in this direction, and in particular the abundance of Faraday screens.

2.2 The data

The present data set was obtained with the WSRT, a 14-element E-W interferometer of which 4 elements are moveable to improve (u,v) coverage. We used the mosaicking technique to map an area of about 7×7 degrees^2 with 49 pointings. The distance between pointings was chosen such that instrumental polarization is suppressed to less than 1% (Wieringa et al. 1993). In our analysis we leave out the edge of the mosaic where instrumental polarization effects cannot be suppressed by mosaicking. We also exclude lines-of-sight for which instrumental polarization of off-axis sources is an important factor. The central coordinates of this field (in the constellation Gemini) are $\alpha = 7^h18^m$ and $\delta = 36°24'$ (J2000.0), which is $l \approx 181°$ and $b \approx 20°$ in Galactic coordinates. The observations cover the frequency range between 315 and 385 MHz, with 213 usable independent spectral channels of about 0.4 MHz each. The field was observed for 6 nights (@ 12 hrs each) in December 2002 and January 2003. This yielded visibilities at baselines from 36 to 2760 meters, with an increment of 12 meters. The results we

discuss here were obtained with a Gaussian taper that decreases the resolution to $2.2' \times 3.7'$ (FWHM at 350 MHz).

The data were reduced using the NEWSTAR data reduction package. Dipole gains and phases and leakage corrections were determined using the unpolarized calibrators 3C48, 3C147 and 3C295. Due to an a-priori unknown phase offset between the horizontal and vertical dipoles, signal can leak from Stokes U into Stokes V. We corrected for this by rotating the polarization vector in the Stokes (U, V) plane back to the U axis, assuming that there is no signal in V. The polarized calibrator sources 3C345 and DA240 defined the sense of derotation (i.e. to the positive or negative U-axis). Special care was taken to avoid automatic flagging of real signal on the shortest baselines. From 2 lines-of-sight with a strong polarized signal we estimate that the amounts of ionospheric Faraday rotation in the 6 nights are identical to within $\sim 10^\circ$, so we did not correct for that.

Structure on large angular scales in Stokes Q and U will have been filtered out because we have no information on baselines below 36 meters. We discuss the influence of this on our results in Sect. 2.3.2.

2.3 Analysis

2.3.1 Methods

The wide coverage in λ^2 space (from 0.6 m^2 $\lesssim \lambda^2 \lesssim$ 0.9 m^2), combined with the relatively small channel width, allows us to do Faraday tomography, also known as Rotation Measure Synthesis (see e.g. Brentjens & De Bruyn 2005), which probes the distribution of Faraday rotating and synchrotron emitting regions along the line-of-sight. In Faraday tomography the polarization vectors of the individual channels are 'coherently added' by derotating the vectors using an assumed Faraday depth $\mathcal{R}$: $\vec{P}(\mathcal{R}) = \int P(\lambda^2)\, \mathrm{e}^{2\mathrm{i}\Phi(\lambda^2)} \mathrm{e}^{-2\mathrm{i}\mathcal{R}\lambda^2} \mathrm{d}\lambda^2$, where $P(\lambda)$ and $\Phi(\lambda)$ are the polarized intensity and polarization angle of an individual channel at wavelength λ. $P(\mathcal{R}) = |\vec{P}(\mathcal{R})|$ is the intensity of the polarized emission at Faraday depth $\mathcal{R}$, and a Faraday depth spectrum (or $\mathcal{R}$ spectrum) can be constructed by calculating $P(\mathcal{R})$ and $\arg(\vec{P}(\mathcal{R}))$ for many values of $\mathcal{R}$. We calculated $\mathcal{R}$ spectra between -72 rad/m^2 and +72 rad/m^2 in steps of 1 rad/m^2. Previous surveys indicate that the $\mathcal{R}$ of the diffuse emission in this volume of the Galaxy lie well within this range (see e.g. Spoelstra 1984). The Rotation Measure Spread Function (RMSF) of the $P(\mathcal{R})$-determination, which is the Fourier Transform of the λ^2-sampling of the data, has for our data a FWHP of about 12 rad/m^2. From simulations of the noise in the individual channels we estimate that 99% of the noise realisations will lie below the 0.7 K level in our $\mathcal{R}$ spectra.

We quantified the behaviour of the $\mathcal{R}$ spectrum in two ways. First, we derived a measure of the symmetry of the $\mathcal{R}$ spectrum as a whole, by calculating the reduced χ^2 (χ^2_{red}) of a linear fit to the $\Phi(\lambda^2)$ data. A Faraday screen or a symmetric distribution of Faraday rotating and synchrotron emitting regions along the line-of-sight (for example a Burn slab) will show a linear $\Phi(\lambda^2)$ dependence. The χ^2_{red} of a linear fit to the $\Phi(\lambda^2)$ distribution can therefore separate symmetric and more complex distributions along the line-of-sight.

Fitting periodic data like polarization angles requires that the $n180^\circ$ periodicity of

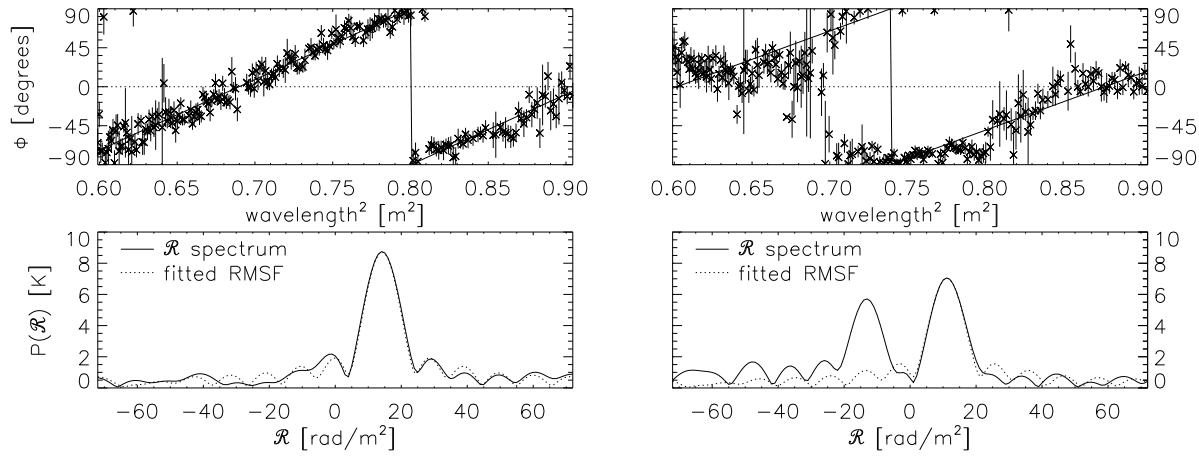

Figure 2.1 — $\Phi(\lambda^2)$ distribution (top panels) and $\mathcal{R}$ spectrum (bottom panels) for a line-of-sight with a main peak that is similar to a Faraday screen (low Δ; left column), and for a line-of-sight with two peaks in the $P(\mathcal{R})$ spectrum (right column). The $\chi^2_{\rm red}$ of the RM fit to the polarization angles in the top left panel is 1.02, and the RM fit to the polarization angles in the top right panel has a $\chi^2_{\rm red}$ = 10.58 (determined by using the RM with the maximum P(RM) - see the text).

$\Phi(\lambda)$ is properly taken into account. In chapter 8 we will introduce a method that finds the lowest-$\chi^2_{\rm red}$ straight-line fit to polarization angle data by going through all the possible 180° wraps of polarization angles that are allowed by the data. However, the number of configurations of wraps of the individual datapoints increases strongly with the number of datapoints. For the present data set, with of order 200 $\Phi(\lambda)$-values for each line-of-sight, application of that method is thus not practical.

However, by writing $\Phi(\lambda^2)$ as the complex number $e^{2i\Phi(\lambda^2)}$, the RM spectrum can be calculated: $P(\mathrm{RM}) = |\vec{P}(\mathrm{RM})| = |\int e^{2i\Phi(\lambda^2)} e^{-2i\ \mathrm{RM}\lambda^2} d\lambda^2|$. The power P(RM) shows which RM 'frequencies' create the observed $\Phi(\lambda^2)$ dependence. If Φ depends linearly on λ^2, the RM with the maximum P(RM) will be the best fitting slope for the data. If the RM spectrum is more complicated, the RM with the maximum P(RM) will not give the best linear fit to the $\Phi(\lambda^2)$, and the $\chi^2_{\rm red}$ of this fit will be higher than that of the best linear fit to the $\Phi(\lambda^2)$. Even the best linear fit to the $\Phi(\lambda^2)$ will then have a large $\chi^2_{\rm red}$.

The second criterion quantifies the deviation of the main peak in the $\mathcal{R}$ spectrum from a Faraday screen, in the presence of noise. We define Δ as the root-mean-square vertical separation in the $\mathcal{R}$ spectrum between a peak in the $\mathcal{R}$ spectrum and the RMSF that is scaled to the same height as the peak. Δ is calculated over the RMSF out to the point where the RMSF goes through its first minimum, at a distance of 10 rad/m^2 from the centre of the peak. A Faraday screen will show up as an unresolved peak in the $\mathcal{R}$ spectrum, which means that its Δ will be lower than that of a peak in the $\mathcal{R}$ spectrum that is too broad to be fitted by a RMSF. By comparing the Δ we find for the main peak in each line-of-sight to the distribution of Δ of a Faraday screen + noise, we can quantify how improbable it is that the main peak is due to a Faraday screen.

In Fig. 2.1 we show the $\Phi(\lambda^2)$ distributions and $\mathcal{R}$ spectra for two lines-of-sight that have a main peak that is similar to a Faraday screen (i.e. low Δ). The line-of-sight plotted in the left column has a simple $\mathcal{R}$ spectrum and low $\chi^2_{\rm red}$, the line-of-sight plotted in the right column has a complicated $\mathcal{R}$ spectrum and high $\chi^2_{\rm red}$. The column

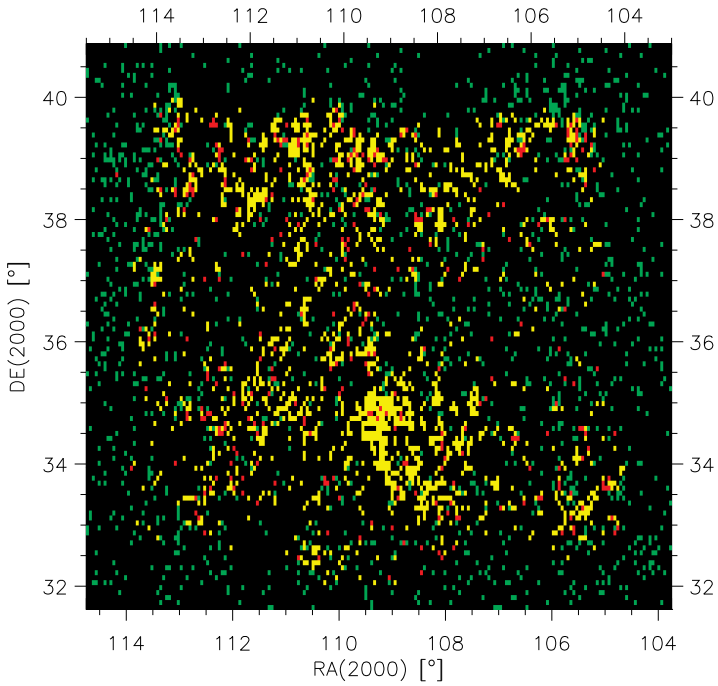

Figure 2.2 — Distribution of independent lines-of-sight with a main peak that satisfies the Δ criterion (green pixels), or with $\chi^2_{\rm red} < 2$ and $\max(P(\mathcal{R})) > 2$ K (yellow pixels), or that satisfy all three criteria (red pixels). Lines-of-sight that did not pass these criteria are shown as black pixels. The pixel size is $2.2' \times 2.2' \csc(\delta)$. The outer edges of the mosaic show an increase in $\chi^2_{\rm red}$, which explains the absence of yellow pixels. Page 188 shows a colour version of this figure from chapter 3.

on the right of Fig. 2.1 shows that low Δ are also found for lines-of-sight with higher $\chi^2_{\rm red}$. In this case the high $\chi^2_{\rm red}$ is due to the presence of multiple components in the $\mathcal{R}$ spectrum.

2.3.2 Results

From a total of 22.800 independent lines-of-sight in our data set, 1757 lines-of-sight have a $\chi^2_{\rm red} < 2$ and a maximum in the $\mathcal{R}$ spectrum > 2 K, about 2.5 times the level below which 99% of the noise $P(\mathcal{R})$ lie. In Fig. 2.2 we plot the sky distribution of these 1757 lines-of-sight as yellow pixels. We indicate the lines-of-sight that furthermore have a main peak whose Δ is less than 99% of the Δ that we found in our simulations of a Faraday screen + noise as red pixels. The pixels in Figs. 2.2 to 2.4 indicate independent lines-of-sight. These figures cover Galactic longitudes from $(l, b) = (178^\circ, 26^\circ)$ in the top left corner to $(l, b) = (185^\circ, 15^\circ)$ in the bottom right corner. The Galactic plane has a position angle (north through east) of about 21° relative to the vertical axis in these plots.

In Figs. 2.3 and 2.4 we plot the distribution on the sky of $P(\mathcal{R})$ and $\mathcal{R}$ of the main peak in the $\mathcal{R}$ spectrum. Ionosphere models indicate that it contributes only 0.6 rad/m^2 to the $\mathcal{R}$ shown in Fig. 2.4 (Johnston-Hollitt, private communication). For these maps we selected lines-of-sight where the $\mathcal{R}$ spectrum is dominated by a main peak, by requiring that this peak should be at least twice as high as the second bright-

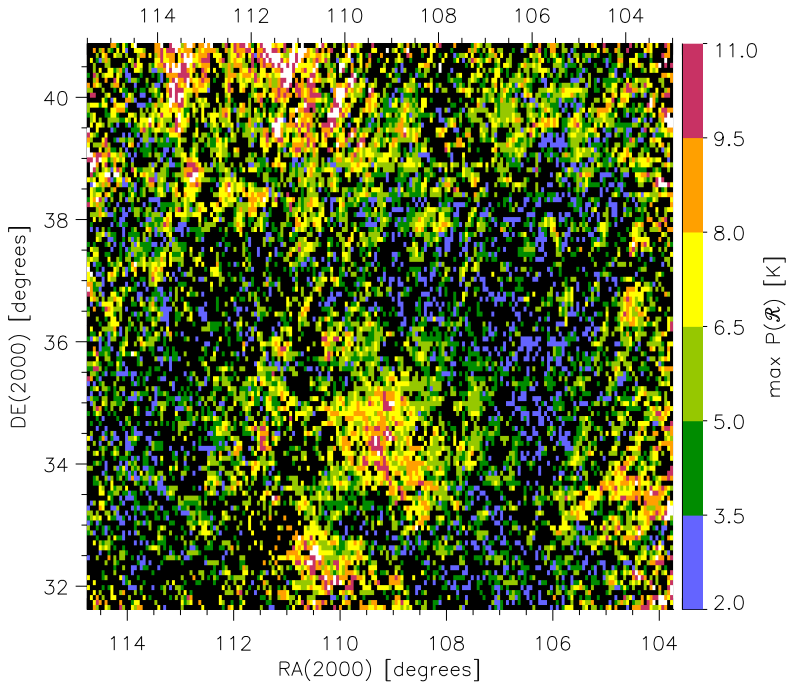

Figure 2.3 — $P(\mathcal{R})$ of the highest peak in the $\mathcal{R}$ spectrum for lines-of-sight where the secondary peak in the $\mathcal{R}$ spectrum has at most half the strength of the main peak. Lines-of-sight that do not pass the selection criteria are shown in black, together with 455 lines-of-sight that have $P(\mathcal{R}) < 2$ K. Page 186 shows a colour version of this figure from chapter 3.

est peak. Lines-of-sight selected in this way show a tight correlation between $\mathcal{R}$ and RM, with a 1σ scatter of about 0.2 rad/m^2.

Structure on large angular scales in Stokes Q and U (and therefore in polarized intensity P and polarization angle Φ) will not be picked up by an interferometer. However, if large-scale structure were produced at the same $\mathcal{R}$ as the emission visible in Fig. 2.3, the large $\mathcal{R}$ gradients per pointing in Fig. 2.4 create structure in Φ on small enough angular scales that can be picked up by the WSRT. Large-scale structure would then become 'visible' by passing through the Faraday rotating foreground with these $\mathcal{R}$ gradients, and Figs. 2.3 and 2.4 therefore form more or less 'complete' maps in that they contain most of the emission at those Faraday depths. In Sect. 3.4.2 we worked out this idea quantitatively, and there we show that the Faraday depth gradients from Fig. 2.4 are strong enough to make the large-scale structure emitted at these Faraday depths visible.

2.3.3 Faraday screens

The main peak in 3086 lines-of-sight (14% of the total number of independent lines-of-sight) has a Δ that is less than 99% of the Δ we found in our simulations of a Faraday screen + noise, making these main peaks indistinguishable from Faraday screens. These lines-of-sight are indicated as green pixels in Fig. 2.2. These peaks also closely follow the $\mathcal{R}$ = RM relation expected for Faraday screens, with a 1σ scatter of about 0.2 rad/m^2. The actual fraction of lines-of-sight with Faraday screen components in

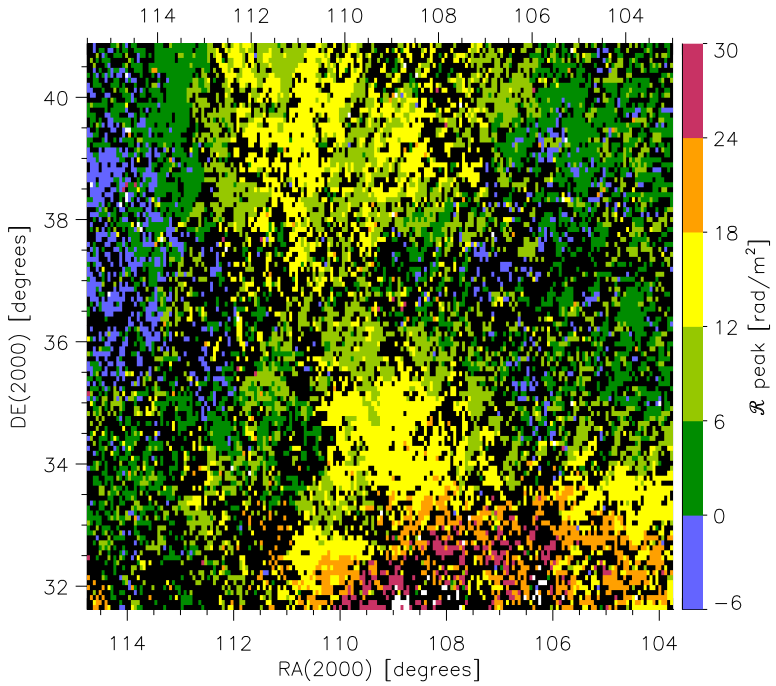

Figure 2.4 — $\mathcal{R}$ corresponding to the $P(\mathcal{R})$ plotted in Fig. 2.3. The lines-of-sight plotted in these figures are selected by using the same criteria. Lines-of-sight indicated in white have $\mathcal{R} > 30$ rad/m^2. Lines-of-sight indicated in black either did not pass the selection criteria or have $\mathcal{R} <$ -6 rad/m^2 (652 and 9734 lines-of-sight resp.). Page 187 shows a colour version of this figure from chapter 3.

their $\mathcal{R}$ spectrum can be higher than 14% since we only tested the main peak of the $\mathcal{R}$ spectrum with our Δ criterion.

Radio frequency interference and/or an underestimation of the noise levels will increase the values of Δ expected for a Faraday screen + noise. The lines-of-sight that already pass this criterion with our conservative choice for calculating Δ will then still pass the Δ criterion; there could however be more lines-of-sight that would qualify as Faraday screens.

2.4 Discussion

We first estimate the implied value of the large-scale magnetic field, for a representative value of $\mathcal{R} = +10$ rad/m^2 (Fig. 2.3). If the Faraday rotating region has a depth L and consists of clumps of electrons with a constant density n_e that occupy a fraction f of L, with $n_e = 0.08$ cm^{-3} and $f = 0.4$ (Reynolds 1991), L follows from observations of the emission measure, EM. The EM from the Wisconsin Hα mapper (WHAM; Haffner et al. 2003) are on average 2 Rayleigh in this region, or 4 cm^{-6}pc for a 10^4 K gas, which indicates a line-of-sight of 1.5 kpc length. For these lines-of-sight extinction of the Hα line plays only a minor role. The DM = 50 cm^{-3}pc implied by this model agrees well with the DM = 54 cm^{-3}pc calculated from the NE2001 model by Cordes & Lazio (2003) for a line-of-sight in the same direction and of the same length.

For this model the integral for $\mathcal{R}$ is also easy to solve. By using the same n_e, f and L, the large-scale magnetic field component along the line-of-sight, $B_{\mathrm{reg},\parallel}$, must be about

0.2 μG to explain the average $\mathcal{R}$ = 10 rad/m^2 present in our data. If part of the Hα emission is coming from beyond the Faraday rotating region, we would overestimate the depth L of the Faraday rotating layer, and the $B_{\mathrm{reg},\parallel}$ we derive would be too low. A reasonable upper limit for $B_{\mathrm{reg},\parallel}$ can be found by adopting a pitch angle of 8° and a total strength of 4 μG for the large-scale field (both values from Beck 2007a), which gives $B_{\mathrm{reg},\parallel,\mathrm{max}} \approx 0.6$ μG. Note that the change of sign of $\mathcal{R}$ in Fig. 2.4 indicates that the observed features are also partly due to variations in the magnetic field geometry and not only to variations in the electron density.

From the Haslam et al. (1982) 408 MHz data we estimate that the Galactic foreground in this direction has a brightness temperature of 36 K at 350 MHz, assuming a -2.7 spectral index for the synchrotron brightness temperature. For a completely uniform magnetic field and without internal Faraday rotation the peak in the $\mathcal{R}$ spectrum would have a polarized brightness temperature, $T_{\mathrm{b,pol}}$, of 70% of this, or 25 K, but the $T_{\mathrm{b,pol}}$ of the peak in the $\mathcal{R}$ spectrum is on average only 5 K. A similar discrepancy between the expected and measured $T_{\mathrm{b,pol}}$ was noted for a field observed with the WSRT at (l, b)=(110°,71°) (De Bruyn et al. 2006).

If the $\mathcal{R}$ distribution has a finite width, the 25 K is diluted over the entire width, and the peak of the distribution will have lower $P(\mathcal{R})$. Any further reduction of $P(\mathcal{R})$ requires a turbulent magnetic field in the emitting region. For lines-of-sight with a single, essentially unresolved peak in the $\mathcal{R}$ spectrum (i.e. with a low value of Δ) it is not trivial to separate the two effects. We simulated a layer with both uniform and Gaussian distributions of coexisting Faraday rotation and synchrotron emission. From these simulations we conclude that it is not possible to reduce the $T_{\mathrm{b,pol}}$ of the maximum in the $P(\mathcal{R})$ spectrum below 20 K, and be consistent with the observed low value of Δ. Therefore a turbulent magnetic field component is required to explain the observed $T_{\mathrm{b,pol}}$.

Another possible picture for these lines-of-sight with small Δ could be a combination of an $\mathcal{R}$-extended structure and an emission region with a turbulent magnetic field. However, since the $\mathcal{R}$-extended structure has to be narrow to pass our Δ criterion, the depth of this structure will not be enough to explain the 10 rad/m^2 average Faraday depth in Fig. 2.3. A Faraday screen is then required to produce the bulk of this Faraday depth.

An extreme example of this would be an emission region with a turbulent field, observed through a Faraday screen, which would be the simplest and most straightforward explanation. In that case we can also estimate the relative strengths of the turbulent magnetic field and the magnetic field component perpendicular to the line-of-sight, B_{turb} and $B_{\mathrm{reg},\perp}$ resp. If the synchrotron emitting region contains both $B_{\mathrm{reg},\perp}$ and B_{turb}, the expected polarization fraction is reduced by a factor of $B^2_{\mathrm{reg},\perp}/(B^2_{\mathrm{reg},\perp} + B^2_{\mathrm{turb}})$ (Burn 1966). To reduce the expected 25 K polarized brightness temperature to 5 K then requires $B_{\mathrm{turb}}/B_{\mathrm{reg},\perp} \approx 2$. This ratio is an upper limit if there are other components in the $\mathcal{R}$ spectrum that contribute to the predicted $T_{\mathrm{b,pol}}$ = 25 K.

The region around (α, δ) = (109°,35°) shows some conspicuous features. It is bright in polarized intensity, shows a low χ^2_{red}, and also contains a number of lines-of-sight that could be Faraday screens. The band between $36° \lesssim \delta \lesssim 38°$ contains many lines-of-sight with high χ^2_{red} and broad main peaks and/or significant secondary peaks in

the $\mathcal{R}$ spectrum. We will discuss these regions in a future article.

2.5 Conclusions

We used high spectral resolution radio polarization data to study the Galactic ISM, and we demonstrated a number of tools that can be used for this purpose. In the present data set we identified a significant number of lines-of-sight that show an unresolved peak in their Faraday depth spectrum, similar to a Faraday screen. We also studied the spatial behaviour of the principal component in the Faraday depth spectrum, and for the lines-of-sight that only have one unresolved component in their $\mathcal{R}$ spectrum, we showed that a model of a Faraday rotating region in front of a synchrotron emitting region that contains a turbulent magnetic field component can explain the data.

Acknowledgements

We would like to thank Dan Stinebring for his comments on an earlier version of the manuscript. DS would also like to thank Russ Taylor and Jeroen Stil for pointing out an important flaw in an earlier version of the 'missing large-scale structure' argument. The Westerbork Synthesis Radio Telescope is operated by the Netherlands Foundation for Research in Astronomy (NFRA) with financial support from the Netherlands Organization for Scientific Research (NWO). The Wisconsin H-Alpha Mapper is funded by the National Science Foundation.

Chapter 3

WSRT Faraday tomography of the Galactic ISM at $\lambda \sim 0.86$ m - I. The GEMINI data set at $(l, b) = (181^\circ, 20^\circ)$

Abstract. We investigate the properties of the Galactic ISM by applying Faraday tomography to a radio polarization dataset in a direction towards the Galactic anti-centre. We address the problem of missing large-scale structure in our data, and show that this does not play a role for the results we present. The main peak of the Faraday depth spectra in our dataset is not measurably resolved for about 8% of the lines-of-sight. An unresolved peak indicates a separation between the regions with Faraday rotation and synchrotron emission. However, cosmic rays pervade the ISM, and synchrotron emission would therefore also be produced where there is Faraday rotation. We suggest that the orientation of the magnetic field plays an important role in separating the two effects. By modeling the thermal electron contribution to the Faraday depth, we map the strength of the magnetic field component along the line-of-sight. Polarized point sources in our dataset have rotation measures that are comparable to the Faraday depths of the diffuse emission in our data. With the thermal electron density model, we estimate that even though the line-of-sight towards extragalactic sources is longer than the line-of-sight towards the diffuse emission, this only gives a small increase in rotation measure for extragalactic sources in this part of the Galaxy, compared to the Faraday depths of the diffuse emission. Our Faraday depth maps show narrow canals of low polarized intensity. We conclude that depolarization over the telescope beam plays an important role in creating at least some of these canals. Finally, we investigate the properties of one conspicuous region in this dataset and argue that it is created by a decrease in line-of-sight depolarization compared to its surroundings.

D. H. F. M. Schnitzeler, P. Katgert and A. G. de Bruyn
Submitted to Astronomy & Astrophysics

3.1 Introduction

FARADAY rotation, the rotation of the plane of linear polarization due to the birefringence of a magneto-ionic medium, provides a powerful tool to explore the magnetic universe, complementing effects such as Zeeman splitting and the alignment of ellipsoidal dust grains perpendicular to magnetic field lines. From external galaxies we have learnt about the global structure of the magnetic field, its alignment with the galactic spiral arms, and that the magnetic pressure is an important factor in ISM dynamics, comparable to the thermal pressure in the cold and warm neutral phases of the ISM (see Beck 2007a, 2007b).

In the Milky Way, rotation measures of pulsars, combined with dispersion measures, yield a rather complicated picture of the large-scale Galactic magnetic field, with evidence for several field reversals (see e.g. Han 2006). Rotation measures of extragalactic sources from the International Galactic Plane Survey (IGPS) indicate a simpler structure of the large-scale field, without much evidence for many field reversals (Brown et al. 2007)

Studies of Faraday rotation of the diffuse Galactic ISM offer a big advantage over other investigations based on pulsars and extragalactic sources, and that is that the diffuse emission is visible in all directions. This has been spectacularly demonstrated by the 1.41 GHz survey carried out with the DRAO 26m telescope by Wolleben et al. (2006). A milestone in this type of work is the polarization survey by Brouw & Spoelstra in the late 1970s (Brouw & Spoelstra 1976 and Spoelstra 1984), which has the largest sky coverage in rotation measures of the diffuse emission to date. Since the 1990s interferometric studies at low frequencies have led to new insights in e.g. the properties of the ISM on small scales, and on turbulence in the Galactic ISM (Wieringa et al. 1993; Haverkorn et al. 2004a and 2006a).

Recently, a method called Faraday tomography has been developed with which one can study the relative distribution of synchrotron emitting and Faraday rotating regions along the line-of-sight (see Brentjens & De Bruyn 2005). Application of this technique for studying the Galactic ISM is a very new field of research, and not much literature is available on this subject. In chapter 2 we discussed a low-frequency dataset that covers $\approx\ 50^{\square}$ in the direction of (l, b) = (181°, 20°), that we obtained with the WSRT. We concluded that many lines-of-sight contain at least one Faraday screen, a region in which Faraday rotation and synchrotron emission are not mixed. This result appears counterintuitive, since one would expect synchrotron-emitting cosmic rays to be present everywhere there are magnetic fields. In this chapter we present the full analysis of this dataset.

Faraday tomography promises to become an interesting and exciting way to investigate the Galactic ISM that will become more and more available in the near future, with the advent of new surveys and radio telescopes that combine high spatial resolution with high frequency resolution, like the GALFACTS survey that is carried out with the Arecibo telescope (Taylor 2004), the LOFAR array (Röttgering et al. 2006), and the MWA SKA-precursor (Bowman et al. 2006). A better understanding of the Galactic foreground will also be useful for studies of the cosmic microwave background.

This chapter is the first in a series of chapters in which we discuss different regions

in the second Galactic quadrant. In this chapter we discuss some of the observational features that we encounter, and we extend some of the techniques that have been used to study the diffuse Galactic ISM with a relatively small number of frequency channels to the many-channel regime. First, we give a short overview of Faraday tomography in Sect. 3.2, and we illustrate its potential with a couple of examples. In Sect. 3.3 we discuss the observational characteristics of the GEMINI dataset, and in Sect. 3.4 we present the GEMINI data. We show that Faraday modulation in the foreground can convert polarized emission on large angular scales to smaller angular scales, that can be picked up by an interferometer that has no short baselines. We derive the magnetic field strengths implied by the observed Faraday depths of the diffuse emission in Sect. 3.5, and in Sect. 3.6 we compare the Faraday depths we derive for the GEMINI dataset with the rotation measures that we find for polarized point sources. One conspicuous feature in the GEMINI data are the dark canals in the maps at constant Faraday depth, and we investigate their origin in Sect. 3.7. In Sect. 3.8 we present an explanation for a large and bright polarized region in our dataset.

3.2 Notes on Faraday tomography

3.2.1 Faraday tomography

The wide coverage in λ^2 space of our data (from 0.6 $\mathrm{m}^2 \lesssim \lambda^2 \lesssim 0.9\ \mathrm{m}^2$), combined with the relatively small channelwidth ($\delta\lambda^2 \approx 1.5 \times 10^{-3}\ \mathrm{m}^2$), allows us to do Faraday tomography, also known as Rotation Measure Synthesis (see e.g. Brentjens & De Bruyn 2005). In this section we introduce the concept of Faraday tomography, and we illustrate how it can be used to study the properties and the relative distribution of regions with Faraday rotation and synchrotron emission along the line-of-sight.

The observed Stokes parameters $Q(\lambda)$ and $U(\lambda)$ are the 2 orthogonal components of the polarization vector $\vec{P}(\lambda) = Q(\lambda) + \mathrm{i}U(\lambda)$. $\vec{P}(\lambda)$ is the vector sum of all polarization vectors that are emitted along the line-of-sight and that are Faraday rotated in the ISM between the point of emission and the observer:

$$\vec{P}(\lambda) \;=\; \int_0^\infty \vec{P}(\mathrm{x})\, \mathrm{e}^{2\mathrm{i}\mathcal{R}(\mathrm{x})\lambda^2} \mathrm{dx} \;=\; \int_{-\infty}^{\infty} \vec{P}(\mathcal{R})\, \mathrm{e}^{2\mathrm{i}\mathcal{R}\lambda^2} \mathrm{d}\mathcal{R} \tag{3.1}$$

where the first integral is over physical distance 'x', and the Faraday depth of point 'x'

$$\mathcal{R}(x)\,[\mathrm{rad/m^2}] \;=\; 0.81 \int_{\text{source at 'x'}}^{\text{observer}} n_e\,[\mathrm{cm^{-3}}]\, \vec{B}\,[\mu\mathrm{G}] \cdot \mathrm{d}\vec{l}\,[\mathrm{pc}] \tag{3.2}$$

measures the total amount of Faraday rotation between the point of emission 'x' and the observer. In the second integral of Eqn. 3.1 we have replaced the integral over physical distance by an integral over Faraday depth. If there is a one-to-one correspondence between x and $\mathcal{R}$, this change in coordinate is trivial. However, a change in the direction of the magnetic field component along the line-of-sight $B_\parallel = \vec{B} \cdot \mathrm{d}\vec{l}$ assigns the same $\mathcal{R}$ to different x. To go back from $\mathcal{R}$ to 'x' thus requires assumptions

on the magnetic field geometry. In a future article we will return to this issue. Faraday tomography is based on the inversion of the second integral in Eqn. 3.1:

$$\vec{P}(\mathcal{R}) = K \int_{-\infty}^{\infty} \vec{P}(\lambda^2)\, \mathrm{e}^{-2\mathrm{i}\mathcal{R}\lambda^2} \mathrm{d}\lambda^2 \tag{3.3}$$

$$K = \left(\int_{-\infty}^{\infty} W(\lambda^2)\, \mathrm{d}\lambda^2 \right)^{-1} \tag{3.4}$$

produces the correct normalization for $\vec{P}(\mathcal{R})$. $W(\lambda^2) = 1$ if the λ^2 has been observed, otherwise $W(\lambda^2) = 0$. This inversion can be interpreted either as a 'coherent addition' of the observed $\vec{P}(\lambda)$ by using an assumed Faraday depth to derotate the polarization vectors, or, similarly, as a Fourier transform from λ^2 space to $\mathcal{R}$ space. Note that the integral is also calculated over negative values of λ^2, which is physically impossible. If the measured $P(\lambda^2)$ are in K (mJy/beam), then also the $P(\mathcal{R})$ will be in K (mJy/beam), or, more precisely, in K/RMSF width (mJy/beam/RMSF width). If we want to compare different data sets, with different RMSFs, it is necessary to convert this quantity to K/rad/m^2 instead of K/RMSF (equivalently for mJy/rad/m^2). Here we only consider one dataset, and we did not convert the measured $P(\mathcal{R})$ to K/rad/m^2.

The complex polarization vector $\vec{P}(\lambda)$ can be written in terms of the observed polarized intensity $P(\lambda)$ and polarization angle $\Phi(\lambda)$ as $\vec{P}(\lambda) = P(\lambda)\, \mathrm{e}^{2\mathrm{i}\Phi(\lambda)}$. Similarly, $\vec{P}(\mathcal{R}) = P(\mathcal{R})\, \mathrm{e}^{2\mathrm{i}\Phi(\mathcal{R})}$, where $P(\mathcal{R})$ is the intensity of the polarized emission at Faraday depth $\mathcal{R}$, and $\Phi(\mathcal{R})$ is the orientation of the electric field vector of the synchrotron radiation emitted at Faraday depth $\mathcal{R}$, which is perpendicular to the local direction of the magnetic field at that Faraday depth. A Faraday depth spectrum (or $\mathcal{R}$ spectrum) can be constructed by calculating $P(\mathcal{R})$ and $\Phi(\mathcal{R})$ for many values of $\mathcal{R}$.

The Fourier-transform nature of Eqn. 3.3 implies that it shares some characteristics with other Fourier-transform based methods like radio interferometry. Eqns. 61 to 63 from Brentjens & De Bruyn (2005) describe this behaviour quantitatively, and for convenience we reproduce these equations here. We assume here that the observations uniformly span the λ^2 range from λ^2_{min} to $\lambda^2_{\mathrm{max}} = \lambda^2_{\mathrm{min}} + \Delta\lambda^2$ with weight 1, and with weight 0 outside this range.

The finite extent in the $\Delta\lambda^2$ coverage of the data introduces an instrumental response along the $\mathcal{R}$ axis, known as the RMSF (Rotation Measure Spread Function), with which the P($\mathcal{R}$) spectrum is convolved. The shape of the (normalized) RMSF is given by

$$\mathrm{RMSF}\,(\mathcal{R}) = K \int_{-\infty}^{\infty} W(\lambda^2)\, \mathrm{e}^{-2\mathrm{i}\mathcal{R}\lambda^2} \mathrm{d}\lambda^2 \tag{3.5}$$

The FWHM of the RMSF depends on the total range in λ^2 space covered by the observations, $\Delta\lambda^2$, according to

$$\text{FWHM [radians/m}^2\text{]} \;=\; \frac{3.8}{\Delta\lambda^2} \tag{3.6}$$

We replaced the factor of $2\sqrt{3}$ from the original paper by Brentjens & De Bruyn by 3.8, because 3.8 is closer to the FWHM of the sinc RMSF response than $2\sqrt{3} \;\approx\; 3.5$.

In general the observations will not cover all wavelengths down to 0 m^2, which means that $\mathcal{R}$-extended structures will be missing from the $P(\mathcal{R})$ spectra. This is similar to the missing large-scale structure problem interferometers suffer from when observing extended emission. If the source has a Gaussian $\vec{P}(\mathcal{R})$ distribution along the line-of-sight, Brentjens & De Bruyn calculate that in the reconstructed $\vec{P}(\mathcal{R})$ spectrum $\mathcal{R}$ scales larger than

$$\text{maximum scale [radians/m}^2\text{]} \;\approx\; \frac{\pi}{\lambda^2_{\text{min}}} \tag{3.7}$$

are suppressed by more than 50% by the missing short wavelengths.

Analogous to how in an interferometer the size of the individual dishes sets the field-of-view, the channelwidth expressed in λ^2, $\delta\lambda^2$, determines the $\mathcal{R}$ for which the sensitivity has dropped to 50% due to smearing of the polarization angles over individual channels, $\mathcal{R}_{\text{max}}$:

$$|\mathcal{R}_{\text{max}}| \text{ [radians/m}^2\text{]} \;=\; \frac{1.9}{\delta\lambda^2} \tag{3.8}$$

Also in this equation we replaced the $\sqrt{3}$ from the paper by Brentjens & De Bruyn by 1.9 because this is closer to the correct value for the HWHM of the sinc RMSF response. Brentjens & De Bruyn discuss the (minor) effect of using (possibly non-contiguous) channels with constant width in frequency instead of λ^2.

The addition of polarization vectors originating at different distances along the line-of-sight in general leads to depolarization, either because the vectors are emitted with different orientations and/or because different amounts of Faraday rotation induce misalignment of the polarization vectors. Faraday tomography can separate the emission coming from subregions with different $\mathcal{R}$ along the line-of-sight, thereby reducing the influence of these sources of depolarization.

Brentjens & De Bruyn (2005) note that one can also derotate the polarization angles of $\vec{P}(\mathcal{R})$ to $\lambda^2 \neq 0$. In that case the λ^2 in the complex exponentials of Eqns. 3.3 and 3.5 are replaced by $(\lambda^2 - \lambda^2_0)$. Brentjens & De Bruyn showed that derotating to the weighted average of the observed λ^2,

$$\lambda^2_0 \;=\; \frac{\int\limits_{-\infty}^{\infty} W(\lambda^2)\lambda^2 \mathrm{d}\lambda^2}{\int\limits_{-\infty}^{\infty} W(\lambda^2)\mathrm{d}\lambda^2} \tag{3.9}$$

minimizes the polarization angle variation over the main peak of the RMSF. However, now the polarization angle at the peak of the RMSF at Faraday depth $\mathcal{R}_{\rm peak}$ is no longer perpendicular to the magnetic field component in the plane of the sky. To determine the orientation of this magnetic field component, one needs to correct the polarization angles Φ by

$$\Phi_0(\mathcal{R}) \; = \; \Phi(\mathcal{R}) - \mathcal{R}_{\rm peak}\lambda_0^2 \tag{3.10}$$

We derotated the polarization angles in the bottom panels of Fig. 3.1 in this way.

3.2.2 Examples

We illustrate for a number of geometries of synchrotron emitting and Faraday rotating regions the resulting $P(\lambda)$ and $\Phi(\lambda)$, as well as the $\vec{P}(\mathcal{R})$ that is reconstructed from the observations.

First, consider the case where there is only one infinitely thin source of emission along the line-of-sight, at Faraday depth $\mathcal{R}_1$: $\vec{P}(\mathcal{R}) \; = \; P_1 \; \delta(\mathcal{R} - \mathcal{R}_1)$, where $\delta(x)$ is the Dirac delta function. Then $\vec{P}(\lambda) = P_1 \; {\rm e}^{2{\rm i}\mathcal{R}_1\lambda^2}$: the $P(\lambda)$ are identical for all observing wavelengths λ, where we assumed that the synchrotron emission has a spectral index of 0. As Brentjens & De Bruyn (2005) have discussed, a non-zero spectral index introduces only a distortion in the RMSF away from the main peak. Φ depends linearly on λ^2, and since the rotation measure RM $\equiv \; \partial \; \Phi / \partial \; \lambda^2$, RM = $\mathcal{R}$ in this case. The $P(\mathcal{R})$ spectrum that is reconstructed from the observed $P(\lambda)$ and $\Phi(\lambda)$ is identical to the original $P(\mathcal{R})$ spectrum, convolved with the RMSF. The situation described in this paragraph occurs in our data: in the left column of Fig. 3.1 we show the measured $\vec{P}(\lambda^2)$ and reconstructed $\vec{P}(\mathcal{R})$ spectra for a line-of-sight with an essentially unresolved $P(\mathcal{R})$ spectrum.

Next, consider the case where there are two peaks of height P_1 and P_2 at Faraday depths $\mathcal{R}_1$ and $\mathcal{R}_2$. In this case $\vec{P}(\lambda) = P_1{\rm e}^{2{\rm i}\mathcal{R}_1\lambda^2} + P_2{\rm e}^{2{\rm i}\mathcal{R}_2\lambda^2}$. This configuration produces a beat in $P(\lambda)$, because the 2 polarization vectors of length P_1 and P_2 rotate at different speeds $\mathcal{R}_1$ and $\mathcal{R}_2$ in the Stokes (Q,U) plane. Note that Φ no longer depends linearly on λ^2, which means that RM will not be constant. The $P(\mathcal{R})$ spectrum that is reconstructed from the observed $\vec{P}(\lambda)$ will show the sum of 2 δ-functions convolved with the RMSF. The peaks in the reconstructed $P(\mathcal{R})$ spectrum will not lie at exactly $\mathcal{R}_1$ and $\mathcal{R}_2$, because the presence of the other peak will influence the shape of both peaks. Therefore, since $\Phi(\mathcal{R})$ is derived for the Faraday depth of the peak in the reconstructed $P(\mathcal{R})$ spectrum, the derived $\Phi(\mathcal{R})$ will not be the intrinsic position angle of the electric field of the emitted synchrotron radiation. When a polarized extragalactic point source is producing one of the 2 peaks, and the diffuse Galactic emission produces the second peak, the $\chi^2_{\rm red}$ of the linear fit of Φ vs. λ^2 will be very high. In the right column of Fig. 3.1 we illustrate this case. The peak at $\mathcal{R}$ = -28 rad/m^2 is produced by an extragalactic source, and the region around $\mathcal{R}$ = +5 rad/m^2 is produced by Galactic emission in the foreground, as we established by comparing this line-of-sight to adjacent lines-of-sight, where the extragalactic source is not present.

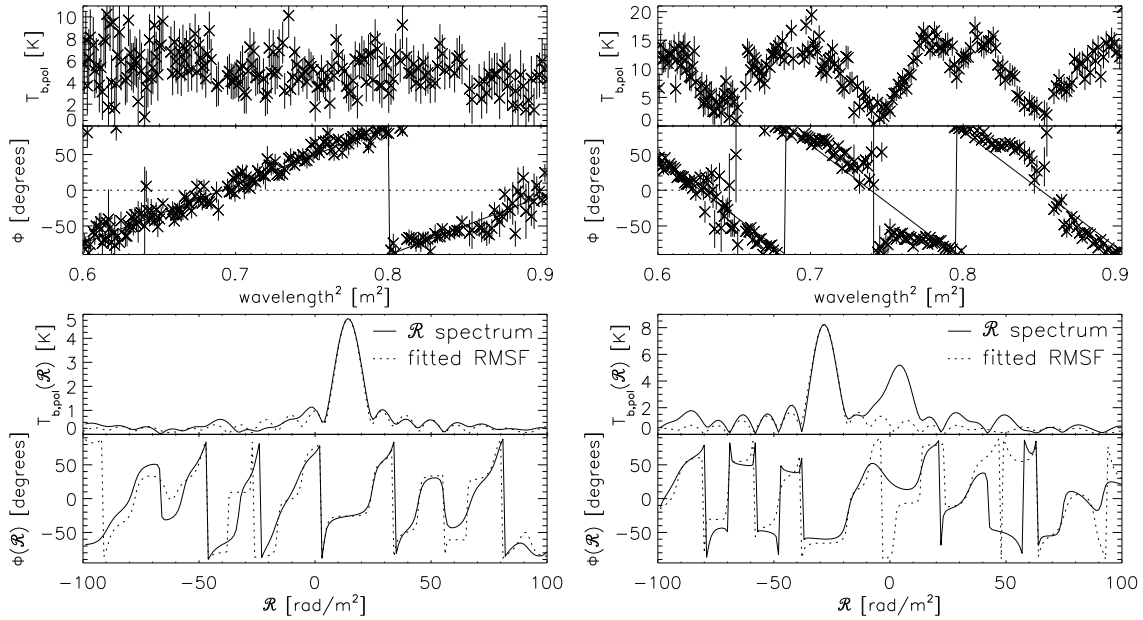

Figure 3.1 — P(λ^2) and $\Phi(\lambda^2)$ distributions (top 2 panels), and P($\mathcal{R}$) and $\Phi(\mathcal{R})$ spectra (bottom 2 panels) for a line-of-sight with a barely resolved main peak that is similar to a Faraday screen (left column) and for a line-of-sight towards a polarized extragalactic source that also contains diffuse Galactic emission (right column). In the text we describe how we derotated the polarization angles in the bottom panel of this figure. The $\chi^2_{\rm red}$ of the RM fit to the polarization angles in the left column is 0.99, and the $\chi^2_{\rm red}$ of the RM fit to the polarization angles in the right column is 8.72 (determined by using the RM with the maximum P(RM)). The $\mathcal{R}$ spectra are sampled from -100 rad/m^2 to +100 rad/m^2 in steps of 1 rad/m^2. In the bottom 2 panels, solid lines indicate the calculated $P(\mathcal{R})$ and $\Phi(\mathcal{R})$ spectra, and the dashed lines indicate the fitted RMSF.

The previous two examples dealt with infinitely thin emission regions. If the emission region has a finite depth, but is not mixed with Faraday rotating ISM, the results we discussed in the previous sections still hold. However, if the emitting and Faraday rotating regions are mixed, the $P(\mathcal{R})$ distribution along the line-of-sight will no longer be a δ-function, and the reconstructed $P(\mathcal{R})$ spectrum will be wider than the width of the RMSF. If the synchrotron-emitting and Faraday rotating regions are fully mixed, and if the emissivity and the amount of Faraday rotation per parsec are independent of the position along the line-of-sight, then

$$\vec{P}(\lambda) \;=\; P_{\rm i}\,\frac{\sin(\mathcal{R}_{\rm max}\lambda^2)}{\mathcal{R}_{\rm max}\lambda^2}\;{\rm e}^{2{\rm i}(\frac{1}{2}\mathcal{R}_{\rm max})\lambda^2} \tag{3.11}$$

where $\mathcal{R}_{\rm max}$ is the Faraday depth of the far side of the slab, and assuming that all radiation along the line-of-sight is emitted with a position angle of 0°. This result was first obtained by Burn (1966), and the distribution of synchrotron-emitting and Faraday-rotating regions along the line-of-sight that produces it has become known as a 'Burn slab'. Note that Φ again depends linearly on λ^2, but that RM = $0.5\mathcal{R}_{\rm max}$. Sokoloff et al. (1998) have shown that a linear dependence of Φ on λ^2 occurs not only for a Burn slab, but for every distribution of synchrotron emitting and Faraday rotating regions that is symmetric along the line-of-sight between the observer and $\mathcal{R}_{\rm max}$. The reconstructed

Table 3.1 — Characteristics of the GEMINI dataset. Observing dates and times are given for each of the 12 hr observing runs, which have been indicated by their shortest baseline length.

Central position	$(\alpha,\delta)_{2000}$ = (109°,36.5°); (l,b) = (181°,20°)					
Mosaic size	$9^\circ \times 9^\circ$					
Pointings	7×7					
Frequencies	324–387 MHz					
	202 independent frequency channels (Hamming taper)					
Resolution[a]	$2.76' \times 4.70'$					
Stokes V noise level	6.2 mJy (2.0 K)					
$\mathcal{R}$ noise level[b]	0.5 mJy (0.14 K)					
Conversion Jy–K[c]	1 mJy/beam = 0.32 K					
Shortest baseline (m)	36	48	60	72	84	96
Observing date (yy/mm/dd)	03/01/17	03/01/21	02/12/18	02/12/05	03/01/22	03/01/13
Start time (UT)	17:04	16:37	18:45	19:36	16:39	17:32
End time (UT)	05:04	04:36	06:43	07:34	04:37	05:31

[a] We tapered the individual frequency channel maps in such a way that the synthesized beamsize for all maps is that of the 385 MHz beam of $2.76' \times 4.70'$(RA×DEC).

[b] This is the noise level in individual $\mathcal{R}$ maps, which we determined from maps at $|\mathcal{R}| > 200$ rad/m^2, that we assume contain no signal. Instrumental polarization increases towards the edges of the maps, therefore we excluded these in determining the noise level.

[c] This is the conversion factor at 345 MHz, the average of the λ^2 sampling of the (usable) frequency channels in our dataset. We used the FWHM of a Gaussian fitted to the central peak of the synthesized PSF to calculate the beamsize required in this conversion.

$P(\mathcal{R})$ spectrum of a Burn slab, has a finite extent, and may even be wider than the width of a single RMSF.

It is important to realize that for a general distribution of emitting and Faraday rotating regions, only those structures show up in the $P(\mathcal{R})$ spectrum that illuminate a column of Faraday rotating ISM from the back. If Faraday rotation occurs also at larger distances, but is not illuminated from the back by synchrotron emission, this will not appear in the $\vec{P}(\mathcal{R})$ spectrum.

3.3 The data

The present dataset was obtained with the WSRT, a 14-element E-W interferometer of which 4 elements are moveable to improve (u,v) coverage. Each of the telescope dishes is 25 m in diameter. The central coordinates of the region we study (in the constellation Gemini) are $\alpha = 7^h18^m$ and $\delta = 36^\circ24'$ (J2000.0), which is $l \approx 181^\circ$ and $b \approx 20^\circ$ in Galactic coordinates. The GEMINI region was observed in 6 12 hour observing runs in December 2002 and January 2003 (see Table 3.1). This yielded visibilities at baselines from 36 to 2760 meters, with an increment of 12 meters. We tapered the individual frequency channel maps in such a way that the synthesized beamsize for all maps is

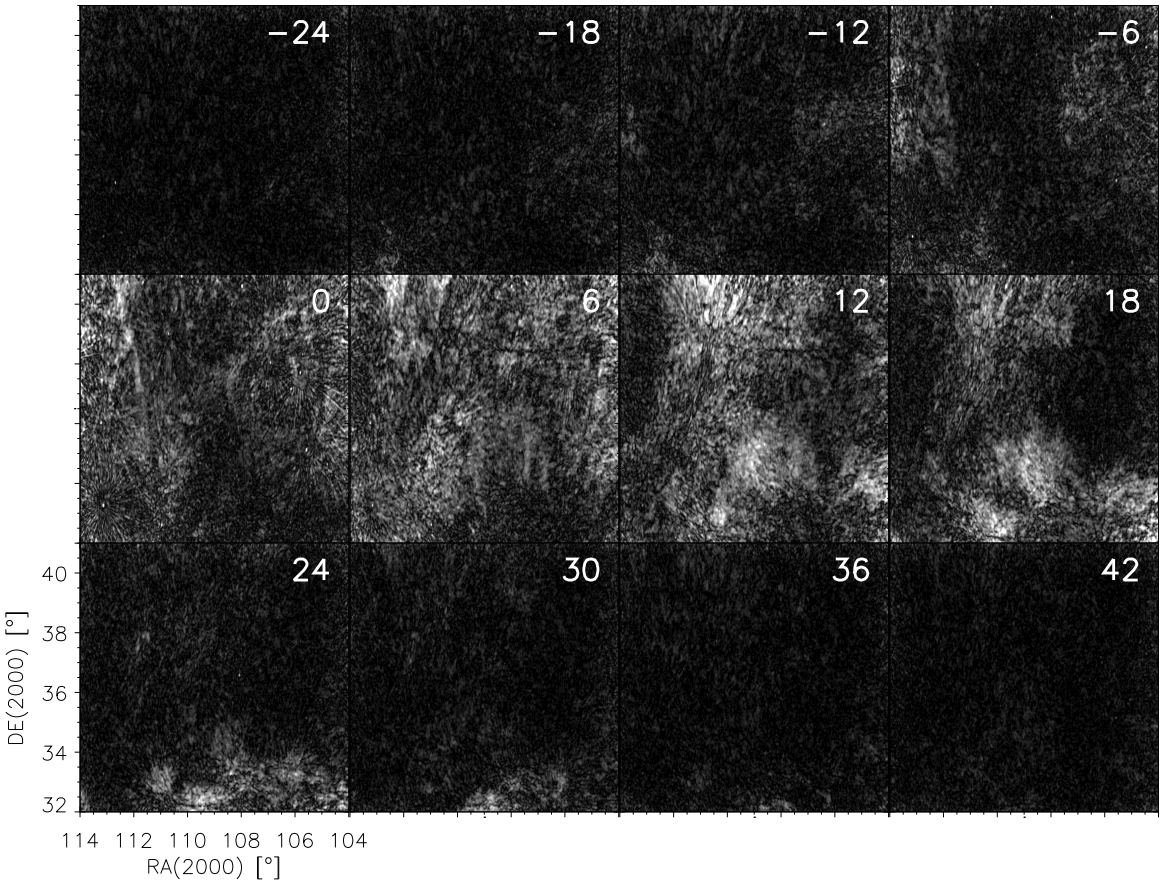

Figure 3.2 — Slices through the $P(\mathcal{R})$ cube that show the strongest diffuse emission. The $\mathcal{R}$ of each slice is indicated in rad/m^2 in the upper right corner of each image. The RMSF has a FWHM of 12 rad/m^2, and we sampled each RMSF with 2 images. The intensity scale is the same for all panels, and it saturates at 6.4 K.

that of the 385 MHz beam of $2.76' \times 4.70'$ (RA $\times$ DEC). Combining the 6 12 hr observing runs puts the first grating ring at 4.1° (at 350 MHz) from the pointing centre, outside the $3° \times 3°$ area that we mapped for each individual pointing.

We mapped an area of about $9° \times 9°$ with a 7×7 pointing mosaic. In each night the same field was observed about 16 times, resulting in visibilities on 16 'spokes' in the (u,v) plane, each time integrating for 40 seconds before moving to the next field. The 1.5° distance between pointing centres suppresses off-axis instrumental polarization to less than 1% (Wieringa et al. 1993). In our analysis we leave out the edges of the mosaic where instrumental polarization effects are not suppressed by mosaicking.

The observations cover the frequency range between 324 and 387 MHz. 202 independent spectral channels are usable from a maximum of 224, each channel being 0.4 MHz wide (where we used a Hamming taper). 10 channels were flagged because Stokes V was contaminated by radio frequency interference, and one channel was manually flagged in all 6 12 hr runs.

The data were reduced using the `NEWSTAR` data reduction package. Dipole gains and phases and leakage corrections were determined using the unpolarized calibrators

3C48, 3C147 and 3C295. The flux scales of both unpolarized and polarized calibrators are set by the calibrated flux of 3C286 (26.93 Jy at 325 MHz - Baars et al. 1977). Due to an a-priori unknown phase offset between the horizontal and vertical dipoles, signal can leak from Stokes U into Stokes V. We corrected for this by rotating the polarization vector in the Stokes (U,V) plane back to the U axis, assuming that there is no signal in V. The polarized calibrator sources 3C345 and DA240 defined the sense of derotation (i.e. to the positive or negative U-axis). Special care was taken to avoid automatic flagging of real signal on the shortest baselines. From Stokes V, which we assume to be empty, we estimate that the average noise level in the mosaics of the individual channels is 6.2 mJy (2.0 K).

These observations were carried out in the evening and at night to limit solar interference and to reduce the importance of ionospheric RM variations. From 2 lines-of-sight with a strong polarized signal we estimate that the amounts of ionospheric Faraday rotation in the 6 nights are identical to within $\sim 10^\circ$, so we did not correct for this. Ionosphere models indicate that the ionospheric contribution to RM during the observing nights was only 0.6 rad/m^2 (Johnston-Hollitt, private communication).

An interferometer will not cover all baseline lengths down to 0m, which means that maps of the sky that were made using an interferometer will miss structure on large angular scales. We will return to this point in Sect. 3.4.2.

3.4 Analysis

3.4.1 The $\mathcal{R}$ datacube

We calculated $\vec{P}(\mathcal{R})$ maps of the sky for Faraday depths from -1000 rad/m^2 to +998 rad/m^2 in steps of 6 rad/m^2. As the width of the RMSF along the $\mathcal{R}$ axis of the datacube is about 12 radians/m^2 for our dataset, this gives Nyquist sampling in Faraday depth. Due to the finite channelwidth of the data, the sensitivity of the $P(\mathcal{R})$ spectra will drop at large $\mathcal{R}$, as described by Eqn. 3.8. This becomes important for $|\mathcal{R}| \gtrsim 1.9/\delta\lambda^2 \approx 1250$ rad/m^2.

In Fig. 3.2 we show slices through our $\mathcal{R}$ datacube that show strong Galactic emission. All of the images saturate at 6.4 K. In Figs. 3.3 and 3.4 we summarize the information in the $\mathcal{R}$ datacube by plotting for each line-of-sight the maximum $P(\mathcal{R})$ along that line-of-sight, and the $\mathcal{R}$ at which this maximum occurs. We only plotted lines-of-sight where the main peak is more than twice as high as the second highest peak. From these figures it is clear that the majority of the lines-of-sight satisfies this condition. Because we treated the data in a slightly different way from what we described in chapter 2, there are some minor differences with the corresponding figures in that chapter. From the $P(\mathcal{R})$ maps at $|\mathcal{R}| > 200$ rad/m^2 we estimate that the noise level in the $P(\mathcal{R})$ slices is 0.5 mJy (0.14 K).

The complexity of a line-of-sight depends on whether the main peak is resolved, and on how strong second and higher-order peaks are. The Δ criterion that we introduced in chapter 2 can be used to address the issue of resolution. We defined Δ as the root-mean-square vertical separation in the $\mathcal{R}$ spectrum between the main peak in the $P(\mathcal{R})$ spectrum and the best-fitting RMSF, and we compare the observed Δ to the distribution of Δ that we simulated for an input signal of the appropriate strength + noise.

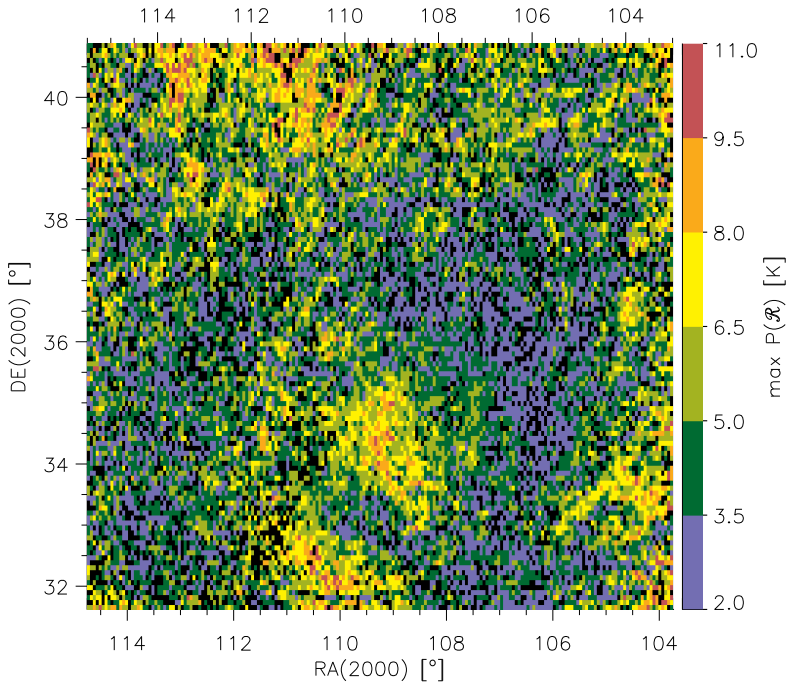

Figure 3.3 — $P(\mathcal{R})$ of the highest peak in the $\mathcal{R}$ spectrum. Each pixel represents one telescope beam, and the pixel size is $2.8' \times 4.9'$. The lines-of-sight that are shown in this plot have a second peak in the $P(\mathcal{R})$ spectrum that is at most half the strength of the main peak. Out of a total of 22.800, lines-of-sight 2720 do not obey this selection criterium, and they are shown in black, as are the 769 lines-of-sight that have $P(\mathcal{R}) < 2$ K. The 1σ noise level in the $P(\mathcal{R})$ maps is 0.14 K. Page 186 shows a colour version of this figure.

In Fig. 3.5 we plot the lines-of-sight that have an unresolved main peak as green pixels. 'Unresolved' means that the Δ value of the main peak is $\leq$ the Δ that we found for 99% of our simulations of signal + noise ($\approx$ the 3σ level of the Rayleigh distribution).

Lines-of-sight with linear $\Phi(\lambda^2)$ relations have special geometries of Faraday-rotating and synchrotron-emitting regions along the line-of-sight, as discussed in Sect. 3.2. We therefore fitted a straight line to our $\Phi(\lambda^2)$ datapoints, where we included the periodicity of the data by using the procedure described in chapter 2. Lines-of-sight with $\chi^2_{\rm red} < 2$ are indicated in Fig. 3.5 as yellow pixels, and lines-of-sight that have both a not measurably resolved main peak and a low $\chi^2_{\rm red}$ are indicated as red pixels. Since many lines-of-sight have a low $\chi^2_{\rm red}$, but a high Δ, there are many yellow pixels, but relatively few red pixels.

We simulated the $P(\mathcal{R})$ response from the main peak plus noise by calculating the Fourier transform from Eqn. 3.3 for an input signal of a given strength + the noise levels that we derived from the Stokes V maps of the individual frequency channels. We assume that the Stokes V maps contain no signal. We ran our simulations for a grid of input signal strengths, that was matched to the strengths of the main peak in the $P(\mathcal{R})$ spectra that we encountered in the data. In this way we calculated for each $\mathcal{R}$ in the spectrum the level below which 99% of the RMSF plus noise simulations lie.

The main peak in the $P(\mathcal{R})$ spectrum is not measurably resolved for about 8% of the lines-of-sight in the current dataset, in the sense that its value of Δ is lower than

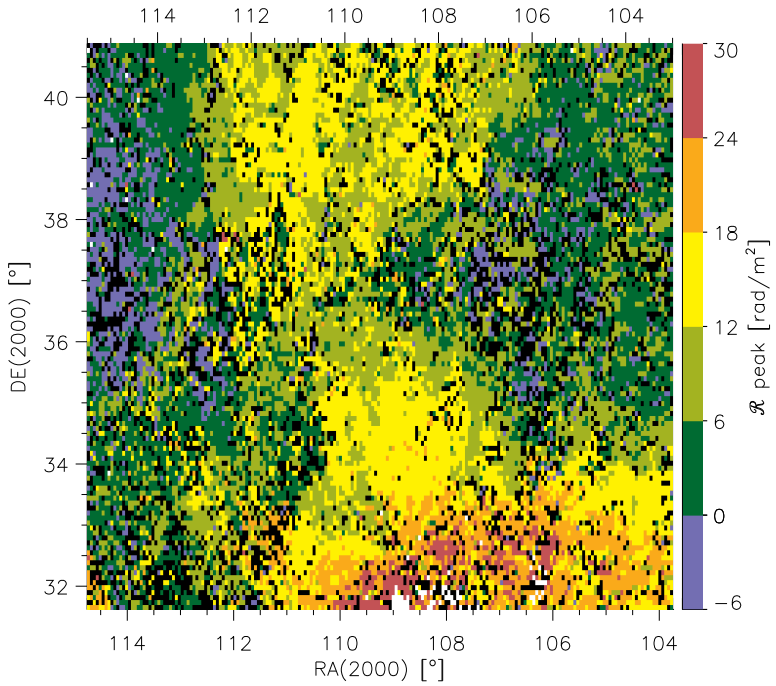

Figure 3.4 — $\mathcal{R}$ corresponding to the $P(\mathcal{R})$ plotted in Fig. 3.3. The lines-of-sight plotted in these figures are selected by using the same criterium. Lines-of-sight indicated in white have $\mathcal{R} > 30$ rad/m^2. Lines-of-sight indicated in black either did not pass the selection criterium or have $\mathcal{R} <$ -6 rad/m^2 (2720 and 727 lines-of-sight resp.). Page 187 shows a colour version of this figure.

the Δ that we find for 99% of our simulations of a RMSF + noise. This value is lower than the 14% quoted in chapter 2. This difference might be produced because we now use frequency channel maps that all have been tapered to the same beamsize. A not measurably resolved peak means that a Faraday rotating regions is physically separated from a region with synchrotron emission; mixing of the 2 regions produces broad peaks in the $P(\mathcal{R})$ spectrum. Since we only tested the main peak in our $P(\mathcal{R})$ spectra, and no other features in the $P(\mathcal{R})$ spectrum, emission regions with a Faraday screen in front of them will be even more numerous than in 8% of the lines-of-sight. RFI and calibration errors can only increase Δ, which is another reason why there are probably more Faraday screens present in the ISM.

Intuitively one would not expect such a separation between the emitting and Faraday rotating regions along the line-of-sight: cosmic rays that produce synchrotron radiation are expected to be present wherever there is a magnetic field. Therefore one possibility could be that we simply don't see the synchrotron emission because the full magnetic field vector is pointing along the line-of-sight. The magnetic field component perpendicular to the line-of-sight, which determines the synchrotron emissivity, is in that case 0. Such a region would from our point-of-view then only produce Faraday rotation. Even though the strengths of the magnetic field component along the line-of-sight that we determine in Sect. 3.5 are low, these are averages over the line-of-sight, and they are biased towards regions where the thermal (i.e. 10^4 K) electron density is higher.

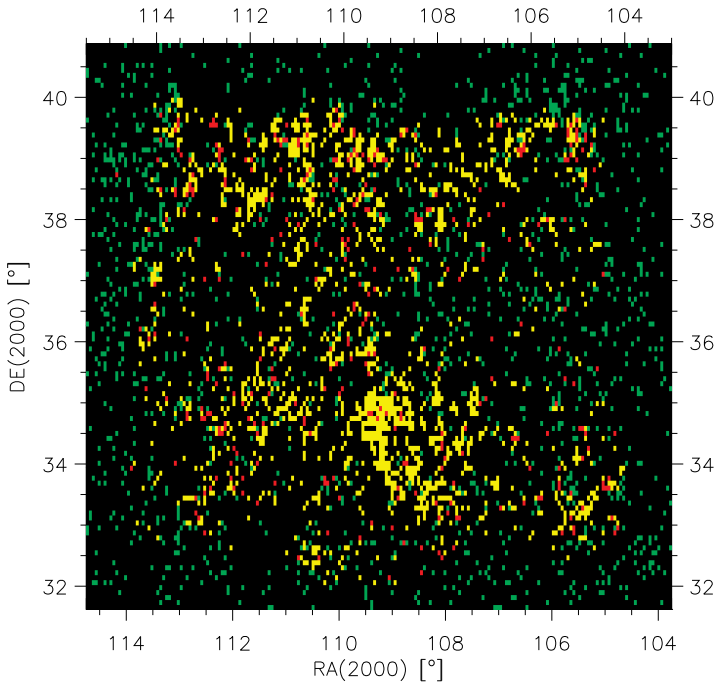

Figure 3.5 — Distribution of independent lines-of-sight with a main peak that satisfies the Δ criterion (green pixels), or with $\chi^2_{\rm red} < 2$ and $\max(P(\mathcal{R})) > 2$ K (yellow pixels), or that satisfy all three criteria (red pixels). Lines-of-sight that did not pass these criteria are shown as black pixels. The outer edges of the mosaic show an increase in $\chi^2_{\rm red}$, which explains the absence of yellow pixels. Page 188 shows a colour version of this figure.

The majority of lines-of-sight in our data have a secondary peak that is higher than what would be expected for one in 10^4 noise realisations. However, the main peak is typically more than twice as high as the secondary peak, and thus dominates most of the lines-of-sight in the GEMINI region. This makes these lines-of-sight relatively simple, and we did not deconvolve the $P(\mathcal{R})$ spectra. The reason why these lines-of-sight are not very complex could be because we are looking in the direction of the Galactic anti-centre, at an intermediate Galactic latitude.

3.4.2 Missing large-scale structure

Structure on large angular scales is missing from interferometric observations if information on short baselines is not available. Differences in Faraday rotation in between the source of the polarized emission and the observer can for neighboring lines-of-sight 'transfer' polarized signal from large angular scales to small enough angular scales so that it can be picked up by the interferometer. Since this effect does not operate on Stokes I, this is the canonical explanation why structure in polarized intensity does not appear have a counterpart in total intensity. In this section we expand on this idea, and we show that modulation by a linear gradient in Faraday depth $\mathcal{R}$ shifts the angular frequency spectrum as a whole.

For a linear variation of $\mathcal{R}$ with position l (i.e. a fixed gradient $\nabla\mathcal{R}$), and wavelength λ, this modulation of the polarization vector $\vec{P}$ can be expressed as

$$\vec{P}_{\rm obs}(l) \;=\; \vec{P}_{\rm em}(l)\,{\rm e}^{2{\rm i}\nabla\mathcal{R}\lambda^2 l} \tag{3.12}$$

where subscripts 'em' and 'obs' refer to the emission before and after it gets modulated by the foreground gradient in $\mathcal{R}$. This linear modulation with position shifts the angular frequency spectrum as a whole:

$$\begin{aligned}
{\rm FT}(\vec{P}_{\rm obs})(u) &= \int_{-\infty}^{\infty} {\rm d}l\; \vec{P}_{\rm obs}(l)\,{\rm e}^{2\pi{\rm i}ul} = \int_{-\infty}^{\infty} {\rm d}l\; \vec{P}_{\rm em}(l)\,{\rm e}^{2{\rm i}\nabla\mathcal{R}\lambda^2 l}{\rm e}^{2\pi{\rm i}ul} \\
&= \int_{-\infty}^{\infty} {\rm d}l\; \vec{P}_{\rm em}(l)\,{\rm e}^{2\pi{\rm i}(\frac{1}{\pi}\nabla\mathcal{R}\lambda^2+u)\;l} \\
&= {\rm FT}(\vec{P}_{\rm em})(u+\frac{1}{\pi}\nabla\mathcal{R}\lambda^2)
\end{aligned} \tag{3.13}$$

One consequence of this is that foreground Faraday modulation makes the 0-angular frequency from $\vec{P}_{\rm em}(l)$ visible if $|\nabla\mathcal{R}|$ is large enough. To make it detectable at the 25 m (projected) baseline length, which can be obtained with the WSRT, requires a $|\nabla\mathcal{R}| \;\approx\; 6$ rad/m^2/field-of-view at 350 MHz (where 1 field-of-view is 3° wide for our observations). Since we observe gradients of this magnitude in the individual pointings of the GEMINI dataset (Fig. 3.4), Fig. 3.3 and Fig. 3.4 contain at least the 0-angular frequency = total polarized intensity component of $\vec{P}_{\rm em}$.

The direction of the shift in Eqn. 3.13 is set by the sign of $\nabla\mathcal{R}$. Since the WSRT only measures one half of the (u,v)-plane, this means that the angular frequency spectrum could move away from the measurement points in the (u,v)-plane. However, $\vec{P}_{\rm obs}(l) = Q_{\rm obs}(l) + {\rm i}U_{\rm obs}(l)$, and since $Q_{\rm obs}(l)$ and $U_{\rm obs}(l)$ are real quantities, their Fourier transforms are hermitian. The gradient from Eqn. 3.13 always moves both the positive and the negative angular frequencies of $Q_{\rm em}(l)$ and $U_{\rm em}(l)$ towards or away from the origin in the (u,v)-plane. Therefore, $\vec{P}_{\rm obs}(l)$ can be reconstructed even if only one half of the (u,v)-plane is observed.

Note that foreground Faraday modulation shifts some angular frequencies from $\vec{P}_{\rm em}(l)$ towards smaller (in an absolute sense) angular frequencies. At some point these angular frequencies from $\vec{P}_{\rm em}(l)$ will no longer be visible for an interferometer, because it can only measure visibilities from a certain shortest baseline. For the analysis that we present in the remainder of this article it is sufficient that our data contain the total polarized intensity component of $\vec{P}_{\rm em}$. Single-dish observations are therefore still required to produce maps that contain all angular frequencies.

If Faraday rotation in the foreground produces strong variations in $\mathcal{R}$ over the telescope beam, then this will also lead to beam depolarization. For a Gaussian beam, a gradient of more than 12 radians/m^2/field-of-view is required to give more than 10% beam depolarization (Sokoloff et al. 1998), and such steep gradients are not observed in the GEMINI data.

As a final note in this section, in chapter 8 we will present polarization angle gradients in the WENSS data set, in the region $130^\circ < l < 170^\circ$, $-5^\circ < b < 30^\circ$ that are on average about 2 radians/m^2/° along Galactic latitude, which translates into the

6 radians/m^2/field-of-view required to shift the angular frequency spectrum towards observable frequencies. These WENSS gradients therefore also show at least the total polarized intensity component of the angular frequency spectrum.

3.5 The line-of-sight component of the large-scale magnetic field

In this section we derive the strength of the magnetic field component along the line-of-sight, $B_\parallel$. We use the Faraday depths from Fig. 3.4, and we determine the contribution from thermal electrons to $\mathcal{R}$ (Eqn. 3.2) by combining emission measures $EM = \int_0^\infty n_e^2 \mathrm{d}l$ from the WHAM survey (Haffner et al. 2003) with the Reynolds model for a clumpy ISM (Reynolds 1991). The integral for EM is over the entire line-of-sight, $[EM]$=cm^{-6}pc, $[n_e]$=cm^{-3} and $[\mathrm{d}l]$=pc. In the top panel of Fig. 3.6 we plot the Hα intensities in Rayleigh for WHAM lines-of-sight in the GEMINI region.

In the Reynolds model, Faraday rotation occurs in clumps that each have a uniform electron density of 0.08 cm^{-3}, and that cover 40% of the line-of-sight. For this model the length L of the line-of-sight that produces a measured Hα intensity $I_{\mathrm{H}\alpha}$ can be calculated: L [kpc] = 1.027$\times I_{\mathrm{H}\alpha}$[R]. Here we used Eqn. 1 from Haffner et al. (1998), from which it follows that 1 Rayleigh = 2.63 cm^{-6}pc for a 8×10^3 K gas, a typical value for the WIM (Reynolds 1985), and an E(B-V) = 0.071 magnitudes for (α, δ)=(110°,37°), which we found using the NED Galactic extinction calculator[1], which is based on Schlegel et al. (1998). The average EM=1.78 R of the WHAM datapoints in the GEMINI region, and with it we find an average length of the line-of-sight of 1.8 kpc where the $\mathcal{R}$ is built up. This puts the far end of the line-of-sight at about the same distance as the Perseus arm at this longitude.

To test how reliable it is to combine the Reynolds model with the EM derived from WHAM, we calculated the dispersion measure DM = $\int_0^\infty n_e \mathrm{d}l$, and compared it to the DM predicted by the Cordes & Lazio (2003) model, which is based on pulsar DM, for a line-of-sight in the same direction and of the same length. Using the average WHAM Hα intensity = 1.78 Rayleigh, both the Cordes & Lazio model and the Reynolds model predict DM = 59cm^{-3}pc. As the electron density from the Reynolds model is a factor of 10 larger than the electron density in the hot intercloud medium as determined from ROSAT diffuse X-ray background maps (Snowden et al. 1997), we neglected the DM contribution from the hot intercloud medium.

With the Reynolds model, it is also possible to calculate $B_\parallel$ from the measured values of $\mathcal{R}$ in Fig. 3.4, in combination with the WHAM EM: $B_\parallel = \mathcal{R}\ n_e/(0.81 \times 2.63\ I_{\mathrm{H}\alpha})$, where $B_\parallel$ is in μG, $\mathcal{R}$ is in rad/m^2, and $I_{\mathrm{H}\alpha}$ is in R. In the bottom panel of Fig. 3.6 we show the values of $B_\parallel$ that we calculated with this expression. Since the WHAM beam (FWHM $\approx 1°$) is much larger than the WSRT beam, we used the $P(\mathcal{R})$-weighted $\mathcal{R}$ average over the WHAM beam to calculate $B_\parallel$. Because we calculate the average $\mathcal{R}$ over the WHAM beam, negative $\mathcal{R}$ from Fig. 3.4 are averaged out in the bottom panel Fig. 3.6 and do not show up as strong negative $B_\parallel$.

If the line-of-sight that produces the Hα emission is longer than the line-of-sight that produces $\mathcal{R}$, the L we derive is an upper limit for the real L, and the $B_\parallel$ we derive is then a lower limit. A reasonable upper limit for $B_\parallel$ can be found by using a pitch angle

[1] `http://nedwww.ipac.caltech.edu/forms/calculator.html`

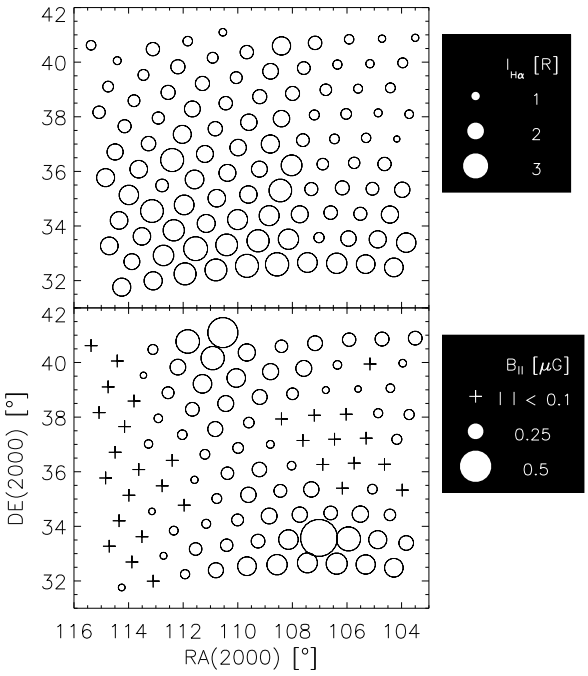

Figure 3.6 — WHAM Hα intensities in Rayleigh (top panel) and derived strengths of the magnetic field component parallel to the line-of-sight $B_{\parallel}$ in μG (bottom panel). Open circles indicate positive $B_{\parallel}$; there are no negative $B_{\parallel} <$ -0.1 μG in this figure since we average $\mathcal{R}$ over the entire WHAM beam. $|B_{\parallel}| < 0.1$ μG are shown as '+'.

of 8° for the magnetic field, and a total strength of 4 μG for the large-scale field (both values from Beck 2007a), which gives $B_{\mathrm{reg},\parallel,\mathrm{max}} \approx 0.6$ μG. In the presence of a random magnetic field, $B_{\parallel}$ approaches the $B_{\mathrm{reg},\parallel}$ component of the regular field if either the reversals in the direction of the random field are unimportant, or if the line-of-sight is long enough so that the contributions to $\mathcal{R}$ from such small-scale reversals cancel each other along the line-of-sight. As discussed in Haverkorn et al. (2004a), the random magnetic field has a correlation length of order 10 parsec. In combination with the 1.8 kpc length of the line-of-sight that we derived earlier in this paragraph, the line-of-sight would be long enough that the contributions to $\mathcal{R}$ from the random magnetic field cancel themselves, and the $\mathcal{R}$ that we observe only contains the contribution from the regular field to $\mathcal{R}$.

The $B_{\parallel}$ we derive are small, which can be expected since we are looking in the direction of the Galactic anti-centre, where the regular magnetic field is mostly perpendicular to the line-of-sight. It is clear from the bottom panel in Fig. 3.6 that variations in EM alone are not enough to explain the measured variation in $\mathcal{R}$, but that variations in $B_{\parallel}$ are required as well. Further support for this is given by the fact that $\mathcal{R}$ in Fig. 3.4 changes sign in the area covered by the GEMINI data, which can only be explained by a change in the direction of $B_{\parallel}$. The $B_{\parallel}$ structure in Fig. 3.4 is not associated with any of the 3 largest non-thermal loops in the Galaxy, the North Polar Spur, Cetus Arc and Loop III. The locations of these structures are described in Elliott (1970).

3.6 Polarized point sources

Since the line-of-sight towards extragalactic sources passes through the entire Milky Way, whereas different depolarization effects limit the line-of-sight of the diffuse emission, the information we obtain from the $\mathcal{R}$ of extragalactic sources can complement

Table 3.2 — Properties of the polarized point sources we found in our data. Shown are the equatorial coordinates (J2000.0) of the source in decimal degrees, the RM that we fitted and its error (both in rad/m^2), the reduced χ^2 ($\chi^2_{\rm red}$) of the fit, the maximum $P(\mathcal{R})$ along the line-of-sight and the total intensity I (both in mJy), and the polarization fraction (in %).

(RA, DEC)	RM	$\chi^2_{\rm red}$	$P(\mathcal{R})_{\rm max}$	I	$P(\mathcal{R})_{\rm max}/I$
(°,°)	[rad/m^2]		[mJy]	[mJy]	%
(113.60, 35.12)	-27.6 ± 0.1	0.5	23.4	329	7.1
(113.25, 36.92)	14.2 ± 0.3	0.6	6.1	177	3.4
(113.34, 39.09)	9.6 ± 0.4	0.7	7.9	236	3.3
(113.20, 38.69)	11.7 ± 0.4	0.8	5.8	184	3.2
(112.84, 36.38)	14.3 ± 0.5	1.1	6.9	337	2.0
(112.04, 35.11)	8.7 ± 0.4	0.8	4.6	214	2.2
(111.91, 40.23)	18.9 ± 0.4	1.1	6.2	151	4.1
(111.54, 40.17)	13.8 ± 0.5	1.4	5.7	272	2.1
(111.32, 35.69)	6.5 ± 0.3	0.5	10.9	277	3.9
(111.42, 40.07)	11.8 ± 0.3	0.9	5.3	152	3.5
(111.24, 39.36)	16.3 ± 0.6	1.4	7.0	333	2.1
(111.02, 38.05)	13.3 ± 0.2	0.5	10.0	375	2.7
(110.77, 32.65)	-9.8 ± 0.7	2.8	5.4	232	2.3
(110.68, 32.51)	-7.8 ± 0.6	2.1	4.8	242	2.0
(110.74, 39.97)	9.4 ± 0.3	0.6	11.8	239	4.9
(110.29, 35.82)	5.7 ± 0.5	0.9	6.3	258	2.4
(108.90, 38.64)	19.0 ± 0.4	1.9	4.5	197	2.3
(108.42, 34.52)	20.5 ± 0.2	1.0	17.4	828	2.1
(108.31, 36.93)	22.2 ± 0.2	1.0	5.3	214	2.5
(108.27, 36.95)	25.7 ± 0.6	2.7	4.4	210	2.1
(106.30, 37.31)	-12.7 ± 0.4	1.2	4.4	195	2.3
(105.76, 38.38)	-12.3 ± 0.6	1.4	3.1	150	2.0
(104.81, 35.88)	-33.4 ± 0.4	1.6	15.1	625	2.4

what we learn from the diffuse emission. However, extragalactic sources will also have an intrinsic $\mathcal{R}$.

To find polarized point sources, we first made maps that only contain baselines $>$ 250 m, to filter out the strong diffuse emission from our $P(\mathcal{R})$ datacube. These maps use a Gaussian taper that reaches a value of 0.25 at a baseline length of 2500 m. We then constructed $P(\mathcal{R})$ maps from $\mathcal{R}$ = -1000 rad/m^2 to $\mathcal{R}$ = +998 rad/m^2, in steps of 6 rad/m^2, by Fourier transforming these channel maps from λ^2 space to $\mathcal{R}$ space, in a way identical to what we described in Sect. 3.4.1.

The polarized intensity of an extragalactic source with rotation measure RM will be attenuated by bandwidth depolarization according to sinc($|$RM$|\delta\lambda^2$), if the polarization angle varies linearly with λ^2, and where $\delta\lambda^2$ is the λ^2 width of the frequency channels. The channels that we use have on average a $\delta\lambda^2 \approx 1.5 \times 10^{-3}$ m^2, therefore bandwidth depolarization of a point source with $|\mathcal{R}|$ = 1000 rad/m^2 will reduce the signal to 66%, which would still be detectable.

We looked for each line-of-sight in the $P(\mathcal{R})$ datacube if 1) there was a Stokes I

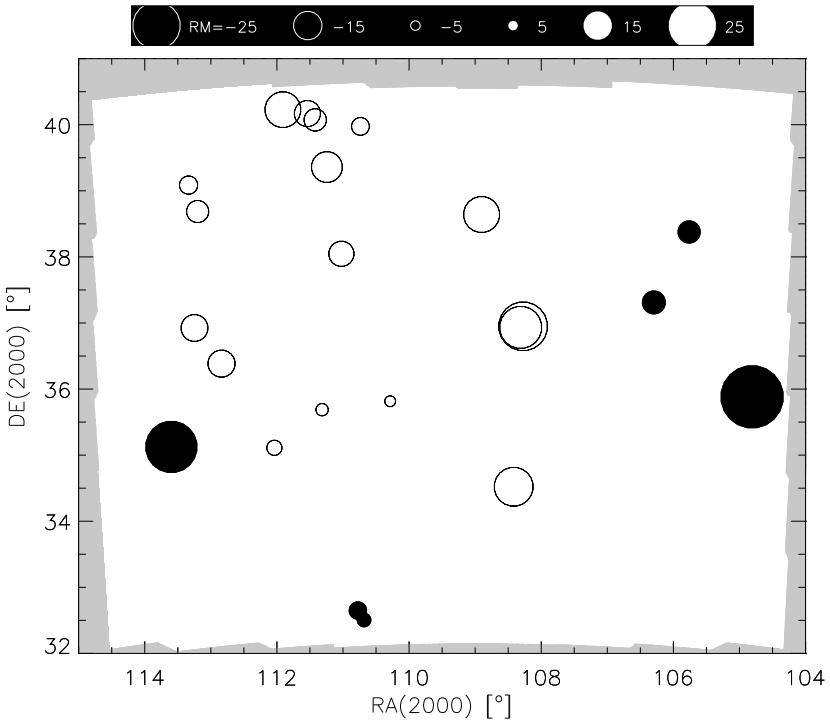

Figure 3.7 — RM distribution for the polarized point sources from table 3.2. The size of the circles is proportional to RM, shown in the scale on top of the figure in units of radians/m^2. Black circles indicate negative RM, and white circles indicate positive RM. $|\mathrm{RM}| \lesssim 4$ rad/m^2 are missing from this figure because of our selection criteria. We excluded the grey region when looking for polarized point sources, because here instrumental polarization levels are higher.

counterpart brighter than 150 mJy, 2) if the maximum $P(\mathcal{R})$ along the line-of-sight was more than a 5σ detection and 3) if the ratio of the maximum $P(\mathcal{R})$ along the line of sight/ total intensity I was larger than 0.02, meaning that this source is more than 2% polarized (the instrumental polarization level is about 1%). We also exclude sources with $|\mathcal{R}| \leq 4$ rad/m^{2}because instrumentally polarized point sources will show up in the $P(\mathcal{R})$ datacube at 0 rad/m^2, and the finite width of the RMSF along the $P(\mathcal{R})$ axis will produce a strong signal also in the vicinity of 0 rad/m^2. Furthermore we excluded a region of about 0.9° from the edge of the mosaic, where there is no overlap between pointings, and instrumental polarization levels are therefore much higher here. We then fitted an RM to the $\Phi(\lambda^2)$ distribution of the sources that satisfy these criteria in the way described in chapter 2.

In Table 3.2 we list the properties of the sources that we found, and we plot the RM of these sources in Fig. 3.7. The low $\chi^2_{\mathrm{red}}$of the RM fits indicate that there is only one $P(\mathcal{R})$ component along the $\mathcal{R}$ axis, and that we have effectively filtered out the diffuse Galactic contribution to the $P(\mathcal{R})$ spectrum. This, in combination with the fact that these sources are detected in maps where we left out low angular frequencies on the sky, means that the sources that we detected are compact in all 3 dimensions of the $P(\mathcal{R})$ cube, and are therefore likely to be either polarized pulsars or polarized extragalactic sources. Since the surface density of the latter is so much larger than that of the former, the sources that we detected are probably extragalactic in origin.

Most of the sources in the upper left quadrant of Fig. 3.7 show positive RMs of $\approx$ 5–15 rad/m^2, similar to the RM of the main peak of the diffuse emission along the line-of-sight, shown in Fig. 3.4. The source density in other regions is insufficient to reach definite conclusions.

The RM that we observe for an extragalactic source is the combination of a Galactic RM and an RM that is intrinsic to the source. Since a number of sources show the same RM, and since the intrinsic RM of these sources are uncorrelated, what we see is probably mostly the Galactic RM contribution for the entire line-of-sight through the Galaxy. We can estimate in the following way what the contribution is from the extra stretch through the layer with Faraday rotating clumps beyond the WHAM line-of-sight that we estimate in the previous section. The thickness of the Faraday rotating layer is 1 kpc for a model where the density of Faraday rotating clumps does not change with height above the Galactic plane (Reynolds 1991). Therefore, at a Galactic latitude of 20°, the line-of-sight that passes through this layer has a total length of 2.9 kpc, which is 1.1 kpc longer than the length of the WHAM line-of-sight. This produces an extra
DM = 37 cm^{-3}pc, and an extra $\mathcal{R}$ = 6 rad/m^2 compared to the WHAM line-of-sight, if the $B_{\parallel}$ is kept the same as along the WHAM line-of-sight. This is only a modest increase, and we cannot determine from our data on extragalactic sources what the structure is of the magnetic field beyond the WHAM line-of-sight.

3.7 Depolarization canals in $P(\mathcal{R})$ maps

Dark, narrow channels ('canals') can be clearly seen in the images of Fig. 3.2. Canals have been known to exist in $P(\lambda)$ images (e.g. Haverkorn et al. 2000), but, as far as we know, canals in $P(\mathcal{R})$ maps have only been mentioned by De Bruyn et al. (2006).

In Fig. 3.8 we show slices through the $P(\mathcal{R})$ cube that have particularly strong depolarization canals. It appears from this figure that the canals essentially are not changing position with changing $\mathcal{R}$. This is demonstrated by the reference crosses that we positioned on three canals in this figure. In the first and second rows of Fig. 3.9 we plot the $P(\lambda^2)$ (left column) and $\Phi(\lambda^2)$ (right column) spectra for the two canal pixels from the top row of Fig.3.8 ('CH 1' and 'CH 2' resp.). In the bottom row of Fig. 3.9 we plot the spectra for the canal pixel in the bottom row of Fig. 3.8.

In Fig. 3.9 we also plot the $P(\lambda^2)$ and $\Phi(\lambda^2)$ spectra for 2 lines-of-sight that lie on either side of the central canal pixel, at half a (synthesized) beamwidth away. These adjacent lines-of-sight share pixels with the line-of-sight that is centered on the canal pixel, and with these lines-of-sight we can investigate the nature of the canal pixels.

The $\Phi(\lambda^2)$ spectra of the neighbouring lines-of-sight were unwrapped by fitting a straight line to the polarization angles by hand. As a first guess for the slope of this line, we used the $\mathcal{R}$ at which the $P(\mathcal{R})$ of the neighbouring lines-of-sight is high. Furthermore we required that for each line-of-sight the difference in polarization angle between the successive (plotted) wavelength^2 channels must be smaller than 90°.

The difference in $\Phi(\lambda^2)$ for lines-of-sight adjacent to the canal pixels is large, often even almost 90°, averaged over the available λ^2. Also, the polarized brightness temperature of the 2 neighbouring lines-of-sight of each canal pixel are on average comparable. These 2 facts combined indicates that beam depolarization, i.e. summing

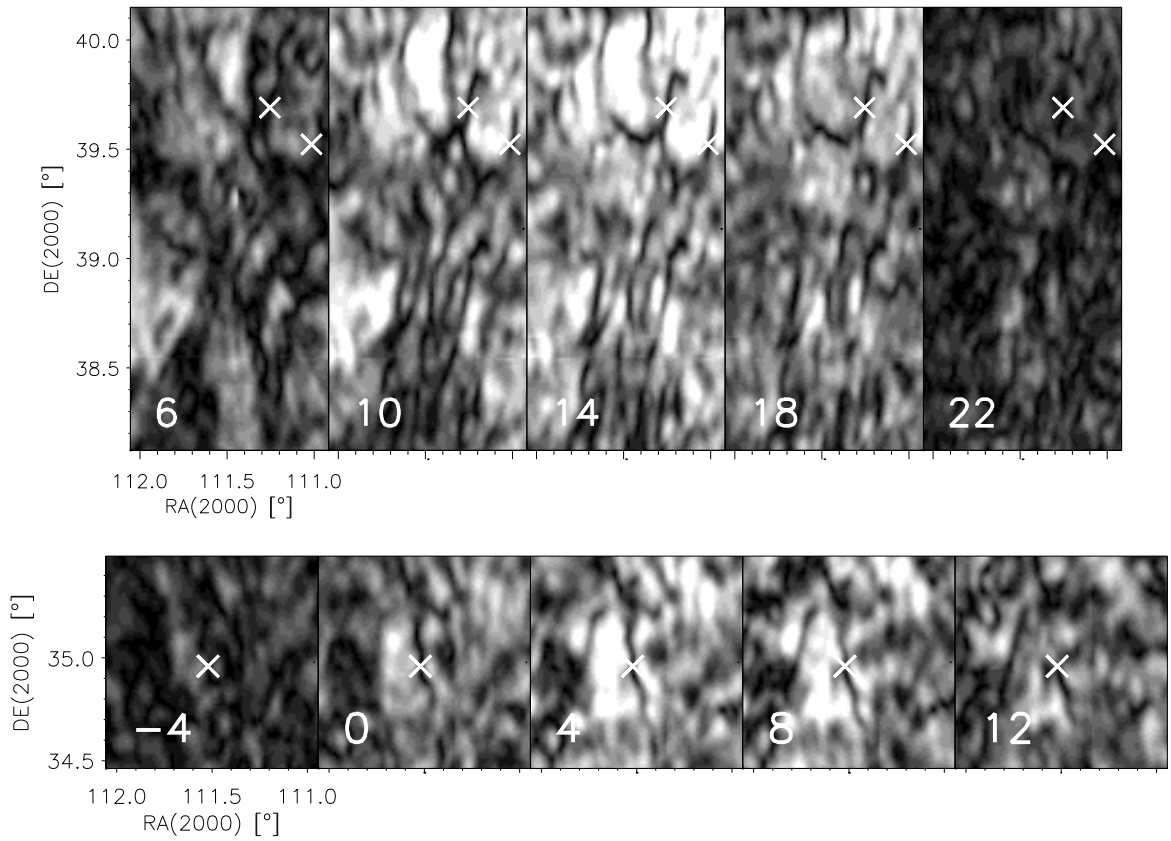

Figure 3.8 — Depolarization canals in the $P(\mathcal{R})$ datacube. The $\mathcal{R}$ [rad/m^2] of each of the $P(\mathcal{R})$ slices is indicated in the lower left. All maps have the same linear greyscale that saturates at 4.8 K. The area shown in the top row of this figure lies in the upper left of Fig. 3.2. For the 2 pixels that are indicated by crosses, and that lie in depolarization canals, we plot the $P(\lambda^2)$ and $\Phi(\lambda^2)$ spectra in the first row of Fig. 3.9 (left cross, 'CH 1' in Fig. 3.9) and middle row of Fig. 3.9 (right cross, 'CH 2'). The bottom row shows a canal in a different part of the mosaic, and the $P(\lambda^2)$ and $\Phi(\lambda^2)$ spectra of the canal pixel that is indicated by a cross are shown in the bottom row of Fig. 3.9 ('CH 3').

polarization vectors with similar lengths but different orientations over the (synthesized) telescope beam, is an important factor in creating canals in the $P(\mathcal{R})$ maps. In Haverkorn et al. (2000) the same mechanism was identified to be producing canals in $P(\lambda^2)$ maps. Line-of-sight depolarization, occurring for example as the nulls in Eqn. 3.11, produces canals only at certain wavelength^2. Shukurov & Berkhuijsen (2003) suggested that this mechanism is producing canals that are seen towards M31. This type of canal is characterized as extended along the $\mathcal{R}$ axis of the $P(\mathcal{R})$ cube, contrary to the properties of the canal pixels we present here.

3.8 The area around (l, b) = (109°,34.5°)

The 2°×2° area centred on (l, b) = (109.5°, 34.5°) is bright in polarized intensity (Fig. 3.3), shows a very uniform distribution in $\mathcal{R}$ (Fig. 3.4), and has a relatively small surface density of strong depolarization canals. Furthermore the $\chi^2_{\rm red}$ fitted to the $\Phi(\lambda^2)$ spectra are low (Fig. 3.5): 30% of the lines-of-sight in this area have a $\chi^2_{\rm red} < 2$, and

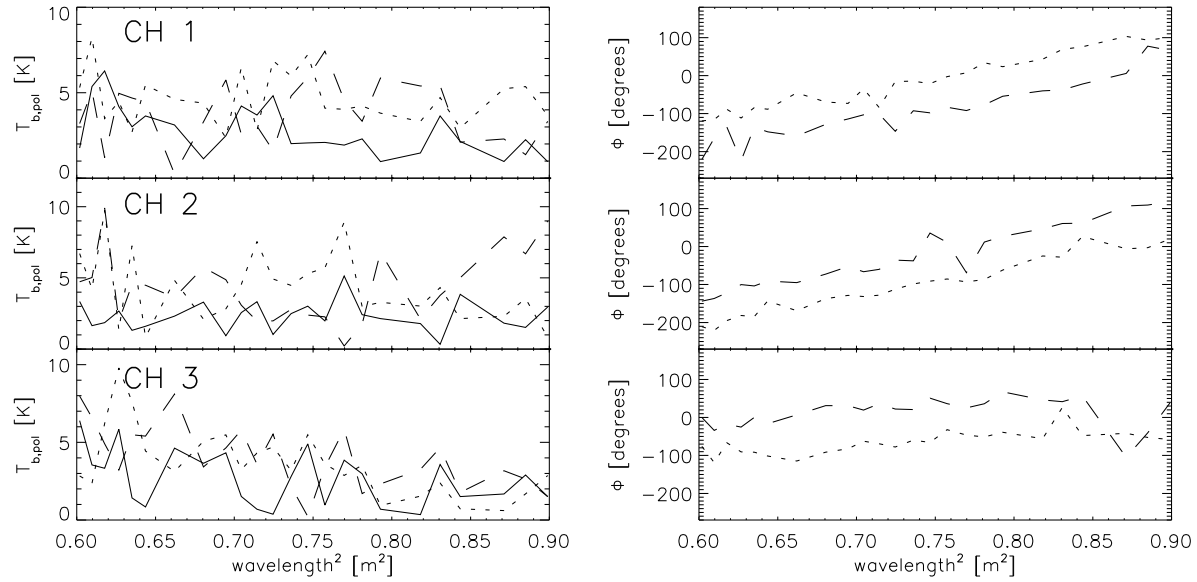

Figure 3.9 — Polarized brightness temperature $T_{b,pol}$ [K] and polarization angle Φ [degrees] spectra for 3 canal pixels, and two adjacent pixels half a beamwidth from each canal pixel. Top row: canal pixel at (α, δ)=(111.24°,39.72°), and two adjacent lines-of-sight at α=111.27° (dotted line), and α=111.21° (dashed line). Middle row: canal pixel at (α, δ)=(110.98°,39.57°), and adjacent lines-of-sight at α=111.01° dotted line, and α=110.95°, dashed line. Bottom row: canal pixel at (α, δ)=(111.50°,34.94°), and two adjacent lines-of-sight at α=111.53°, dotted line, and α= 111.47°, dashed line. The 1σ errors for polarized intensity and polarization angle are 2 K and 15° (for a S/N = 2 detection) resp. Every 8th channel is plotted. Bad frequency channels were selected using the same selection criteria as in Sect. 3.3, and discarded.

nearly 75% have a $\chi^2_{\rm red} < 3$. There is no enhanced Hα emission in this region (see the top panel of Fig. 3.6), and $B_{\|}$ varies only little (bottom panel of Fig. 3.6). The single-dish 408 MHz total intensity map by Haslam et al. (1982) shows hardly an increase in brightness temperature in this region, and there are not enough lines-of-sight in the Brouw & Spoelstra (1976) data set to discern the area around (l, b) = (109.5°, 34.5°) from its surroundings.

The increased $T_{\rm b,pol}$ w.r.t. its surroundings could be due to enhanced synchrotron emission, or a local decrease in depolarization, or to a combination of these. The polarized brightness temperature of this region is more than 3K larger than that of its surroundings, and this would translate into a brightness temperature difference of at least 3K/0.7 = 4.3K, assuming that the radiation is 70% polarized. Lower polarization percentages increase this brightness temperature contrast even further. An enhancement in synchrotron emission can be ruled out as an explanation for the increased $T_{\rm b,pol}$ of this area, since this is not observed, and since beam averaging is not strong enough to attenuate the total intensity signal (the Haslam beam measures $0.85° \times 0.85°$).

The small variation in $\mathcal{R}$ over this region, combined with an underabundance of strong depolarization canals, furthermore indicates that depolarization across the synthesized telescope beam is not a strong effect. This leaves a decrease in the amount of depolarization along the line-of-sight as an explanation for the observed increase in $T_{\rm b,pol}$. The low $\chi^2_{\rm red}$of lines-of-sight in this area, in combination with secondary peaks that are not stronger than half the strength of the main peak, also indicates that the

lines-of-sight in this area are not very complex, and line-of-sight depolarization effects are therefore not very important. We thus think that the origin of this particular region lies in a decreased amount of depolarization compared to its surroundings.

3.9 Conclusions

We applied Faraday tomography to high spectral-resolution radio polarization data to study the properties of the magnetized Galactic ISM. We showed that differential Faraday modulation in the foreground can shift the emitted angular frequency spectrum as a whole. In particular the 0-angular frequency from the emitted radiation is modulated in this way towards smaller angular scales, that are observable with an interferometer. We quantified how strong a linear gradient in $\mathcal{R}$ should be to accomplish this, and we showed that the gradients in $\mathcal{R}$ that we find for the main peak in the $P(\mathcal{R})$ spectra are indeed strong enough so that we are sensitive to the 0-angular frequency that is emitted at these Faraday depths.

The main peak in the $P(\mathcal{R})$ spectrum is not measurably resolved for 8% of the lines-of-sight in our dataset. An unresolved peak means that there is no synchrotron emission occurring in the Faraday rotating region. This is unexpected, since cosmic rays that produce synchrotron emission pervade the ISM. We propose that the magnetic field orientation plays an important role in this, in that a magnetic field that is oriented along the line-of-sight produces only synchrotron emission perpendicular to the line-of-sight, hiding it from our view. By using the observed emission measures from the WHAM survey as input, and by simulating the thermal electron contribution to $\mathcal{R}$, we could determine the magnetic field strength along the line-of-sight, and we mapped this quantity over the area covered by our GEMINI data. The polarized point sources we found in our data have RMs that are comparable to the $\mathcal{R}$ we find for the diffuse emission. By modeling the electron density distribution, we find that the difference in length of the line-of-sight towards an extragalactic source and the length of the line-of-sight towards the diffuse emission only produces a limited additional rotation measure for the extragalactic source, compared to the Faraday depth of the diffuse emission. In our $P(\mathcal{R})$ maps we found depolarization canals, narrow structures with only a small fraction of the polarized intensity of adjacent lines-of-sight. We established that for a number of deep canals the polarization angle changes in many frequency channels by a large amount, in some cases 90°, over the canal. We therefore argue that depolarization over the synthesized telescope beam is producing (at least) these canals. Finally, we investigated the properties of a large, conspicuous area in our data, and we argue that a decrease in depolarization along the line-of-sight as compared to its surroundings is probably responsible for the observational features of this region.

Acknowledgements

The Westerbork Synthesis Radio Telescope is operated by the Netherlands Foundation for Research in Astronomy (NFRA) with financial support from the Netherlands Organization for Scientific Research (NWO). The Wisconsin H-Alpha Mapper is funded by the National Science Foundation.

Chapter 4

WSRT Faraday tomography of the Galactic ISM at $\lambda \sim 0.86$ m - II. The CEPHEUS data set at $(l, b) = (102^\circ, 15^\circ)$

Abstract. In this chapter we present Faraday tomography observations carried out with the WSRT towards $(l, b) = (102^\circ, 15^\circ)$. We use the novel technique of Faraday tomography to study the distribution of Faraday-rotating and synchrotron-emitting regions along the line-of-sight. First we discuss the Faraday depths and peak heights of the strongest peak in the $P(\mathcal{R})$ spectrum for the lines-of-sight in our mosaic. The strongest diffuse emission is found for Faraday depths between -22 rad/m^2 and +8 rad/m^2, and it shows an overall strong alignment with Galactic latitude, with angular structure on scales from degrees down to the synthesized telescope beamsize of $\approx 3'$. If the Faraday depth varies sufficiently over the telescope's field, large-scale structure is modulated to smaller scales, and this applies to the present area. To build up the Faraday depths of the main peak in the $P(\mathcal{R})$ spectrum requires (on average) a magnetic field component of -0.1 μG, which is much smaller than the -3.6 μG we would expect for the regular magnetic field in the direction of our CEPHEUS mosaic. The average magnetic field strength that we derive from the Faraday depths of the diffuse emission is however a lower limit because our method overestimates the electron density contribution to the Faraday depth. We illustrate the richness and diversity of the structures that we find in the $P(\mathcal{R})$ spectra, by showing $P(\mathcal{R})$ spectra for lines-of-sight on a rectangular 10 $\times$ 12 grid. To prove that these $P(\mathcal{R})$ spectra are not the product of noise or instrumental artefacts, we also show $P(\lambda^2)$ and $\Phi(\lambda^2)$ spectra for a subset of 20 of those lines-of-sight. Finally we discuss the rotation measures of the extragalactic sources that we detected in our data set. The Faraday depths of the diffuse emission has over most of the mosaic a different sign than the rotation measures of the extragalactic sources. This is a clear indication that 1) there is a large-scale field reversal somewhere along the line-of-sight, and 2) the diffuse emission does not sample the entire line-of-sight through the Galaxy. We construct a simple model of the Galactic ISM that includes a field reversal at a certain height above the midplane. The field reversal allows two possible lengths of the line-of-sight of the diffuse emission, one of 110 pc and one of 3.4 kpc. We argue that the observational characteristics of the 110 pc line-of-sight make it an unlikely solution.

D. H. F. M. Schnitzeler, P. Katgert and A. G. de Bruyn

4.1 Introduction

FARADAY tomography is a novel technique that permits studying the distribution of Faraday rotation and synchrotron emission along the line-of-sight (see Brentjens & De Bruyn 2005). This is a big step forward compared to previous studies where information was only available for the line-of-sight as a whole. In Sect. 3.2.1 we presented a brief introduction to Faraday tomography and we gave some examples of how Faraday tomography can reveal different configurations of Faraday rotating and synchrotron emitting regions along the line-of-sight. Here we briefly introduce the basics behind Faraday tomography. We start by writing the polarization vector as a complex number, with its Stokes Q and U components as its real and imaginary parts. The amount of Faraday rotation between the observer and the point of emission that lies at a distance 'x' is given by

$$\mathcal{R}(x)\,[\mathrm{rad/m^2}] \;=\; 0.81 \int_{\text{source at 'x'}}^{\text{observer}} n_e\,[\mathrm{cm^{-3}}]\;\vec{B}\,[\mu\mathrm{G}]\cdot \mathrm{d}\vec{l}\,[\mathrm{pc}] \tag{4.1}$$

where n_e is the electron density, $\vec{B}$ the magnetic field vector, and $\mathrm{d}\vec{l}$ an infinitesimal piece of the line-of-sight towards the observer. $\mathcal{R}$ is also known as the Faraday depth corresponding to the distance 'x'. By writing the polarization vector as a complex quantity, we can also express the amount of Faraday rotation between the point of emission and the observer as the complex number $\mathrm{e}^{2\mathrm{i}\mathcal{R}(\mathrm{x})\lambda^2}$. If we sum over all contributions from the different parts of the line-of-sight, we find:

$$\vec{P}(\lambda) \;=\; \int_0^\infty \vec{P}(\mathrm{x})\,\mathrm{e}^{2\mathrm{i}\mathcal{R}(\mathrm{x})\lambda^2}\mathrm{dx} \;=\; \int_{-\infty}^{\infty} \vec{P}(\mathcal{R})\,\mathrm{e}^{2\mathrm{i}\mathcal{R}\lambda^2}\mathrm{d}\mathcal{R} \tag{4.2}$$

where the first integral is over physical distance 'x', and the second integral is over Faraday depth. Faraday tomography utilizes the orthogonality of the $\mathrm{e}^{2\mathrm{i}\mathcal{R}\lambda^2}$ to determine the strength and orientation of the polarization vector at Faraday depth $\mathcal{R}$:

$$\vec{P}(\mathcal{R}) \;=\; K \int_{-\infty}^{\infty} \vec{P}(\lambda^2)\,\mathrm{e}^{-2\mathrm{i}\mathcal{R}\lambda^2}\mathrm{d}\lambda^2 \tag{4.3}$$

$$K \;=\; \left(\int_{-\infty}^{\infty} W(\lambda^2)\,\mathrm{d}\lambda^2 \right)^{-1} \tag{4.4}$$

$W(\lambda^2) = 1$ for observed wavelengths, and = 0 elsewhere. The K factor in Eqn. 4.4 takes care of the correct normalization of $P(\mathcal{R})$. If the measured $P(\lambda^2)$ are in K (mJy/beam), then also the $P(\mathcal{R})$ will be in K (mJy/beam), or, more precisely, in K/RMSF width (mJy/beam/RMSF width). If we want to compare different data sets, with different RMSFs, it is necessary to convert this quantity to K/rad/m^2 instead of K/RMSF

(equivalently for mJy/rad/m^2). Here we only consider one dataset, and we did not convert the measured $P(\mathcal{R})$ to K/rad/m^2.

We distinguish here between the Faraday depth $\mathcal{R}$ and the rotation measure RM $\equiv \partial\ \Phi/\partial\ \lambda^2$, the derivative of the observed polarization angles with respect to λ^2. One must realize that with Eqn. 4.3 we determine the strength and the orientation of the polarization vector $\vec{P}(\mathcal{R})$ at a certain Faraday depth, which is not the same as physical depth. To translate Faraday depths into physical depths one needs to make assumptions on the geometry of the magnetic field and on the distribution of synchrotron emission and thermal electrons. In particular, reversals in the direction of the magnetic field produce ambiguities, since these will assign the same Faraday depth to different physical depths.

De Bruyn & Brentjens (2005) used Faraday tomography to study the Perseus cluster, and we used Faraday tomography to investigate the properties of the Galactic ISM in the direction of the Galactic anti-centre (chapters 2 and 3). We found that an unexpectedly large fraction of the lines-of-sight in our data contain unresolved main peaks in the $P(\mathcal{R})$ spectrum. This can only be explained when the region with synchrotron emission that produces the peak is not mixed with Faraday rotating electrons, since mixing between such regions would produce resolved structures in the $P(\mathcal{R})$ spectrum. One possible explanation could be a magnetic field that lies perpendicular to the line-of-sight: the line-of-sight component of the magnetic field, which determines RM, is then 0.

This is the third chapter in which we apply Faraday tomography to WSRT observations, with the goal of studying the properties of the magnetized ISM in the second Galactic quadrant. We present the observational characteristics of the present data set ('CEPHEUS') and discuss the reduction of the data in Sect. 4.2. In Sect. 4.3 we briefly describe the properties of the Faraday tomography datacube that we calculated from our observations. We discuss the Faraday depths of the main peak in the $P(\mathcal{R})$ spectra, which we use in Sect. 4.4 to estimate the strength of the line-of-sight component of the magnetic field. To illustrate how rich the $P(\mathcal{R})$ spectra in the CEPHEUS data set are, we present a grid of 10×12 $P(\mathcal{R})$ spectra in Sect. 4.5. For a subset of these lines-of-sight we also show the $P(\lambda^2)$ and $\Phi(\lambda^2)$ spectra that were used to calculate the $P(\mathcal{R})$ spectra that we present, to support our conclusion that the $P(\mathcal{R})$ spectra are not the product of noise or instrumental artefacts. Extragalactic sources probe the entire line-of-sight through the Galaxy. One of the main conclusions of this chapter is that the diffuse emission not necessarily samples the entire line-of-sight through the Galaxy as the extragalactic sources do. The rotation measures of extragalactic sources therefore produce valuable additional information to the Faraday depths of the diffuse emission. We describe our detection algorithm for polarized extragalactic pointsources in Sect. 4.6, and we present the 12 sources that we found in our data set. Over the largest part of the mosaic, the diffuse emission is strongest at negative Faraday depths, whereas most of the extragalactic sources that we find show positive rotation measures. This requires a large-scale reversal in the direction of the magnetic field somewhere along the line-of-sight, and in Sect. 4.7 we model such a geometry. Our model allows two solutions for the length of the line-of-sight of the diffuse emission, and in this section we argue that the longer line-of-sight is most likely.

4.2 The data

With the WSRT we observed a mosaic of pointings that is centered on $\alpha = 20^h40^m$ and $\delta = 67^\circ$ (J2000.0), or $l \approx 102^\circ$ and $b \approx 15^\circ$ in Galactic coordinates. We refer to this mosaic as the 'CEPHEUS' mosaic. The WSRT is a 14-element E-W interferometer of which 4 elements are moveable to improve (u,v) coverage. Each of the telescope dishes has a diameter of 25 meters. To minimize the influence of the sun and the Earth's ionosphere we conducted our observations mostly at night. By virtue of its right ascension, the CEPHEUS mosaic culminates at midnight around the middle of August, but at that time the nights are not long enough to complete one 12 hr observing run. We therefore split the observations over 2 runs of ≈ 6 hr (allowing for an ≈ 1.5 hr overlap between these runs), observing one half in June 2004, and one half in September/October 2004 (see Table 4.1). Over the two observing periods we fill half the (u,v) plane with about 19 HA per pointing. The combined observations yielded visibilities at baselines from 36 to 2760 meters, with an increment of 12 meters. We tapered the individual frequency channel maps in such a way that the synthesized beamsize for all maps is $3.02' \times 3.28'$ (RA $\times$ DEC). Combining the 6 12 hr observing runs puts the first grating ring at 4.1° (at 350 MHz) from the pointing centre, outside the $3^\circ \times 3^\circ$ area that we mapped for each individual pointing.

We mapped an area of about $10^\circ \times 10^\circ$ with 7×7 pointings. In June we observed the first ~ 7 hr each night, and in September/October we observed the remaining ~ 7 hr to complete one half of the (u,v) plane. Each HA was observed for 40 seconds before the telescope moved to the next pointing. For a rectangular grid in equatorial coordinates, off-axis instrumental polarization can be reduced to less than 1% by carefully positioning the pointing centers 1.25° apart (Wieringa et al. 1993). However, our pointing grid is rectangular in Galactic coordinates. For such a grid the antenna dipoles in adjacent fields do not nicely align to reduce off-axis instrumental polarization. Nevertheless, we think that, even with our choice of pointing centers, instrumental polarization should only play a minor role: in Sect. 4.6 we will present significant detections of point sources that are polarized at the $\gtrsim 2\%$ level.

We reduced our data with the `NEWSTAR` data reduction package. Dipole gains and phases and leakage corrections were determined using the unpolarized calibrators 3C48, 3C147 and 3C295. The flux scales of both unpolarized and polarized calibrators are set by the calibrated flux of 3C286 (26.93 Jy at 325 MHz - Baars et al. 1977). Due to an a-priori unknown phase offset between the horizontal and vertical dipoles, signal can leak from Stokes U into Stokes V. We corrected for this by rotating the polarization vector in the Stokes (U, V) plane back to the U axis, assuming that there is no signal in V. The polarized calibrator sources 3C345 and DA240 defined the sense of derotation (i.e. to the positive or negative U-axis). For each telescope pointing we then self calibrated the combination of the June and the September/October data sets. 13 pointings did not have strong enough point sources to calculate the self calibration solution. For these pointings we copied the selfcal solutions from adjacent pointings. To check that this is an acceptable procedure, we compared for 2 pointings the phase corrections in a small number of frequency channels found by the selfcal pipeline. These corrections are very stable, and therefore we can copy the selfcal solutions between ad-

Table 4.1 — Characteristics of the CEPHEUS data set. Observing dates and times are given for each of the observing runs, which have been indicated by their shortest baseline length.

Central position	$(\alpha, \delta)_{2000}$ = (310°, 67°); (l, b) = (102°, 15°)					
Size ($l \times b$)	$10^\circ \times 10^\circ$					
Pointings	7×7					
Frequencies	314–381 MHz					
	213 independent frequency channels					
Resolution[a]	$3.02' \times 3.28'$					
Stokes V noise level	5.5 mJy (2.3 K)					
$\mathcal{R}$ noise level[b]	0.3 mJy (0.13 K)					
Conversion Jy–K[c]	1 mJy/beam = 0.42 K					
Spacing (m)	36a	48a	60a	72a	84a	96a
Observing date (yy/mm/dd)	04/06/21	04/06/28	04/06/14	04/06/12	04/06/24	04/06/30
Start time (UT)	20:01	19:47	20:57	19:18	19:49	19:47
End time (UT)	02:25	01:58	02:53	03:00	02:13	01:49
Spacing (m)	36b	48b	60b	72b	84b	96b
Observing date (yy/mm/dd)	04/09/20	04/09/25	04/09/27	04/10/02	04/10/04	04/10/06
Start time (UT)	19:01	18:42	18:34	18:14	18:06	17:58
End time (UT)	02:44	01:56	02:02	02:04	01:08	01:20

[a] We tapered the individual frequency channel maps in such a way that the synthesized beamsize for all maps is $3.02' \times 3.28'$ (RA $\times$ DEC).

[b] This is the noise level in individual $\mathcal{R}$ maps, which we determined from maps at $|\mathcal{R}| > 200$ rad/m^2, that we assume contain no signal. Instrumental polarization levels increases towards the edges of the maps, therefore we excluded these in determining the noise level.

[c] This is the conversion factor at 344 MHz, the average of the λ^2 sampling of the (usable) frequency channels in our dataset.We used the FWHM of a Gaussian fitted to the central peak of the synthesized PSF to calculate the beamsize required in this conversion.

jacent pointings. When looking for polarized point sources in our data (see Sect. 4.6), we encountered calibration problems with the longest baselines. For that part of our analysis we had to leave out the 2 movable telescopes that are found in the longest (u,v) baselines, and we also could not use the highest and lowest frequency bands there. We did not encounter problems when we were studying the diffuse emission, since the tapers used in those maps assign to the long (u,v) baselines with the faulty telescopes weights $\lesssim 3\%$ of the weight of the 0-m baseline.

We selected usable frequency channels on the basis of the width of the Stokes Q, U and V distributions. In determining these widths we left out the edge of the mosaic where instrumental polarization produces strong artefacts. 213 out of the maximum of 224 available frequency channels turn out to be usable. These channels cover the frequency range between 314 and 381 MHz, and each channel is 0.4 MHz wide, where we used a Hanning taper. Our automated clipping process will create 'holes' in the λ^2 coverage of our data, and these will result in higher sidelobes of the RMSF, which

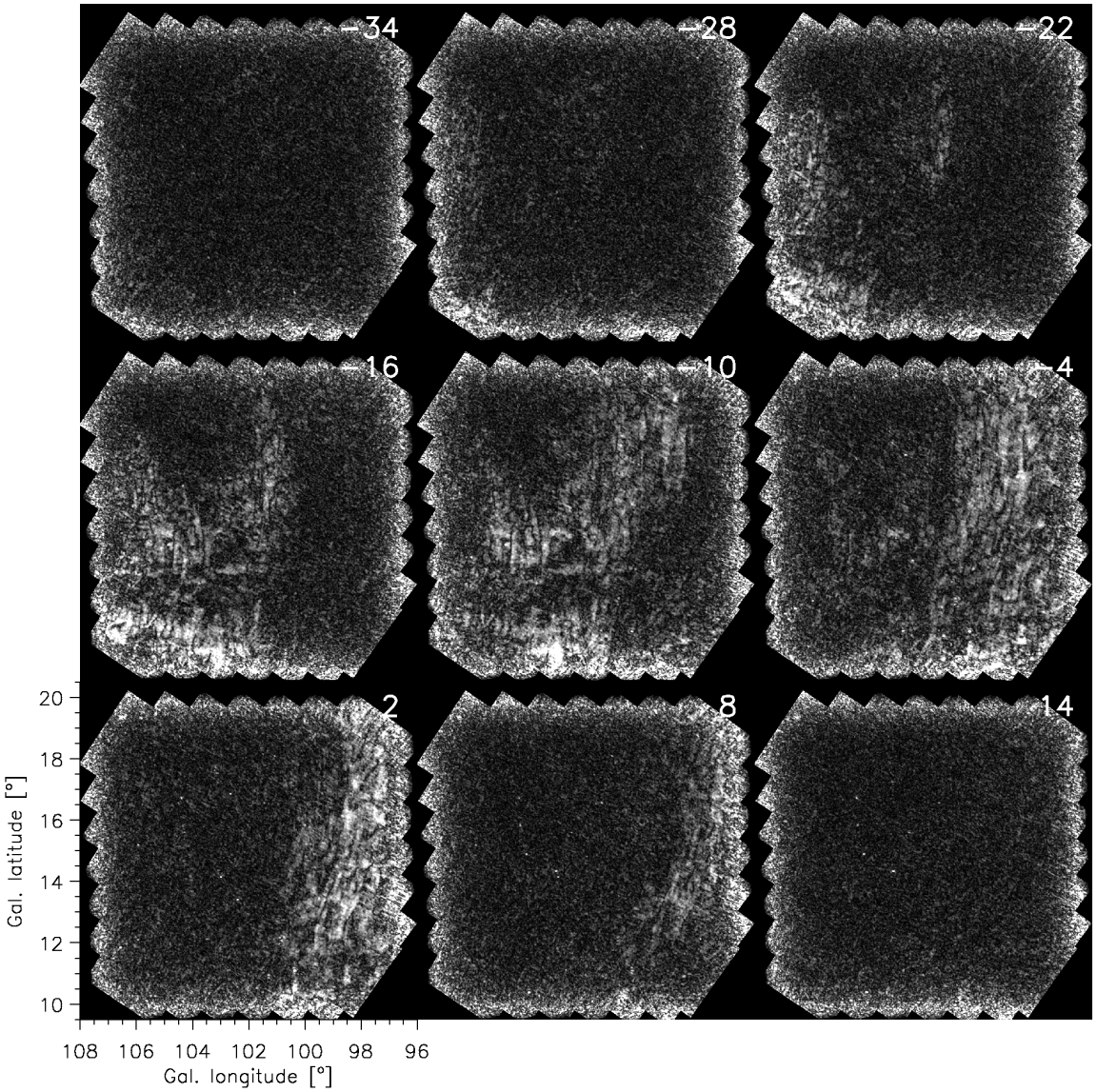

Figure 4.1 — Images of $P(\mathcal{R})$ maps with the strongest diffuse emission. We indicate the $\mathcal{R}$ of each 'slice' through our image cube in the upper right corner of each image in units of rad/m^2. The RMSF has a FWHM of about 15 rad/m^2, and we sampled each RMSF with 2 images. All panels have the same linear intensity scale that saturates at 3.5 K, whereas the GEMINI maps in Fig. 3.2 saturated at 6.4 K. The 1σ noise level in the $P(\mathcal{R})$ maps is 0.13 K. To convert our mosaic maps from equatorial to Galactic coordinates we regridded the Stokes Q and U mosaics from equatorial to Galactic coordinates, after which we calculated the polarized intensity from these regridded maps.

is the equivalent in Faraday tomography of the PSF in radio synthesis imaging. From Stokes V, which we assume to be empty, we estimate that the average noise level in the final mosaics of the individual channels is 5.5 mJy (2.3 K).

The CEPHEUS observations were carried out in the evening and at night to limit solar interference and to reduce the importance of ionospheric rotation measure (RM) variations. From the polarization angles of the polarized calibrators we estimated how strong the ionospheric RM contribution varied over the different observing runs. The

average difference in polarization angle over the 6 observing nights in June is about 5°, and over the September/October observations the average difference was about 0°. The difference between the averages in the June and September/October observing periods is only about 5°. Since these differences are so small, we did not correct for them. The ionospheric RM is at most 1 rad/m^2 during our observations in June and in September/October (Johnston-Hollitt, private communication), which is so small that we did not correct our data for it.

An interferometer will not cover all baseline lengths down to 0 meters, which means that maps of the sky that were made using an interferometer will miss structure on large angular scales. In Sect. 3.4.2 we determined how strong a linear gradient in Faraday depth over the telescope field-of-view has to be, to modulate the 0 angular frequency component (total polarized intensity) component to scales that are small enough so that they can be observed with the WSRT. For our observing wavelengths and dimensions of the field-of-view this requires a linear gradient in $\mathcal{R}$ of ≈ 6 rad/m^2. In Fig. 4.3 we plot for each line-of-sight the Faraday depth of the highest peak in the Faraday depth spectrum. Although some regions in the mosaic are dominated by noise, over most of the mosaic the gradients in Faraday depth are strong enough so that the 0-angular frequency component that is emitted at these Faraday depths should become visible for the WSRT.

4.3 Analysis

We calculated $\vec{P}(\mathcal{R})$ maps of the sky for Faraday depths from -1000 rad/m^2 to +998 rad/m^2 in steps of 6 rad/m^2. The RMSF has for our data a width along the $\mathcal{R}$ axis of about 15 radians/m^2. With a stepsize of 6 rad/m^2 we therefore have more than Nyquist sampled in Faraday depth. Due to the finite λ^2 width of the frequency channels, $\delta\lambda^2$, the sensitivity of the $P(\mathcal{R})$ spectra will drop for large values of $\mathcal{R}$, similar to how the size of the single-dish antenna in a synthesis array determines the field-of-view in radio synthesis interferometry. Brentjens & De Bruyn (2005) determined that the sensitivity has dropped to 50% at $\mathcal{R}_{\rm max} = 1.9/\delta\lambda^2$ (the 1.9 replaces the $\sqrt{3}$ from their article because the sinc response to the λ^2 coverage they assume has a HWHM that can be better approximated by 1.9 than by $\sqrt{3}$). In our data set on average $\delta\lambda^2 \approx 1.5 \times 10^{-3}$ m^2, which means that we should still be $> 50\%$ sensitive for values of $\mathcal{R} < 1250$ rad/m^2.

In Fig. 4.1 we show slices through our $\mathcal{R}$ datacube with strong Galactic emission. All of the images saturate at 3.5 K. To create Fig. 4.1 we first regridded the Stokes $Q(\mathcal{R})$ and $U(\mathcal{R})$ mosaics at the Faraday depths of the panels in this figure from equatorial to Galactic coordinates, and then we calculated the polarized intensity from these regridded maps. In Figs. 4.2 and 4.3 we summarize the information in the $\mathcal{R}$ datacube by plotting for each line-of-sight the maximum $P(\mathcal{R})$ along that line-of-sight, and the $\mathcal{R}$ at which this maximum occurs. The $P(\mathcal{R})$ slices from Fig. 4.1 show a very clear stratification with Galactic latitude, which becomes again apparent in Figs. 4.2 and 4.3. From the $P(\mathcal{R})$ maps at $|\mathcal{R}| > 200$ rad/m^2 we estimate that the noise level in the $P(\mathcal{R})$ slices is 0.3 mJy (0.13 K). This is consistent with the noise per frequency channel (~ 2.3 K), and the number of channels that contribute to a given $P(\mathcal{R})$ (~ 200).

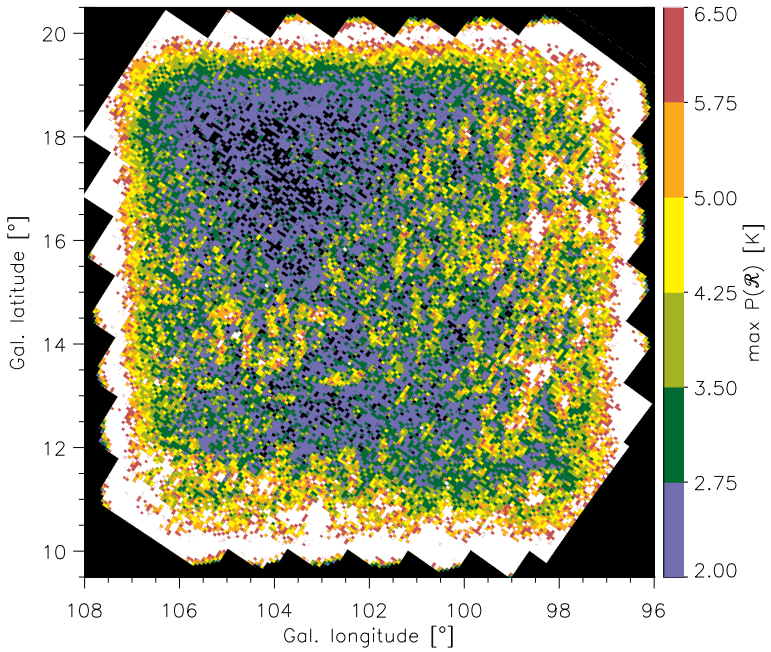

Figure 4.2 — $P(\mathcal{R})$ [K] of the highest peak in the $\mathcal{R}$ spectrum. Each pixel represents one telescope beam, and the pixel size is $3.0' \times 3.3'$. Out of a total of about 28.000 lines-of-sight, 1287 lines-of-sight have $P(\mathcal{R}) < 2$ K, shown in black, and 3894 lines-of-sight have $P(\mathcal{R}) > 6.5$ K, which are shown in white. The 1σ noise level is 0.13 K. On page 189 we show a colour version of this figure.

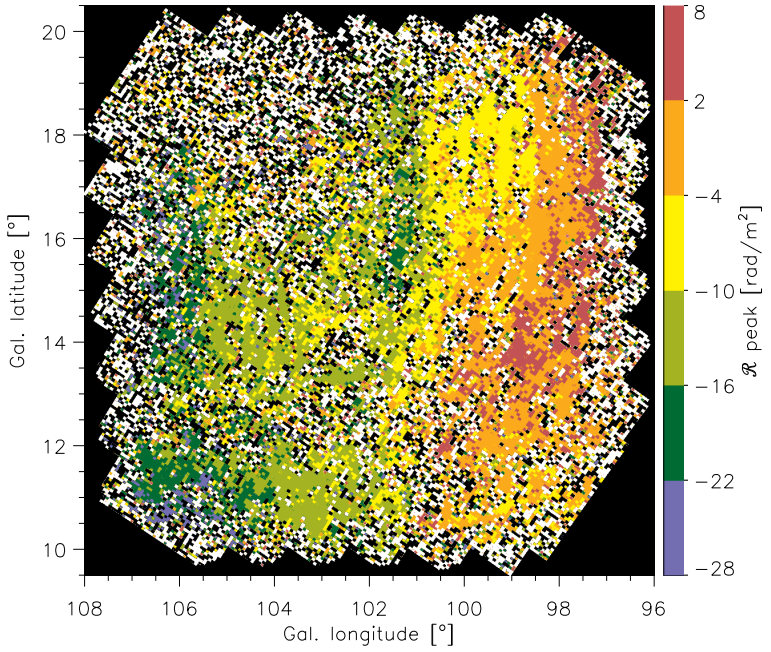

Figure 4.3 — $\mathcal{R}$ corresponding to the $P(\mathcal{R})$ plotted in Fig. 4.2. Lines-of-sight with $\mathcal{R}$ < -28 rad/m^2 are shown in white, lines-of-sight indicated in black have $\mathcal{R} > 8$ rad/m^2 (5009 and 5670 lines-of-sight respectively). Most of the discarded lines-of-sight fall either on the edge of the mosaic, or in the upper left region with low signal strength. On page 190 we show a colour version of this figure.

4.4 The line-of-sight component of the magnetic field

In this section we derive the strength of the line-of-sight magnetic field component, $B_\parallel$, required to produce the Faraday depth $\mathcal{R}$ of the strongest peak in the $P(\mathcal{R})$ spectrum, as shown in Fig. 4.3. Basically, we convert the WHAM Hα intensities observed towards the CEPHEUS mosaic to emission measures, which we then translate to dispersion measures using an empirical relation that Berkhuijsen et al. (2006) determined for Galactic pulsars. The emission measure EM and dispersion measure DM are defined by EM[cm^{-6}pc] = $\int_0^\infty n_\mathrm{e}^2 \mathrm{d}l$ and DM[cm^{-3}pc] = $\int_0^\infty n_\mathrm{e} \mathrm{d}l$, where n_e is the electron density in cm^{-3}, and dl is an infinitesimal element of the line-of-sight in parsec. Using the dispersion measures derived from the emission measures and the $\mathcal{R}$ from Fig. 4.3, we can then calculate the electron-density weighted average $B_\parallel$ along the line-of-sight, $\langle B_\parallel \rangle$.

There are alternative models that can be used for calculating DM. The Reynolds (1991) model contains clumps of Faraday rotating electrons that fill 40% of the line-of-sight. Each clump has the same electron density of 0.08 cm^{-3}. The Reynolds model is however based on only a small number of lines-of-sight towards high-latitude pulsars in globular clusters. Cordes & Lazio have used a sample of about 1200 Galactic sources + about 100 extragalactic sources to model the electron density distribution of the Milky Way, but its major components (thin and thick disk, spiral arms) are still very smoothly modeled. The Cordes & Lazio model includes small-scale structure as a list of clumps and voids. The Berkhuijsen et al. model uses a sample of 157 pulsars with measured DM. From the WHAM survey they determine the EM in the direction of the observed pulsars, and they correct these EM both for emission coming from beyond the pulsar, and for interstellar reddening occurring in front of the pulsar. From their data they determine a relation between DM and EM, and the variation of the electron density and the electron filling factor with distance above the Galactic plane. By combining the WHAM Hα intensities, that have been measured on an approximately $1^\circ \times 1^\circ$ grid, with the Berkhuijsen et al. statistical description of the ISM, we can probably more accurately determine DM for specific regions on the sky than by using the models by Reynolds or by Cordes & Lazio.

Until now we have discussed Faraday rotation occurring in the warm ionized medium (WIM). The only other ISM phase with sufficient free electrons to produce Faraday rotation is the hot intercloud phase (HIM). Snowden et al. (1997) modeled the HIM electron density in the plane of the Galaxy, and found that this density is lower by a factor of 10 compared to the electron density in the warm ionized ISM. We therefore neglect the HIM contribution to Faraday rotation.

In the top panel of Fig. 4.4 we plot the WHAM Hα intensities in the CEPHEUS mosaic. To convert these to emission measures we can use Eqn. 1 from Haffner et al. (1998):

$$\mathrm{EM} \;=\; 2.75 T_4^{0.9}\; I_{\mathrm{H}\alpha}(\mathrm{R})\; \mathrm{e}^{2.2\;\mathrm{E(B-V)}} \tag{4.5}$$

T_4 is the temperature of the WIM gas in units of 10^4 K, which is typically 0.8 (Reynolds 1985). $I_{\mathrm{H}\alpha}$ is the Hα intensity in Rayleigh, and E(B-V) is the interstellar B-V reddening,

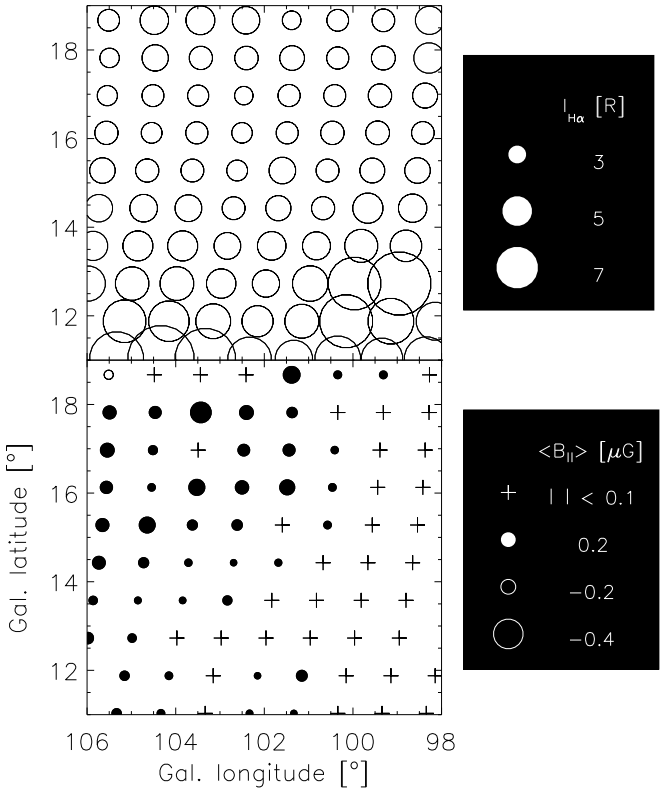

Figure 4.4 — WHAM Hα intensities in Rayleigh (top panel) and the strengths of the magnetic field component parallel to the line-of-sight $\langle B_\parallel \rangle$ in μG (bottom panel) that we derived. In Sect. 4.4 we describe how we derived $\langle B_\parallel \rangle$ from the WHAM Hα intensities and the Faraday depths from Fig. 4.3. Open circles indicate positive $\langle B_\parallel \rangle$, filled circles negative $\langle B_\parallel \rangle$. $|\langle B_\parallel \rangle| < 0.1$ μG are shown as '+'.

which we found with the NED extinction calculator[1], that is based on Schlegel et al. (1998). For the centre of the mosaic E(B-V) = 0.527. E(B-V) varies over the mosaic, from about 0.2 in the upper right to 0.7 in the bottom left. With an E(B-V) = 0.527 we find that 1 Rayleigh = 7.17 cm^{-6}pc, and the average Hα intensity in the CEPHEUS mosaic of 5 Rayleigh then translates into an emission measure of about 36 cm^{-6}pc.

To convert the EM to DM we use the following relation that Berkhuijsen et al. established for a sample of 157 Galactic pulsars with $|b| > 5^\circ$:

$$\mathrm{EM} \;=\; 0.042 \pm 0.014\ \mathrm{DM}^{1.47\pm0.09} \tag{4.6}$$

Given the definition of DM we can then calculate the strength of the magnetic field component along the line-of-sight, weighted with the electron-density:

$$\langle B_\parallel \rangle \equiv \frac{\int\limits_{\text{line-of-sight}}^{\text{observer}} n_e \vec{B} \cdot \mathrm{d}\vec{l}}{\int\limits_{\text{line-of-sight}} n_e \mathrm{d}l} \;=\; \frac{\mathcal{R}}{0.81\ \mathrm{DM}} \tag{4.7}$$

where $\langle B_\parallel \rangle$ is in μG. We determined EM for the entire line-of-sight through the Galaxy. As we will shortly show, the Faraday depths of the diffuse emission and the rotation measures of the polarized extragalactic sources in CEPHEUS have different signs. This

[1] `http://nedwww.ipac.caltech.edu/forms/calculator.html`

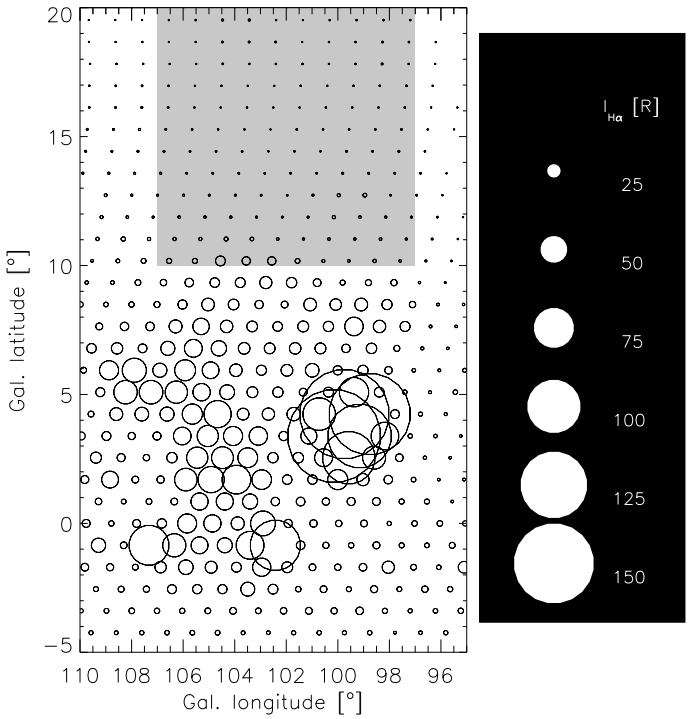

Figure 4.5 — WHAM Hα intensities in Rayleigh for the CEPHEUS mosaic and the HII regions in the vicinity of the CEP OB2 association. The grey region indicates the location of the CEPHEUS mosaic. The lowest plotted Hα intensity is 3 Rayleigh. The highest Hα intensities are found in the Sharpless 131 star forming region.

means that most of the diffuse emission that we observe comes from a nearby part from the line-of-sight towards the extragalactic sources. If we then use the EM of the entire line-of-sight to calculate $\langle B_\parallel \rangle$ from the $\mathcal{R}$ of the diffuse emission, the $|\langle B_\parallel \rangle|$ we find are lower limits to the actual $|\langle B_\parallel \rangle|$.

For an average $\mathcal{R}$ = –10 rad/m^2 and average Hα intensity of 5 Rayleigh, we find $\langle B_\parallel \rangle$ = –0.1 μG. In the bottom panel of Fig. 4.4 we show the $\langle B_\parallel \rangle$ that we calculated in this way for the Faraday depths of the diffuse emission in Fig. 4.3. There is a 30% uncertainty in $\langle B_\parallel \rangle$ due to width of the relation between EM and DM. Since the WHAM beam (FWHM $\approx 1^\circ$) is much larger than the WSRT beam, we used the $P(\mathcal{R})$-weighted $\mathcal{R}$ average over the WHAM beam to calculate $\langle B_\parallel \rangle$. According to Beck (2007a) the large-scale Galactic magnetic field in the vicinity of the sun has a strength of $4 \pm 1 \mu$G, and points towards $l = 82^\circ$. By projecting these values onto the line-of-sight towards the centre of the CEPHEUS mosaic, we would expect to find a regular magnetic field $B_{\mathrm{reg},\parallel}$ = –3.6 μG, which is much smaller than the $\langle B_\parallel \rangle$ that we find in the bottom panel of Fig. 4.4. We return to this in Sect. 4.7.

There is an additional complication to calculating the EM for the entire line-of-sight through the Galaxy. Closer to the Galactic plane lies the CEP OB2 association with its associated HII regions. CEP OB2 is spread out over $96^\circ < l < 108^\circ$ and -1° < b <12°, and lies at a distance of about 600 pc (De Zeeuw et al. 1999). Humphreys (1978) lists 8 O (with 2 'doubtful' members) and 12 B stars as its members. In Fig 4.5 we map the distribution of Hα intensities over our CEPHEUS mosaic and the CEP OB2 association (note the large difference in scale between Figs. 4.4 and 4.5!). If most of the Hα emission that we see originates close to us, in or in front of the HII regions in CEP OB2, and if we would therefore assume E(B-V) = 0 instead of E(B-V) = 0.527, then the $\langle B_\parallel \rangle$ we derived would double.

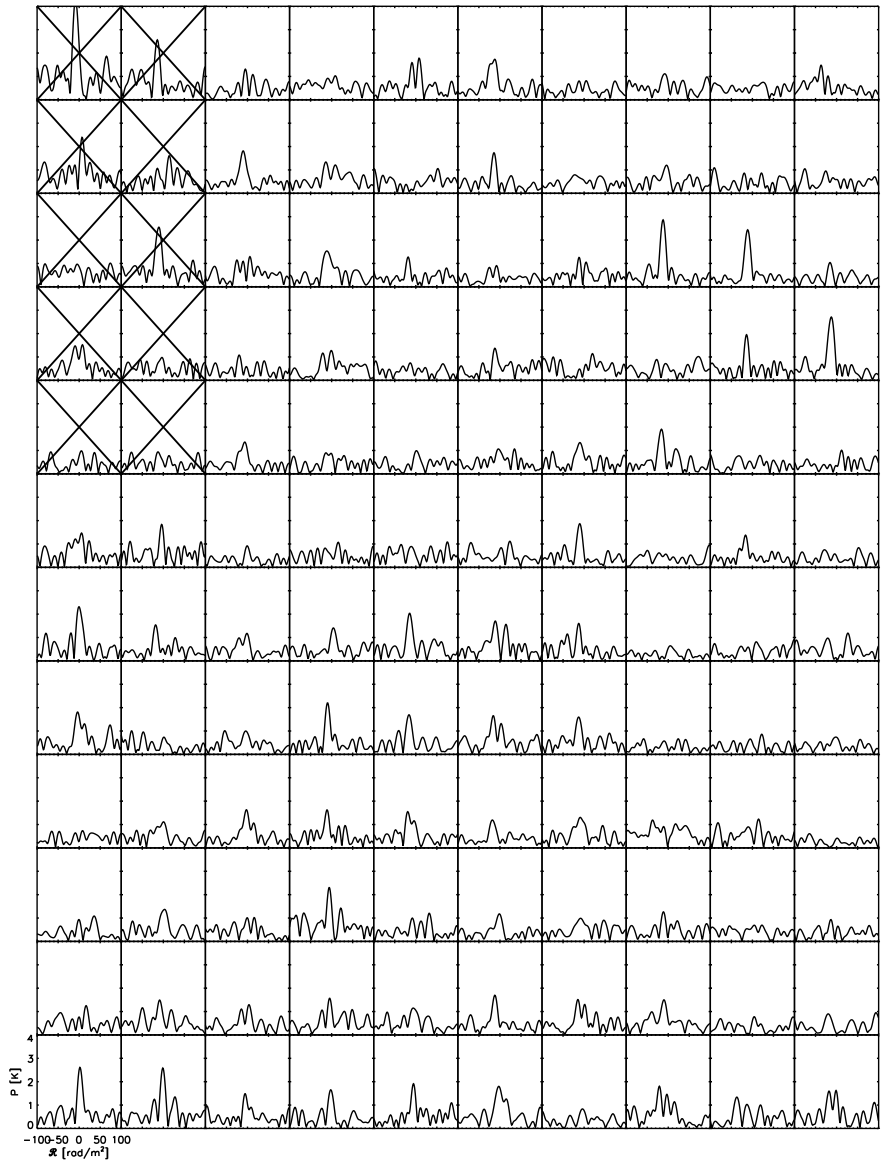

Figure 4.6 — $P(\mathcal{R})$ spectra for a rectangular grid of lines-of-sight through the CEPHEUS datacube. Faraday depths [rad/m^2] between -100 rad/m^2 and +100 rad/m^2 are plotted along the x-axis, and polarized intensities from 0 – 4 K along the y-axis. The noise level in these spectra is 0.13 K. We chose lines-of-sight that lie far enough from the mosaic edges where instrumental polarization levels are higher. The crossed-out lines-of-sight in the upper left of the grid of spectra lie in a region that is affected by calibration problems. Clearly there is a wide variety of structure for the different lines-of-sight. We plot the $P(\mathcal{R})$, $P(\lambda^2)$ and $\Phi(\lambda^2)$ spectra for some conspicuous lines-of-sight in Fig. 4.7 to show that the $P(\mathcal{R})$ spectra are not the result of low signal to noise or radio frequency interference, but are the product of a real signal.

4.5 Structure in the $P(\mathcal{R})$ spectra

The previous section dealt with the properties of the highest peak in the $P(\mathcal{R})$ spectrum, in this section we argue that the rest of the $P(\mathcal{R})$ spectrum is also varied in structure. To illustrate the richness and diversity in the $P(\mathcal{R})$ spectra of the CEPHEUS mosaic, we plot a 10×12 grid of $P(\mathcal{R})$ spectra in Fig. 4.6. There are lines-of-sight with

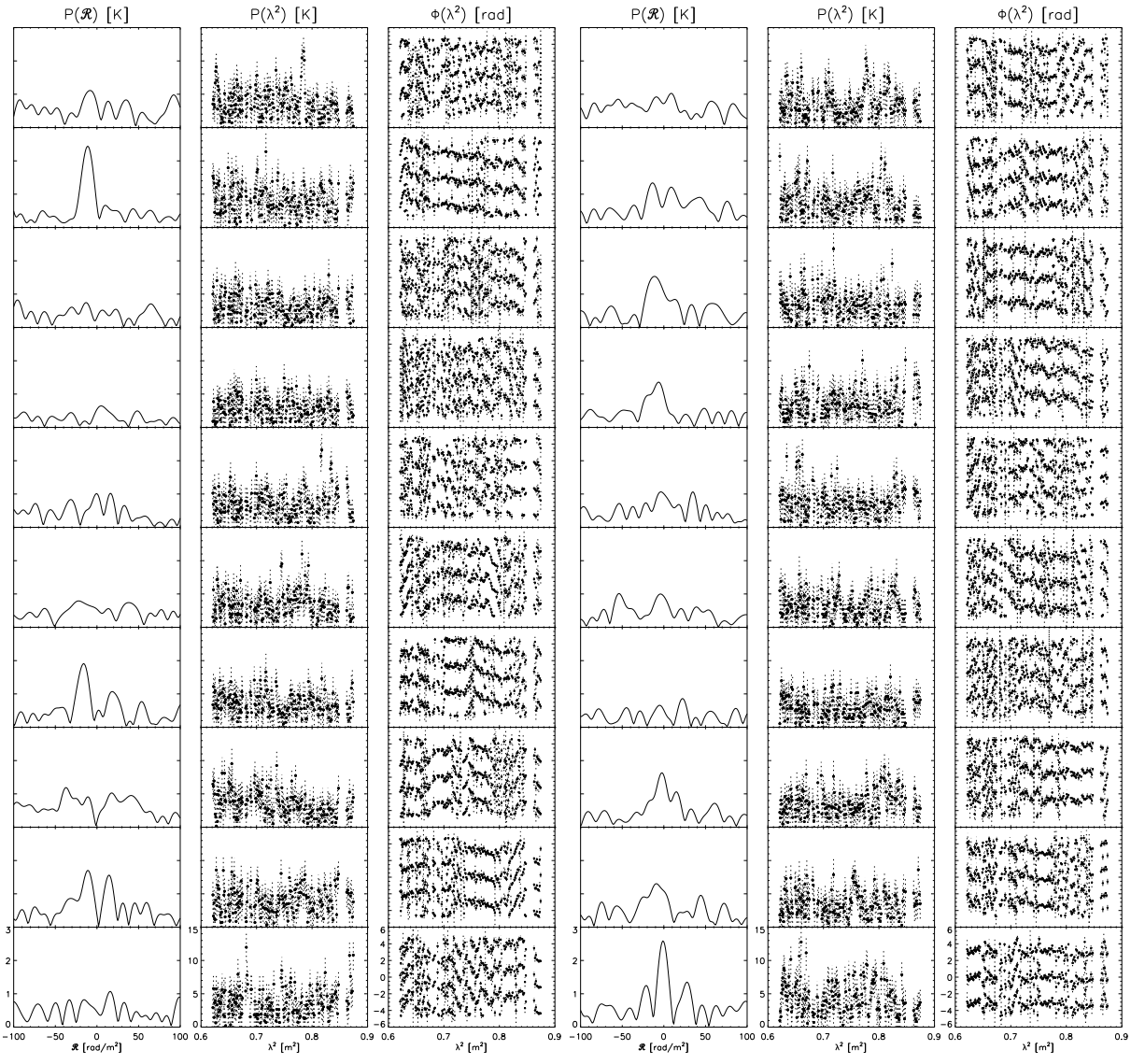

Figure 4.7 — $P(\mathcal{R})$ spectra, and the $P(\lambda^2)$ and $\Phi(\lambda^2)$ data they are based on, for 2×10 lines-of-sight with diffuse emission. For each group of 10 lines-of-sight, the left column shows the $P(\mathcal{R})$ spectra for Faraday depths between -100 rad/m^2 and +100 rad/m^2, and the $P(\mathcal{R})$ along the y axis go from 0–3 K. The $P(\mathcal{R})$ noise level is 0.13 K. The middle column shows the $P(\lambda^2)$ spectrum for 0.6 m^2 $\lesssim \lambda^2 \lesssim$ 0.9 m^2. The vertical scale for the panels in the middle column goes from 0–15 mJy (the noise level is 5.5 mJy). The right column shows the $\Phi(\lambda^2)$ spectrum. We replicated the spectra at the observed $\Phi(\lambda^2) \pm \pi$ to make the structure in polarization angle more clear.

a strong main peak, with double and multiple peaks, as well as $\mathcal{R}$-extended features. In Fig. 4.7 we plot the $P(\mathcal{R})$, $P(\lambda^2)$ and $\Phi(\lambda^2)$ spectra for a selection of lines-of-sight from Fig. 4.6. To make structures in $\Phi(\lambda^2)$ more clear, we replicated the $\Phi(\lambda^2)$ spectrum at $\pm \pi$ from the observed $\Phi(\lambda^2)$ spectrum in the middle of the plot. The signal/noise levels in the $P(\lambda^2)$ spectra are relatively low, therefore the $\Phi(\lambda^2)$ spectra are maybe the best indication that there is polarized signal present. But from these it is clear that the $P(\mathcal{R})$ spectra that we plot in the first column and in Fig. 4.6 are not the product of a low signal-to-noise ratio, or of radio-frequency interference. In chapter 7 we will apply

Table 4.2 — Properties of the polarized point sources that we found in our data. Shown are the Galactic coordinates of the source in decimal degrees, the RM that we fitted and the error in the RM fit, the reduced χ^2 ($\chi^2_{\rm red}$) of the fit, the $P(\mathcal{R})$ and total intensity I of the source, and its polarization percentage. The RM of the sources will because of the ionospheric RM that we did not correct for lie within about 1 rad/m^2 of the RM in this table.

Source	(l, b) (°,°)	RM [rad/m^2]	$\chi^2_{\rm red}$	$P(\mathcal{R})_{\rm max}$ [mJy]	I [mJy]	$P(\mathcal{R})_{\rm max}/I$ %
1	(106.13, 13.91)	-12.0 $\pm$ 0.4	1.1	6.4	249	2.6
2	(104.42, 17.32)	20.8 $\pm$ 0.4	0.9	9.4	359	2.6
3	(104.16, 15.38)	12.3 $\pm$ 0.2	0.7	15.3	706	2.2
4	(104.10, 16.60)	30.4 $\pm$ 0.5	1.0	5.2	183	2.8
5	(102.73, 11.34)	34.6 $\pm$ 0.4	1.7	10.1	410	2.5
6	(102.01, 11.15)	9.3 $\pm$ 0.3	0.8	9.5	266	3.6
7	(101.44, 17.15)	7.9 $\pm$ 0.2	0.5	9.8	271	3.6
8	(100.36, 11.30)	35.9 $\pm$ 0.5	2.1	9.6	357	2.7
9	(99.76, 19.41)	51.0 $\pm$ 0.2	1.8	18.1	595	3.0
10	(99.52, 16.59)	31.4 $\pm$ 0.5	0.9	3.7	160	2.3
11	(99.25, 12.87)	27.8 $\pm$ 0.5	1.1	4.4	194	2.3
12	(98.00, 17.67)	41.0 $\pm$ 0.5	1.7	5.0	202	2.5
13	(97.95, 12.04)	25.2 $\pm$ 0.7	2.9	4.2	204	2.1
14	(97.93, 13.33)	16.4 $\pm$ 0.5	2.0	5.0	218	2.3

a similar analysis to the one we present here to a $P(\mathcal{R})$ datacube calculated from MHD simulations. Then we can compare the observed $P(\mathcal{R})$ spectra to the physical properties of the simulated volume of ISM. Note that the spectra in Fig. 4.6 have not been deconvolved to remove the RMSF response. Some of the $P(\mathcal{R})$ structures with low power can therefore be produced by the RMSF response from stronger nearby peaks.

One must take caution not to over-interpret these spectra. The Stokes Q and U maps that these spectra are based on were produced with an interferometer that filters out extended structure on the sky, which will also have consequences for the calculated $P(\mathcal{R})$ spectra. We argued in Sect. 4.2 that the main peak in the $P(\mathcal{R})$ spectra should contain the 0-angular frequency that is emitted at the Faraday depths of the main peak. For the rest of the spectrum we can only argue that the features that we see in the $P(\mathcal{R})$ spectra can occur in nature, but they might also be affected to some extent by artefacts due to missing large-scale angular structure.

4.6 Polarized point sources

The RMs of polarized point sources form a valuable additional source of information for the Faraday depths that we derived for the diffuse emission. As we will show in this section, most of the extragalactic sources that we find have a positive RM, which is different from the Faraday depths with the strongest diffuse emission that over most of the mosaic are negative (see Fig. 4.3). Since the extragalactic sources sample the entire line-of-sight through the Galaxy, by comparing their RM with the Faraday depths of the diffuse emission we can learn more about where the diffuse emission that we

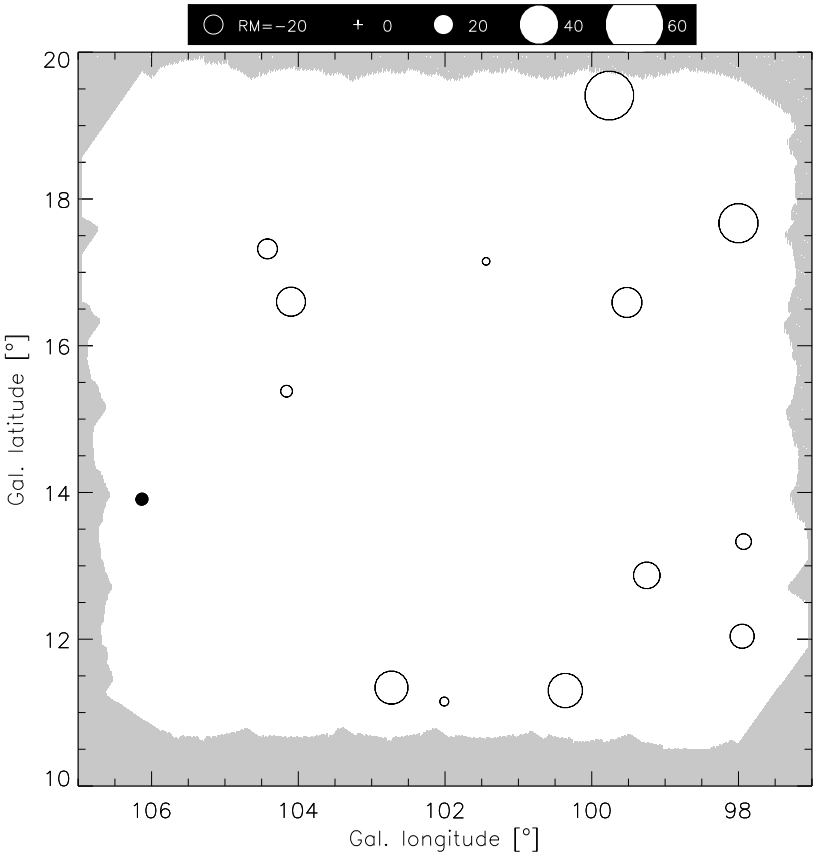

Figure 4.8 — RM distribution for the polarized point sources from table 4.2. The size of the circles is proportional to the RM, shown in the scale on top of the figure in units of radians/m^2. Black circles indicate negative RM, and white circles indicate positive RM. $|\mathrm{RM}| \lesssim 4$ rad/m^2 are missing from this figure because of our selection criteria. We excluded the grey region when looking for polarized point sources, because instrumental polarization levels are higher there.

observe is coming from. By filtering out the contribution from the diffuse emission to the $P(\mathcal{R})$ spectra it becomes easier to detect polarized point sources. We therefore calculated a new $P(\mathcal{R})$ cube from frequency channel maps that were made by using only baselines > 250 m. We tapered the maps of the individual frequency channels to a synthesized beamsize of $58'' \times 63''$ (RA $\times$ DEC). With these maps we calculated Faraday depth spectra for the range -1000 rad/m^2 $< \mathcal{R} <$ +998 rad/m^2 in steps of 6 rad/m^2 to give Nyquist sampling of the RMSF. The amount by which a polarized signal is attenuated by a linear RM gradient over a channel of width $\delta\lambda^2$ can be described by sinc($|\mathrm{RM}|\ \delta\lambda^2$). A RM = 1000 rad/m^2 gives an attenuation of only 34%, and we would probably detect most of the brighter sources with such large RMs.

When deciding which frequency channels we could use to calculate the new $P(\mathcal{R})$ cube, we lowered the 'acceptable' widths of the Stokes Q, U and V distributions because of the calibration problems with the long (u,v) baselines. This made the clipping used to find point sources more conservative than the one we discussed in Sect. 4.2 when we calculated a $P(\mathcal{R})$ cube to study the diffuse emission. After this clipping we still had 161 usable frequency channels, that cover the frequency range between 321

and 381 MHz, that we used to calculate Faraday depth spectra. The sources we find must satisfy the following criteria: 1) They must be brighter than 150 mJy in Stokes I, which excludes many grating artefacts from Stokes I, 2) The maximum $P(\mathcal{R})$ along the line-of-sight must be detected at the $\gtrsim 11\sigma$ level. This is higher than the 5σ level that we required for our GEMINI data because of calibration problems with some of the longer baselines in the CEPHEUS data set 3) The sources should be more than 2% polarized, which is twice the expected level of instrumental polarization. 4) Instrumental polarization can turn an unpolarized source into a polarized source with an RM = 0 rad/m^2, and the finite width of the RMSF will make this spurious polarization leak into nearby RM. To filter out such instrumentally polarized sources, we limit ourselves to looking for sources with $|\mathrm{RM}| > 4$ rad/m^2. 5) We also excluded an area of about 0.9° from the edge of the mosaic (the grey region in Fig. 4.8), where instrumental polarization levels are higher. Finally, we selected only those sources where the RM fit to the polarization angles from the short-baseline taper maps that we discussed in Sect. 4.3 has a reduced $\chi^2 < 3$.

We fitted an RM to the $\Phi(\lambda^2)$ distribution of the sources that satisfy these criteria as described in chapter 2. The characteristics of the sources we found are listed in Table 4.2, and the RM distribution of these sources over the CEPHEUS mosaic is shown in Fig. 4.8. Since extragalactic sources have a much larger surface density than Galactic pulsars, most of the sources that we detected will be extragalactic. The number of extragalactic sources that we found is clearly much smaller than the number of sources that we found in the GEMINI mosaic (chapter 3), and also smaller than in the TRIANGULUM and CAMELOPARDALIS mosaics (chapters 5 and 6). This is likely due to the fact that real sources in the CEPHEUS mosaic have to be detected at the $> 11\sigma$ level, which corresponds to about 3.4 mJy, whereas in the GEMINI, TRIANGULUM and CAMELOPARDALIS mosaics we included all sources down to the 5σ level, or about 1.5 mJy (TRIANGULUM, CAMELOPARDALIS) – 2.5 mJy (GEMINI). The CEPHEUS total intensity mosaic however shows an abundance of sources. To check that the sources that we found are real, we plot their Faraday depth spectra in Figs. 4.9 and 4.10. The solid line spectrum was calculated from short-baseline taper (low angular resolution) maps that we described in 4.3, and the dotted line spectrum was calculated from the long-baseline taper (high angular resolution) maps that we introduced in the current section. Both the diffuse emission and the extragalactic sources contribute to the spectra calculated with the low-resolution maps, but because we left out baselines < 250 m in the high-resolution maps, the contribution from the diffuse emission is much reduced in the $P(\mathcal{R})$ spectra calculated with the high-resolution maps. Next to the spectrum of each source we plot the polarized intensity and polarization angle spectra of the short-baseline taper maps as a function of λ^2. Even though the peaks in the solid line and dotted line $P(\mathcal{R})$ spectra do not always reach the same height, the agreement is in general good. We will come back to this when we discuss some of the individual sources. From these spectra it is also clear that by using only baselines > 250 m we effectively filter out the contributions from the diffuse emission to the Faraday depth spectra, which also brings out better the RMSF around the RM of the extragalactic source. From the $\mathrm{P}(\lambda^2)$ and $\Phi(\lambda^2)$ spectra it is clear that in most cases we are dealing with real sources, and not with instrumental artefacts. The final column

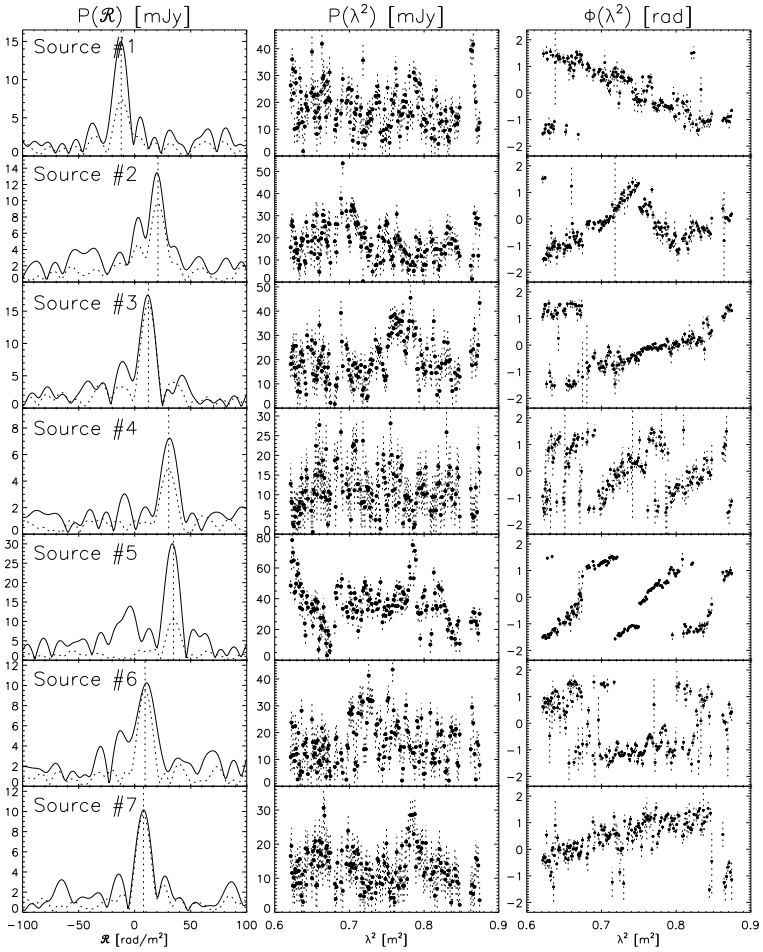

Figure 4.9 — $P(\mathcal{R})$ spectra for sources 1 – 6 from Table 4.2, for the short-baseline taper (low-resolution) maps that we discussed in Sect. 4.3 (solid line) and the long-baseline taper (high-resolution) maps that we discussed in Sect. 4.6 (dotted line). The Faraday depths plotted along the horizontal axis range from -100 rad/m^2 to +100 rad/m^2, and the vertical axis shows the source flux density in mJy. The vertical dotted line indicates the RM that we fitted to the peak in the $P(\mathcal{R})$ spectrum calculated from the long-baseline taper maps. The second and third columns show for each line-of-sight the polarized intensity and polarization angle spectra from the short-baseline taper maps. The $P(\mathcal{R})$ noise level is 0.3 mJy, and the $P(\lambda^2)$ noise level is 5.5 mJy. The low-resolution maps contain polarized signals from both the diffuse Galactic emission and the point sources. The high-resolution maps do not contain baselines $<$250 m, which efficiently reduces the $P(\mathcal{R})$ contribution from the diffuse (extended) Galactic emission, and making the $P(\mathcal{R})$ signal from the point sources more prominent.

of Figs. 4.9 and 4.10 also shows that the difference in sign of the RMs of the different sources is genuine, and that the RMs of the extragalactic sources are different from the Faraday depths of the strongest diffuse emission.

Comments on specific sources

Source 1 shows a clear negative RM, even though other sources show positive RMs. The large difference between the solid and dotted lines is caused by nearby bright diffuse emission at the same Faraday depth as the point source.

Sources 3 and 6 nicely illustrate how the $P(\mathcal{R})$ contribution from the diffuse (extended)

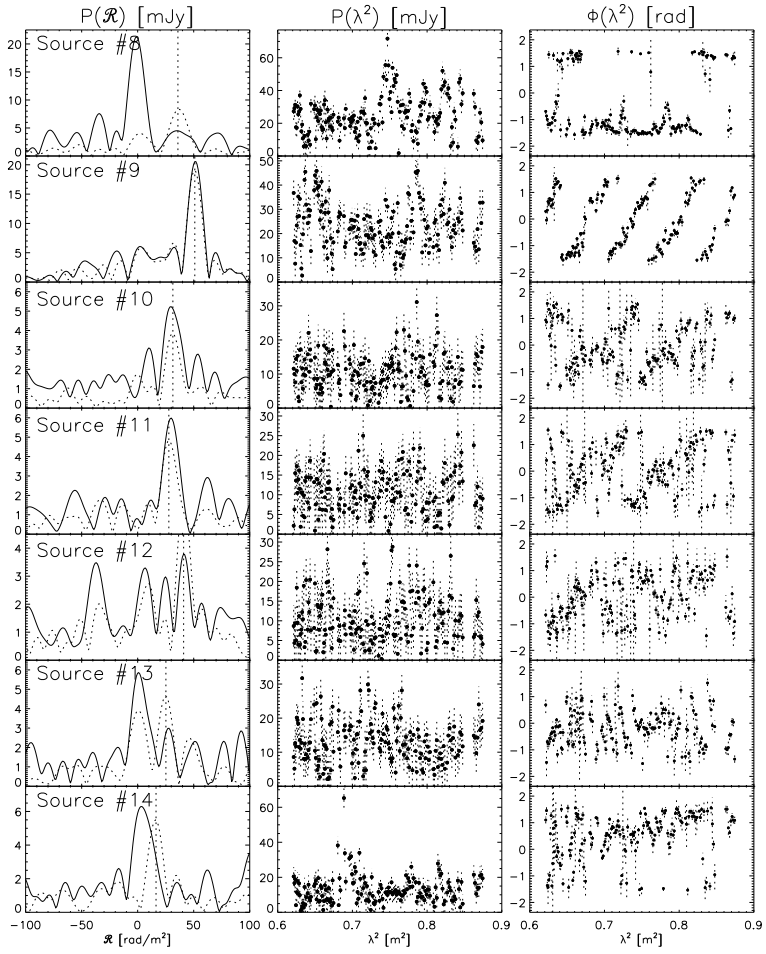

Figure 4.10 — Similar to Fig. 4.9, but for sources 7 – 12.

foreground can be separated from the contribution from the polarized source.
Source 5: The large separation between the peaks of the solid and dotted $P(\mathcal{R})$ spectra is produced by the difference in synthesized beamsize between the two short- and long-baseline taper maps. In the long-baseline taper map at the Faraday depth of the peak in the $P(\mathcal{R})$ spectrum there is one neighbouring pixel that has a polarized intensity of 28 mJy, close to the 29 mJy peak of the solid-line spectrum. Applying a short-baseline taper to maps with only baselines > 250 meter produces for this line-of-sight a flux density of 29 mJy at the $\mathcal{R}$ of the peak in the $P(\mathcal{R})$ spectrum.
Source 12 has a complicated spectrum, and is distorted in the $P(\mathcal{R})$ map at $\mathcal{R} = 40$ rad/m^2, which means that this can be a spurious detection due to instrumental artefacts. However, it is possible that the height of the peak that is produced by the extragalactic source does actually increase by leaving out the diffuse contribution to the $P(\mathcal{R})$ spectrum. This is because the RMSF is a complex quantity, and it not only has a length but also a direction. Therefore the $\vec{P}(\mathcal{R})$ from the diffuse emission adds vectorially to the $\vec{P}(\mathcal{R})$ contribution from the polarized point source, and they can partially cancel one another. The amplitude of the $\vec{P}(\mathcal{R})$ spectrum (which we plot here) is then reduced by having contributions from both the diffuse Galactic emission and a

polarized point source along the line-of-sight. A similar brightening of the $P(\mathcal{R})$ peak from the extragalactic source can be seen in *source 8*.

With the average RM = 24 rad/m^2 of the extragalactic sources we find that $\langle B_\parallel \rangle$ = 0.3 μG, which, compared to the -3.6 μG that we would expect for the large-scale field towards CEPHEUS, is not only of the wrong magnitude, but also has the wrong sign. For comparison: almost all sources from the Canadian Galactic plane survey (CGPS - Taylor et al. 2003) between $90^\circ < l < 110^\circ$ and $-3^\circ < b < 5^\circ$ show negative RMs, as would be expected for a large-scale magnetic field pointing away from us (Brown, private communication). The difference in sign of the RMs of the extragalactic sources close to the Galactic plane and in the CEPHEUS mosaic adds further supports to the idea of a large-scale field reversal along the line-of-sight towards the CEPHEUS data, and we return to this point in Sect. 4.7. Note that the $\mathcal{R}$ of the main peak in the $P(\mathcal{R})$ spectra of the diffuse emission and the RMs of extragalactic CGPS sources agree in sign.

4.7 A simple model

The basic properties of the data that a model should try to explain are the average Faraday depth of the main peak in the Faraday depth spectra at $\approx$ -10 rad/m^2, and the average RM of the extragalactic radiosources at +24 rad/m^2. Since the extragalactic sources 'see' also the line-of-sight that is covered by the diffuse emission, this difference between the signs of the $\mathcal{R}$ of the diffuse emission and the RM of the extragalactic sources points at a large-scale reversal in the Galactic magnetic field. Furthermore, most of the diffuse emission that we observe must be coming from the part of the line-of-sight towards the extragalactic sources that lies close to the observer.

Assume that this field reversal occurs at a certain height h above the Galactic plane. Below h the magnetic field is pointing away from us, as indicated by the RMs of extragalactic CGPS sources that lie in the same Galactic longitude range as CEPHEUS, but at lower Galactic latitudes (Brown, private communication). Above h the field points towards us, and it has the same strength as below h. It is reasonable to assume that the strength of the regular magnetic field is constant over the 1 kpc thickness of the Reynolds layer: Beck (2007c) argues that the magnetic field scale height is about 4 times the height of the synchrotron-emitting thick disk, and with the 1.8 kpc scale height for the synchrotron-emitting thick disk in the Milky Way from the Beuermann et al. (1985) model, the magnetic field scale height would then be 7.2 kpc.

We use the Berkhuijsen et al. (2006) model to calculate the electron density distribution in the Faraday rotating layer. They describe the dispersion measure at height z [kpc] above the Galactic plane in kpc by

$$\mathrm{DM} \sin|b| \;=\; 22.1 \pm 1.3\;|z|^{1.04\pm0.05} \tag{4.8}$$

where b is the Galactic latitude of the line-of-sight. To calculate the DM built up in an arbitrary direction we need the derivative dDM/dz. Since dDM/dz depends very

weakly on z, DM is built up nearly isotropically, and by taking the derivative of Eqn. 4.8 we find that dDM/dr $\approx$ 23 cm^{-3}pc/kpc for an arbitrary radial direction r (for comparison, the Reynolds (1991) model builds up 32 cm^{-3}pc/kpc line-of-sight) To explain the average DM = 99 cm^{-3}pc of the CEPHEUS mosaic (which we calculated using the average EM = 36 cm^{-3}pc - see Sect. 4.4) then requires a line-of-sight of 4.3 kpc length, that reaches a height of about 1.1 kpc above the Galactic midplane.

Now that we now the DM that is built up per kpc line-of-sight, we can calculate the RM of the extragalactic sources. Using $B_{\mathrm{reg},\parallel}$ = 3.6 μG for the strength of the large-scale magnetic field component along the line-of-sight (as we argued in Sect. 4.4), and using the Galactic latitude = 15° from the centre of the CEPHEUS mosaic, we find that

$$\mathrm{RM} \;=\; \frac{0.81\; B_{\mathrm{reg},\parallel}}{\sin(15^\circ)} \frac{\mathrm{dDM}}{\mathrm{dr}} [1100 \;-\; 2h[\mathrm{pc}]] \tag{4.9}$$

where 1100 parsec is the height of the layer from the Berkhuijsen et al. model that produces the DM observed towards CEPHEUS. With the average RM = +24 rad/m^2 of the extragalactic sources, we calculate that $h \approx 500$ pc. Studies of the RMs of extragalactic sources, and of the RM and DM of pulsars, indicate that the coherence length of the random magnetic field is typically < 100 pc (Clegg et al. 1992, Minter & Spangler 1996, Ohno & Shibata 1993). Observations of starlight polarization would indicate a coherence length ~ 500 pc (Jones et al. 1992). If the coherence length is < 100 pc, there are enough reversals of the random field along the line-of-sight that this component gives no net contribution to the RM of the extragalactic sources.

Due to the magnetic field reversal there a 2 possible solutions for the length of the line-of-sight of the diffuse emission. In the 'shallow' solution the Faraday depth of the main peak in the $P(\mathcal{R})$ spectrum is built up over a short line-of-sight that does not cross into the region with a reversed magnetic field. This line-of-sight has a length of about 150 pc. In the 'deep' solution the line-of-sight does cross into the region with the reversed magnetic field. Below h = 500 pc a large negative $\mathcal{R}$ is accumulated, after which it will again get closer to 0 rad/m^2 in the reversed-field layer above h = 500 pc. This requires a line-of-sight of 3.8 kpc length.

A big problem with the shallow scenario is to come up with a mechanism that produces such a short line-of-sight. Depolarization by a turbulent magnetic field over the narrow WSRT beam requires strong fluctuations over physical distances smaller than the telescope beam at 150 pc, which is 0.13 pc. This therefore seems an unlikely explanation for limiting the line-of-sight in the 'shallow' scenario. Another option is that there simply is no synchrotron emission at larger (in an absolute sense) Faraday depths. This is the case when the magnetic field would be completely aligned with the line-of-sight. In the shallow scenario it is difficult to understand how this alignment can happen throughout the bulk of the Reynolds layer. Also, in the Reynolds model the shallow line-of-sight builds up an EM of only 0.25 cm^{-6}pc, which is equivalent to an Hα intensity of 0.03 Rayleigh (using E(B-V) = 0.527), whereas the deep line-of-sight produces an EM of 11.3 cm^{-6}pc, or an Hα intensity of 1.6 Rayleigh, which is closer to the observed values from Fig. 4.4. Finally, if the $P(\mathcal{R})$ of the main peak has to be built up over a 150 pc line-of-sight, the amount of polarized synchrotron emission/kpc line-

of-sight would have to be huge, about 17 K/kpc to produce the average $P(\mathcal{R})$ from Fig. 4.2 = 2.5 K over only 150 pc. Even in the direction of the Galactic anti-centre, where the magnetic field lies more perpendicular to the line-of-sight and therefore produces more synchrotron emission, this is an absurdly high value. For comparison: the model by Beuermann et al. (1985) produces a 8.3 K brightness temperature/kpc (5.8 K/kpc polarized brightness temperature assuming a polarization percentage of 70%) towards the GEMINI mosaic that lies in the direction of the Galactic anti-centre (see chapters 2 and 3). These arguments thus favour the deep scenario. One other observational characteristic of the deep scenario is that it builds up large Faraday depths of up to ≈ 160 rad/m^2. Synchrotron emission along the line-of-sight would then produce a tapestry of structure within this range of Faraday depths. The range of available Faraday depths in the shallow scenario is limited to -10 $< \mathcal{R} <$ 0 rad/m^2. If we accept that the deep scenario is correct, then we must also conclude that many features in the $P(\mathcal{R})$ spectra from Fig. 4.6 are real. In this model we only considered one magnetic field reversal. It is not possible to exclude multiple reversals along the line-of-sight, but this adds many more parameters to the model that can be tweaked. By including only one reversal the model is much simpler, and also more suited to study the consequences that the reversal can have on the modeling and interpretation of the data.

In chapter 9 we will return to the modeling of the magnetized ISM in the second Galactic quadrant.

4.8 Conclusions

In this chapter we presented the results of a Faraday tomography analysis for observations that we carried out with the WSRT in the direction of (l, b) = (102°, 15°). The diffuse emission is strongest at Faraday depths between -22 rad/m^2 and +8 rad/m^2, and it shows a clear stratification in Faraday depth perpendicular to the Galactic plane. Also, for the current data set we find gradients in Faraday depth of the strongest peak in the $P(\mathcal{R})$ spectra over the mosaic so that the total polarized intensity component that is emitted at these Faraday depths will be modulated to scales that can be observed with the WSRT. We used WHAM Hα intensities to calculate dispersion measures that, in combination with the Faraday depths of the main peak of the diffuse emission, can tell us about the average strength of the magnetic field along the line-of-sight. Typically we find a field strength of -0.1 μG, which is much smaller than the -3.6 μG we would expect for the large-scale Galactic magnetic field close to the sun when viewing the CEPHEUS. For a 10 $\times$ 12 grid of lines-of-sight we present $P(\mathcal{R})$ spectra to illustrate how rich and diverse these spectra are. We also show the $P(\lambda^2)$ and $\Phi(\lambda^2)$ spectra for a subset of 10 lines-of-sight to demonstrate that the $P(\mathcal{R})$ spectra are produced by a real signal, and not by instrumental artefacts or noise. In this data set we found 12 polarized point sources. Also for these sources we show the $P(\lambda^2)$ and $\Phi(\lambda^2)$ spectra that we used to calculate the $P(\mathcal{R})$ spectra. We calculated a new $P(\mathcal{R})$ cube by taking out the short-baselines to reduce the contribution from the diffuse emission to the $P(\mathcal{R})$ spectra. By plotting the $P(\mathcal{R})$ spectra for these point sources both with and without the short baselines we show that this is a very effective way to detect polarized point sources when diffuse emission also produces a strong $P(\mathcal{R})$ response. The rotation

measures for almost all the extragalactic sources that we find have a different sign than the Faraday depth of the strongest peak of the diffuse emission (over the largest part of the mosaic). We see this as a clear indication that towards this part of the Galaxy, 1) the diffuse emission that we observe only comes from a part of the line-of-sight towards the extragalactic sources and 2) there is a large-scale reversal in the direction of the magnetic field at some height above the Galactic plane. Extragalactic sources from other data sets in this longitude range but at lower Galactic latitudes also have different signs for the rotation measures of 'our' extragalactic sources. We construct a simple model of the magnetized Galactic ISM that contains such a field reversal, and determine the height at which the field reversal occurs, and the length of the line-of-sight of the diffuse emission (which is shorter than the line-of-sight towards the extragalactic sources). Due to the field reversal the line-of-sight of the diffuse emission can have two lengths, one of 110 pc and one of 3.4 kpc. We compare the properties of the 'shallow' and 'deep' line-of-sight lengths to our observations and conclude that the 'deep' line-of-sight matches the observations better. One should not exclude the possibility of multiple reversals along the line-of-sight. Here we used the simplest possible model that is still consistent with the data, to study what consequences the field reversal has on the interpretation of the data.

Acknowledgements

The Westerbork Synthesis Radio Telescope is operated by the Netherlands Foundation for Research in Astronomy (NFRA) with financial support from the Netherlands Organization for Scientific Research (NWO). The Wisconsin H-Alpha Mapper is funded by the National Science Foundation.

Chapter 5

WSRT Faraday tomography of the Galactic ISM at $\lambda \sim 0.86$ m - III. The TRIANGULUM data set at $(l, b) = (137^\circ, -23^\circ)$

Abstract. We present a Faraday tomography analysis of a WSRT data set that we observed towards (l, b) = (137°, -23°), and we discuss the properties of both the diffuse emission and of the extragalactic sources that we detected. Faraday tomography is a brand-new tool which allows us to study the properties of synchrotron-emitting and Faraday rotating regions along the line-of-sight. The diffuse emission in our data set is strongest between Faraday depths $\approx$ -46 rad/m^2 and +8 rad/m^2. At these Faraday depths, the diffuse emission is highly structured on scales from degrees to the size of the synthesized beam of about $3'$. We also find a conspicuous $\approx 6^\circ \times 2^\circ$ region at Faraday depths around -34 rad/m^2, or about twice the average Faraday depth that we find for the diffuse emission elsewhere in the mosaic. By using the WHAM Hα intensities to determine the electron density contribution to the Faraday depth, we derive how strong the magnetic field has to be to build up the Faraday depths of the main peak in the $P(\mathcal{R})$ spectrum. The average $\langle B_\parallel \rangle$ = -0.6 μG that we find are much lower than the $B_{\mathrm{reg},\parallel} \approx$ -2 μG we would expect for the large-scale magnetic field. The $|\langle B_\parallel \rangle|$ we derive for the diffuse emission are however lower limits. We present a grid of $P(\mathcal{R})$ spectra for 10×15 lines-of-sight to show how rich and varied the $P(\mathcal{R})$ spectra are that we find in our data set. For a subset of 10 lines-of-sight we also present the $P(\lambda^2)$ and $\Phi(\lambda^2)$ spectra, to demonstrate that the $P(\mathcal{R})$ spectra are not the result of noise or instrumental artefacts. We also detected 25 polarized point sources in our data set. The surprising result is that their average rotation measure of -75 rad/m^2 is about four times larger than the average Faraday depth of the strongest diffuse emission in our mosaic. This also means that the line-of-sight towards the extragalactic sources extends beyond the line-of-sight that produces the bulk of the diffuse emission. Using the average rotation measure of -75 rad/m^2 of the extragalactic sources, we find $\langle B_\parallel \rangle$ = -2.2 μG, which is also what we would expect to find for the large-scale field. In chapter 9 we combine the observational characteristics of the four Faraday tomography data sets that we have to describe the properties of the magnetized warm ISM in the second Galactic quadrant.

D. H. F. M. Schnitzeler, P. Katgert and A. G. de Bruyn

5.1 Introduction

FARADAY tomography, also known as rotation measure synthesis, is a valuable new tool for studying the distribution of regions with Faraday rotation and/or synchrotron emission along the line-of-sight. It allows one to disentangle the contributions from the diffuse emission to the polarization angle spectra of extragalactic sources, and study the sometimes complicated polarization angle spectra that we observe for the diffuse emission.

Faraday tomography was introduced by Brentjens & De Bruyn (2005). In chapter 3 we gave a short introduction to how Faraday tomography works. We showed examples of some cases of Faraday rotating and synchrotron emitting regions along the line-of-sight, and we discussed what signature they would leave when we apply Faraday tomography to mock observations. For completeness we present here a brief summary of the ideas behind Faraday tomography. Every point along the line-of-sight that emits polarized synchrotron radiation towards the observer sees a certain amount of magnetic fields and electrons in front of it, that will Faraday rotate the polarized emission. The amount of rotation is proportional to

$$\mathcal{R}(x)\,[\mathrm{rad/m^2}] \;=\; 0.81 \int_{\text{source at 'x'}}^{\text{observer}} n_e\,[\mathrm{cm^{-3}}]\;\vec{B}\,[\mu\mathrm{G}]\cdot \mathrm{d}\vec{l}\,[\mathrm{pc}] \tag{5.1}$$

where n_e is the electron density, $\vec{B}$ the magnetic field vector, and dl an infinitesimal piece of the line-of-sight towards the observer. $\mathcal{R}$ is also known as the Faraday depth of the source. If we write the polarization vector as a complex number, with its Stokes Q and U components as its real and imaginary components, then we can express the amount of Faraday rotation of the polarization vector as $\mathrm{e}^{2\mathrm{i}\mathcal{R}(\mathrm{x})\lambda^2}$. Summing over all points along the line-of-sight then produces the observed polarization vector at wavelength λ we find:

$$\vec{P}(\lambda) \;=\; \int_0^\infty \vec{P}(\mathrm{x})\,\mathrm{e}^{2\mathrm{i}\mathcal{R}(\mathrm{x})\lambda^2}\mathrm{dx} \;=\; \int_{-\infty}^{\infty} \vec{P}(\mathcal{R})\,\mathrm{e}^{2\mathrm{i}\mathcal{R}\lambda^2}\mathrm{d}\mathcal{R} \tag{5.2}$$

where the first integral is over physical distance 'x', and the second integral is over all Faraday depths. The second integral is similar to a Fourier transform, and it can therefore be inverted to

$$\vec{P}(\mathcal{R}) \;=\; K \int_{-\infty}^{\infty} \vec{P}(\lambda^2)\,\mathrm{e}^{-2\mathrm{i}\mathcal{R}\lambda^2}\mathrm{d}\lambda^2 \tag{5.3}$$

$$K \;=\; \left(\int_{-\infty}^{\infty} W(\lambda^2)\,\mathrm{d}\lambda^2 \right)^{-1} \tag{5.4}$$

$W(\lambda^2) = 1$ for observed wavelengths, and = 0 elsewhere. The K factor in Eqn. 5.4 takes care of the correct normalization of $P(\mathcal{R})$. By using a large number of narrow frequency

channels we can then use Eqn. 5.3 to obtain the polarization vector $\vec{P}(\mathcal{R})$, i.e. the polarized intensity $P(\mathcal{R})$ emitted at Faraday depth $\mathcal{R}$ and the position angle of the emitted radiation $\Phi(\mathcal{R})$. This is the basis for Faraday tomography. If the measured $P(\lambda^2)$ are in K (mJy/beam), then also the $P(\mathcal{R})$ will be in K (mJy/beam), or, more precisely, in K/RMSF width (mJy/beam/RMSF width). If we want to compare different data sets, with different RMSFs, it is necessary to convert this quantity to K/rad/m^2 instead of K/RMSF (equivalently for mJy/rad/m^2). Here we only consider one dataset, and we did not convert the measured $P(\mathcal{R})$ to K/rad/m^2.

Note that we distinguish here between the Faraday depth $\mathcal{R}$ and the rotation measure RM $\equiv \partial\,\Phi/\partial\,\lambda^2$, the derivative of the observed polarization angles with respect to λ^2. One also has to be aware that with Eqn. 5.3 we find the polarization vector $\vec{P}(\mathcal{R})$ for a certain Faraday depth, which is not the same as physical depth. To determine the physical depth one needs to model the magnetic field geometry, and in particular determine whether magnetic field reversals occur. Such reversals will attribute the same Faraday depth to 2 different physical depths.

Faraday tomography is a very novel technique, and not much literature exists on this topic. De Bruyn & Brentjens (2005) used it to study the Perseus cluster, and in chapters 2 and 3 we used it to investigate the Galactic ISM in the direction of the Galactic anti-centre, towards $(l, b) = (181^\circ, 20^\circ)$. Maybe the most important conclusion from those chapters was that we found that the main peak in an unexpectedly large fraction of lines-of-sight was unresolved, which means that the synchrotron emission that produces that peak and Faraday rotation cannot occur in the same place. Mixing of the two results in a resolved main peak. One explanation for this would be a magnetic field that lies perpendicular to the line-of-sight. For such a configuration the line-of-sight component of the magnetic field, and therefore RM, is 0.

In chapters 2 – 4 we presented WSRT data sets towards $(l, b) = (181^\circ, 20^\circ)$ and $(l, b) = (102^\circ, 15^\circ)$, and we discussed the results of applying Faraday tomography to these data sets, both for the diffuse emission and for the extragalactic sources that we detected in these data sets. In this chapter we present Faraday tomography results for a data set towards $(l, b) = (137^\circ, -23^\circ)$ that we observed with the WSRT. We discuss the characteristics of our observations in Sect. 5.2, and in Sect. 5.3 we present the characteristics of the Faraday depth cube that we derive. The diffuse emission is strongest at Faraday depths between $\approx$ -46 rad/m^2 and +8 rad/m^2, and shows structure on a wide range of angular scales. In Sect. 5.4 we determine how strong the magnetic field along the line-of-sight has to be on average to produce the Faraday depths of the main peak in the $P(\mathcal{R})$ spectrum, and we compare this to what we would expect for the strength of the large-scale Galactic magnetic field. The $P(\mathcal{R})$ spectra show all sorts of structures, and in Sect. 5.5 we present a grid of $P(\mathcal{R})$ spectra for 10×15 lines-of-sight. For a small subset of interesting $P(\mathcal{R})$ spectra we also show the $P(\lambda^2)$ and $\Phi(\lambda^2)$ spectra to indicate that these structures are not the product of noise or instrumental polarization. Using the detection method from chapter 3 we could find rotation measures for 25 polarized extragalactic sources. In Sect. 5.6 we discuss the properties of these sources, and we show how the rotation measures of these sources are distributed on the sky. We conclude this chapter by giving in Sect. 5.7 an overview of the different sources of information that we presented in this chapter. We postpone modeling of the Faraday

depths of the diffuse emission and the rotation measures of the extragalactic sources to chapter 9, where we combine the properties of the warm ISM that we derived for all four Faraday tomography data sets that we have.

5.2 The data

We have used the WSRT to observe a $11^\circ \times 9^\circ$ region around $\alpha = 2^h00^m$, $\delta = 37^\circ$, or $(l, b) = (140^\circ, -25^\circ)$ in Galactic coordinates. We will refer to this as the TRIANGULUM data set (or TRI for short). The WSRT is a 14-element E-W interferometer with 4 movable elements to improve (u,v) coverage. Each of the WSRT's telescope dishes is 25 meters in diameter. We observed mostly at night to minimize solar interference and variations in the ionospheric rotation measure during the observations (see Table 5.1).

We observed the TRI mosaic in 5 12 hr runs. The data of a 6^{th} 12 hr period could not be properly calibrated, and we therefore did not use them. In each run the minimum baseline in the (u,v) plane was different to improve (u,v) coverage. If all 6 nights would have been available, we would have measured visibilities for baselines from 36 meters to 2760 meters in intervals of 12 meters. In each night the WSRT observes baselines from a certain minimum baseline length in intervals of 72 meters. Since we could not use one observing night of the TRI mosaic we miss baselines from 36 meters to 2700 meters in steps of 72 meters, which leaves holes in the (u,v) coverage compared to the case where all 6 instead of only 5 observing nights are available. We tapered the individual frequency channel maps to a synthesized beamsize of $3.38' \times 5.62'$ (RA $\times$ DEC). We checked the antenna pattern that with the 5 instead of 6 available 12 hr observing runs the first grating ring still lies at about 4° (at 350 MHz) from the pointing centre, outside the $3^\circ \times 3^\circ$ area that we mapped for each individual pointing.

We mapped an area of about $11^\circ \times 9^\circ$ with 8×6 pointings. In each night (i.e. for each baseline setting) we observed each pointing in the mosaic 17 times, which yields 17 HA 'spokes' in the (u,v) plane per night. Each HA was observed for 40 seconds before moving to the next pointing. Wieringa et al. (1993) determined that instrumental polarization levels for the WSRT can be reduced to about 1% by using a rectangular pointing grid with a 1.25° grid spacing. Whereas the pointing grid by Wieringa et al. was rectangular in equatorial coordinates, the grid that we observed is rectangular in Galactic coordinates. Even though the pointing grid we use is rotated by about 30° with respect to the equatorial coordinate system, we do not expect instrumental polarization levels to be much higher than 1%: in Sect. 5.6 we present significant detections of point sources that are polarized at the $\gtrsim 2\%$ level.

We reduced our data set using the `NEWSTAR` data reduction package. Dipole gains and phases and leakage corrections were determined using the unpolarized calibrator 3C147. The flux scales of both unpolarized and polarized calibrators are set by the calibrated flux of 3C286 (26.93 Jy at 325 MHz - Baars et al. 1977). Due to an a-priori unknown phase offset between the horizontal and vertical dipoles, signal can leak from Stokes U into Stokes V. We corrected for this by rotating the polarization vector in the Stokes (U, V) plane back to the U axis, assuming that there is no signal in V. The polarized calibrator source DA240 defined the sense of derotation (i.e. to the positive or negative U-axis). After this we self calibrated each of the telescope pointings. 6 point-

Table 5.1 — Characteristics of the TRIANGULUM data set. Observing dates and times are given for each of the observing runs, which have been indicated by their shortest baseline length.

Central position	$(\alpha, \delta)_{2000}$ = (30°, 37°); (l, b) = (140°, -25°)				
Size ($l \times b$)	$11^\circ \times 9^\circ$				
Pointings	8×6				
Frequencies	316 – 379 MHz				
	163 independent frequency channels				
Resolution[a]	$3.38' \times 5.62'$				
Stokes V noise level	5.2 mJy (1.1 K)				
$\mathcal{R}$ noise level[b]	0.3 mJy (0.06 K)				
Conversion Jy – K[c]	1 mJy/beam = 0.21 K				
Spacing (m)	48	60	72	84	96
Observing date (yy/mm/dd)	06/12/07	06/12/06	06/12/05	06/12/04	06/11/30
Start time (UT)	14:40	14:22	15:00	14:20	14:54
End time (UT)	02:37	02:21	02:59	02:19	02:53

[a] We tapered the individual frequency channel maps to a synthesized beamsize of $3.38' \times 5.62'$ (RA$\times$DEC).

[b] This is the noise level in individual $\mathcal{R}$ maps, which we determined from maps at $|\mathcal{R}| > 200$ rad/m^2, that we assume contain no signal. Instrumental polarization levels increases towards the edges of the maps, therefore we excluded these in determining the noise level.

[c] This is the conversion factor at 348 MHz, the average of the λ^2 sampling of the (usable) frequency channels in our data set. We used the FWHM of a Gaussian fitted to the central peak of the synthesized PSF to calculate the beamsize required in this conversion.

ings did not have strong enough point sources (i.e. < 500 mJy) to calculate the self calibration solution. For these pointings we copied the selfcal solutions from adjacent pointings. We compared the phase corrections found by our self calibration pipeline for 7 pointings that did not give problems in the self calibration process. These corrections are very stable, and therefore we can copy the selfcal solutions between adjacent pointings. A group of 4 pointings and one other pointing showed strong variations in the source fluxes in the sky model that was used for the self calibration. Also for these pointings we copied the selfcal solution from adjacent pointings. One of the corner pointings contains a > 10 Jy source, that the selfcal pipeline could not properly handle: about 75% of the (u,v) datapoints for this pointing were clipped. Because this is the only pointing that showed this problem, and because it lies in one of the corners of the mosaic, we did not look further into this problem.

We selected usable frequency channels on the basis of the widths of their Stokes Q, U and V distributions. We left out the edge of the mosaic when determining these widths, because instrumental polarization levels are higher there due to incomplete overlap between pointings. Out of a maximum of 224 available frequency channels we selected 163 independent channels that were not corrupted by calibration problems or by radio frequency interference. Our observations cover the frequency range between

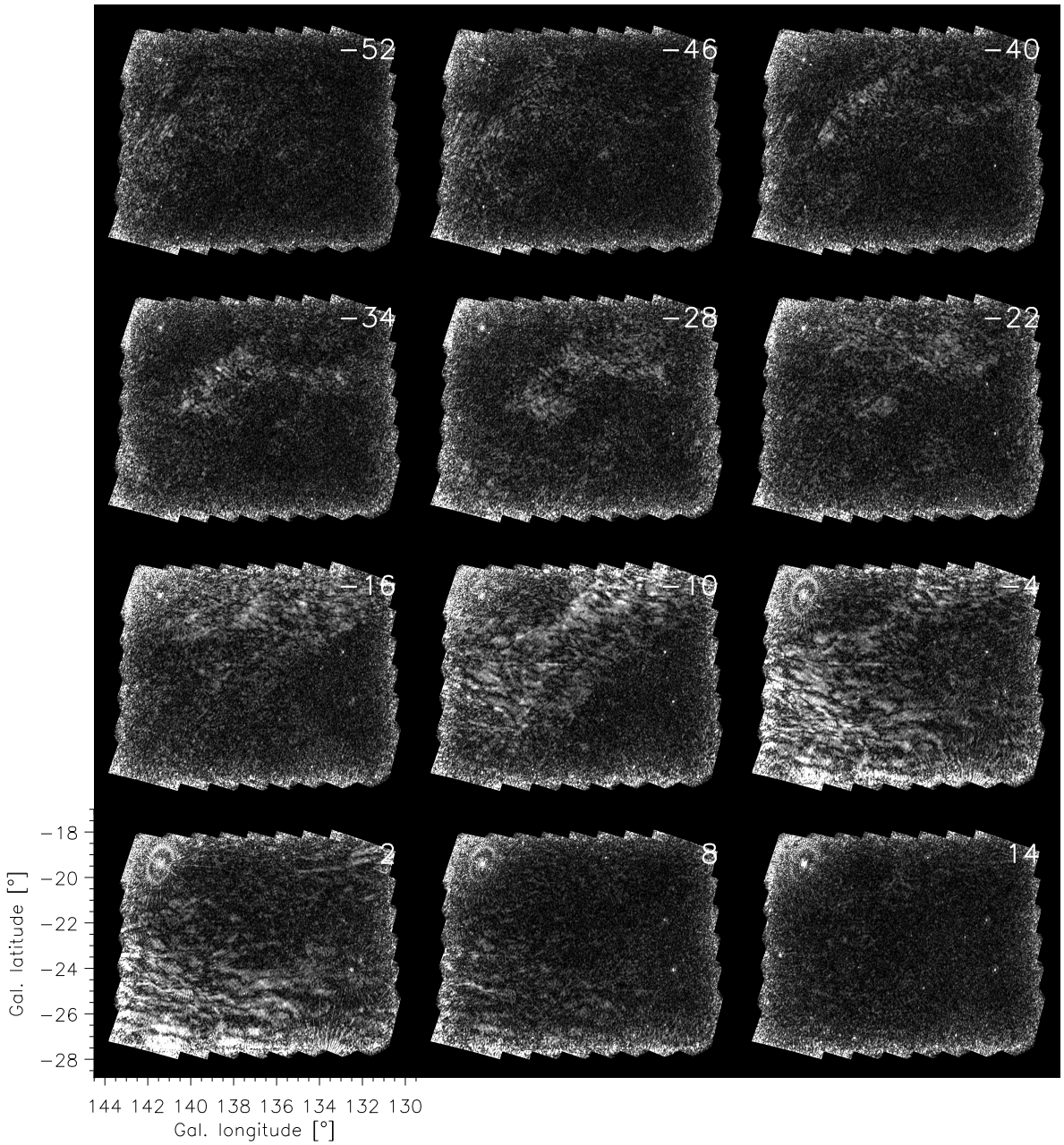

Figure 5.1 — Images of $P(\mathcal{R})$ maps with the strongest diffuse emission. We indicate the $\mathcal{R}$ of each 'slice' through our image cube in the upper right corner of each image in units of rad/m^2. The RMSF has a FWHM of 14 rad/m^2, and we sampled each RMSF with 2 slices. All panels have the same linear intensity scale that saturates at 2.5 K, whereas the GEMINI maps saturated at 6.4K and the CEPHEUS maps at 3.5 K. The 1σ noise level in the $P(\mathcal{R})$ maps is 0.06 K. To convert our mosaic maps from equatorial to Galactic coordinates we regridded the Stokes Q and U mosaics from equatorial to Galactic coordinates, after which we calculated the polarized intensity from these regridded maps.

316 and 379 MHz. Each channel is 0.4 MHz wide, where we used a Hanning taper in frequency. Note that our automated clipping process will create holes in the λ^2 coverage of our data. This produces higher sidelobes in the RMSF, which is the equivalent

in Faraday tomography of the PSF in aperture synthesis. From Stokes V, which we assume to be empty, we estimate that the average noise level in the final mosaics of the individual channels is 5.2 mJy (1.1 K).

To minimize the effects of solar interference and strong variation in ionospheric rotation measure (RM) we carried out our observations in the afternoon and at night during the winter. The overall variation between the different nights of the polarization angles of the polarized calibrator source DA240 is $< 5^\circ$, which is so small that we did not correct our observations for this. The ionospheric RM is at most 0.7 rad/m^2 during our observations (Johnston-Hollitt, private communication), which is so small that we did not correct our data for it.

An interferometer like the WSRT cannot observe all baselines down to 0 meters, which means that extended structure on the sky is missing from maps made with the WSRT. We showed in chapter 3 that a large enough gradient in Faraday depth can modulate structure on large angular scales to smaller scales that can be observed with an interferometer. For the size of the field-of-view in our observations, and for our observing frequencies, a gradient of 6 rad/m^2/field-of-view is needed to make the 0 angular frequency (total polarized intensity) component visible. Most of the pointings from Fig. 5.1 indeed show such strong gradients, except for those in the lower right of the mosaic where there is no strong polarized signal.

5.3 Analysis

With the mosaics of usable frequency channels we calculated a $P(\mathcal{R})$ cube for Faraday depths -1000 rad/m^2 $< \mathcal{R} <$ +998 rad/m^2 in steps of 6 rad/m^2. The RMSF (which is the equivalent in Faraday tomography of the PSF in synthesis imaging) has a FWHM of about 14 rad/m^2, which means that we have Nyquist sampled of the Faraday depths. At large $\mathcal{R}$ the sensitivity in the $P(\mathcal{R})$ spectra will drop due to the finite width of the frequency channels, $\delta\lambda^2$, similar to how the size of an individual telescope dish in an interferometer sets the size of the field-of-view in radio synthesis interferometry. Brentjens & De Bruyn (2005) determined that the sensitivity has dropped to 50% at $\mathcal{R}_{\rm max} = 1.9/\delta\lambda^2$ (the 1.9 replaces the $\sqrt{3}$ from their article because it is closer to the HWHM of the sinc RMSF response to the λ^2 coverage they assume). In our data set $\delta\lambda^2 \approx 1.5 \times 10^{-3}$ m^2 on average, which means that we should still be for more than 50% sensitive for $\mathcal{R} < 1250$ rad/m^2.

In Fig. 5.1 we show the maps from our $P(\mathcal{R})$ datacube with the strongest diffuse emission. All panels saturate at the 2.5 K level. To create this figure we regridded the Stokes Q and U images at each Faraday depth from equatorial to Galactic coordinates, and then we calculated the polarized intensity from the regridded Q and U images. There is a conspicuous region between $\approx 136^\circ < l < 142^\circ$ and $-23^\circ < b < -20^\circ$ at Faraday depths of about -34 rad/m^2, which is more than twice the Faraday depth of the main peak of the diffuse emission elsewhere in the mosaic. In Figs. 5.2 and 5.3 we show how the $P(\mathcal{R})$ and $\mathcal{R}$ of the main peak in the $P(\mathcal{R})$ spectra are distributed over the TRI mosaic. From the $P(\mathcal{R})$ maps at $|\mathcal{R}| > 200$ rad/m^2 we estimate that the $P(\mathcal{R})$ noise level is about 0.06 K, which is slightly less than the $1.1/\sqrt{163} = 0.09$ K we expect to find for 163 independent frequency channels that each have a noise level of 1.1 K.

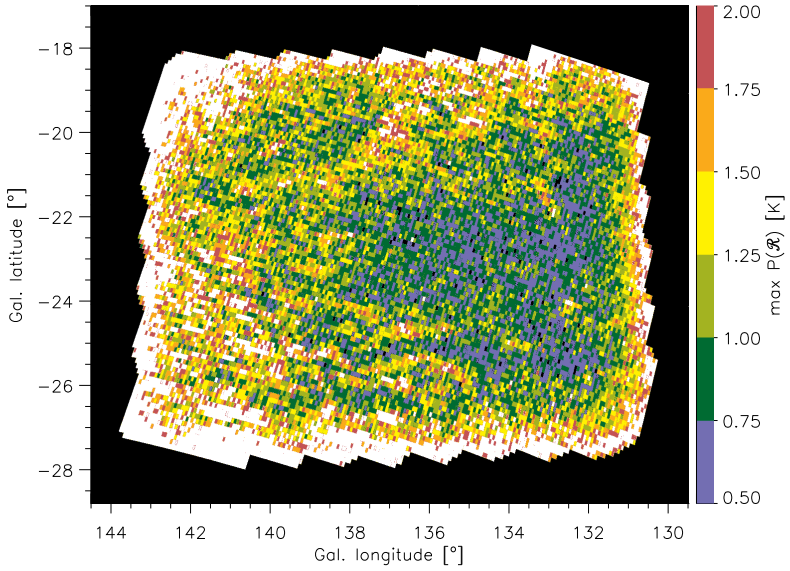

Figure 5.2 — $P(\mathcal{R})$ [K] of the highest peak in the $\mathcal{R}$ spectrum. Each pixel represents one telescope beam, and the pixel size is $3.4' \times 5.6'$. Out of a total of about 18.500 lines-of-sight, 111 lines-of-sight have $P(\mathcal{R}) < 0.5$ K, shown in black, and 3402 lines-of-sight have $P(\mathcal{R}) > 2.0$ K, that are shown in white. The 1σ noise level is 0.06 K. On page 191 we show a colour version of this figure.

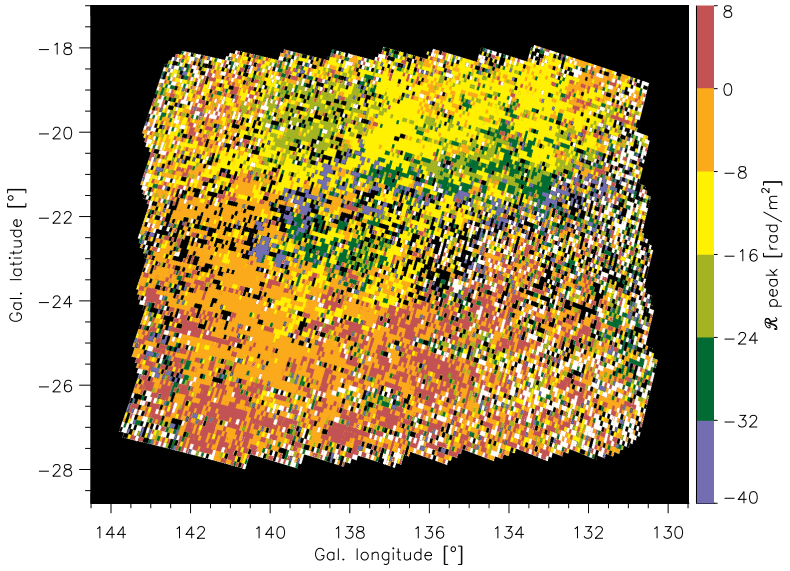

Figure 5.3 — $\mathcal{R}$ corresponding to the $P(\mathcal{R})$ plotted in Fig. 5.2. The 2233 lines-of-sight indicated in white have $\mathcal{R} > 8$ rad/m^2, and the 1698 black lines-of-sight that fall inside the mosaic have $\mathcal{R} <$ -40 rad/m^2. On page 192 we show a colour version of this figure.

5.4 The line-of-sight component of the magnetic field

In this paragraph we determine the average strength of the magnetic field component parallel to the line-of-sight, $B_{\parallel}$, by using the Faraday depth of the main peak in the $P(\mathcal{R})$ spectrum in combination with a description of the electron-density contribution to the Faraday depth. To calculate the latter we use the method that we describe in

chapter 3. First we convert Hα intensities from the WHAM survey (Haffner et al. 2003) to emission measures (EM). The emission measure EM and dispersion measure DM are defined by EM[cm^{-6}pc] = $\int_0^\infty n_e^2 dl$ and DM[cm^{-3}pc] = $\int_0^\infty n_e dl$, where n_e is the electron density in cm^{-3}, and dl is an infinitesimal element of the line-of-sight in parsec. Berkhuijsen et al. (2006) determined an empirical relation between the emission measures and dispersion measures (DMs) of pulsars, that we use to calculate DM from the WHAM EM. With the DM we can then determine the electron-density weighted average $B_\parallel$ along the line-of-sight, $\langle B_\parallel \rangle$, that is needed to explain the observed Faraday depths from Fig. 5.3. The Berkhuijsen et al. model uses a sample of 157 pulsars with measured DM. From the WHAM survey they determine the EM in the direction of the observed pulsars, and they correct these EM both for emission coming from beyond the pulsar, and for interstellar reddening occurring in front of the pulsar. From their data they determine a relation between DM and EM, and the variation of the electron density and the electron filling factor with distance above the Galactic plane. By combining Berkhuijsen et al.'s statistical description of the ISM with the WHAM Hα intensities that are available on a $1^\circ \times 1^\circ$ grid for the northern sky, we can determine DM more accurately in a certain region compared to the predictions from either the electron density models by Reynolds (1991) or by Cordes & Lazio (2003). The Reynolds model is based on pulsars observed in 4 high Galactic latitude globular clusters. Cordes & Lazio (2003) model the Milky Way as a smooth structure consisting of a thin and thick disk + spiral arms, with a small number of superposed local enhancements and voids of electrons in specific regions to explain the observed anomalous DM of some of the pulsars in their sample.

The warm ionized medium (WIM) that is traced by the WHAM emission measures is not the only phase where Faraday rotation occurs; also the hot intercloud medium (HIM) contains free electrons, and Faraday rotation will therefore also take place here. Snowden et al. (1997) modeled the electron density of the HIM in the Galactic plane. The electron densities they find for the HIM are an order of magnitude lower than the electron densities in the WIM, and we therefore neglect the HIM contribution to Faraday rotation.

In the top panel of Fig. 5.4 we plot the WHAM Hα intensities seen towards the TRI mosaic. To convert these to emission measures we can use Eqn. 1 from Haffner et al. (1998):

$$\mathrm{EM} \;=\; 2.75 T_4^{0.9}\; I_{\mathrm{H}\alpha}(\mathrm{R})\; \mathrm{e}^{2.2\;\mathrm{E(B-V)}} \tag{5.5}$$

T_4 is the temperature of the WIM gas in units of 10^4 K, and $I_{\mathrm{H}\alpha}$ is the Hα intensity in Rayleigh. Using 8000 K as a typical temperature for the WIM (Reynolds 1985), and with an interstellar reddening E(B-V) = 0.058 for the centre of the TRI mosaic, we find that 1 Rayleigh = 2.56 cm^{-6}pc. We took the E(B-V) value from the NED extinction calculator[1], that is based on Schlegel et al. (1998). E(B-V) varies between 0.05 and 0.08

[1] `http://nedwww.ipac.caltech.edu/forms/calculator.html`

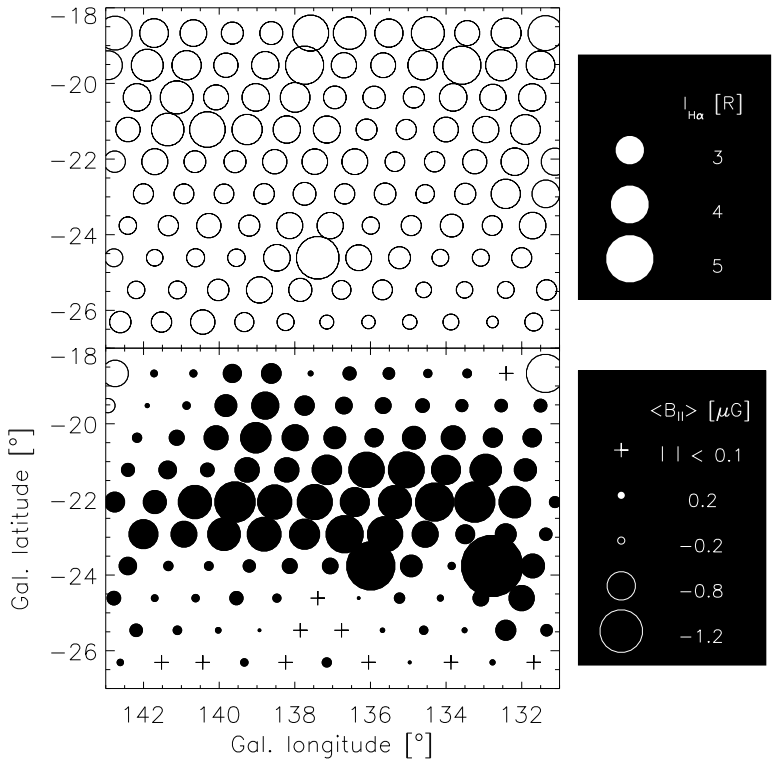

Figure 5.4 — WHAM Hα intensities in Rayleigh (top panel) and the strengths of the magnetic field component parallel to the line-of-sight $\langle B_\parallel \rangle$ in μG (bottom panel) that we derived. In Sect. 5.4 we describe how we derived $\langle B_\parallel \rangle$ from the WHAM Hα intensities and the Faraday depths from Fig. 5.3. Open circles indicate positive $\langle B_\parallel \rangle$, filled circles negative $\langle B_\parallel \rangle$. $|\langle B_\parallel \rangle| < 0.1$ μG are shown as '+'.

over the TRI mosaic. The average Hα intensity in TRI of ≈ 4 Rayleigh then translates into an average EM = 10.24 cm^{-6}pc.

To convert the EM to DM we use the following relation that Berkhuijsen et al. established for a sample of 157 Galactic pulsars with $|b| > 5°$:

$$\mathrm{EM} \;=\; 0.042 \pm 0.014\ \mathrm{DM}^{1.47 \pm 0.09} \tag{5.6}$$

Given the definition of DM we can then calculate the strength of the magnetic field component along the line-of-sight, weighted with the electron-density:

$$\langle B_\parallel \rangle \equiv \frac{\int\limits_{\mathrm{line-of-sight}}^{\mathrm{observer}} n_e \vec{B} \cdot \mathrm{d}\vec{l}}{\int\limits_{\mathrm{line-of-sight}} n_e \mathrm{d}l} \;=\; \frac{\mathcal{R}}{0.81\ \mathrm{DM}} \tag{5.7}$$

where $\langle B_\parallel \rangle$ is in μG. The scatter in the conversion from EM to DM produces a 30% uncertainty in $\langle B_\parallel \rangle$.

The E(B-V) reddening factor is the reddening for the entire line-of-sight through the Galaxy, therefore the EM and DM that we calculate from the WHAM Hα intensities are the EM and DM for the entire line-of-sight through the Galaxy. In the CEPHEUS data set (chapter 4) we noted that the Faraday depths of the strongest diffuse polarized emission and the rotation measures of the extragalactic sources have opposite signs. As we will show in the next section, the rotation measures of the extragalactic sources

that we found in TRI are by a factor of 4 more negative than the Faraday depths of the strongest diffuse emission in TRI. It therefore appears that the bulk of the diffuse emission that we observe samples only the nearby part of the line-of-sight towards the extragalactic sources. By using the DM for the entire line-of-sight through the Galaxy in combination with the Faraday depths of the diffuse emission we therefore underestimate $|\langle B_{\parallel} \rangle|$. Note also that reversals in the direction of the magnetic field will reduce $|\mathcal{R}|$, and in that case we will underestimate the strength that the magnetic field can have locally.

In the bottom panel of Fig. 5.4 we show the $\langle B_{\parallel} \rangle$ that we calculated for the Faraday depths of the diffuse emission in Fig. 5.3. We calculated $\langle B_{\parallel} \rangle$ for the centres of the WHAM pointings, and since the WHAM beam (FWHM $\approx 1^{\circ}$) is much larger than the WSRT beam, we used the $P(\mathcal{R})$-weighted $\mathcal{R}$ average over the WHAM beam to calculate $\langle B_{\parallel} \rangle$. For the average Faraday depth in TRI of -20 rad/m^2 in combination with the average Hα intensity of 4 Rayleigh we find $\langle B_{\parallel} \rangle$ = -0.6 μG. Beck (2007a) indicates that the large-scale magnetic field in the Galaxy has a strength of 4 ± 1 μG and a pitch angle of -8°. With these values we can then calculate how strong the magnetic field in the solar neighbourhood is in the direction of the TRI mosaic, and this turns out to be -2.1 μG, which is much larger than the $\langle B_{\parallel} \rangle$ = -0.6 μG we derive.

5.5 Structure in the $P(\mathcal{R})$ spectra

In the previous section we discussed the properties of the main peak in the $P(\mathcal{R})$ spectrum, and how the Faraday depth of the main peak can be used for deriving the average magnetic field component along the line-of-sight. In Fig. 5.5 we present a 10×15 grid of $P(\mathcal{R})$ spectra to illustrate how diverse the $P(\mathcal{R})$ structures are that we find in the TRI data set. When constructing this grid we excluded lines-of-sight that lie within 1.75° from the edge of the mosaic. Close to the mosaic edges instrumental polarization levels are higher, and by keeping a large distance from the mosaic edge we will have a purer sample of $P(\mathcal{R})$ spectra for lines-of-sight that are not affected by instrumental artefacts. Many lines-of-sight show strong single or multiple peaks. Also $\mathcal{R}$-extended structures can be found in these spectra, as well as regions with a low signal/noise ratio (as in the bottom row-right of the middle). In Fig. 5.6 we present for a subset of lines-of-sight the $P(\lambda^2)$ and $\Phi(\lambda^2)$ spectra that are used to construct the $P(\mathcal{R})$ spectra. These spectra show a highly complex ISM, with different regions of Faraday rotation and synchrotron emission along the line-of-sight.

However, one must be careful not to over interpret these spectra. The interferometer observations that are used to calculate the $P(\mathcal{R})$ datacube do not contain short-baseline information, and therefore they are insensitive to extended structures on the sky. This will also affect the $P(\mathcal{R})$ spectra to some extent. We argued in Sect. 5.4 that a gradient in Faraday depth over the single-dish field-of-view can modulate large-scale structure in the emitted signal to small angular scales that can be picked up by an interferometer. We then continued by arguing that at least for the main peak in the $P(\mathcal{R})$ spectrum the Faraday depth gradients are large enough so that the WSRT can detect the total polarized intensity (0-angular frequency) component that is emitted at these Faraday depths. For the moment we cannot generalize this statement to other peaks

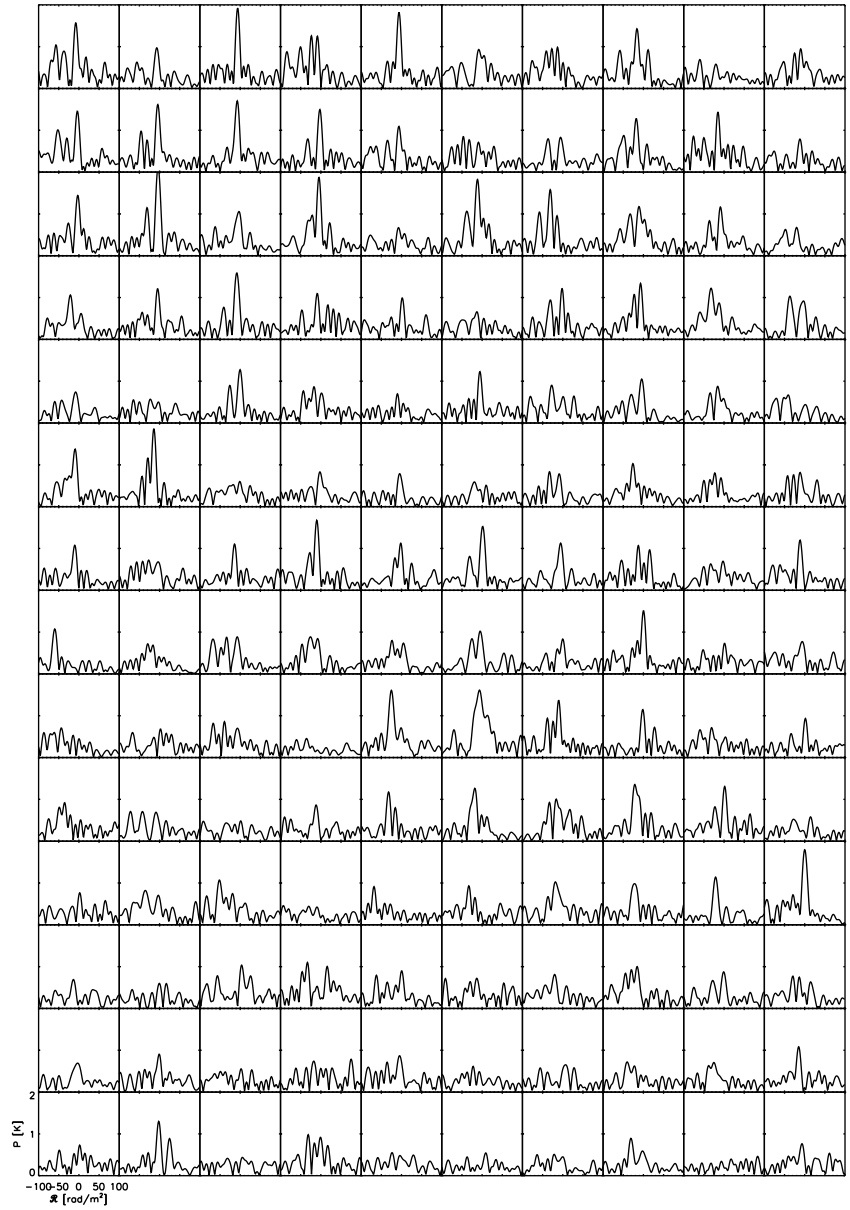

Figure 5.5 — $P(\mathcal{R})$ spectra for a rectangular grid of lines-of-sight through the TRIANGULUM datacube. Faraday depths from -100 rad/m^2 to +100 rad/m^2 are plotted along the x-axis, and polarized intensities between 0 and 2 Kelvin along the y-axis. The noise level in these spectra is 0.06 K. We chose lines-of-sight on a rectangular grid that lie more than 1.75° from the mosaic edges. The instrumental polarization levels are higher closer to the mosaic border, and this would affect the $P(\mathcal{R})$ spectra. Clearly there is a wide variety of structure for the different lines-of-sight. We plot the $P(\mathcal{R})$, $P(\lambda^2)$ and $\Phi(\lambda^2)$ spectra for some conspicuous lines-of-sight in Fig. 5.6 to show that most of the $P(\mathcal{R})$ spectra are not the result of low signal to noise or radio frequency interference, but are the product of a real signal.

in the $P(\mathcal{R})$ spectrum let alone to the $P(\mathcal{R})$ spectrum as a whole. However, physical structures like the ones we observe in these $P(\mathcal{R})$ spectra can exist in the ISM. In chapter 7 we calculate $P(\mathcal{R})$ spectra for a 3D MHD simulation of the Galactic ISM, and there we will investigate how the observed spectra are produced by the physical properties of the simulated volume of ISM.

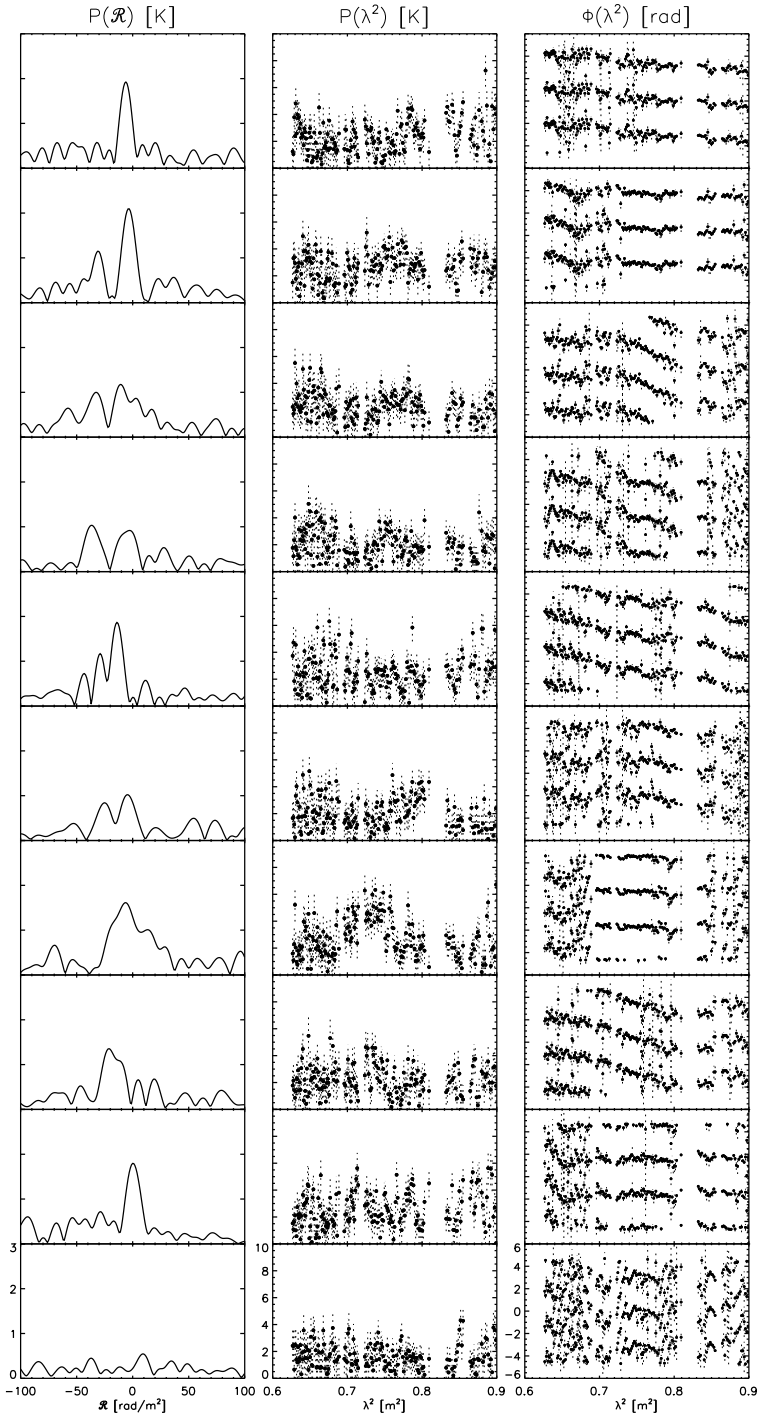

Figure 5.6 — $P(\mathcal{R})$ spectra, and the $P(\lambda^2)$ and $\Phi(\lambda^2)$ data they are based on, for lines-of-sight with diffuse emission. The $P(\mathcal{R})$ spectra cover Faraday depths between -100 rad/m^2 and +100 rad/m^2, and the vertical axis of the $P(\mathcal{R})$ spectra goes from 0 – 3K. The $P(\mathcal{R})$ noise level is 0.06 K. The $P(\lambda^2)$ and $\Phi(\lambda^2)$ spectra range from 0.6 m^2 $\lesssim \lambda^2 \lesssim$ 0.9 m^2. We plotted $P(\lambda^2)$ between 0 and 10 mJy; the $P(\lambda^2)$ noise level 1.1 K. The $\Phi(\lambda^2)$ spectra were replicated at the observed $\Phi(\lambda^2)$ $\pm\pi$ to make the structure in polarization angle more clear. The bottom row shows a line-of-sight with a very low signal-to-noise ratio.

5.6 Polarized point sources

The RMs of polarized extragalactic sources form an important complement to the Faraday depths that we determined for the diffuse emission. In chapter 4 we showed that the RMs of the extragalactic sources in our CEPHEUS mosaic have a different sign than the Faraday depths of the brightest diffuse emission in the $P(\mathcal{R})$ spectra over most of that mosaic. This must mean that the diffuse emission that we observe must come from only a relatively nearby part of the line-of-sight towards the extragalactic sources. By combining the rotation measures from extragalactic sources with the Faraday depths of the diffuse emission we can therefore say something about structure in the nearby and far parts of the line-of-sight through the Milky Way.

The $P(\mathcal{R})$ cube that we discussed in Sects. 5.3 and 5.4 contains both the signal from the extragalactic sources and a strong signal from the diffuse Galactic emission, which complicates looking for the signal from the extragalactic sources. We solved this by using maps that only contain baselines > 250 m to reduce the contribution from the diffuse emission to $P(\mathcal{R})$. In chapters 3 and 4 we showed that this is an effective way to detect the $P(\mathcal{R})$ contribution from the extragalactic source. The individual frequency channel mosaics that we need to calculate the new $P(\mathcal{R})$ cube were all tapered to a synthesized beamsize of $42'' \times 70''$ (RA$\times$DEC). In this new $P(\mathcal{R})$ cube we look for polarized sources with -1000 rad/m^2 $< \mathcal{R} <$ +998 rad/m^2. Depolarization over a frequency channel of width $\delta\lambda^2$ gives a sinc($|\mathrm{RM}|\ \delta\lambda^2$) attenuation. The narrow frequency channels that we use have on average a $\delta\lambda^2 \approx 1.5 \times 10^{-3}$ m^2. For RM=1000 rad/m^2 this gives an attenuation of only 34%, which we think we could still detect. We use the following selection criteria to look for extragalactic sources: 1) the source must have a total intensity > 150 mJy, which excludes many grating artefacts from Stokes I,
2) the source should be detected in the $P(\mathcal{R})$ cube at the $\gtrsim 5\sigma$ level 3) the source should be more than 2% polarized (the instrumental polarization level is about 1%) and 4) to avoid spurious detections of instrumentally polarized sources that because of the finite RMSF width also show up at RM $\neq 0$ rad/m^2, we only look for sources with $|\mathrm{RM}| > 4$ rad/m^2. We also excluded the region within 0.9° from the mosaic edge (indicated in grey in Fig. 5.7), where instrumental polarization levels are higher. We left out the pointing in the upper left part of the mosaic, where a bright source produces artefacts that our source detection algorithm cannot properly handle. Finally, we only selected sources where the reduced χ^2 of the RM fit to the polarization angles from short-baseline taper maps (that we discussed in Sect. 5.3) < 3.

The properties of the polarized sources that we found are listed in Table 5.2, and in Fig. 5.7 we plot the distribution of the RMs of the polarized sources on the sky. We fitted an RM to the polarization angles of the sources from Table 5.2 in the way described in chapter 2. In Figs. 5.8, 5.9 and 5.10 we plot for each source the $P(\mathcal{R})$ spectra that we calculated from the short-baseline taper maps (solid line spectrum) and from the long-baseline taper maps that we introduced in the current section (dotted line spectrum), and we plot the $P(\lambda^2)$ and $\Phi(\lambda^2)$ spectra of the short-baseline taper maps that we used to calculate the solid line spectra. All sources appear to be reliable detections except for sources #20 and #21, that could be affected by calibration problems in the lowest frequency band. Interestingly, these are the only sources in Fig. 5.7 with a small $|\mathrm{RM}|$.

Table 5.2 — Properties of the polarized point sources that we found in our data. Shown are the Galactic coordinates of the source in decimal degrees, the RM that we fitted and its error, the reduced χ^2 ($\chi^2_{\rm red}$) of the fit, the $P(\mathcal{R})$ and total intensity I of the source, and its polarization percentage. The RM we indicate for each source can be off by $\lesssim 0.7$ rad/m^2 from the true RM of the source, because we did not correct for ionospheric RM.

Source	(l, b) $(^\circ, ^\circ)$	RM [rad/m^2]	$\chi^2_{\rm red}$	$P(\mathcal{R})_{\rm max}$ [mJy]	I [mJy]	$P(\mathcal{R})_{\rm max}/I$ %
1	(141.65, -21.87)	-91.5 $\pm$ 0.3	1.6	7.7	312	2.5
2	(141.44, -25.92)	-44.4 $\pm$ 0.1	0.6	21.1	350	6.0
3	(141.34, -21.56)	-91.6 $\pm$ 0.1	0.8	17.6	224	7.8
4	(141.33, -21.55)	-90.9 $\pm$ 0.4	1.6	7.5	367	2.1
5	(141.00, -19.21)	-86.1 $\pm$ 0.2	1.3	19.3	351	5.5
6	(140.86, -24.18)	-61.8 $\pm$ 0.4	0.8	5.2	234	2.2
7	(139.85, -20.58)	-82.2 $\pm$ 0.2	0.6	9.9	183	5.4
8	(139.82, -20.60)	-83.1 $\pm$ 0.3	0.6	7.3	358	2.0
9	(139.77, -26.24)	-51.7 $\pm$ 0.6	1.8	3.9	192	2.0
10	(139.49, -20.54)	-78.2 $\pm$ 0.5	1.0	3.1	155	2.0
11	(137.08, -21.41)	-83.2 $\pm$ 0.4	0.8	4.4	160	2.7
12	(136.90, -19.06)	-75.3 $\pm$ 0.3	1.0	10.6	157	6.7
13	(136.75, -23.98)	-106.7 $\pm$ 0.4	0.7	6.0	272	2.2
14	(136.46, -21.91)	-74.0 $\pm$ 0.4	0.7	4.3	179	2.4
15	(136.42, -22.67)	-78.2 $\pm$ 0.1	1.4	25.3	615	4.1
16	(136.13, -24.04)	-85.9 $\pm$ 0.1	0.7	16.1	407	3.9
17	(135.62, -19.22)	-71.4 $\pm$ 0.2	2.3	20.4	764	2.7
18	(135.53, -20.79)	-67.9 $\pm$ 0.2	0.6	11.5	337	3.4
19	(133.89, -22.83)	-88.6 $\pm$ 0.4	1.0	6.2	154	4.0
20	(133.50, -25.71)	-6.6 $\pm$ 0.7	2.0	7.3	315	2.3
21	(133.39, -25.62)	6.7 $\pm$ 0.7	1.6	4.3	151	2.8
22	(133.26, -19.05)	-73.2 $\pm$ 0.5	2.7	6.8	243	2.8
23	(133.23, -19.08)	-69.6 $\pm$ 0.5	1.7	5.7	212	2.7
24	(132.88, -21.98)	-104.6 $\pm$ 0.5	1.0	5.1	225	2.3
25	(132.82, -22.01)	-107.2 $\pm$ 0.1	1.8	57.1	434	13.1
26	(132.45, -24.14)	-86.9 $\pm$ 0.1	2.9	80.3	1293	6.2
27	(132.42, -24.17)	-86.2 $\pm$ 0.2	2.4	16.0	593	2.7
28	(132.36, -23.76)	-65.9 $\pm$ 0.5	1.0	4.1	157	2.6
29	(131.93, -23.61)	-86.2 $\pm$ 0.4	1.1	5.8	224	2.6

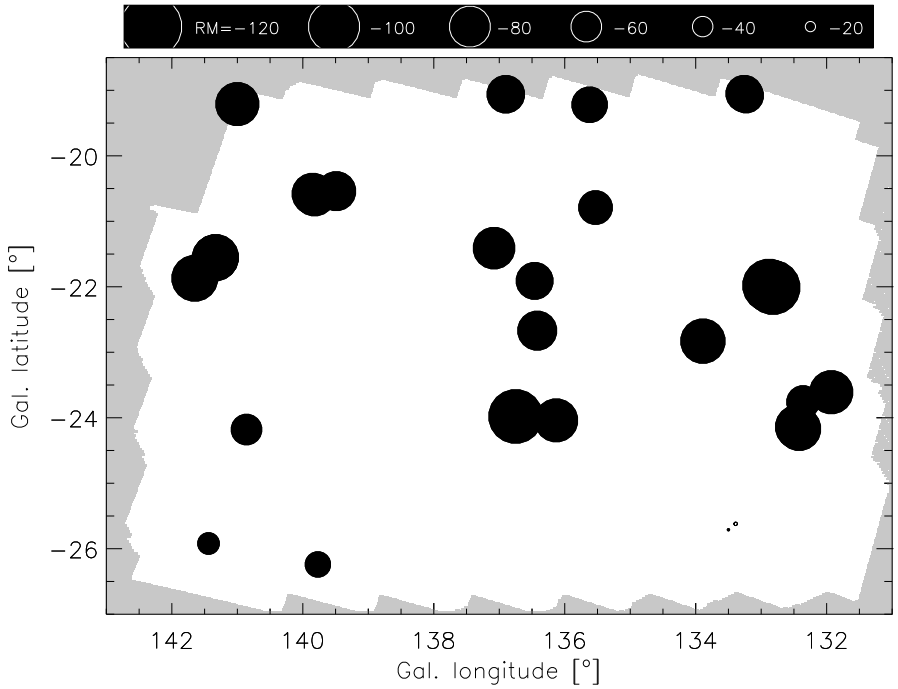

Figure 5.7 — RM distribution for the polarized point sources from table 5.2. The size of the circles is proportional to the RM, shown in the scale on top of the figure in units of radians/m^2. Black circles indicate negative RM, and white circles indicate positive RM. $|\mathrm{RM}| \lesssim 4$ rad/m^2 are missing from this figure because of our selection criteria. We excluded the grey region when looking for polarized point sources, because here instrumental polarization levels are higher. We also excluded the pointing in the upper left, because a bright source in this field produces instrumental artefacts that our source detection algorithm identifies as sources. Sources #20 and #21 at (l, b) = (133.5°, -25.7°) and (l, b) = (133.4°, -25.6°) can be the result of instrumental artefacts, see the text and Fig. 5.9.

Most of the sources that we detected must have an extragalactic origin, because of the much higher surface density of extragalactic sources compared to the surface density of pulsars.

It is interesting to note that in some of the spectra in Figs. 5.8 to 5.10 there is significant signal between the peak in the $P(\mathcal{R})$ spectrum that is produced by the extragalactic source and the strongest peak from the diffuse emission. In some cases this signal is even so strong that it cannot be explained as the combined RMSF responses from the extragalactic source and the strongest peak of the diffuse emission. Thus, if these are real signals, this would have interesting consequences for structure in synchrotron emission and Faraday rotation beyond the part of the ISM that generates the strongest polarized emission in the $P(\mathcal{R})$ spectra.

For an average RM = -75 rad/m^2 and an average Hα intensity of 4 Rayleigh, $\langle B_\parallel \rangle \approx$ -2.2 μG, close to the -2 μG that we would expect for the large-scale magnetic field (Sect. 5.4). Compared to the average Faraday depth that we found for the peak of the diffuse emission along the line-of-sight in Fig. 5.3, the average RM of the extragalactic sources is larger by a factor of about 4. This also means that the line-of-sight towards the extragalactic sources is longer than the line-of-sight where the bulk of the diffuse emission is produced. In chapter 4 where we describe the CEPHEUS data set

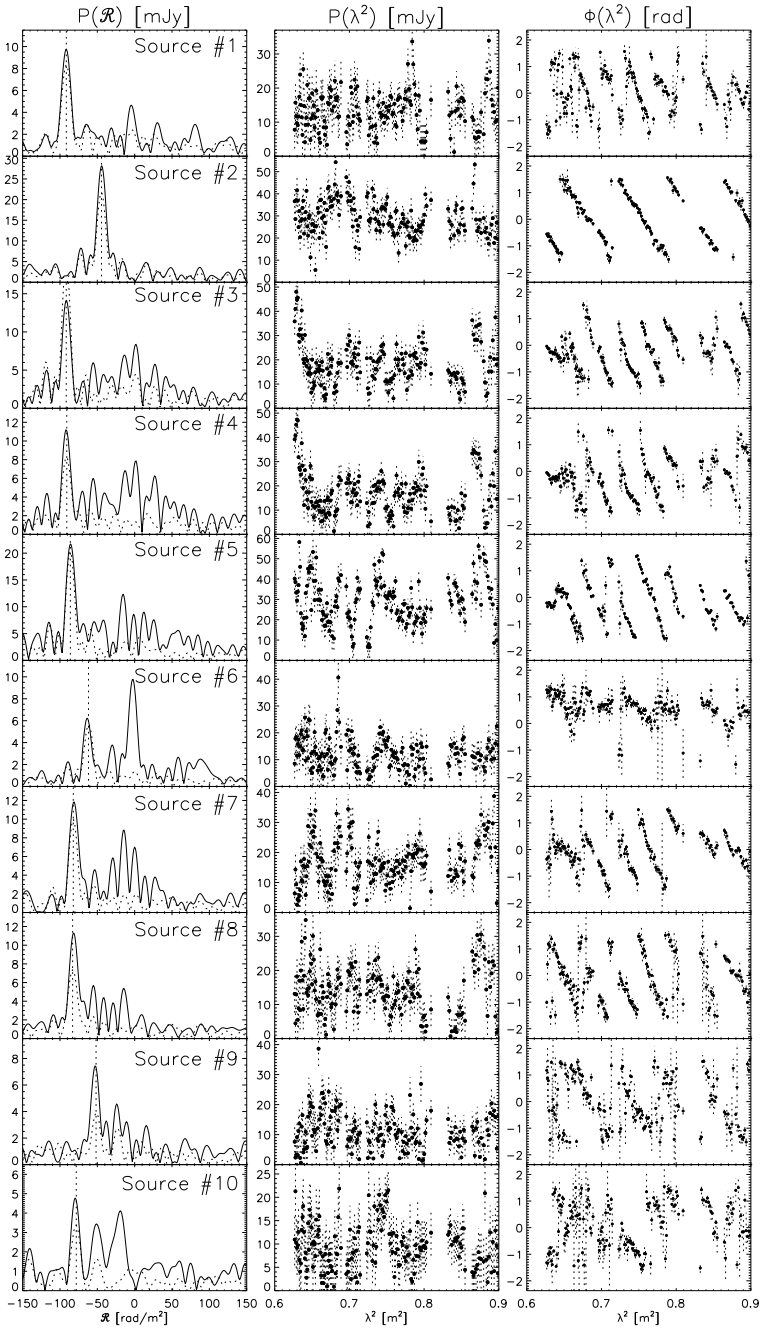

Figure 5.8 — $P(\mathcal{R})$ spectra for sources 1 – 9 from Table 5.2, for the short-baseline taper maps that we we discussed in Sect. 5.3 (solid line) and the long-baseline taper maps that we discuss in Sect. 5.6 (dotted line). The Faraday depths along the horizontal axis range from -150 rad/m^2 to +150 rad/m^2, and the vertical scale is in mJy. The vertical dotted line indicates the RM that we fitted to the peak in the $P(\mathcal{R})$ spectrum of long-baseline taper maps. The second and third columns show for each line-of-sight the polarized intensity [mJy] and polarization angle [rad] spectra that we used to calculate the solid line $P(\mathcal{R})$ spectra. The $P(\mathcal{R})$ noise level is 5.2 mJy, and the $P(\lambda^2)$ noise level is 0.3 mJy. The low-resolution maps that we used to calculate the solid-line $P(\mathcal{R})$ spectra contain signal from both the diffuse emission and from the extragalactic source. In the high-resolution maps (and the dotted-line spectra) we left out baselines < 250 m. This reduces the strength of the signal from the diffuse emission in the $P(\mathcal{R})$ spectra, which makes the $P(\mathcal{R})$ feature of the extragalactic source more pronounced.

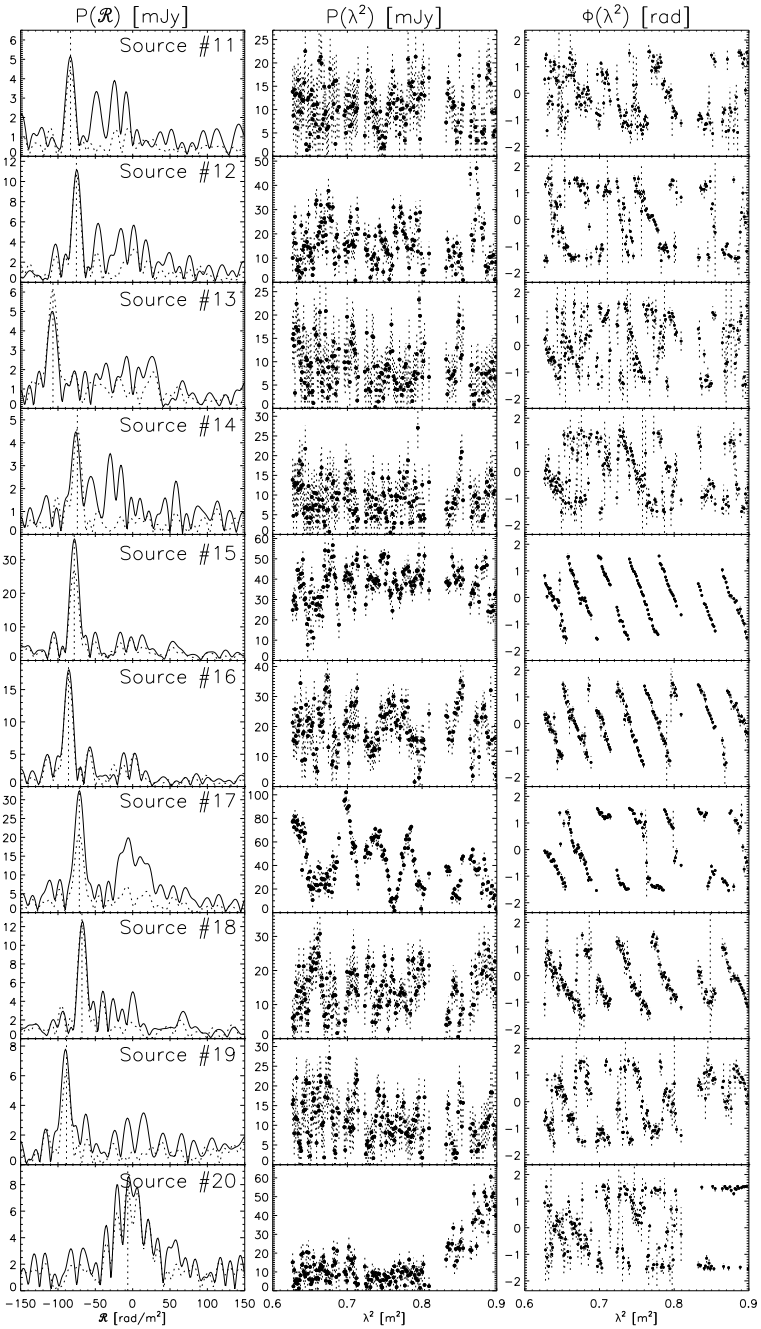

Figure 5.9 — Identical to Fig. 5.8, but for sources 10 – 19 from Table 5.2.

and its analysis, we came to a similar conclusion. Since we calculated the EM and DM for the entire line-of-sight through the Galaxy, the $|\langle B_{\parallel}\rangle|$ we found from the diffuse emission are lower limits to the actual $|\langle B_{\parallel}\rangle|$, but the extragalactic sources should have the correct values for DM and therefore for $\langle B_{\parallel}\rangle$. In chapter 9 we combine the observational characteristics of our 4 Faraday tomography data sets to get a better overview of the properties of the magnetized warm ISM in the second Galactic quadrant.

Extragalactic sources from the Broten et al. catalogue (1988) in the vicinity of the TRI mosaic also show strong negative RMs ranging from about -90 rad/m^2 to

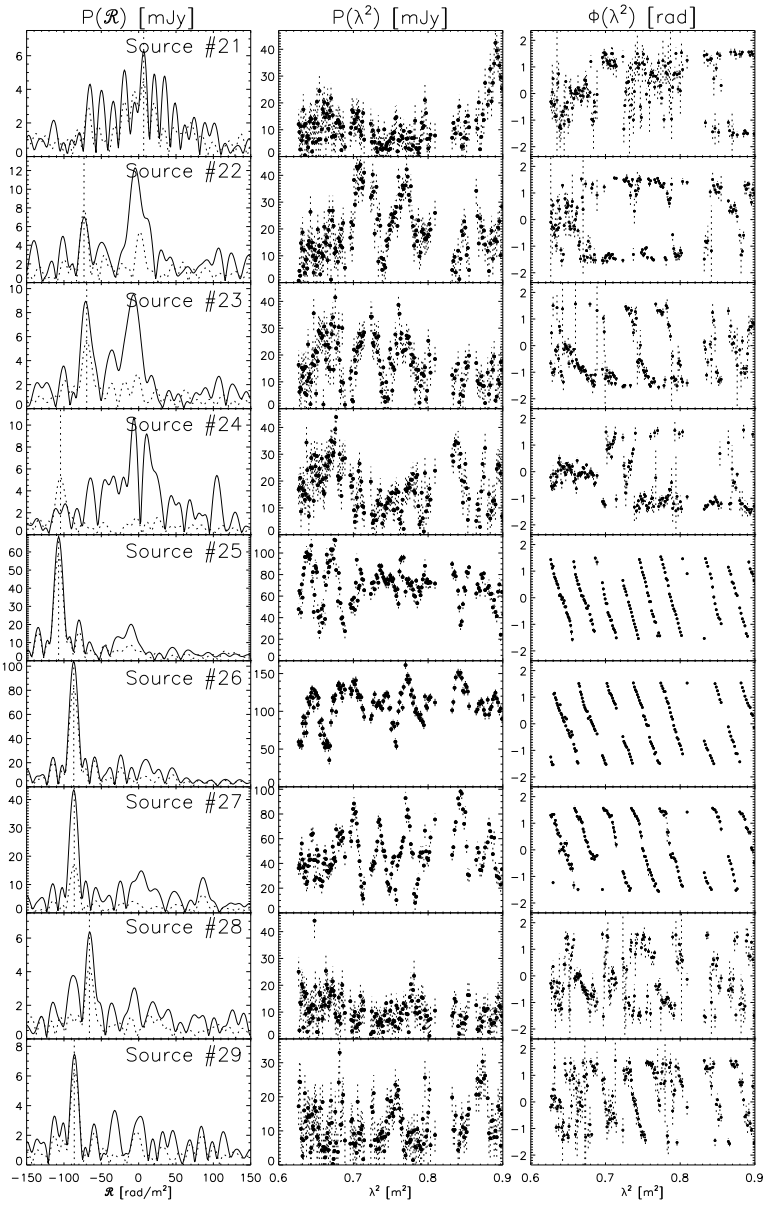

Figure 5.10 — Identical to Fig. 5.8, but for sources 21 – 29 from Table 5.2.

-120 rad/m^2. The TRI region and its vicinity are not part of the North Polar Spur, Loop II or Loop III (the coordinates of the centres of these objects and their diameters are given in Elliott 1970). Simard-Normandin & Kronberg (1980) also note the strong negative RM of the extragalactic sources and a lack of extragalactic sources with small |RM| < 30 rad/m^2 in the region $60^\circ < l < 140^\circ$ and $-40^\circ < b < +10^\circ$. They come to the conclusion that these RMs are likely produced in a large ($> 0.5 - 3$kpc) region at a distance $\gtrsim 3$ kpc, with an electron density ~ 0.03 – 0.08 cm^{-3}.

5.7 Summary and conclusions

In this chapter we presented the results from a Faraday tomography analysis of our WSRT observations towards (l, b) = (137°, -23°). The $P(\mathcal{R})$ mosaics with a strong signal from the diffuse emission show fascinating structures on scales from degrees down to the synthesized beam of order arcminutes. These maps also show strong gradients in Faraday depth, similar to what we noticed for the GEMINI and CEPHEUS mosaics that we discussed previously. There is a conspicuous $\approx 6^\circ \times 3^\circ$ region at a Faraday depth of about -32 rad/m^2, which is about twice the Faraday depth of the diffuse emission elsewhere in the mosaic. We have not yet identified the physical origin of this region. From the WHAM Hα intensities we derived that on average the magnetic field along the line-of-sight has to be -0.6 μG to explain the observed Faraday depths of the diffuse emission. This is much smaller than the $\approx$ -2 μG we would expect for the line-of-sight component of the regular magnetic field. However, the way we calculated the average magnetic field strength results in lower limits to the field strengths that we need to explain the Faraday depths of the diffuse emission. To illustrate the richness of the $P(\mathcal{R})$ spectra in TRIANGULUM, we present $P(\mathcal{R})$ spectra for a 10×15 grid of lines-of-sight, and to indicate that these spectra are not the product of noise or instrumental artefacts, we also show $P(\lambda^2)$ and $\Phi(\lambda^2)$ spectra for a subset of 10 lines-of-sight. However, care should be taken not to over interpret these spectra, because our interferometer observations do not include information on short baselines. We detected 29 polarized extragalactic sources in our data set. Their average rotation measure of -75 rad/m^2 is about 4 times larger than most of the Faraday depths of the strongest peak of the diffuse emission, which would indicate that the bulk of the diffuse emission that we observe is generated only along a fraction of the line-of-sight towards the extragalactic sources. Such large rotation measures are also found for extragalactic sources outside the TRI mosaic. We postpone modeling of this additional Faraday depth of the extragalactic sources to chapter 9. If we calculate the average magnetic field strength necessary to explain the rotation measures of the extragalactic sources in the same way as we did for the diffuse emission, we find $\langle B_\parallel \rangle$ = -2.2 μG, similar to what we would expect for the large-scale magnetic field.

Acknowledgements

The Westerbork Synthesis Radio Telescope is operated by the Netherlands Foundation for Research in Astronomy (NFRA) with financial support from the Netherlands Organization for Scientific Research (NWO). The Wisconsin H-Alpha Mapper is funded by the National Science Foundation.

Chapter 6

WSRT Faraday tomography of the Galactic ISM at $\lambda \sim 0.86$ m - IV. The CAMELOPARDALIS data set at $(l, b) = (138^\circ, 30^\circ)$

Abstract. We present WSRT observations of a region around (l, b) = (138°,30°), and we discuss the results of applying Faraday tomography to this data set. Faraday tomography is a novel technique with which we can study the relative distributions of synchrotron emission and Faraday rotation along the line-of-sight. The strongest diffuse emission in our $P(\mathcal{R})$ cube has Faraday depths between -40 rad/m^2 and -10 rad/m^2. At these Faraday depths the diffuse emission shows structures on scales from degrees to arcminutes (the size of the synthesized beam). We describe how we use the WHAM Hα intensities to calculate the average magnetic field strength that is required to explain the observed Faraday depths of the diffuse emission. The line-of-sight component of the magnetic field that we find is typically -2.2 μG, which is close to the -1.9 μG we expect to find for the large-scale magnetic field in the direction of our data set. We show $P(\mathcal{R})$ spectra for a grid of 10 $\times$ 14 lines-of-sight, to underline that these spectra contain interesting features outside the strongest peak that might otherwise be overlooked. We also present the $P(\lambda^2)$ and $\Phi(\lambda^2)$ spectra that we use to calculate the $P(\mathcal{R})$ spectra for a subset of 10 lines-of-sight, to illustrate that the $P(\mathcal{R})$ spectra we show are not the product of noise or instrumental artefacts. However, care should be taken not to over interpret these spectra, since they were calculated from interferometer observations. Finally, we detect 23 polarized extragalactic point sources in our data set. Their average rotation measure of -19 rad/m^2 is close to the average Faraday depth of the strongest peak in the $P(\mathcal{R})$ spectra of the diffuse emission. This is similar to what we found in a data set towards (l, b) = (181°,20°), but in 2 data sets towards (l, b)=(102°,15°) and (l, b) = (137°,-23°) we found large differences between the Faraday depths of the diffuse emission and the rotation measures of the extragalactic sources. In chapter 9 we will combine the information we gathered from our 4 data sets to try to understand the physical properties (also in the depth dimension) of the magnetized warm ISM in the second Galactic quadrant.

D. H. F. M. Schnitzeler, P. Katgert and A. G. de Bruyn

6.1 Introduction

In this chapter we use the novel concept of Faraday tomography, also known as Rotation measure synthesis, to study Faraday rotation and synchrotron emission along the line-of-sight. The possibility to separate the contributions from different parts along the line-of-sight is a big step forward compared to the previous situation, where we only would have one rotation measure for an entire line-of-sight.

Faraday tomography was described in Brentjens & De Bruyn (2005), and for a complete overview of the principles of Faraday tomography we refer to their paper. We gave a short introduction to Faraday tomography chapter 3, and we presented examples of Faraday rotating and synchrotron emitting regions along the line-of-sight, and what signatures they would have when we apply Faraday tomography to simulated observations. For completeness we present Faraday tomography's basic functioning here.

The linearly polarized emission from every point along the line-of-sight will be Faraday rotated between its point of origin and the observer. The amount of Faraday rotation is proportional to

$$\mathcal{R}(x)\,[\mathrm{rad/m^2}] \;=\; 0.81 \int_{\text{source at 'x'}}^{\text{observer}} n_e\,[\mathrm{cm^{-3}}]\;\vec{B}\,[\mu\mathrm{G}]\cdot \mathrm{d}\vec{l}\,[\mathrm{pc}] \tag{6.1}$$

which is known as the Faraday depth of the emission at point 'x'. n_e is the electron density, $\vec{B}$ the magnetic field vector, and dl an infinitesimal piece of the line-of-sight towards the observer. If we express the polarization vector as a complex vector, with the Stokes Q and U components as its real and imaginary parts, then we can write for the observed polarization vector at wavelength λ:

$$\vec{P}(\lambda) \;=\; Q(\lambda) + \mathrm{i}U(\lambda) \;=\; P(\lambda, \mathcal{R}=0)\,\mathrm{e}^{2\mathrm{i}\mathcal{R}(\mathrm{x})\lambda^2} \tag{6.2}$$

Summing over all points along the line-of-sight gives

$$\vec{P}(\lambda) \;=\; \int_0^\infty \vec{P}(\mathrm{x})\,\mathrm{e}^{2\mathrm{i}\mathcal{R}(\mathrm{x})\lambda^2}\mathrm{dx} \;=\; \int_{-\infty}^{\infty} \vec{P}(\mathcal{R})\,\mathrm{e}^{2\mathrm{i}\mathcal{R}\lambda^2}\mathrm{d}\mathcal{R} \tag{6.3}$$

where the first integral is over physical distance 'x', and the second integral is over all Faraday depths. The crucial point about Faraday tomography is that the second integral in Eqn. 6.3 is invertible, similar to a Fourier transform and its inverse:

$$\vec{P}(\mathcal{R}) \;=\; K \int_{-\infty}^{\infty} \vec{P}(\lambda^2)\,\mathrm{e}^{-2\mathrm{i}\mathcal{R}\lambda^2}\mathrm{d}\lambda^2 \tag{6.4}$$

$$K \;=\; \left(\int_{-\infty}^{\infty} W(\lambda^2)\,\mathrm{d}\lambda^2 \right)^{-1} \tag{6.5}$$

$W(\lambda^2) = 1$ for observed wavelengths, and = 0 elsewhere. The K factor in Eqn. 6.5 takes care of the correct normalization of $P(\mathcal{R})$. By observing polarization vectors over a large number of narrow frequency channels, we can apply Eqn. 6.4 to determine the strength and orientation of the polarization vector at Faraday depth $\mathcal{R}$! If the measured $P(\lambda^2)$ are in K (mJy/beam), then also the $P(\mathcal{R})$ will be in K (mJy/beam), or, more precisely, in K/RMSF width (mJy/beam/RMSF width). If we want to compare different data sets, with different RMSFs, it is necessary to convert this quantity to K/rad/m^2 instead of K/RMSF (equivalently for mJy/rad/m^2). Here we only consider one dataset, and we did not convert the measured $P(\mathcal{R})$ to K/rad/m^2.

Note that we distinguish the Faraday depth $\mathcal{R}$ from the rotation measure RM $\equiv \partial\Phi/\partial\lambda^2$, the derivative of the observed polarization angles with respect to λ^2. Finally, it is important to realize that we recover the polarization vector $\vec{P}(\mathcal{R})$ as a function of Faraday depth, which is not the same as physical depth. To calculate physical depths one needs to make assumptions on the geometry of the magnetic field, in particular if there are reversals in the magnetic field direction that assign the same Faraday depth to different physical depths 'x'.

Faraday tomography is a brand-new technique, and it has not yet been used in many publications. De Bruyn & Brentjens (2005) used it to study the properties of the Perseus cluster, and we presented in a short letter our first results for the GEMINI region towards (l, b) = (181°,20°) (chapter 2). We detected an unexpectedly high percentage of lines-of-sight with an unresolved main peak in the $P(\mathcal{R})$ spectra. If synchrotron emission and Faraday rotation occur at the same location, this would widen the signature in the $P(\mathcal{R})$ spectrum. The unresolved peaks therefore indicate that the synchrotron emission that produces the peak in the $P(\mathcal{R})$ spectrum and the Faraday rotation that produces the Faraday depth of this peak are physically separated. This might come as a surprise since the cosmic rays that produce synchrotron emission are expected to pervade the ISM. One possibility is that the magnetic field is locally aligned with the line-of-sight; since synchrotron radiation is then emitted perpendicular to the line-of-sight, we would not observe the synchrotron emission coming from such a magnetic field geometry.

In chapters 2 – 5 we presented Faraday tomography analyses for data sets towards (l, b) = (181°,20°) ('GEMINI'), (l, b) = (102°,15°) and (l, b) = (137°,-23°) ('CEPHEUS' and 'TRIANGULUM'), and we discussed the properties of both the diffuse emission from the Galactic ISM and of the extragalactic point sources that we detected in our data. In this chapter we present the final of the 4 data sets that are spread over the fourth Galactic quadrant. First we discuss the characteristics of our observations in Sect. 6.2. We tapered the mosaics of the individual frequency channels to a common beamsize before we calculated the $P(\mathcal{R})$ datacube. We describe this process in Sect. 6.3, and there we also present slices through our $P(\mathcal{R})$ datacube with the strongest diffuse emission, at Faraday depths between -46 rad/m^2 and +8 rad/m^2. W e derive the average strength of the magnetic field along the line-of-sight in Sect. 6.4 by combining the Faraday depth of the main peak in the $P(\mathcal{R})$ spectrum with dispersion measures that we calculate from the WHAM survey. To demonstrate that the main peak in the $P(\mathcal{R})$ spectra is not the only interesting feature of these spectra, we present in Sect. 6.5 a grid of $P(\mathcal{R})$ spectra for 140 lines-of-sight that show a wide variety of features, with strong single- or

multiple-peaks and even extended structures. For a subset of 10 lines-of-sight we also present $P(\lambda^2)$ and $\Phi(\lambda^2)$ spectra that we used to calculate the $P(\mathcal{R})$ spectra, to show that the $P(\mathcal{R})$ spectra are not the product of noise or instrumental artefacts. In Sect. 6.6 we describe how we detected 23 polarized point sources in our data set, and we show their RM distribution on the sky. The average RM of about -19 rad/m^2 is very comparable to the average Faraday depth of the main peak of the diffuse emission. Finally, we summarize the properties of the diffuse emission and the extragalactic point sources in the CAMELOPARDALIS data set in Sect. 6.7. In chapter 9 we combine the information that we gathered from our four data sets with data from the literature to describe and model the properties of the magnetized warm ISM in the second Galactic quadrant. We therefore postpone modeling of the CAMELOPARDALIS data set to chapter 9.

6.2 The data

With the WSRT we observed a $11^\circ \times 8^\circ$ area around $\alpha = 8^h00^m$ and $\delta = 76^\circ$ (J2000.0), or $(l, b) = (138^\circ, 30^\circ)$ in Galactic coordinates. We will refer to this area as CAMELOPARDALIS, or CAM for short. The WSRT is a 14-element E-W interferometer of which 4 elements are moveable to improve (u,v) coverage. Each of the telescope dishes is 25 meters in diameter. The CAM region was observed for 6 12 hour observing runs in December 2003 and January 2004 (see Table 6.1). This produced visibilities at baselines from 36 to 2760 meters, with an increment of 12 meters. Combining the 6 12 hour observing runs puts the first grating ring at 4.1° from the pointing centre (at 350 MHz), outside the $3^\circ \times 3^\circ$ area that we mapped for each individual pointing. We tapered the individual frequency channel maps in such a way that the synthesized beamsize for all maps is $2.94' \times 3.03'$ (RA $\times$ DEC).

We mapped the CAM region with a grid of 6 $\times$ 8 telescope pointings. In each night the same pointing was observed about 16 times, resulting in visibilities on 16 'spokes' in the (u,v) plane. Each time we integrated for 40 seconds before moving to the next field. For a rectangular grid in equatorial coordinates, off-axis instrumental polarization can be reduced to less than 1% positioning the pointing centres 1.25° apart (Wieringa et al. 1993). However, our pointing grid is rectangular in Galactic coordinates. The instrumental polarization levels cannot be much higher than 1% also with our grid, because in Sect. 6.6 we will present significant detections of point sources that are polarized at the $> 2\%$ level.

The data were reduced using the `NEWSTAR` data reduction package. Dipole gains and phases and leakage corrections were determined using the unpolarized calibrators 3C147 and 3C295. The flux scales of both unpolarized and polarized calibrators are set by the calibrated flux of 3C286 (26.93 Jy at 325 MHz - Baars et al. 1977). Due to an a-priori unknown phase offset between the horizontal and vertical dipoles, signal can leak from Stokes U into Stokes V. We corrected for this by rotating the polarization vector in the Stokes (U, V) plane back to the U axis, assuming that there is no signal in V. The polarized calibrator sources 3C345 and DA240 defined the sense of derotation (i.e. to the positive or negative U-axis). We copied the calibration corrections from these sources to the data. For each telescope pointing we then self calibrated the data, where in each step we include fainter sources. 2 pairs of pointings contained a strong

Table 6.1 — Characteristics of the CAMELOPARDALIS data set. Observing dates and times are given for each of the observing runs, which have been indicated by their shortest baseline length.

Central position	$(\alpha, \delta)_{2000}$ = (120°,76°); (l, b) = (138°,30°)					
Mosaic size	$11^\circ \times 8^\circ$					
Pointings	6×8					
Frequencies	317-379 MHz					
	149 independent frequency channels					
Resolution[a]	$2.94' \times 3.03'$					
Stokes V noise level	5.1 mJy (2.3 K)					
$\mathcal{R}$ noise level[b]	0.3 mJy (0.15 K)					
Conversion Jy – K[c]	1 mJy/beam = 0.45 K					
Shortest baseline (m)	36	48	60	72	84	96
Observing date (yy/mm/dd)	03/12/06	04/01/13	04/01/14	04/01/15	04/01/19	04/01/20
Start time (UT)	20:20	18:29	17:23	17:57	18:33	17:26
End time (UT)	07:27	06:27	05:22	05:56	08:05	07:04

[a] We tapered the individual frequency channel maps to a synthesized beamsize of $2.94' \times 3.03'$ (RA $\times$ DEC).

[b] This is the noise level in the individual $P(\mathcal{R})$ maps, which we determined from $P(\mathcal{R})$ maps at $|\mathcal{R}| \geq 202$ rad/m^2, that we assume contain no signal. Instrumental polarization levels increase towards the edges of the maps, therefore we excluded these in determining the noise level.

[c] This is the conversion factor at 348 MHz, the average of the λ^2 sampling of the (usable) frequency channels in our data set. We used the FWHM of a Gaussian fitted to the central peak of the synthesized PSF to calculate the beamsize required in this conversion.

extragalactic source (of 5 and 7.5 Jy respectively) that our self calibration pipeline could not handle, with the result that many (u,v) points were clipped. These telescope pointings can be found at the edge of the mosaic, in the upper left and bottom right of the mosaic in Fig. 6.1. We checked for 2 pairs of 2 pointings that the phase corrections found by our self calibration pipeline are stable enough so that we can apply the corrections found for a certain pointing to a neighbouring pointing. We then copied the self calibration solutions to the pointings with the strong extragalactic sources.

We selected usable frequency channels on the basis of the widths of their Stokes Q, U and V distributions. We left out the edge of the mosaic when determining these widths, because instrumental polarization levels are higher there due to incomplete overlap between pointings. From a total of 224 independent frequency channels, 149 channels were not corrupted by radio frequency interference or other artefacts. This final set of usable channels covers the frequency range between 317 and 379 MHz, and each frequency channels is 0.4 MHz wide (we used a Hanning taper). The automated clipping process that we use to select 'usable' frequency channels creates holes in the λ^2 coverage of our data. This produces higher sidelobes in the RMSF, which is the equivalent in Faraday tomography of the PSF in aperture synthesis. From Stokes V, which we assume to be empty, we estimate that the average noise level in the final

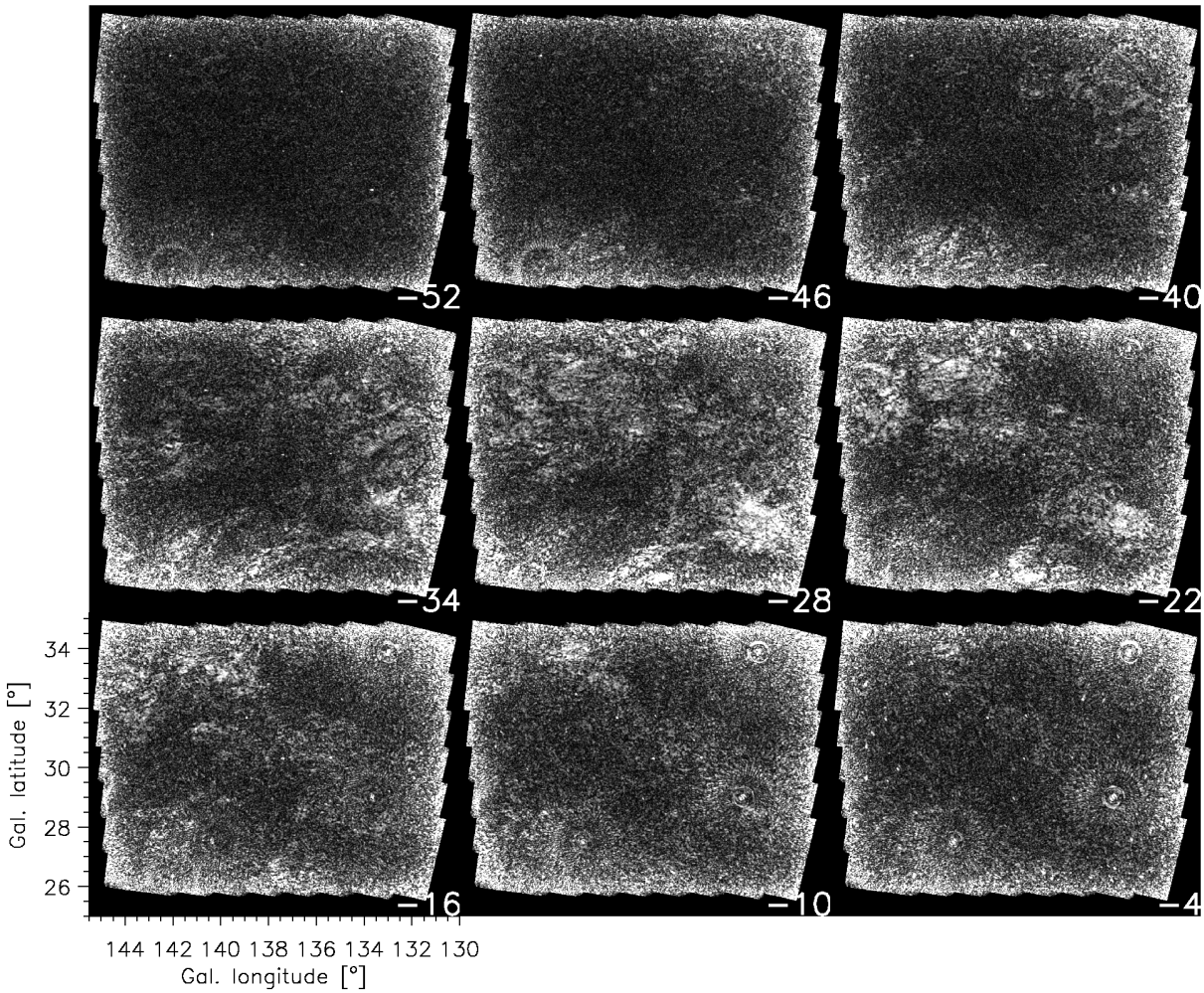

Figure 6.1 — Images of $P(\mathcal{R})$ maps with the strongest diffuse emission. We indicate the $\mathcal{R}$ of each 'slice' through our image cube in the bottom right corner of each image in units of rad/m^2. The RMSF has a FWHM of 14 rad/m^2, and we sampled each RMSF with 2 images. All panels have the same linear intensity scale that saturates at 3.5 K, whereas the GEMINI maps saturated at 6.4 K. The 1σ noise level in the $P(\mathcal{R})$ maps is 0.15 K. To convert our mosaic maps from equatorial to Galactic coordinates we regridded the Stokes Q and U mosaics from equatorial to Galactic coordinates, after which we calculated the polarized intensity from these regridded maps.

mosaics of the individual channels is 5.1 mJy (2.3 K).

We observed mostly in the evening and at night to limit solar interference and to reduce the importance of ionospheric RM variations. The polarized calibrators that we use indicate that the polarization angle variation between the observing runs is less than 5° on average, except for one night that deviates by 30° from the average polarization angle. Although this is a big enough difference that it should be corrected for, it does not influence the RM and Faraday depths that we derive, but only reduces the length of the polarization vectors that we find by 2%. We therefore did not correct our data for ionospheric Faraday rotation. The ionospheric RM is at most 1.5 rad/m^2 during our observations (Johnston-Hollitt, private communication), which is so small that we also did not correct our data this effect.

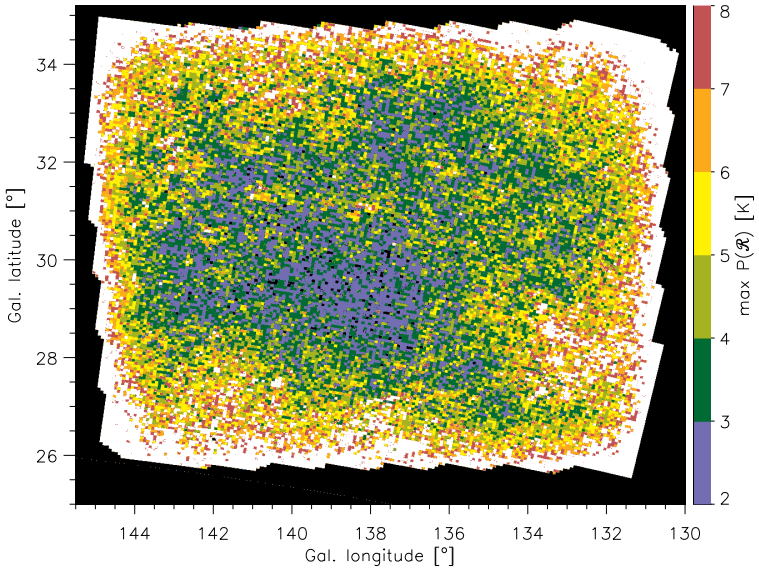

Figure 6.2 — $P(\mathcal{R})$ of the highest peak in the $\mathcal{R}$ spectrum. Each pixel represents one telescope beam, and the pixel size is $2.9' \times 3.0'$. Out of a total of 26.000 lines-of-sight, 5314 lines-of-sight have $P(\mathcal{R}) > 8$ K, and these are shown in white. The 1σ noise level is 0.16 K. On page 193 we show a colour version of this figure.

An interferometer in general does not cover all baseline lengths down to 0 meters, which means that extended structure on the sky will be missing from maps made with an interferometer. In chapter 3 we showed that variations in Faraday depth over the field-of-view can modulate extended structure to angular scales that are small enough so that an interferometer can detect them. In particular, for the size of the field-of-view in our observations, and for our observing frequencies, we showed that a linear gradient in Faraday depth of 6 radians/m^2 is needed to make the 0-angular frequency (total polarized intensity) component visible for the WSRT. Although the diffuse emission in CAM is in general not very strong, there are regions with strong variations in Faraday depth (see Fig. 6.3) where most of the total polarized intensity component that is emitted at these Faraday depths is picked up by the WSRT.

6.3 Analysis

With the 149 usable frequency channels we calculated a $P(\mathcal{R})$ datacube for Faraday depths between -1000 rad/m^2 and +998 rad/m^2 in steps of 6 rad/m^2. The RMSF, which is the Faraday tomography equivalent of the PSF in synthesis imaging, has in our case a FWHM of about 14 rad/m^2. We therefore Nyquist sample the information in our $P(\mathcal{R})$ datacube. At large $\mathcal{R}$ the sensitivity in the $P(\mathcal{R})$ spectra will drop due to the finite width of the frequency channels, $\delta\lambda^2$, similar to how the size of an individual telescope dish in an interferometer sets the size of the field-of-view in radio synthesis interferometry. Brentjens & De Bruyn (2005) determined that the sensitivity has dropped to 50% at $\mathcal{R}_{\rm max} = 1.9/\delta\lambda^2$ (the 1.9 replaces the $\sqrt{3}$ from their article because it is closer to the HWHM of the sinc RMSF response to the λ^2 coverage they assume). In our data set $\delta\lambda^2 \approx\ 1.5 \times 10^{-3}$ m^2 on average, which means that we should still be for

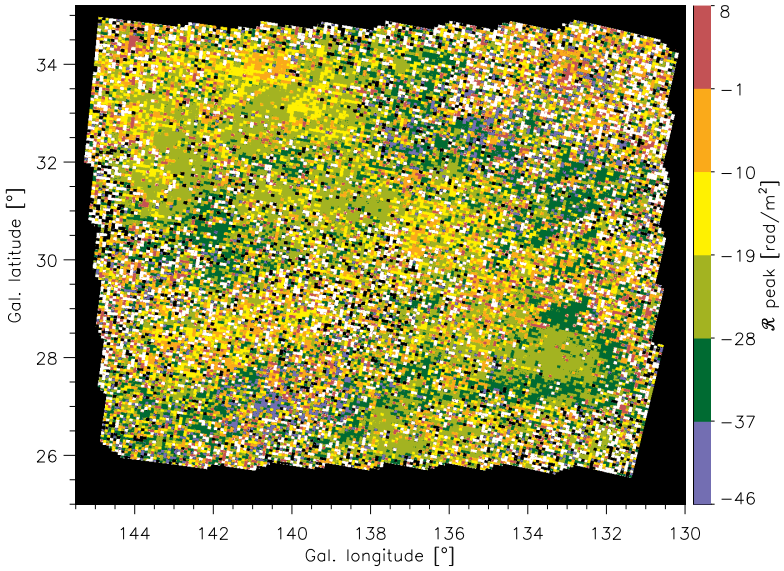

Figure 6.3 — $\mathcal{R}$ corresponding to the $P(\mathcal{R})$ plotted in Fig. 6.2. The 3713 lines-of-sight indicated in white have $\mathcal{R} > +8$ rad/m^2, and the 1482 black lines-of-sight that fall inside the mosaic have $\mathcal{R} < -46$ rad/m^2. On page 194 we show a colour version of this figure.

more than 50% sensitive for $\mathcal{R} < 1250$ rad/m^2.

In Fig. 6.1 we show the maps from our $P(\mathcal{R})$ datacube with the strongest diffuse emission. All panels saturate at the 3.5 K level. To create this figure we regridded the Stokes Q and U images from equatorial to Galactic coordinates, and then we calculated the polarized intensity from the regridded Q and U images. There is a bright circular area around $(l, b) = (133.5°, 28°)$ with a diameter of about 1.5°, that shows up at Faraday depths between -34 rad/m^2 and -22 rad/m^2. At this point we have not looked into the origin of this structure. In Figs. 6.2 and 6.3 we show how the $P(\mathcal{R})$ and $\mathcal{R}$ of the main peak in the $P(\mathcal{R})$ spectra are distributed over the CAM mosaic. From the $P(\mathcal{R})$ maps at $|\mathcal{R}| > 202$ rad/m^2 we estimate that the $P(\mathcal{R})$ noise level is about 0.15 K, which is close to the $2.3/\sqrt{149} = 0.19$ K we would expect to find for 149 independent frequency channels that each have a noise level of about 2.3 K.

6.4 The line-of-sight component of the magnetic field

In this section we determine how strong the magnetic field has to be to explain the Faraday depth of the strongest peak in the $P(\mathcal{R})$ spectra from Fig. 6.3. To do this we follow the same approach as we described for the CEPHEUS and TRIANGULUM mosaics that we discussed elsewhere.

In short, from the WHAM Hα intensities (Haffner et al. 2003) we calculate emission measures EM that we then translate into dispersion measures DM using an empirical relation that was established by Berkhuijsen et al. (2006) for Galactic pulsars. The emission measure EM and dispersion measure DM are defined by EM[cm^{-6}pc] = $\int_0^\infty n_e^2 \mathrm{d}l$ and DM[cm^{-3}pc] = $\int_0^\infty n_e \mathrm{d}l$, where n_e is the electron density in cm^{-3}, and dl is an infinitesimal element of the line-of-sight in parsec. From the $\mathcal{R}$ in Fig. 6.3 and the DM we can then calculate the electron-density weighted magnetic field component along

the line-of-sight, $\langle B_{\parallel} \rangle$. The main advantage that this approach has over using the electron density models by either Reynolds (1991) or by Cordes & Lazio (2003) is that with the fine sampling of the sky that the WHAM survey provides we can probably more accurately model small-scale variations in DM than with the other two models. The Berkhuijsen et al. model uses a sample of 157 pulsars with measured DM. From the WHAM survey they determine the EM in the direction of the observed pulsars, and they correct these EM both for emission coming from beyond the pulsar, and for interstellar reddening occurring in front of the pulsar. From their data they determine a relation between DM and EM, and the variation of the electron density and the electron filling factor with distance above the Galactic plane. For comparison, the Reynolds model is based on 4 lines-of-sight towards globular clusters containing pulsars. The Cordes & Lazio model uses a much larger source sample, but they model the Galaxy as a fairly smooth structure that consists of a thin and thick disk plus spiral arms, and for a small number of regions they add or subtract additional electrons to explain the anomalous DM observed in some pulsars.

Faraday rotation occurs wherever free electrons and magnetic fields coexist. The only other phase apart from the warm ionized medium (WIM) to which WHAM is sensitive and that contains free electrons in abundance is the hot intercloud medium (HIM). Snowden et al. (1997) modeled the HIM electron density in the Galactic plane from ROSAT diffuse X-ray emission maps, and they found that the electron density in the HIM is about a factor of 10 smaller than the electron density in the WIM. Therefore we can safely neglect the HIM contribution to the Faraday depth.

We plot the WHAM Hα intensities in the direction of our CAM in the top panel of Fig. 6.4. The average Hα intensity in this figure is about 1 Rayleigh. To convert the Hα intensities to EM we can use Eqn. 1 from Haffner et al. (1998):

$$\mathrm{EM} \;=\; 2.75 T_4^{0.9}\; I_{\mathrm{H}\alpha}(\mathrm{R})\; \mathrm{e}^{2.2\ \mathrm{E(B-V)}} \tag{6.6}$$

where T_4 is the temperature of the WIM in units of 10^4 K, which is typically 0.8 (Reynolds 1985), and $I_{\mathrm{H}\alpha}$ is the Hα intensity in Rayleigh. To find the amount of interstellar B-V reddening, E(B-V), we used NED's extinction calculator[1], that in turn is based on Schlegel et al. (1998). For the centre of the CAM mosaic E(B-V) = 0.027, and it varies between 0.02 and 0.06 over the mosaic. This means that in CAM 1 Rayleigh = 2.39 cm^{-6}pc, and the average Hα intensity of 1 Rayleigh translates into an average EM = 2.4 cm^{-6}pc.

Berkhuijsen et al. derived from a sample of 157 Galactic pulsars at $|b| > 5^\circ$ a simple relation between DM and EM:

$$\mathrm{EM} \;=\; 0.042 \pm 0.014\ \mathrm{DM}^{1.47 \pm 0.09} \tag{6.7}$$

that we can use to translate the EM we found from WHAM to DM. With the definition of DM we can calculate the electron-density weighted average magnetic field strength that is needed to build up a certain Faraday depth:

[1] `http://nedwww.ipac.caltech.edu/forms/calculator.html`

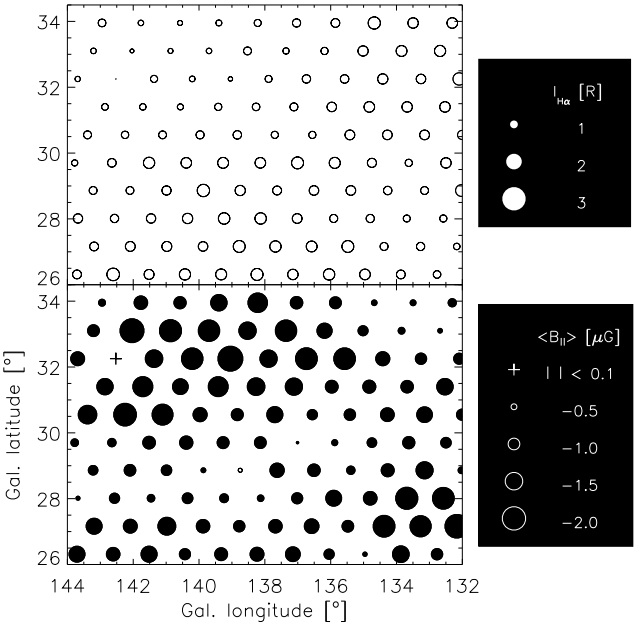

Figure 6.4 — WHAM Hα intensities in Rayleigh (top panel) and the strengths of the magnetic field component parallel to the line-of-sight $\langle B_\parallel \rangle$ in μG (bottom panel) that we derived. In Sect. 6.4 we describe how we derived $\langle B_\parallel \rangle$ from the WHAM Hα intensities and the Faraday depths from Fig. 6.3. Open circles indicate positive $\langle B_\parallel \rangle$, filled circles negative $\langle B_\parallel \rangle$. $|\langle B_\parallel \rangle| < 0.1$ μG are shown as '+'.

$$\langle B_\parallel \rangle \equiv \frac{\int_{\text{line-of-sight}}^{\text{observer}} n_e \vec{B} \cdot \mathrm{d}\vec{l}}{\int_{\text{line-of-sight}} n_e \mathrm{d}l} = \frac{\mathcal{R}}{0.81 \text{ DM}} \tag{6.8}$$

where $\langle B_\parallel \rangle$ is in μG. The scatter in Eqn. 6.7, produces about a 30% uncertainty in $\langle B_\parallel \rangle$.

It is important to realize that we calculated EM, and consequently DM, for the entire line-of-sight through the Galaxy. It is therefore OK to use these values to calculate $\langle B_\parallel \rangle$ from the rotation measures of extragalactic sources (as we will do in Sect. 6.6). The CEPHEUS and TRIANGULUM data set however showed that the diffuse emission that we observe not necessarily covers the entire line-of-sight through the Milky Way. In the CEPHEUS mosaic, the strongest diffuse emission in the $P(\mathcal{R})$ spectra occurred at negative Faraday depths over most of the mosaic, whereas 11 out of 12 extragalactic sources showed positive rotation measures. In the TRIANGULUM mosaic the average rotation measure of the 25 extragalactic sources that we found was by a factor of 4 larger than the average Faraday depth of the highest peak in the $P(\mathcal{R})$ spectra! Therefore, if we use Eqn. 6.8 to determine $\langle B_\parallel \rangle$ with the DM for the entire line-of-sight, one should keep in mind that the $|\langle B_\parallel \rangle|$ we find are actually lower limits.

In the bottom panel of Fig. 6.4 we show the $\langle B_\parallel \rangle$ that we determined for the Faraday depths in Fig. 6.3. We calculated $\langle B_\parallel \rangle$ for the centres of the WHAM pointings, and since the WHAM beam (FWHM $\approx 1^\circ$) is much larger than the WSRT beam, we used the $P(\mathcal{R})$-weighted $\mathcal{R}$ average over the WHAM beam to calculate $\langle B_\parallel \rangle$. For the average Faraday depth of about -28 rad/m^2 from Fig. 6.3, and with the average Hα intensity of 1 Rayleigh, we find $\langle B_\parallel \rangle$ = -2.2 μG. Beck (2007a) indicates that the large-scale Galactic field has a strength of 4 ± 1 μG and a pitch angle of -8°. With these values we calculate that in the vicinity of the sun the magnetic field in the direction of our CAM mosaic would have a strength of $B_{\text{reg},\parallel}$ = -1.9 μG.

Reynolds et al. (2001) detected a large arc of ionized hydrogen gas centred on $(l, b) \approx (138^\circ, 17^\circ)$ that reaches Galactic latitudes up to about 25°, which is close to the lower edge of the CAM mosaic. However, there does not seem to be a significant excess of Hα emission in our CAM mosaic that could be associated with this arc.

6.5 Structure in the $P(\mathcal{R})$ spectra

In the previous paragraph we used the Faraday depth of the main peak in the $P(\mathcal{R})$ spectrum to determine the average magnetic field strength along the line-of-sight. To show how varied the structures are that we encounter elsewhere in the $P(\mathcal{R})$ spectrum, we present in Fig. 6.5 $P(\mathcal{R})$ spectra for a grid of 10×14 lines-of-sight. The lines-of-sight that we show here lie on a rectangular grid, and lie further than 1.75° from the mosaic border so that instrumental polarization effects should be minimal. This grid of $P(\mathcal{R})$ spectra contains not only lines-of-sight that are dominated by a single peak, but in many more cases one can find also extended structures, or multiple peaks along the line-of-sight. In Fig. 6.6 we present for a subset of 10 lines-of-sight the $P(\lambda^2)$ and $\Phi(\lambda^2)$ spectra that we used to calculate the $P(\mathcal{R})$ spectra. In the bottom row of this figure we show a $P(\mathcal{R})$ spectrum with a low signal/noise ratio. This illustrates that the $P(\lambda^2)$ and $\Phi(\lambda^2)$ spectra of other lines-of-sight from this figure do actually contain real signal, and consequently that the $P(\mathcal{R})$ spectra we calculate are not the result of only noise or instrumental artefacts.

However, one needs to be careful when interpreting these spectra. The $P(\lambda^2)$ and $\Phi(\lambda^2)$ maps that we need to calculate the $P(\mathcal{R})$ spectra were originally obtained with an interferometer that cannot observe extended structure on the sky. This will of course also have its consequences for the $P(\mathcal{R})$ spectra. In Sect. 6.2 we said that the Faraday depths of the main peak in the $P(\mathcal{R})$ spectra show enough variation over some of our telescope pointings that the Faraday-rotating foreground will modulate extended structures to small enough scales that we can observe with the WSRT. For the moment we have not been able to extend this idea to the line-of-sight as a whole. Without knowing how important the effect of missing large-scale structure is in the CAM mosaic, we cannot determine to what extent leaving out the extended emission on the sky has affected the $P(\mathcal{R})$ spectra. However, in chapter 7 we will calculate $P(\mathcal{R})$ spectra for a simulated MHD cube. By comparing the $P(\mathcal{R})$ spectra from these mock observations to the structures in the simulated volume of ISM, we can better understand how the features in the observed $P(\mathcal{R})$ spectra could be produced in the ISM.

6.6 Polarized point sources

The diffuse polarized emission that we observe not necessarily comes from the entire line-of-sight through the Milky Way. In our CEPHEUS and TRIANGULUM data sets we found strong evidence that the diffuse polarized emission comes from only a part of the line-of-sight through the Milky Way. Since the polarized point sources do probe the entire line-of-sight, the comparison of the Faraday depths of the diffuse emission to the rotation measures of the extragalactic sources can give us important insights on the magnetized warm ISM in particular in the outer reaches of the Galaxy.

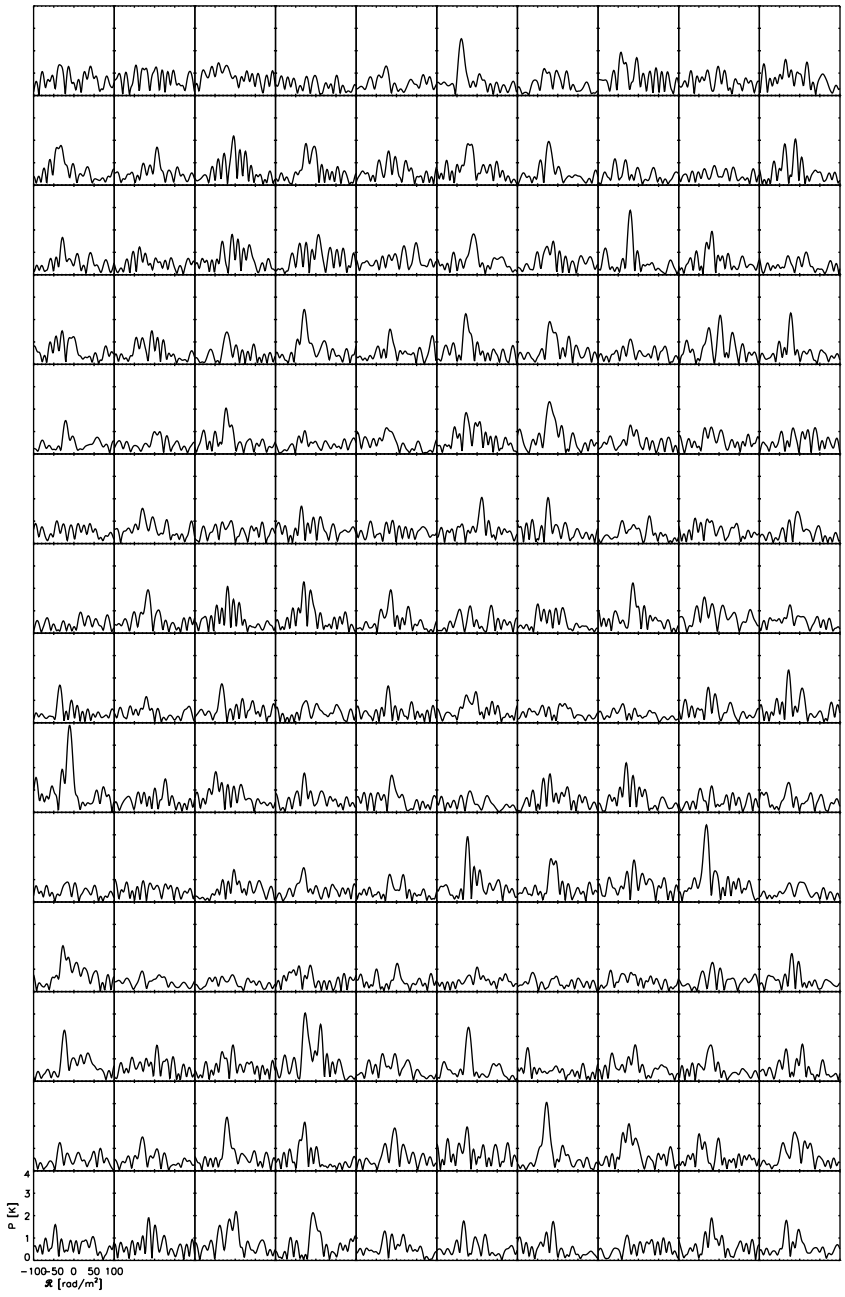

Figure 6.5 — $P(\mathcal{R})$ spectra for a rectangular grid of lines-of-sight through the CAMELOPARDALIS datacube. Faraday depths [rad/m^2] between -100 rad/m^2 and +100 rad/m^2 are plotted along the x-axis, and polarized intensities between 0 K and 4 K along the y-axis. The noise level in these spectra is 0.15 K. We chose lines-of-sight on a rectangular grid that lie more than 1.75° from the mosaic edges. The instrumental polarization levels are higher closer to the mosaic border, and this would affect the $P(\mathcal{R})$ spectra. Clearly there is a wide variety of structure for the different lines-of-sight. We plot the $P(\mathcal{R})$, $P(\lambda^2)$ and $\Phi(\lambda^2)$ spectra for some conspicuous lines-of-sight in Fig. 6.6 to show that most of the $P(\mathcal{R})$ spectra are not the result of low signal to noise or radio frequency interference, but are the product of a real signal.

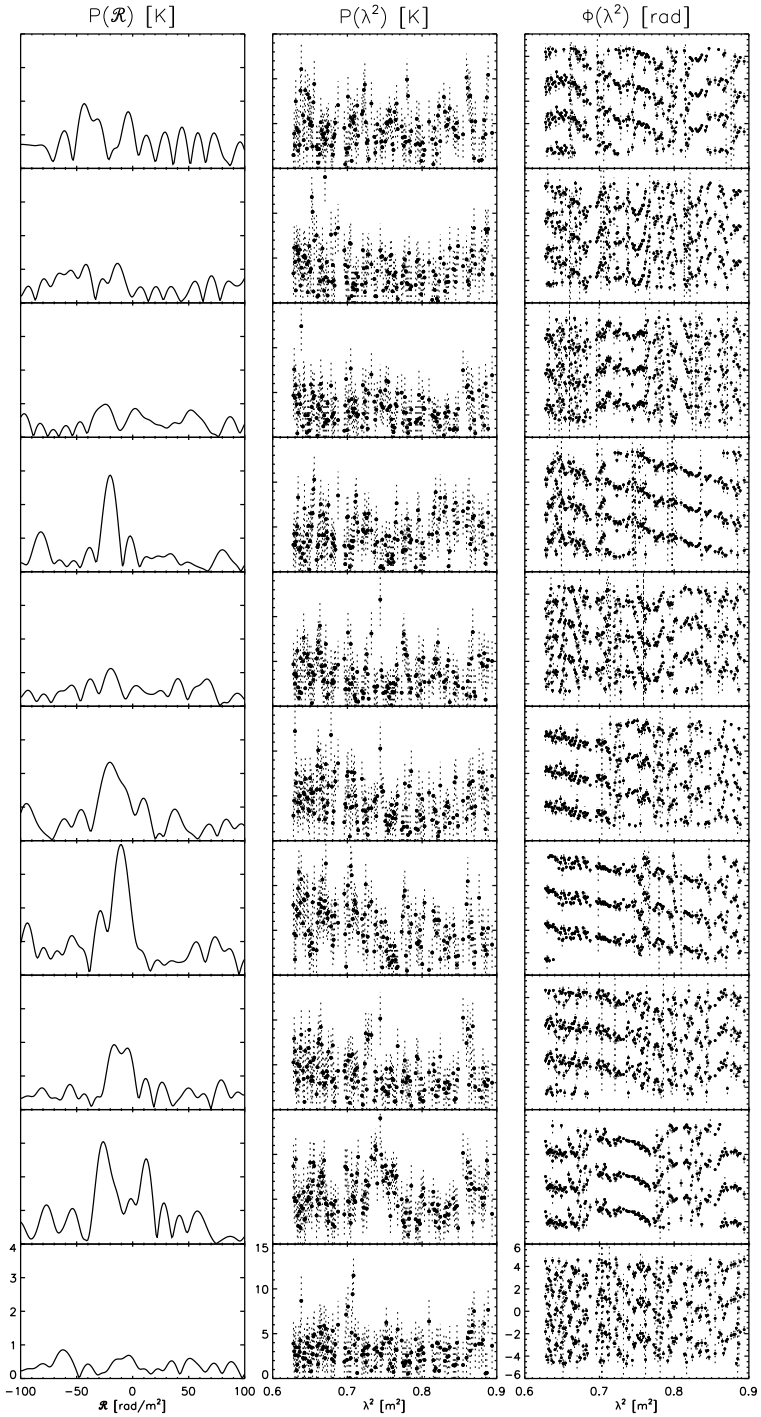

Figure 6.6 — $P(\mathcal{R})$ spectra, and the $P(\lambda^2)$ and $\Phi(\lambda^2)$ data they are based on, for lines-of-sight with diffuse emission. The Faraday depths plotted along the x-axis range from -100 rad/m^2 to +100 rad/m^2, and the polarized brightness temperatures along the y-axis range from 0 K – 4 K. The $P(\mathcal{R})$ noise level is 0.15 K, and the $P(\lambda^2)$ noise level 2.3 K. The $\Phi(\lambda^2)$ spectra were replicated at the observed $\Phi(\lambda^2)$ $\pm\pi$ to make the structure in polarization angle more clear. The bottom row shows a line-of-sight with a very low signal-to-noise ratio.

The problem is that we have to look for polarized point sources in a $P(\mathcal{R})$ cube with complex $P(\mathcal{R})$ structures that are produced by the diffuse Galactic emission. A trick that we first used in chapter 3 was to calculate a new $P(\mathcal{R})$ cube, but this time using only baselines > 250 m to partially filter out the diffuse emission. The maps of the individual frequency channels were tapered to a synthesized beamsize of $85'' \times 87''$ (RA $\times$ DEC). The maps we made showed a checker-board pattern in polarized intensity around the bright sources. We traced this artefact back to the 2 movable telescopes that produced the longest baselines, and we had to flag these in all 6 observing nights to remove the artefacts from our maps. This is also why the synthesized beamsize in these maps is somewhat larger than the $\approx 50''$ beamsize we found for the long-baseline taper maps in our CEPHEUS and TRIANGULUM mosaics. We calculated a new $P(\mathcal{R})$ cube using these long-baseline taper maps for Faraday depths between -1000 rad/m^2 and +998 rad/m^2. Depolarization over a frequency channel of width $\delta\lambda^2$ gives a sinc($|$RM$|$ $\delta\lambda^2$) attenuation. We use narrow frequency channels that on average have a $\delta\lambda^2 \approx 1.5 \times 10^{-3}$ m^2. For RM = 1000 rad/m^2 this gives an attenuation of only 34%, and we think that we could still detect the brighter sources with such large RM. To find polarized point sources we used the following set of criteria: 1) The point source must have a total intensity > 150 mJy, which excludes many grating artefacts from Stokes I, 2) the source should have a $> 5\sigma$ detection in the $P(\mathcal{R})$ cube 3) the source should be polarized by more than 2%, to exclude instrumentally polarized sources that are polarized at the $\approx 1\%$ level 4) we only looked for sources with $|\mathrm{RM}| > 4$ rad/m^2. Instrumentally polarized sources will show up at 0 rad/m^2, but due to the finite width of the RMSF these instrumentally polarized sources will also be visible at nearby RM. Calibration artefacts were also visible as deformations of the strongest sources close to 0 rad/m^2, but they are suppressed at larger Faraday depths (except for the > 5 Jansky sources in our data set that are too strong to be properly calibrated by our self calibration pipeline). This is also a good reason to look for polarized point sources at Faraday depths further from 0 rad/m^2 5) We leave out an area of about 0.9° from the edge of the mosaic (the grey area from Fig. 6.7). Instrumental polarization levels are higher here, and they produce complicated $P(\lambda^2)$ and $\Phi(\lambda^2)$ spectra, hence also complicated $P(\mathcal{R})$ spectra. Finally, we selected only sources where the reduced χ^2 of the RM fit to the polarization angles from the short-baseline taper maps (that we discussed in Sect. 6.3) is less than 3.

We list the polarized sources that we found with these criteria in Table 6.2, and we plotted their RM distribution in the CAM mosaic in Fig. 6.7. We fitted an RM to the polarization angles spectra of the long-baseline taper maps in the way described in chapter 2. In Figs. 6.8 and 6.9 we plot the $P(\mathcal{R})$ spectra of these sources for Faraday depths between -100 rad/m^2 and +100 rad/m^2, using the short-baseline taper maps (solid line) and the long-baseline taper maps that we discuss in this section (dotted lines). We also present the $P(\lambda^2)$ and $\Phi(\lambda^2)$ spectra from the short-baseline tapered maps to show that these are real detections, and are not produced by noise or by artefacts. Sources appear to be absent from the top left and bottom centre/right parts in Fig. 6.7, even though we do find diffuse emission in these regions (Fig. 6.1). By lowering the minimum polarization percentage of the sources from 2% to 1.5% we did find 4 additional sources in the quadrant bounded by $l \lesssim 138°$, $b \lesssim 29°$, and we indicate these

Table 6.2 — Properties of the polarized point sources that we found in our data. Shown are the Galactic coordinates of the source in decimal degrees, the RM that we fitted and its error, the reduced χ^2 ($\chi^2_{\rm red}$) of the fit, the $P(\mathcal{R})$ and total intensity I of the source, and its polarization percentage. The RM we indicate for each source can be off by $\lesssim 1.5$ rad/m^2 from the true RM of the source, because we did not correct for ionospheric RM. We also list 4 sources ('A' to 'D') with polarization percentages between 1.5% and 2.0% that are located in the lower right corner of Fig. 6.7 ($l \lesssim 138°$, $b \lesssim 29°$).

Source	(l, b) (°,°)	RM [rad/m^2]	$\chi^2_{\rm red}$	$P(\mathcal{R})_{\rm max}$ [mJy]	I [mJy]	$P(\mathcal{R})_{\rm max}/I$ %
1	(142.85, 29.41)	-32.9 ± 0.3	2.1	12.0	301	4.0
2	(142.47, 27.25)	-18.4 ± 0.6	2.8	5.3	204	2.6
3	(142.29, 27.56)	-17.6 ± 0.6	2.2	6.1	253	2.4
4	(142.19, 27.07)	-20.0 ± 0.3	2.6	16.0	436	3.7
5	(142.15, 27.06)	-21.5 ± 0.1	1.8	30.2	764	3.9
6	(141.46, 28.91)	-23.5 ± 0.7	2.8	3.8	165	2.3
7	(140.98, 27.75)	-9.3 ± 0.4	2.5	9.1	286	3.2
8	(140.45, 27.72)	-18.3 ± 0.6	2.8	5.0	236	2.1
9	(140.66, 31.21)	-16.2 ± 0.6	2.0	4.3	182	2.4
10	(139.44, 33.08)	-13.3 ± 0.5	1.8	5.4	166	3.2
11	(139.35, 28.50)	-16.9 ± 0.6	2.1	4.1	180	2.3
12	(139.39, 30.34)	-16.1 ± 0.7	2.6	4.1	200	2.0
13	(138.62, 31.61)	-10.2 ± 0.1	2.7	39.1	1120	3.5
14	(137.87, 33.34)	-25.3 ± 0.5	2.8	6.4	256	2.5
15	(137.72, 29.39)	-11.3 ± 0.7	2.7	3.4	160	2.1
16	(137.19, 30.21)	-17.1 ± 0.1	1.0	30.0	278	10.7
17	(137.15, 30.21)	-14.9 ± 0.1	2.8	56.5	1017	5.6
18	(135.88, 32.66)	-28.9 ± 0.6	2.7	4.4	192	2.3
19	(135.52, 30.84)	-11.5 ± 0.2	1.1	16.7	180	9.3
20	(135.24, 30.26)	-15.4 ± 0.2	2.5	23.6	937	2.5
21	(135.18, 31.29)	-34.3 ± 0.6	2.4	4.1	200	2.1
22	(134.99, 32.82)	-28.5 ± 0.6	2.8	5.2	204	2.5
23	(134.28, 31.36)	-16.0 ± 0.4	1.3	7.7	177	4.4
A	(137.49, 29.21)	-15.3 ± 0.7	2.3	3.4	191	1.8
B	(134.78, 27.47)	-52.7 ± 0.7	2.6	2.6	177	1.5
C	(133.70, 29.03)	-16.8 ± 0.7	2.8	3.8	223	1.7
D	(133.37, 27.89)	-9.3 ± 0.7	2.6	3.0	196	1.5

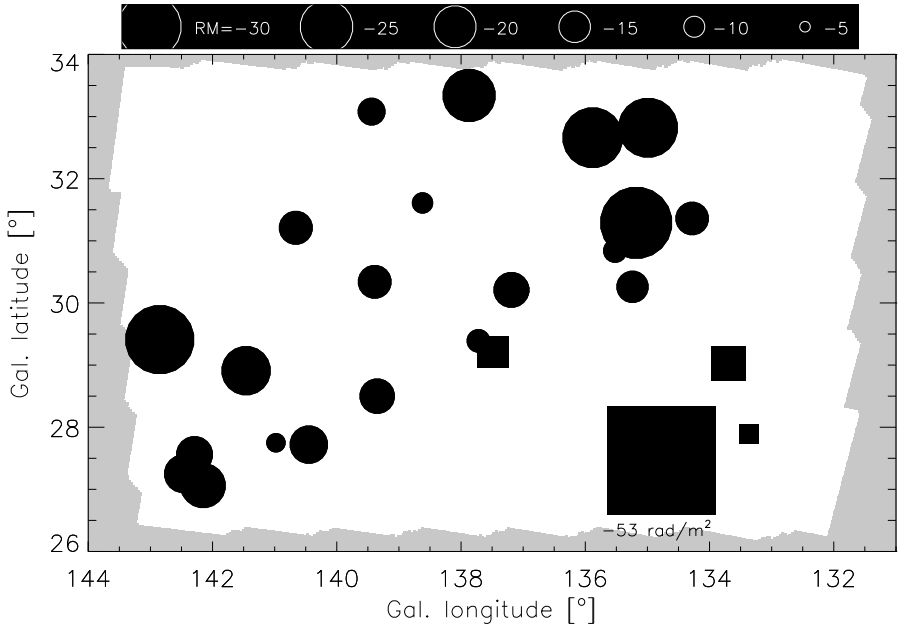

Figure 6.7 — RM distribution for the polarized point sources from table 6.2. The size of the circles is proportional to the RM, shown in the scale on top of the figure in units of radians/m^2. Black circles indicate negative RM, and white circles indicate positive RM. $|\mathrm{RM}| \lesssim 4$ rad/m^2 are missing from this figure because of our selection criteria. We indicate the sources with polarization percentages between 1.5% and 2.0% by squares. We excluded the grey region when looking for polarized point sources, because here instrumental polarization levels are higher.

sources in Fig. 6.7 by squares. In Fig. 6.10 we plotted their $P(\mathcal{R})$, $P(\lambda^2)$ and $\Phi(\lambda^2)$, similarly to how we plotted the spectra in Fig. 6.8. Although we did not find many more sources by lowering the cut-off in polarization percentage, most of the sources that we did find have similar rotation measures to the sources we found earlier, and one 'new' sources had a strong negative rotation measure of approximately -53 radians /m^2. Most of the sources that we detected will be extragalactic in origin, instead of Galactic pulsars, because the former have a much higher surface density than the latter.

For an average RM of the extragalactic sources of -19 rad/m^2 (not including sources A to D) and an average Hα intensity from WHAM, using Eqn. 6.8 we find that the $\langle B_\parallel \rangle$ = -1.5 μG. This is comparable to the $B_{\mathrm{ref},\parallel}$ = -1.9 μG that we would expect for the regular magnetic field of the Galaxy (see Sect. 6.4, keeping in mind that there is a 25% error associated with the assumed 4 μG strength of the regular field).

6.7 Summary and conclusions

In this chapter we presented a Faraday tomography analysis of a data set towards (l, b) = (138°,30°) that we observed with the WSRT. The strongest diffuse emission in our data has Faraday depths between about -40 rad/m^2 and -10 rad/m^2, and at these Faraday depths it shows intricate structure on both large (degree) to small scales (of the size of the synthesized beam). We explain how we used the WHAM Hα intensities together with the Berkhuijsen et al. (2006) description of the ISM to determine

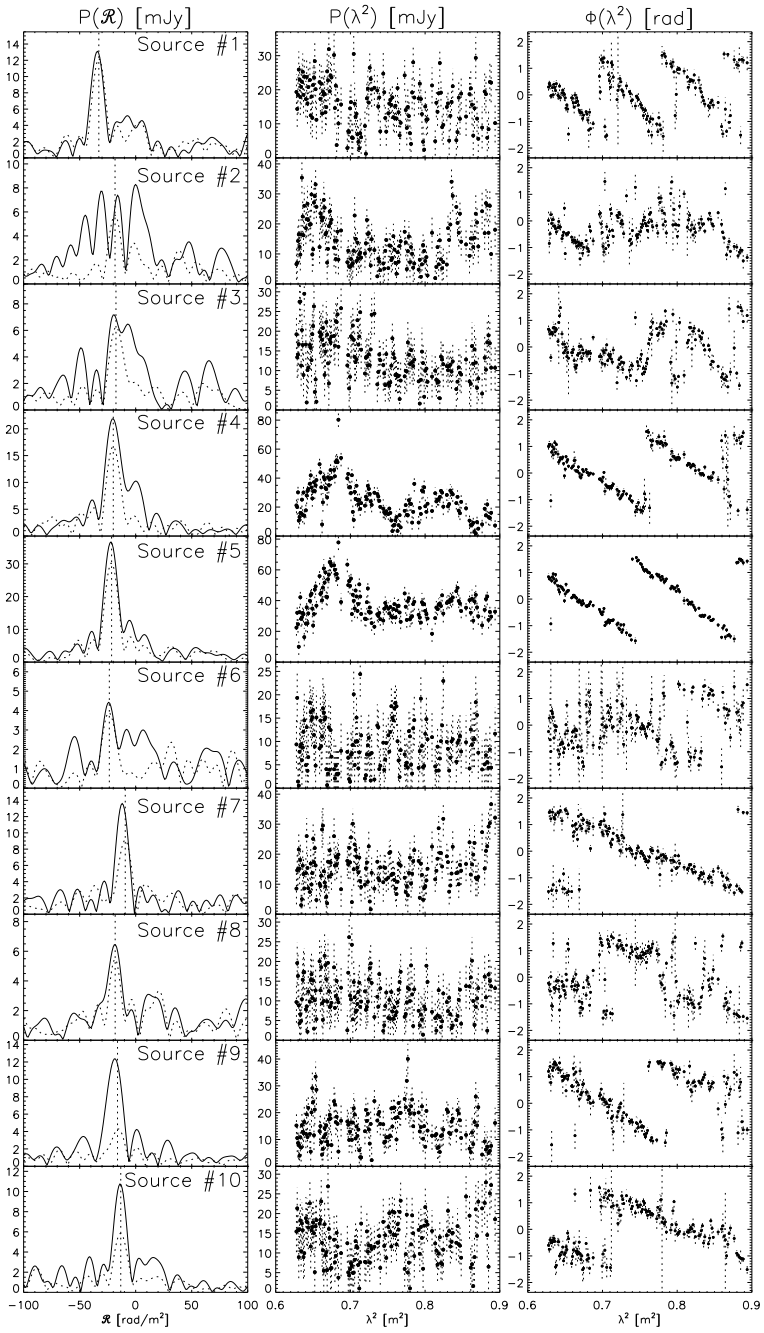

Figure 6.8 — $P(\mathcal{R})$ spectra for sources 1 – 12 from Table 6.2, for the short-baseline taper maps that we discuss in Sect. 6.3 (solid line) and the long-baseline taper maps where we only used baselines $>$ 250 m that we discuss in Sect. 6.6 (dotted line). The Faraday depths along the horizontal axis range from -100 rad/m^2 to +100 rad/m^2, and the flux densities plotted along the vertical axis are in mJy. The vertical dotted line indicates the RM that we fitted to the peak in the $P(\mathcal{R})$ spectrum of the long-baseline taper maps. The second and third columns show for each line-of-sight the polarized intensity [mJy] and polarization angle [rad] spectra from the short-baseline taper maps, for the observed wavelengths between 0.6 m^2 and 0.9 m^2. The $P(\mathcal{R})$ noise level is 0.3 mJy, and the $P(\lambda^2)$ noise level is 5.1 mJy. The spectra that are based on the low-resolution maps contain signals from both the diffuse emission and the extragalactic point sources. Since we excluded baselines $<$ 250 m from our high-resolution maps, we reduce the signal strength from the diffuse emission in the $P(\mathcal{R})$ spectra, but the signal strength from the point sources remains the same. This makes the $P(\mathcal{R})$ signal from the point source more prominent.

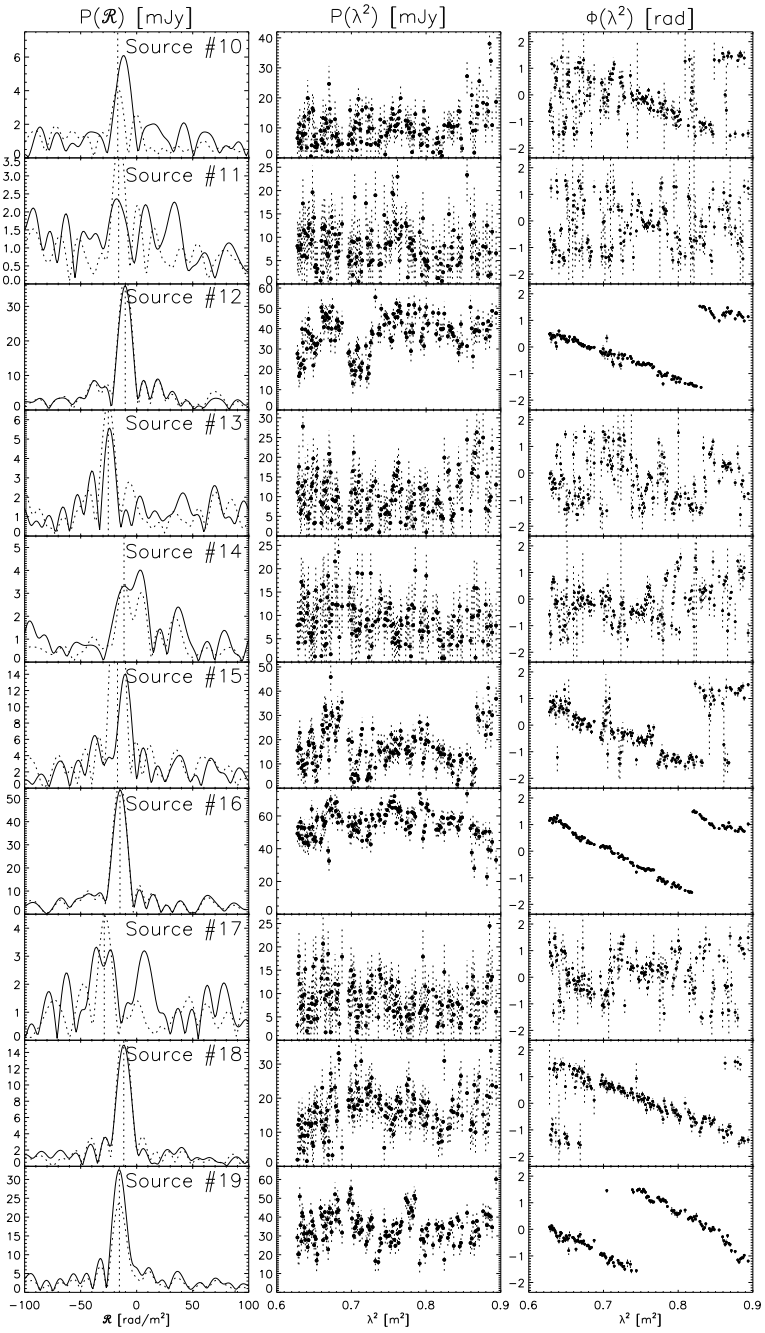

Figure 6.9 — Identical to Fig. 6.8, but for sources 13 – 23 from table 6.2.

the average magnetic field strength that is needed to explain the Faraday depths of the strongest diffuse emission that we see. We find a typical value of $\langle B_{\parallel} \rangle$ = -2.2μG in our mosaic, which is close to the -1.9 μG we would expect to find for the large-scale field in the Milky Way in the direction of CAM. We illustrate the richness and diversity of the structures in the $P(\mathcal{R})$ spectra in CAM by showing a grid of $P(\mathcal{R})$ spectra for 10 $\times$ 14 lines-of-sight. Not only do we see lines-of-sight that are dominated by one peak, these form actually only a minority of lines-of-sight, but we see also lines-of-sight with multiple peaks in their $P(\mathcal{R})$ spectra, and even $\mathcal{R}$-extended structures. This underlines that Faraday tomography promises to be an interesting resource for future

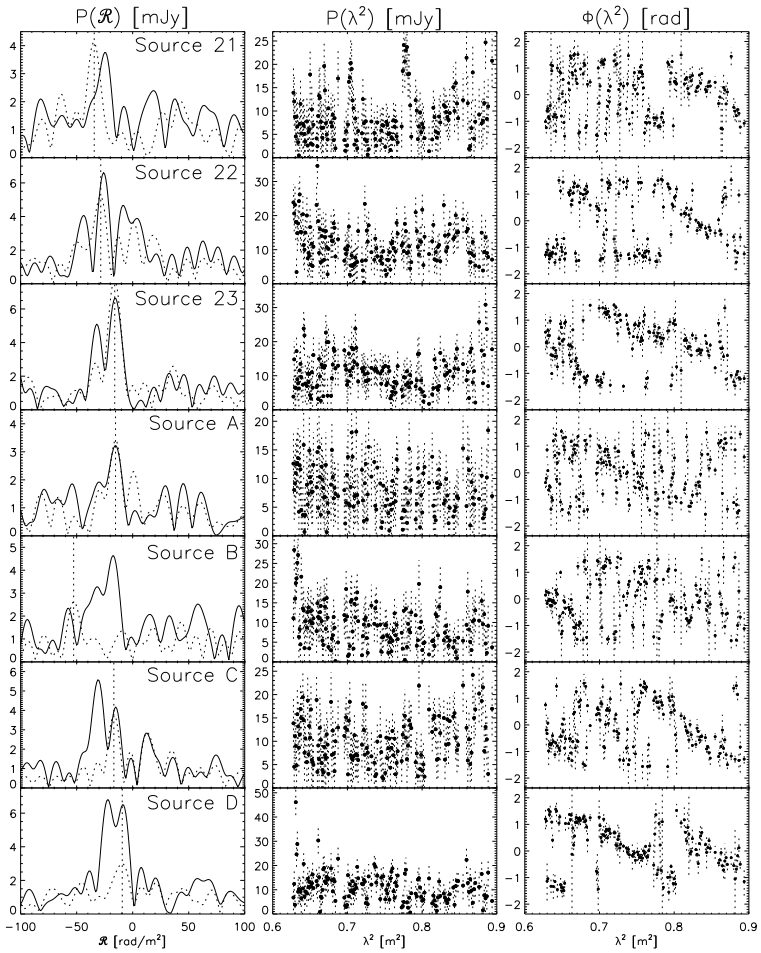

Figure 6.10 — Identical to Fig. 6.8 for sources 21 – 23, and for sources A – D from table 6.2. Sources A – D that we plot in this figure have polarization percentages between 1.5% and 2%, contrary to the sources that we plotted in Figs. 6.8 and 6.9, that have polarization percentages $> 2\%$.

modeling of Faraday rotation and synchrotron emission in the Galactic ISM. One must be careful not to over interpret these spectra since they were calculated from maps of the sky that were observed with an interferometer, and therefore lack extended structure. For a subset of 10 lines-of-sight we also present $P(\lambda^2)$ and $\Phi(\lambda^2)$ spectra to show that the $P(\mathcal{R})$ spectra are not produced by noise or by instrumental artefacts. Finally, we discuss how we detected 23 polarized sources in our data set. The average rotation measure of these sources is -19 rad/m^2, which is close to the -28 rad/m^2 we find for the average Faraday depth of the strongest diffuse emission in CAM. In the GEMINI data set towards (l, b) = (181°,20°) we also found a good agreement between the Faraday depths of the diffuse emission and the rotation measures of the extragalactic sources. This was however not the case for our CEPHEUS and TRIANGULUM data sets (towards (l, b) = (102°,15°) and (l, b) = (137°,-23°) respectively): in CEPHEUS most of the extragalactic sources had a rotation measure of opposite sign to the Faraday depths of the strongest diffuse emission (over most of the mosaic), and in TRIANGULUM the average rotation measure of the extragalactic sources was about 4 times as large as the average Faraday depth of the diffuse emission. For the CEPHEUS and TRIANGULUM mosaic we concluded that the diffuse emission that we observe comes only from a rel-

atively nearby part of the line-of-sight through the Galaxy towards the extragalactic sources. In chapter 9 we will combine the properties of our 4 data sets in the second Galactic quadrant to see what we can learn about structure in the Galactic magnetic field and of the diffuse ISM in this part of the Milky Way.

Acknowledgements

The Westerbork Synthesis Radio Telescope is operated by the Netherlands Foundation for Research in Astronomy (NFRA) with financial support from the Netherlands Organization for Scientific Research (NWO). The Wisconsin H-Alpha Mapper is funded by the National Science Foundation.

Chapter 7

Faraday tomography of an MHD-simulated volume of Galactic ISM

Abstract. We apply Faraday tomography to an MHD simulation of the Galactic ISM, to understand how the properties of the ISM are encoded in the $P(\mathcal{R})$ spectra. The dimensionless electron densities and physical cell sizes from our MHD cube were scaled by combining emission measures from the WHAM survey in the direction of our 4 WSRT data sets with the relation between emission measures and dispersion measures that Berkhuijsen et al. derived from a sample of 157 Galactic pulsars. We used the synchrotron emissivities from the model by Beuermann et al. to scale the magnetic field strengths. Our results do not strongly depend on whether we use a uniform cosmic ray distribution, or a distribution that assumes energy equipartition between the magnetic fields and the cosmic rays. Our MHD cube appears to be more structured than the Galactic ISM, and we find that the length of the line-of-sight required to build up the observed emission measures is shorter than the line-of-sight required to produce the observed synchrotron brightness temperature by a factor of three. This can also be a consequence of the MHD cube containing more structure than the Galactic ISM. However, the Faraday depths and heights of the strongest peak in the $P(\mathcal{R})$ spectra that we calculate for the MHD cube are similar to what we observe in our WSRT data sets. Peaks in the $P(\mathcal{R})$ spectrum at large Faraday depths are in most cases produced by a strong gradient in Faraday depth along the line-of-sight. In most cases these large gradients are produced by localized enhancements of the thermal electron density, and less frequently by strong line-of-sight components of the magnetic field. Most of the broad structures in the Faraday depth spectra are produced by two narrow peaks, and only in a small fraction of the cases they are the result of Faraday rotation and synchrotron emission occurring in the same part of the line-of-sight. However, because of the wide rotation measure spread function (the equivalent of the PSF in synthesis imaging) of our simulations we can only resolve synchrotron-emitting regions that also build up a large Faraday depth.

D. H. F. M. Schnitzeler, F. Heitsch, P. Katgert and M. Haverkorn

7.1 Introduction

FARADAY tomography is a novel technique with which we can study the distributions of Faraday rotation and synchrotron emission along the line-of-sight. Having information also in the depth dimension means a big improvement on studies where we can only get information on the line-of-sight as a whole. The goal of the current chapter is to apply Faraday tomography to an MHD simulation of the Galactic ISM, to better understand how we can interpret real observations in terms of the physical properties of the ISM. Since we can calculate which Faraday depth spectra are produced by which physical features in the MHD cube, we can also learn more about how to interpret the Faraday depth spectra that we obtained for 4 WSRT data sets that we observed in the second Galactic quadrant.

Faraday tomography was first described by Brentjens & De Bruyn (2005), and here we summarize how it works. Linearly polarized radiation that is emitted at a certain point along the line-of-sight will get Faraday rotated between the point of emission and the observer. If we write the polarization vector as a complex quantity, with Stokes Q and U as its real and imaginary components, then we can express the amount of Faraday rotation in the foreground as a complex exponential:

$$\vec{P}(\lambda) \;=\; Q(\lambda) + \mathrm{i}U(\lambda) \;=\; P(\lambda, \mathcal{R} = 0)\, \mathrm{e}^{2\mathrm{i}\mathcal{R}(\mathrm{x})\lambda^2} \tag{7.1}$$

where the Faraday depth $\mathcal{R}$ of the emission indicates the amount of Faraday rotation between the source and the observer:

$$\mathcal{R}(x)\,[\mathrm{rad/m^2}] \;=\; 0.81 \int_{\text{source at 'x'}}^{\text{observer}} n_e\,[\mathrm{cm^{-3}}]\; \vec{B}\,[\mu\mathrm{G}] \cdot \mathrm{d}\vec{l}\,[\mathrm{pc}] \tag{7.2}$$

Summing over all points along the line-of-sight, the observed complex polarization vector can be written as

$$\vec{P}(\lambda) \;=\; \int_0^\infty \vec{P}(\mathrm{x})\, \mathrm{e}^{2\mathrm{i}\mathcal{R}(\mathrm{x})\lambda^2} \mathrm{dx} \;=\; \int_{-\infty}^{\infty} \vec{P}(\mathcal{R})\, \mathrm{e}^{2\mathrm{i}\mathcal{R}\lambda^2} \mathrm{d}\mathcal{R} \tag{7.3}$$

where the first integral is over physical distance 'x', and the second integral is over all Faraday depths. We distinguish between the Faraday depth $\mathcal{R}$ and the rotation measure RM, which is the derivative of the polarization angle with respect to λ^2. If there is only one source along the line-of-sight, $\mathcal{R}$ = RM, but for more complex cases this equality no longer holds (see e.g. also Sokoloff et al. 1998).

The crucial point in Faraday tomography is realizing that Eqn. 7.3 can be inverted, similarly to a Fourier transform.

This gives us the polarization vector at Faraday depth $\mathcal{R}$:

$$\vec{P}(\mathcal{R}) = K \int_{-\infty}^{\infty} \vec{P}(\lambda^2)\, \mathrm{e}^{-2\mathrm{i}\mathcal{R}\lambda^2} \mathrm{d}\lambda^2 \tag{7.4}$$

$$K = \left(\int_{-\infty}^{\infty} W(\lambda^2)\, \mathrm{d}\lambda^2 \right)^{-1} \tag{7.5}$$

$W(\lambda^2) = 1$ for observed wavelengths, and = 0 elsewhere. The K factor in Eqn. 7.5 takes care of the correct normalization of $P(\mathcal{R})$. By observing polarization vectors over a large number of narrow frequency channels, we can apply Eqn. 7.4 to determine the strength and orientation of the polarization vector at Faraday depth $\mathcal{R}$! If the measured $P(\lambda^2)$ are in K (mJy/beam), then also the $P(\mathcal{R})$ will be in K (mJy/beam), or, more precisely, in K/RMSF width (mJy/beam/RMSF width). If we want to compare different data sets, with different RMSFs, it is necessary to convert this quantity to K/rad/m^2 instead of K/RMSF (equivalently for mJy/rad/m^2). Here we only consider one dataset, and we did not convert the measured $P(\mathcal{R})$ to K/rad/m^2.

Unfortunately, Faraday depth and physical depth may be related in a complicated way. This is because reversals in the direction of the magnetic field map the same Faraday depth to different physical depths. To determine the polarization vector as a function of physical depth we therefore need to make assumptions on the magnetic field geometry, and on the distribution of Faraday rotating electrons.

De Bruyn & Brentjens (2005) used Faraday tomography to study Faraday rotation and synchrotron emission in the Perseus cluster. Bower et al. (1999) used a Fourier analysis technique that closely resembles Faraday tomography to study the Faraday depth of Sgr A*. We obtained 4 WSRT data sets in different parts of the second Galactic quadrant that we reduced and analysed using Faraday tomography. These data sets and their analyses are discussed in chapters 2 – 6. The central coordinates of these data sets are given in the second column of Table 7.1, and each data set covers an area of about $10^\circ \times 10^\circ$. We refer to each data set after their parent constellation: GEMINI ('GEM'), CEPHEUS ('CEP'), TRIANGULUM ('TRI') and CAMELOPARDALIS ('CAM'). Our data cover the frequency range between about 315 – 380 MHz with between 150 and 200 frequency channels, depending on the data set, that each are 0.4 MHz wide.

In this chapter we will use similar parameters to construct a 'mock' data set from our MHD simulations. By applying the tools of Faraday tomography to this simulated data set, we hope to learn how the observed $P(\mathcal{R})$ spectra are produced by the magnetic fields and electron densities in the MHD cube. We can then better understand how we should interpret the $P(\mathcal{R})$ spectra of our real data sets.

Throughout this chapter we will frequently use the scale factors that we determined for our GEM data set. We chose this data set because it has the best λ^2 coverage of all our data sets, has comparable noise levels to the other data sets, and its scale factors are close to the averages of the scale factors of the other data sets (if we exclude our

CEPHEUS mosaic because its EM can be influenced by the nearby CEP OB2 association). Note that we do not try to reproduce the GEM observations with our simulations. By applying the GEM scaling parameters we intend to produce a volume of Galactic ISM, which is similar, but not identical in detail, to the data cubes that we observed.

In Sect. 7.2 we summarize how the MHD cube that we use in our analysis was constructed. These simulations provide dimensionless electron densities and magnetic field strengths. In Sect. 7.3 we describe how we used emission measures from the WHAM survey to scale the electron densities in our simulations and the physical size the cube. In this scaling we used the relation between the emission measure and dispersion measure that Berkhuijsen et al. (2006) derived for a sample of 157 Galactic pulsars at $|b| > 5^\circ$. We scaled the magnetic field strengths from our simulations by requiring that the MHD cube should produce the same brightness temperature per unit line-of-sight as predicted by the model of Beuermann et al. (1985) in the vicinity of the sun. We do however find a factor of 3 difference in the length of the line-of-sight needed to build up the observed emission measures and brightness temperatures, which could be an indication that the MHD simulations contain more structure than the Galactic ISM. In Sect. 7.4 we analyse our simulations in an identical fashion to how we analysed our 4 WSRT data sets, described in chapters 2 – 7. The heights and Faraday depths of the strongest peak in the Faraday depth spectra that we calculate are very comparable to what we find in our WSRT data sets. In Sect. 7.5 we present our conclusions on how peaks in the Faraday depth spectra can arise at large Faraday depths, and on how resolved features in the Faraday depth spectra are produced.

7.2 Numerical model

The 'observational' domain is derived from a periodic-box simulation of the turbulent magnetized ISM (Heitsch et al. 2001), at a resolution of 256^3 grid cells. The electron density and the magnetic field strength are rescaled to the values for the warm ISM (see Sect. 7.3). The initially uniform density and magnetic field are perturbed by a fixed velocity field. As described by Mac Low (1999), the velocity field is generated in Fourier space, assigning each wavenumber k an amplitude, populating only the wavenumbers $1 \leq k \leq 2$. The phases are chosen randomly. An inverse Fourier transform then gives the three spatial components of the velocity. At each time step, this velocity field is added to the velocities in the domain such that the energy input rate is constant with time. This driving mechanism is meant to mimic energy input on the largest scales by physical processes such as supernova shock fronts or Galactic shear.

We use a snapshot of the simulation at a time when the full turbulent cascade has developed and a steady state between energy input on the largest scales and numerical dissipation on the smallest scales has been reached. This steady state corresponds to a Mach number of $\mathcal{M} \approx 10$. This is more than the values usually assumed for the warm ISM (namely $\mathcal{M} \approx 1$), thus rendering the turbulence more compressible than intended for this work. However, the turbulent cascade in these types of models does not differ substantially from a Kolmogorov slope of $-5/3$ (see e.g. Cho et al. 2003), so that we can rescale the densities and field strengths to values appropriate for the warm ISM while keeping the spectral distribution of the perturbations.

As we will discuss later on in this chapter, the simulated ISM volume tends to be more structured than the Galactic ISM. This is mainly because (a) at the higher Mach numbers, the turbulence will be more compressive in the model, and (b) the continuous turbulent driving will lead to volume-filling turbulence without allowing for regions of low turbulence. It is not obvious that turbulence in volume-filling in the Galactic ISM.

7.3 Scaling the model to the observations

Before we can apply Faraday tomography to the MHD datacube, we have to find the correct scales for the density of the Faraday rotating electrons $\mathrm{n_e}$, physical cell size Δl, and the magnetic field strength B. After rescaling, the MHD cube should reproduce the observed GEM dispersion measure DM and emission measure EM, which sets the scale for $\mathrm{n_e}$ and Δl. In Sect. 7.3.1 we discuss how we found these parameters. Crucial in this is the assumption that DM and EM are produced by the same electrons, which, according to Heiles (2001), is not necessarily always the case. In Sect. 7.3.2 we show how we can use the average synchrotron emissivity observed towards GEM to find the correct scale for B. Because the synchrotron emissivity depends on the distribution of cosmic rays, we present results for a uniform cosmic ray distribution and for a distribution where the energy densities of the cosmic rays and in the magnetic fields are in equipartition. For the results that we present in Sects. 7.3.1 and 7.3.2 we have assumed that the MHD cube produces all the observed DM, EM and synchrotron brightness temperature T_b.

7.3.1 Scaling of $\mathrm{n_e}$ and the linear cell size Δl

The dispersion measure DM and emission measure EM are defined as $\mathrm{DM} = \int_0^\infty n_\mathrm{e} \mathrm{d}l$ and $\mathrm{EM} = \int_0^\infty n_\mathrm{e}^2 \mathrm{d}l$, the line-of-sight integrals of the electron density n_e and electron density squared. $[\mathrm{DM}] = \mathrm{cm^{-3}pc}$, $[\mathrm{EM}] = \mathrm{cm^{-6}pc}$, $[n_\mathrm{e}] = \mathrm{cm^{-3}}$ and $[\mathrm{d}l] = \mathrm{pc}$. Because DM and EM depend in different ways on the electron density and the length of the line-of-sight, it is possible to solve for the two variables (electron density scale factor $n_\mathrm{e\_scale}$ and linear cell size Δl) in terms of the two observables DM and EM. We assume that the MHD cube produces all the observed DM and EM, and that the DM and EM are created by the same electrons. Writing the electron density in cell i as $n_\mathrm{e,i}[\mathrm{cm^{-3}}] = n_\mathrm{e\_scale}[\mathrm{cm^{-3}}] \times f_\mathrm{i}$, where f_i are the dimensionless values from the simulations, denoting the sum over all cells by 'total', and indicating by brackets the averages over the 3 x = 0, y = 0 and z = 0 planes of the simulated cube, it follows that

$$n_\mathrm{e\_scale} = \frac{\langle \mathrm{EM} \rangle}{\langle \mathrm{DM} \rangle} \frac{\mathrm{total}(f_\mathrm{i})}{\mathrm{total}(f_\mathrm{i}^2)} \tag{7.6}$$

$$\Delta l = \frac{1}{n_\mathrm{e\_scale}^2} \frac{\langle \mathrm{EM} \rangle}{\frac{1}{256^2}\mathrm{total}(f_\mathrm{i}^2)} \tag{7.7}$$

Table 7.1 — Characteristics of the 4 WSRT data sets that we analysed using Faraday tomography, and the physical properties that we derive for each data set after rescaling. $\langle \mathrm{EM} \rangle$ is the average emission measure that we derive from the WHAM Hα intensities. $\langle n_{\mathrm{e\_scale}} \rangle$ and Δl are the average electron density and linear cell size that we find using Eqns. 7.7 and 7.10 for scaling the MHD simulations. We also indicate the total linear dimension of the cube in parsec. We derived the magnetic field scale factor from the Beuermann et al. (1985) Galactic synchrotron emissivity model in the direction of each mosaic ('T_b/kpc'), and by assuming either a uniform cosmic ray (CR) density ('uniform CR'), or a cosmic ray density that is in energy equipartition with the magnetic field energy density ('equip. CR')

Mosaic	(l, b)	$\langle \mathrm{EM} \rangle$	$\langle n_\mathrm{e} \rangle$	Δl	linear cube dimension	T_b/kpc	$\langle B_\mathrm{tot} \rangle$ uniform CR/ equip. CR
		[cm^{-6}pc]	[cm^{-3}]	[pc]	[pc]	[K/kpc]	[μG]
GEM	(181°, 20°)	4.68	3.4×10^{-2}	2.9	730	11	5.2/ 4.4
CEP[a]	(102°, 15°)	35.85	6.5×10^{-2}	6.0	1520	12	5.3/4.5
		(11.25)	(4.5×10^{-2})	(3.9)	(1000)	(12)	(5.3/4.5)
TRI	(137°, -23°)	10.24	4.3×10^{-2}	3.8	970	11	5.1/4.4
CAM	(138°, 30°)	2.39	2.7×10^{-2}	2.2	570	10	4.9/4.3

[a] The WHAM Hα intensities in CEPHEUS are possibly influenced by the HII regions associated with the CEP OB2 cluster that lies in the same Galactic longitude range as CEPHEUS, but at lower Galactic latitudes. For this mosaic we therefore also list in parentheses the values that we would have found if we would have used E(B-V) = 0.

The factor of $\frac{1}{256^2}$ comes from averaging over all 256^2 lines-of-sight through one cube face. Note that the average DM or EM calculated from the simulations is the same over all three cube faces.

Now we have to find values for the observed DM and EM in the regions we mosaicked with the WSRT. We can derive the average EM for each of our data sets from the WHAM survey (Haffner et al. 2003). To convert the Hα intensities from WHAM to EM we can use Eqn. 1 from Haffner et al. (1998):

$$\mathrm{EM} \;=\; 2.75 T_4^{0.9}\; I_{\mathrm{H}\alpha}(\mathrm{R})\; \mathrm{e}^{2.2\;\mathrm{E(B-V)}} \tag{7.8}$$

where T_4 is the temperature of the warm ionized medium in units of 10^4 K, which is typically 0.8 (Reynolds 1985), and $I_{\mathrm{H}\alpha}$ is the Hα intensity in Rayleigh. To find the amount of interstellar B-V reddening, E(B-V), we used NED's extinction calculator[1], that in turn is based on Schlegel et al. (1998). Note that the E(B-V) we use are reddening corrections for the entire line-of-sight through the Galaxy.

The warm ionised medium (WIM) that we model is not the only ISM phase with free electrons that can Faraday rotate, also the hot intercloud medium (HIM) contains (relativistic) charged particles. Snowden et al. (1997) modeled the density of relativistic electrons in the Galactic midplane from diffuse ROSAT X-ray data, and concluded that

[1] `http://nedwww.ipac.caltech.edu/forms/calculator.html`

this density is about a factor of 10 smaller than the electron density in the WIM. We therefore neglect the HIM contribution to the Faraday depth, DM and EM.

Since we do not have observed DM available, we need to assume a model to calculate DM from the EM we derived from the WHAM survey. Berkhuijsen et al. (2006 - which we will refer to as 'BMM') determined the following relation between DM and EM for a sample of 157 Galactic pulsars with $|b| > 5^\circ$:

$$\mathrm{EM} \;=\; 0.042 \pm 0.014 \; \mathrm{DM}^{1.47 \pm 0.09} \tag{7.9}$$

For their sample of pulsars with known DM they took the EM from the WHAM survey, and corrected these for emission coming from beyond the pulsar, as well as interstellar reddening occurring in front of the pulsar. Using Eqn. 7.9 we can rewrite Eqn. 7.6 to:

$$n_{\mathrm{e\_scale}} \;=\; 0.1157 \, \langle \mathrm{EM} \rangle^{0.32} \frac{\mathrm{total}(f_\mathrm{i})}{\mathrm{total}(f_\mathrm{i}^2)} \tag{7.10}$$

The scatter in the EM/DM relation for the BMM pulsar datapoints means that for each EM there is about a 30% uncertainty in DM. The main advantage of using the BMM model over the electron density models by for example Reynolds (1991) or by Cordes & Lazio (2003) is that the former is only based on 4 lines-of-sight towards pulsars in high Galactic latitude globular clusters. The Cordes & Lazio model is based on many more lines-of-sight, but they model the Galaxy as a smooth structure consisting of spiral arms, and a thin and thick disks. Locally they enhance or decrease the electron density to account for anomalous pulsar DM. We expect however, that with BMM's statistical description of the ISM, in combination with the WHAM Hα intensities that have been measured for the northern sky on a $\sim 1^\circ \times 1^\circ$ grid, we can more accurately reproduce small-scale structure in DM.

Since Hα emission can originate at any point along the line-of-sight, we overestimate EM if we use the E(B-V) correction factor for the entire line-of-sight. Eqns. 7.7 and 7.10 show that we will also overestimate the electron densities and physical size of the MHD cube.

In Fig. 7.1 we plot the EM/DM ratio for lines-of-sight through the 3 cube faces of the MHD simulations. In the left panel we used the BMM relation between EM and DM (Eqn. 7.9) to find the scale factors $n_{\mathrm{e\_scale}}$ and Δl. In the right panel we calculated DM from EM by using the Reynolds model or the Cordes& Lazio model; both predict the same DM in the direction of GEM. To find the distance out to which we had to integrate the Cordes&Lazio model we calculated with the Reynolds model the length of the line-of-sight that is required to build up the Hα intensities observed with WHAM towards GEM. In the left panel we also plotted the EM/DM relation that BMM observed (Eqn. 7.9) as a solid line. The dashed line in the right panel is the EM/DM relation from the Reynolds model. The scatter plot of the MHD lines-of-sight does clearly not agree exactly with the DM/EM relation found by BMM (the solid line). However, if we use the Reynolds model or the Cordes & Lazio model in the direction of GEM to determine $n_{\mathrm{e\_scale}}$ and Δl, the agreement between the point cloud for the lines-of-sight through the

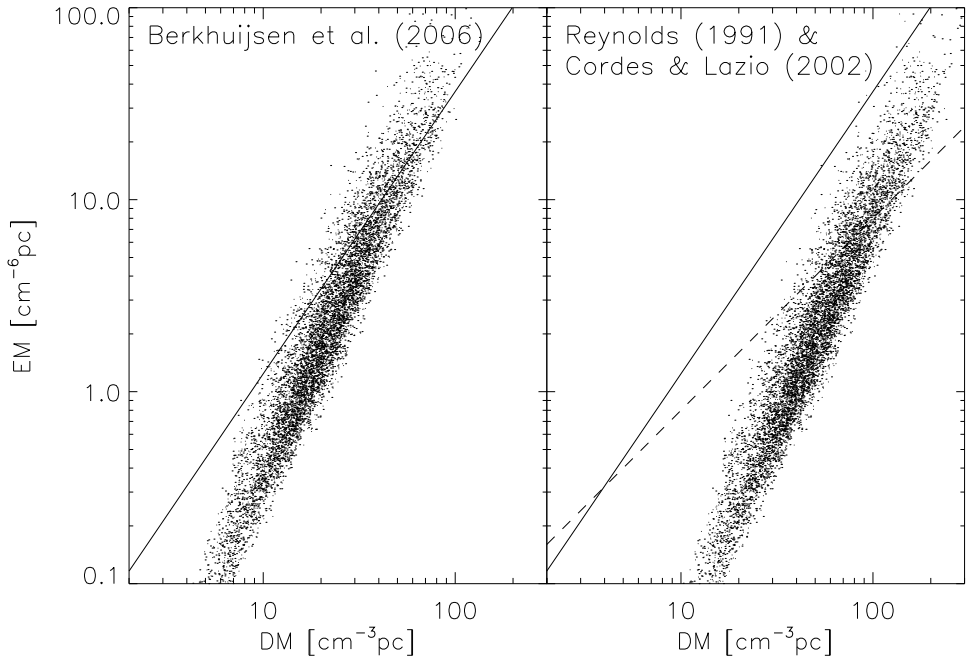

Figure 7.1 — Plots of the emission measure EM versus the dispersion measure DM for lines-of-sight through the x = 0, y = 0 and z = 0 MHD cube faces, where we used the GEM EM and Eqns. 7.7 and 7.10 to determine the scale factors $n_{\mathrm{e\_scale}}$ and Δl. Only one in every 5×5 lines-of-sight is plotted as a dot. In the left panel we used the model by BMM to calculate dispersion measures DM from emission measures EM, and in the right panel we used the models by Reynolds and by Cordes & Lazio (2003). The solid line indicates the EM/DM relation that Berkhuijsen et al. (2006) found (Eqn. 7.9), and the dashed line in the right panel is the EM/DM relation from the (1991) model. The Cordes & Lazio and Reynolds models predict the same DM from the GEM EM, in the direction of GEM.

MHD cube and the EM/DM relation for the Reynolds model (the dashed line) is very much worse. We can shift the point cloud by choosing different $n_{\mathrm{e\_scale}}$ and Δl, but then we would change the EM/DM ratio of the lines-of-sight in the cube, and we would no longer be consistent with the EM/DM predicted by Eqn. 7.9 or by the Reynolds model, or by the Cordes & Lazio model in the direction of GEM. The difference between the solid and dashed lines, and therefore also between these lines and the point cloud of simulated lines-of-sight, reflects a difference in structure of the ISM in each of these models. Our MHD simulations seem to agree best with the relation between EM and DM that BMM found.

In the top panel of Fig. 7.2 we plot the distribution of the simulated electron densities after rescaling. In this example we used the $\langle \mathrm{EM} \rangle$ from the GEM mosaic. The electron density distribution satisfies a power law with index $\approx$ -12. The average electron density is 0.034 cm^{-3}. For comparison, the Reynolds model contains clumps of electrons with density 0.08 cm^{-3}, and a filling factor of 40%, which implies an average of 0.032 cm^{-3} per cell. The Cordes & Lazio model has an average electron density of 0.03 cm^{-3} in the direction of GEM. The Δl that we find is 3 pc, implying that the MHD cube has a total depth of 730 pc.

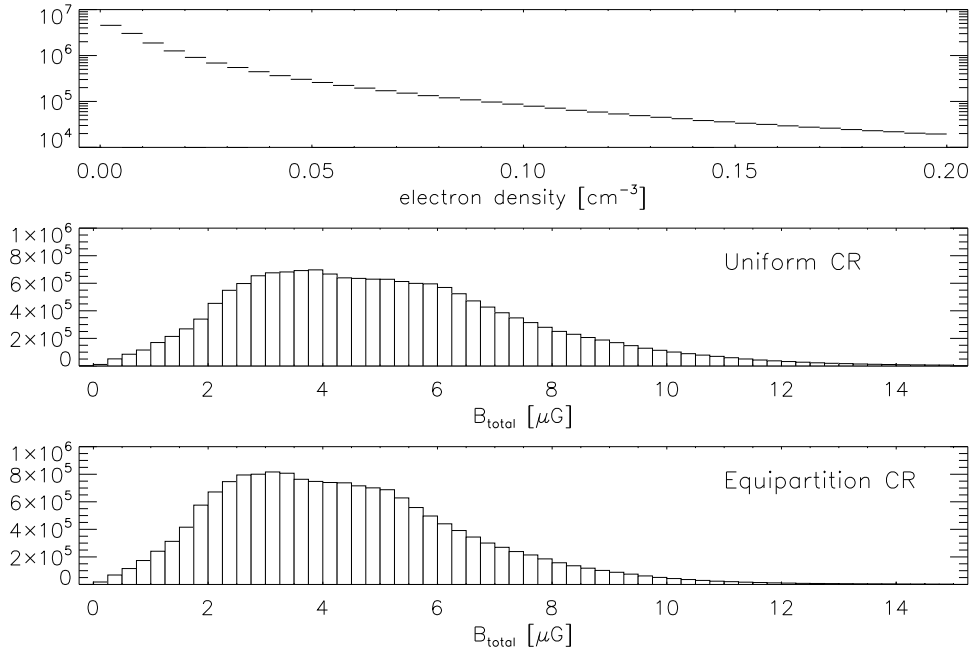

Figure 7.2 — Distribution of electron densities [cm^{-3} (top panel) and strength of the total magnetic field [μG] (middle and lower panels) of our MHD simulations after we rescaled the values in the model to match the GEM observations. For the middle panel we assumed a uniform cosmic ray ('CR') distribution in the MHD cube, and for the bottom we assumed energy equipartition between the magnetic field and cosmic rays.

7.3.2 Scaling of B

To find the correct scaling for the magnetic field, the MHD cube should produce the same amount of synchrotron emission per unit line-of-sight as the model by Beuermann et al. (1985), which we will refer to as 'B85' in the rest of the text. The advantage of scaling the magnetic field strengths from the MHD cube to the amount of Kelvin per unit line-of-sight, and not to the absolute amount of Kelvin, is that the amount of Kelvin emitted per unit line-of-sight does not depend on the physical size of each cell. We therefore do not have to make assumptions on the relative sizes of the synchrotron-emitting and WHAM lines-of-sight. Beuermann et al. indicate that in the second Galactic quadrant at $b = 0^\circ$ about 11 K of synchrotron radiation is emitted (at 408 MHz) within 1 kpc of the sun. Since the linear dimension of our MHD cube is not much larger than this for the each of our data sets (see Table 7.1), we do not have to integrate beyond 1 kpc, where the Beuermann model becomes much more complicated because of the spiral arms (see Fig. 8 in B85).

One complication is that we observe outside the Galactic plane, whereas the 11 K/kpc is valid for the Galactic plane. We introduce $\bar{\epsilon}$ as a shorthand for the number of Kelvin synchrotron radiation emitted per kpc. In the B85 model, the synchrotron emissivity at height z above the Galactic plane consists of a contribution from a thin disk plus a thick disk:

$$\bar{\epsilon}(z) \;=\; \bar{\epsilon}_{0,\mathrm{thin}}\mathrm{sech}(\mathrm{z}/\mathrm{z}_{\mathrm{thin}}) + \bar{\epsilon}_{0,\mathrm{thick}}\mathrm{sech}(\mathrm{z}/\mathrm{z}_{\mathrm{thick}}) \tag{7.11}$$

where $\bar{\epsilon}_{0,\mathrm{thin}}$ and $\bar{\epsilon}_{0,\mathrm{thick}}$ are the amount of Kelvin emitted by the thin and thick synchrotron disks, and z_{thin} and z_{thick} are the scale heights of the thin and thick disks respectively. When calculating the synchrotron emissivity along a line-of-sight at a certain Galactic latitude, we need to take into account the different scale heights of the thin and thick disk. B85 do not specify $\bar{\epsilon}_{0,\mathrm{thin}}$ and $\bar{\epsilon}_{0,\mathrm{thick}}$ in the vicinity of the sun, so from Fig. 6a in B85 we read off their averages along Galactic longitude at the galactocentric radius of the sun of 10 kpc that B85 assume. This gives $\bar{\epsilon}_{0,\mathrm{thin}}$ = 3.5 K/kpc and $\bar{\epsilon}_{0,\mathrm{thick}}$ = 4 K/kpc. Note that these are averages over all Galactic longitudes along the solar circle. However, since these values are close to the $\bar{\epsilon} = \bar{\epsilon}_{0,\mathrm{thin}} + \bar{\epsilon}_{0,\mathrm{thick}}$=7 K/kpc that Beuermann et al. find in the vicinity of the sun, we adopt these values for $\bar{\epsilon}_{0,\mathrm{thin}}$ and $\bar{\epsilon}_{0,\mathrm{thick}}$ However, this is much lower than the 11 K/kpc that different authors observe to originate in front of optically thick HII regions (see references in B85), and also the brightness temperature at the Galactic poles is higher than can be explained by these $\bar{\epsilon}_{0,\mathrm{thin}}$ and $\bar{\epsilon}_{0,\mathrm{thick}}$. B85 therefore multiplied $\bar{\epsilon}_{0,\mathrm{thin}}$ and $\bar{\epsilon}_{0,\mathrm{thick}}$ by a factor of 1.5 to find $\bar{\epsilon}$ = 11 K/kpc. Finally, we need to correct for the updated galactocentric distance of the sun of 8 kpc (Groenewegen et al. 2008 and references therein) instead of the 10 kpc that B85 assume. We therefore find $\bar{\epsilon}_{0,\mathrm{thin}}$ = 6.6 K/kpc, $\bar{\epsilon}_{0,\mathrm{thick}}$ = 7.5 K/kpc and z_{thin} = 8/10×0.19 kpc = 0.15 kpc and z_{thick} = 8/10×1.8 kpc = 1.4 kpc for the half-equivalent widths of the thin and thick disks respectively.

Our MHD simulations do not include cosmic rays (CR). If we want to include synchrotron emission into the simulations, we need to prescribe how the CR densities are distributed throughout the simulated volume. We consider two possible CR distributions. In Sect. 7.3.2.1 we calculate synchrotron emissivities by combining a uniform CR density with our MHD simulations. Note that by 'uniform' we mean that the CR energy spectrum is the same everywhere, not that all CR have the same energy. In Sect. 7.3.2.2 we assume energy equipartition between CR and the magnetic field, which gives a CR density $\propto B^2$, and we discuss the differences with the uniform CR distribution. If the CR are uniformly distributed, they introduce no net pressure gradients. Also the emitted radiation is not re-absorbed at these frequencies: these would show up as deviations from a pure synchrotron spectrum, which in M33 are seen to become important at frequencies $\lesssim$ 200 – 300 MHz (Israel et al. 1992). At the frequencies of our simulations, the generated radiation does not interact with the plasma elsewhere in the simulated volume. We can therefore include a uniform CR distribution after running our simulations, and the end result will still be consistent with our CR-free simulations. On the other hand, for an equipartition CR distribution, the CR density will be higher in regions with larger total magnetic field strengths. This makes it more difficult to deform such regions compared to regions with lower magnetic field strengths, and this will play a role in the MHD dynamics in each step of the simulations. We consider such simulations as a future project, and for the moment we use the equipartition CR densities only after running our simulations.

7.3.2.1 Uniform CR density

Haverkorn et al. (2004a) showed in their Appendix B that the synchrotron volume emissivity at frequency ν, $P(\nu)$, for a cosmic ray energy spectrum $\propto$ energy^{-3} and with 2.9 10^{-5} CR particles m^{-3} GeV^2, is

$$P(\nu) \;=\; 4.2\,10^{-39}\frac{B_{\perp}[\mu\mathrm{G}]^2}{\nu[\mathrm{MHz}]}[\mathrm{Wm}^{-3}\mathrm{Hz}^{-1}] \tag{7.12}$$

By transforming to spherical coordinates, and integrating over the dθ and dϕ directions, the amount of Kelvin brightness temperature produced in an infinitesimal spherical volume element is

$$\mathrm{d}T \;=\; \frac{P(\nu)}{4\pi}\frac{1}{2k}\left(\frac{c}{\nu}\right)^2\mathrm{d}r \tag{7.13}$$

where $P(\nu)$ is given by Eqn. 7.12, k is Boltzmann's constant, c is the speed of light, and dr is the depth in meters of the volume element along the line-of-sight. By combining Eqns. 7.12 and 7.13 and replacing integrals with sums of values for each grid point from the MHD cube, filling in the constants and using the frequency of 408 MHz for which the Beuermann emissivities are given, and writing the magnetic field as $b \;=\; b_{\mathrm{scale}} \times g_{\mathrm{i}}$, where the g_{i} are the dimensionless magnetic field strengths that follow from our simulations, the $\bar{\epsilon}$ can be calculated for a single line-of-sight through the MHD cube from

$$T_{\mathrm{b}}[\mathrm{K}]/\mathrm{kpc} \;=\; 1.9\,10^{-3}b_{\mathrm{scale}}^2\sum_{l.o.s.} g_{\perp,\mathrm{i}}^2 \tag{7.14}$$

where $g_{\perp,\mathrm{i}}^2$ is for cell i the sum of the squares of the magnetic field components perpendicular to the line-of-sight. The WSRT beam is narrow enough so that along the line-of-sight through the MHD cube it sees always only one row of pixels. We then averaged the $\mathrm{T_b}$ over the x = 0 and y = 0 cube faces. We excluded the z = 0 cube face, because the MHD model starts out with a mean field along the z-axis, and the average $\mathrm{T_b}$ over the z = 0 face will then be systematically lower than the averages over the other cube faces (which is indeed visible in Fig. 7.4). We plot the distribution of magnetic field strengths that we find after scaling B in the bottom panel of Fig. 7.2. The average total magnetic field strength of this distribution is 5.1 μG. For comparison, the average total magnetic field strength in the vicinity of the sun is 6 ± 2 μG (Beck 2007a).

7.3.2.2 Equipartition CR density

In the case of (local) equipartition between the CR and magnetic field energy densities, the CR particle density scales with B^2 (Sect. 4.2 from Beck et al. 2003). To gauge this relation, we can use that in the solar neighborhood the CR particle spectrum with spectral index p is $n(E)\mathrm{d}E \;=\; 2.9 \times 10^{-5}E^{-p}\mathrm{d}E$ particles m^{-3} (Longair 1981). In the vicinity of the sun the total magnetic field is about 6 μG (Beck 2007a). Therefore, in the case of energy equipartition between CR and magnetic fields,
$n(E)\mathrm{d}E \;=\; 2.9 \times 10^{-5}(B/6.0\ \mu\mathrm{G})^2E^{-p}\mathrm{d}E$, and the equivalent of Eqn. 7.12 becomes

$$P(\nu) \;=\; 4.2\,10^{-39}\frac{B[\mu\mathrm{G}]^2}{6.0^2}\frac{B_{\perp}[\mu\mathrm{G}]^2}{\nu[\mathrm{MHz}]}[\mathrm{Wm}^{-3}\mathrm{Hz}^{-1}] \tag{7.15}$$

Also

$$T_{\rm b}[{\rm K}]/{\rm kpc} \;=\; 5.4\,10^{-5} b_{\rm scale}^4 \sum_{l.o.s.} g_{\rm total,i}^2\, g_{\perp,{\rm i}}^2 \tag{7.16}$$

where $g_{\rm total,i}^2$ is the square of the length of the full magnetic field vector at cell i. In the bottom panel of Fig. 7.2 we show the distribution of magnetic field strengths after rescaling with the equipartition CR densities. We again average brightness temperatures only over the x = 0 and y = 0 cube faces. The average total magnetic field strength in the case of energy equipartition between the CR and the field is 4.4 μG, i.e. only slightly lower than the average total magnetic field strength in the case of a uniform CR distribution, which was 5.1 μG.

7.3.3 Relative depths of the Faraday-rotating and synchrotron-emitting regions

The Haslam 408 MHz map (Haslam et al. 1982) shows a brightness temperature of 36 K in the direction of our GEM mosaic. The CMB contributes 2.7 K, and extragalactic sources about 25% of 36 K (based on Bridle et al. 1972), which means that about 24 K is generated in the Milky Way. To build up this brightness temperature requires a line-of-sight of at least 2.2 kpc, using the $\bar{\epsilon}$ = 11 K/kpc that the Beuermann et al. model generates in the direction of GEM. However, from the GEM EM and with the BMM model we derived that our MHD cube is only about 700 pc deep. This would then mean that there is a region in the Milky Way beyond the MHD cube where there is only synchrotron rotation, and no Faraday rotation.

As an extreme alternative, we could require that the entire 24 K synchrotron brightness temperature is generated within the cube. This would increase Δl by a factor of about 3. Since we still observe the same EM (assuming that there is no Hα emission that we miss due to extinction or scattering, that we did not correct for by using Eqn. 7.8), this means that $n_{\rm e\_scale}$ decreases. However, since EM and DM depend in different ways on $n_{\rm e}$ and Δl, it is now no longer possible to satisfy the EM/DM relation by BMM. It is therefore not possible to generate all the observed EM and synchrotron brightness temperature in the same simulated volume, and still be consistent with the EM/DM relation found by BMM. This could in part be due to how the MHD cube and the BMM ISM are structured; the left panel of Fig. 7.1 showed that our simulations probably have a different structure than BMM observe. In Sect. 7.2 we mentioned a number of reasons why the MHD cube could not be perfectly identical to the real ISM as seen by e.g. BMM. For now we choose to stick to reproducing the observed EM and have the MHD cube satisfy BMM's EM/DM relation, instead of producing all synchrotron emission in the MHD cube. The result of this is that our MHD cube generates only about 8 K synchrotron brightness temperature. If we assume that the synchrotron radiation is 70% polarized, this means that the MHD cube is illuminated from behind by about 0.7$\times$(24 K - 8 K) = 11 K polarized brightness temperature, which gets Faraday rotated when it passes the cube. This would show up as strong peaks in the $P(\mathcal{R})$ spectra at large RM, which is not what we observe in our data sets. However, in part this could also be due to the fact that we observed with an interferometer, which is not sensitive to extended structure on the sky. To correctly reproduce our observations, we

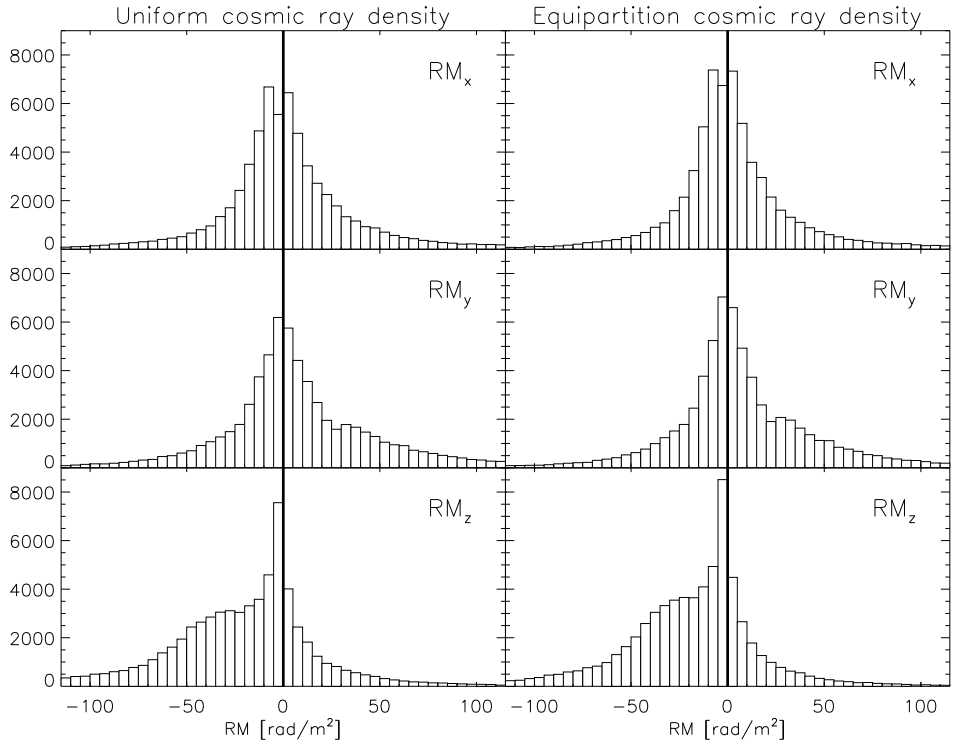

Figure 7.3 — Rotation measures through the x, y and z faces of the MHD cube, calculated by combining the scaled electron densities, cell size, and magnetic field strengths (assuming a uniform cosmic ray density in the left column, and a cosmic ray density that is in energy equipartition with the magnetic field in the right column).

would therefore have to filter out extended structures in our simulated maps of Stokes Q and U to see how we would detect the 20 K peak in the $P(\mathcal{R})$ spectra with the WSRT. Our results should therefore be taken with some caution, and be seen primarily as a demonstration of how we can better understand the results of Faraday tomography by using MHD simulations.

7.3.4 Results: rotation measures and synchrotron emissivities

By combining the $n_e, \Delta l$ and B from our simulations, we calculated the distribution of RM along the 3 cube axes, shown in the left column of Fig. 7.3. The RM distribution along the z-axis is wider, probably because this is the direction along which the magnetic field vectors are aligned at the start of the turbulent driving in the simulations.

In Fig. 7.4 we compare the $\bar{\epsilon}$ distributions for the x, y and z cube faces between the uniform CR distribution (top row of panels) and the equipartition CR distribution (bottom row of panels). Clearly the equipartition densities produces a broader $\bar{\epsilon}$ distribution, the average of each distribution however is nearly identical between the uniform and equipartition densities. By combining Δl with the B that we obtained from $\bar{\epsilon}$, we can calculate the total brightness temperature generated in each line-of-sight. The large spread in the $\bar{\epsilon}$ of the simulations produces a large range of observed brightness temperatures. However, the brightness temperatures that we calculated for the narrow WSRT beam will be averaged over the wider Haslam beam (FWHM = 0.85°), which will reduce the spread in the observed brightness temperatures.

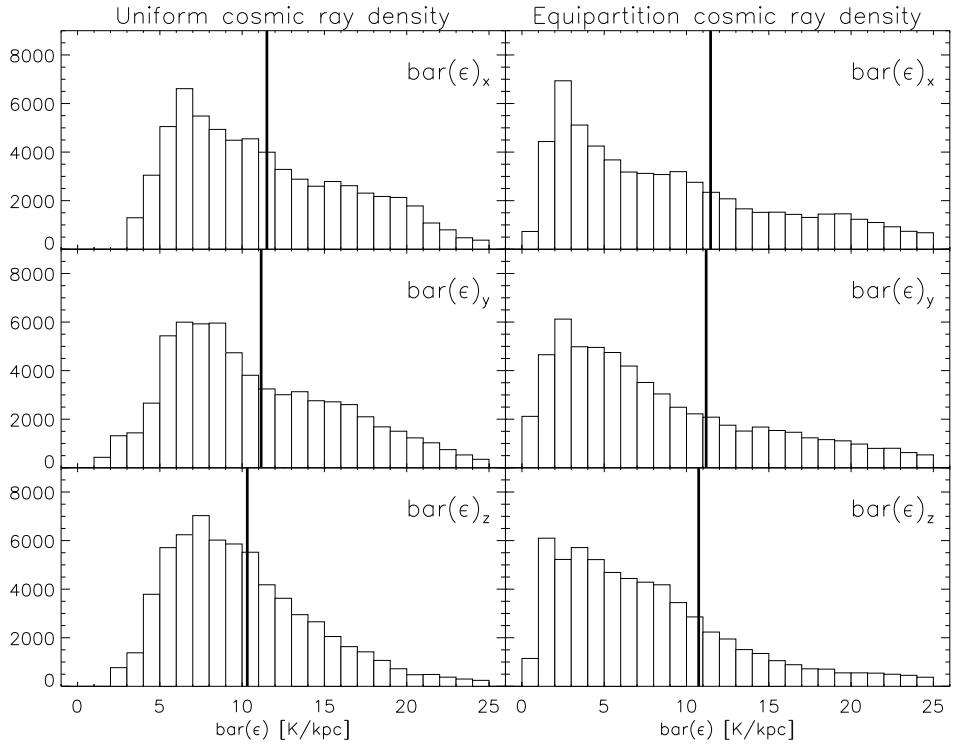

Figure 7.4 — Distribution of the emitted synchrotron brightness temperature per kpc, $\bar{\epsilon}$, at 408 MHz through the x, y and z faces of the MHD cube, for a uniform CR distribution (left column) and an equipartition CR distribution (bottom row). An equipartition CR distribution gives a broader distribution of $\bar{\epsilon}$, but the averages hardly change (top row averages: 11.5 – 11.2 – 10.3 K/kpc, bottom row averages: 11.5 – 11.2 – 10.7 K/kpc). The average $\bar{\epsilon}$ of each histogram is indicated by the heavy solid line.

Since our results for the Faraday depths and synchrotron emissivities per unit line-of-sight to first order do not appear to depend on whether we use a uniform cosmic ray density distribution or an equipartition distribution, we will consider for simplicity only the uniform cosmic ray density distribution in the rest of this chapter.

7.4 Faraday tomography: observations vs. simulations

From the MHD simulations that we scaled using the GEM EM, and by using a uniform cosmic ray density distribution, we calculated maps of Stokes Q and U for the same wavelengths that we used in our Faraday tomography analysis of the GEM data set. The $P(\mathcal{R})$ spectra that we calculate for our simulation will therefore have the same RMSF as the GEMINI data. In Fig. 7.5 we show a map of Stokes I at 408 MHz at the z = 0 face of the MHD cube. Note that this map shows structure on scales that are small enough for the WSRT to detect: the standard deviation $\sigma_{\rm I}$ = 3.5 K, whereas previous WSRT observations established upper limits of $\sigma_{\rm I} \lesssim$ 1.5 – 2.5 K (Haverkorn et al. 2004a) This is another indication that the real ISM is less structured than our MHD cube.

We added Gaussian noise to each $Q(\lambda^2)$ and $U(\lambda^2)$ map; we estimated the noise levels from Stokes V map in GEM, which we assume to contain only noise. This produced 201 frequency channel maps that cover the frequency range between 324 and 387 MHz (λ^2 between 0.60 and 0.86 m^2) in intervals of about 0.4 MHz. From these maps we then calculated $P(\mathcal{R})$ spectra in a similar way to how we analysed our 4 WSRT data sets.In

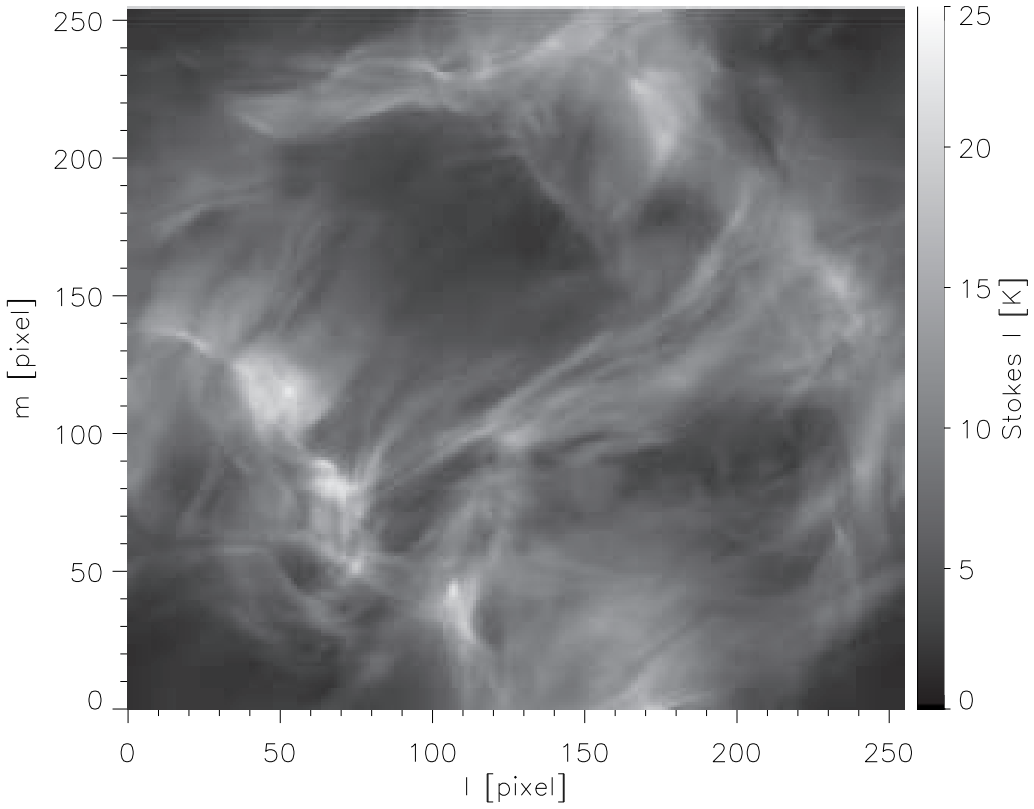

Figure 7.5 — Distribution of synchrotron brightness temperatures at 408 MHz over the z-face of the MHD simulations. We used the GEM EM to find the correct scaling for the electron densities and the physical cell size, and we scaled the magnetic fields using the 11 K/kpc synchrotron emissivity that we calculated with the Beuermann et al. (1985) model in the direction of GEM. We used a uniform CR distribution to calculate the brightness temperatures. Each pixel represents one line-of-sight through the MHD cube, parallel to the z-axis.

Figs. 7.6 and 7.7 we plot for each line-of-sight the peak P($\mathcal{R}$) and the $\mathcal{R}$ at which this peak occurs. These maps are similar to the maps that we published for the GEM data set (chapters 2 and 3). Most lines-of-sight have a main peak in the $P(\mathcal{R})$ spectrum of about 3 K, which is lower than the 5 K we found in GEM. The Faraday depth of this main peak typically lies between -20 $< \mathcal{R} <$ 20 rad/m^2, which is comparable to the values observed towards GEM. Lines-of-sight with strong $P(\mathcal{R})$ also seem to have large $|\mathcal{R}|$ and a large synchrotron brightness temperatures. In Fig. 7.8 we plot $P(\mathcal{R})$ spectra for a 10 $\times$ 10 grid of lines-of-sight along the z-axis of our MHD cube. The structure in these $P(\mathcal{R})$ spectra is in general similar to what we found for our 4 WSRT data sets.

7.5 Simulated ISM structure from $P(\mathcal{R})$ spectra

The physics of the ISM is encoded in the $P(\mathcal{R})$ spectra in a complicated way. However, since we calculated $P(\mathcal{R})$ spectra for the MHD simulations, we can study how $P(\mathcal{R})$ spectra are built up by synchrotron emission and Faraday rotation along the line-of-sight. Here we want to focus on 2 questions: what produces peaks in the $P(\mathcal{R})$ spectrum at large $|\mathcal{R}|$, and how are broad (resolved) peaks in the $P(\mathcal{R})$ spectrum formed.

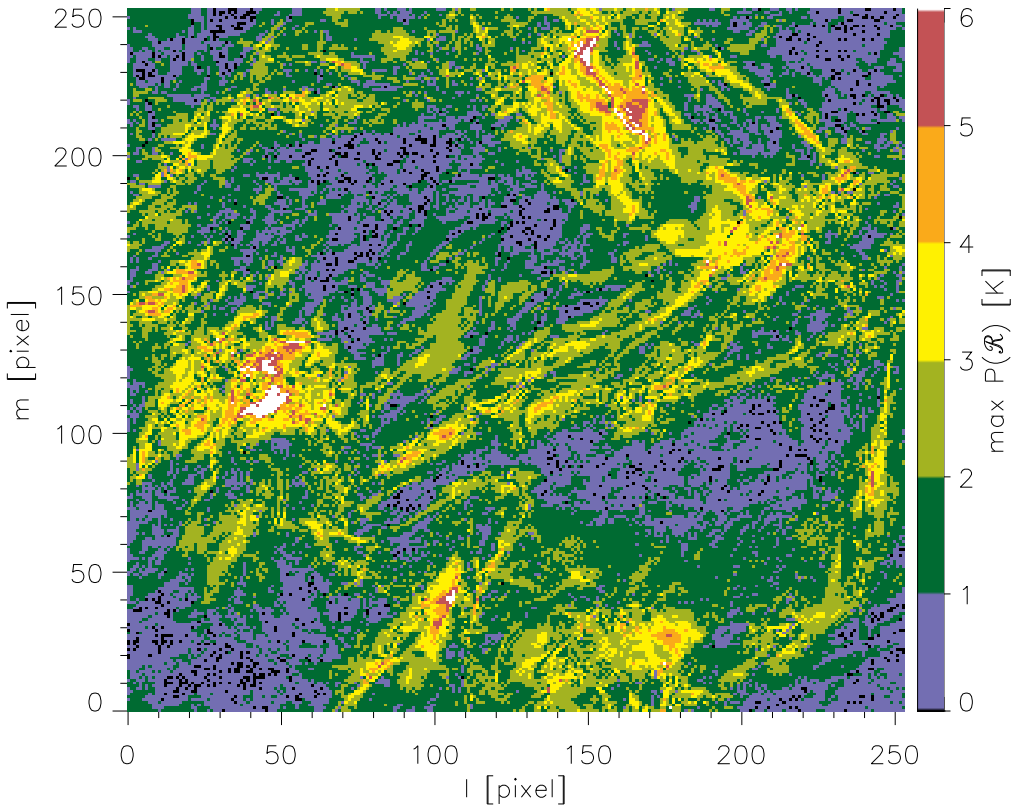

Figure 7.6 — Polarized brightness temperature (in Kelvin) of the highest peak in the $P(\mathcal{R})$ spectrum in the MHD cube. We used lines-of-sight parallel to the z-axis of our cube. To calculate the synchrotron emissivities we used a uniform cosmic ray density distribution. Each pixel represents one line-of-sight. The 176 lines-of-sight indicated in white have $P(\mathcal{R}) > 6$K. Since we added the noise levels of our GEMINI data set to calculate the $P(\mathcal{R})$ spectra from the MHD cube, the 1σ noise level is the same as the 1σ noise level = 0.14 K of the GEMINI $P(\mathcal{R})$ spectra. On page 195 we show a colour version of this figure.

To address the first question we studied 3 groups of $P(\mathcal{R})$ spectra: strong single $P(\mathcal{R})$ peaks close to $\mathcal{R} = 0$ rad/m^2, single peaks at large $|\mathcal{R}|$, and double-peaked $P(\mathcal{R})$ spectra with a large separation between the two peaks. We studied in detail how the synchrotron emissivity and Faraday depth vary along the lines-of-sight from each group. In Fig. 7.9 we plot these physical properties for the different lines-of-sight we investigated; each line-of-sight is represented by a different colour. The first two columns are for lines-of-sight with a single narrow peak at small $|\mathcal{R}|$ and at large $|\mathcal{R}|$ respectively, and they contain 20 and 10 lines-of-sight respectively. The next two columns show the properties of lines-of-sight with two strong and narrow peaks in the $P(\mathcal{R})$ spectrum, that have a large separation in $\mathcal{R}$. To avoid confusion we plotted only 10 lines-of-sight in each of these two columns.

The first row of panels in this figure shows the strength of the magnetic field component perpendicular to the line-of-sight, which, since we assumed a uniform cosmic ray density distribution, directly translates into a synchrotron brightness temperature (Eqn. 7.13). From the panels in this row it is clear that synchrotron radiation is emitted in more than one region along the line-of-sight, and this implies that it is the variation in Faraday depth along the line-of-sight (shown in the second row of panels in Fig. 7.9)

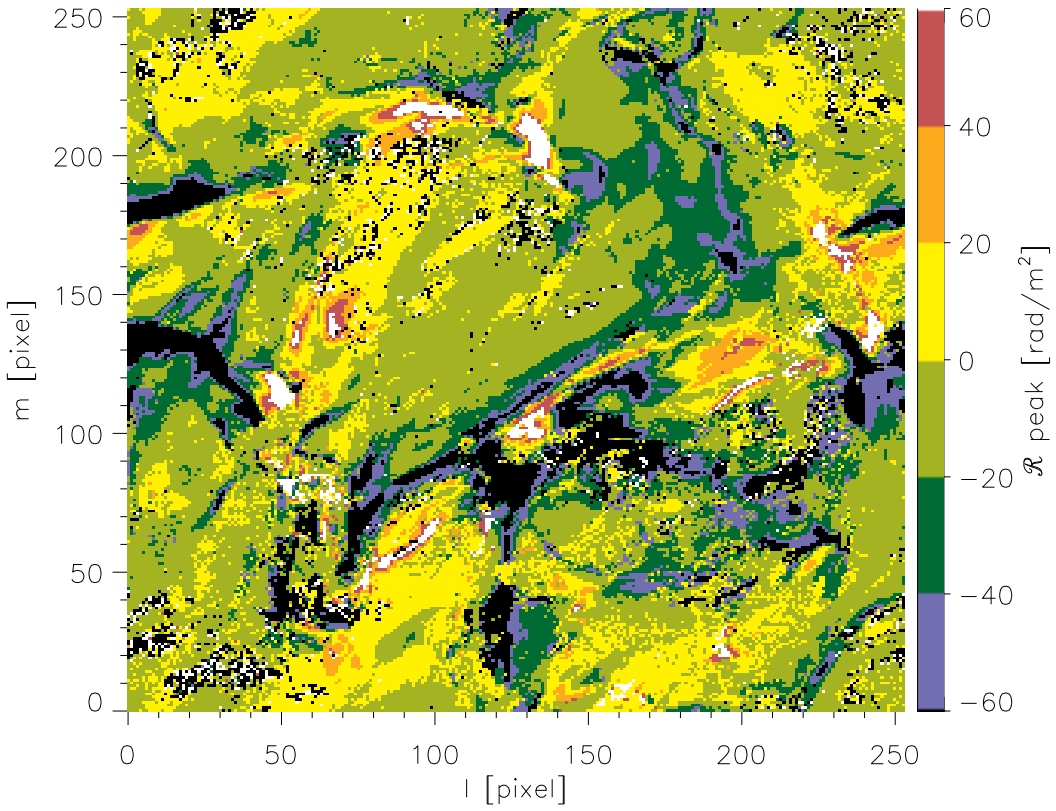

Figure 7.7 — Identical to Fig. 7.6, but for the Faraday depth $\mathcal{R}$ of the highest peak in the $P(\mathcal{R})$ spectrum. The 4910 lines-of-sight indicated in black have $\mathcal{R}$ < -60 rad/m^2, and the 1724 lines-of-sight indicated in white have $\mathcal{R} > 60$ rad/m^2. On page 196 we show a colour version of this figure.

that determines what the $P(\mathcal{R})$ spectrum of one of these lines-of-sight will eventually look like. It is clear that $P(\mathcal{R})$ spectra with a single peak close to $\mathcal{R} = 0$ rad/m^2 are produced when the Faraday depth does not vary too much along the line-of-sight. A line-of-sight with a single peak at large $|\mathcal{R}|$ can be produced in two ways (illustrated in more detail in Fig. 7.10): a large Faraday depth is built up close to the observer from a strong Faraday depth gradient, or, for a minority of cases, it is built up gradually along the line-of-sight. The latter scenario requires that the Faraday depth gradient over a synchrotron-emitting region cannot be very large, otherwise the peak in the $P(\mathcal{R})$ spectrum could become so broad that we would resolve it. If a $P(\mathcal{R})$ spectrum has two peaks with a large separation in Faraday depth (shown in the 3$^{\rm rd}$ and 4$^{\rm th}$ columns of Fig. 7.9), we find in almost all cases that this separation is built up by a strong gradient in Faraday depth over a small number of pixels. The position of the gradient therefore determines if the $P(\mathcal{R})$ spectrum shows only one strong peak at large Faraday depth (if the gradient lies close to the observer), or contains two peaks at different Faraday depths. More complex $P(\mathcal{R})$ spectra, for example with multiple peaks, or with 2 nearby peaks, can probably be explained as well in terms of the magnitude and location along the line-of-sight of such a gradient in Faraday depth.

The question then becomes what produces these strong gradients in $\mathcal{R}$. In the third and fourth rows of panels in Fig. 7.9 we plot the distribution along the line-of-sight

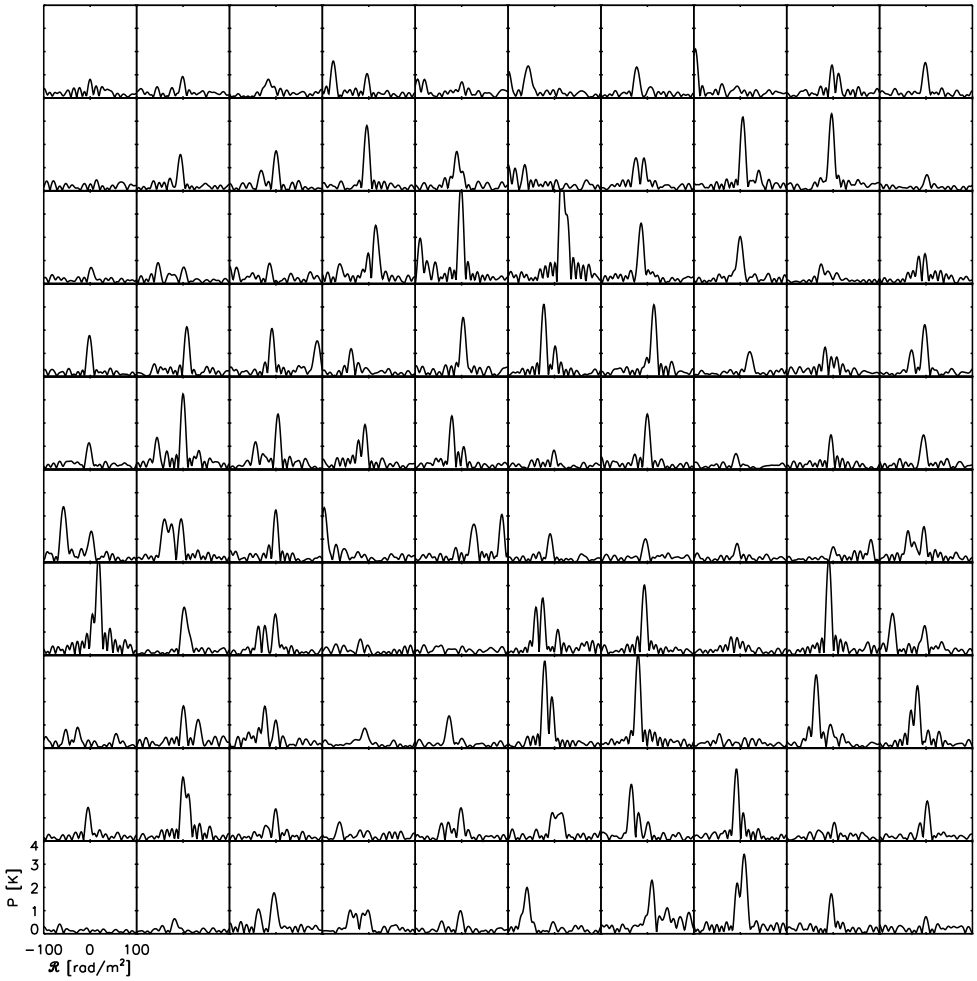

Figure 7.8 — Grid of $P(\mathcal{R})$ spectra observed at the z = 0 face of the MHD cube. The x-axis covers Faraday depths between -100 rad/m^2 and +100 rad/m^2, and the y-axis covers polarized brightness temperatures between 0 and 4 K. To calculate these $P(\mathcal{R})$ spectra we assumed a uniform cosmic ray density distribution.

of the thermal electron density and of the line-of-sight magnetic field component. The electron density shows strong spikes that occur over a small number of pixels, and these coincide with some of the strongest Faraday depth gradients in columns 2 to 4. A strong spike in the thermal electron density not always produces a strong $\mathcal{R}$ gradient, since the Faraday depth that is built up in a pixel also depends on the strength of the magnetic field component along the line-of-sight. To investigate this correlation between peaks in the thermal electron density and gradients in $\mathcal{R}$, we plotted in the left column of Fig. 7.11 the average electron density per pixel versus the average Faraday depth gradient per pixel. The right column shows the correlation between the average Faraday depth gradient per pixel and the average absolute value of the line-of-sight magnetic field strength in a pixel. We calculated averages over pixel intervals, instead of plotting the electron densities and magnetic field strengths of individual pixels, because the large gradients in $\mathcal{R}$ that we are interested in are in most cases built up over a group of pixels. By averaging we also weaken the impact of individual pixels on

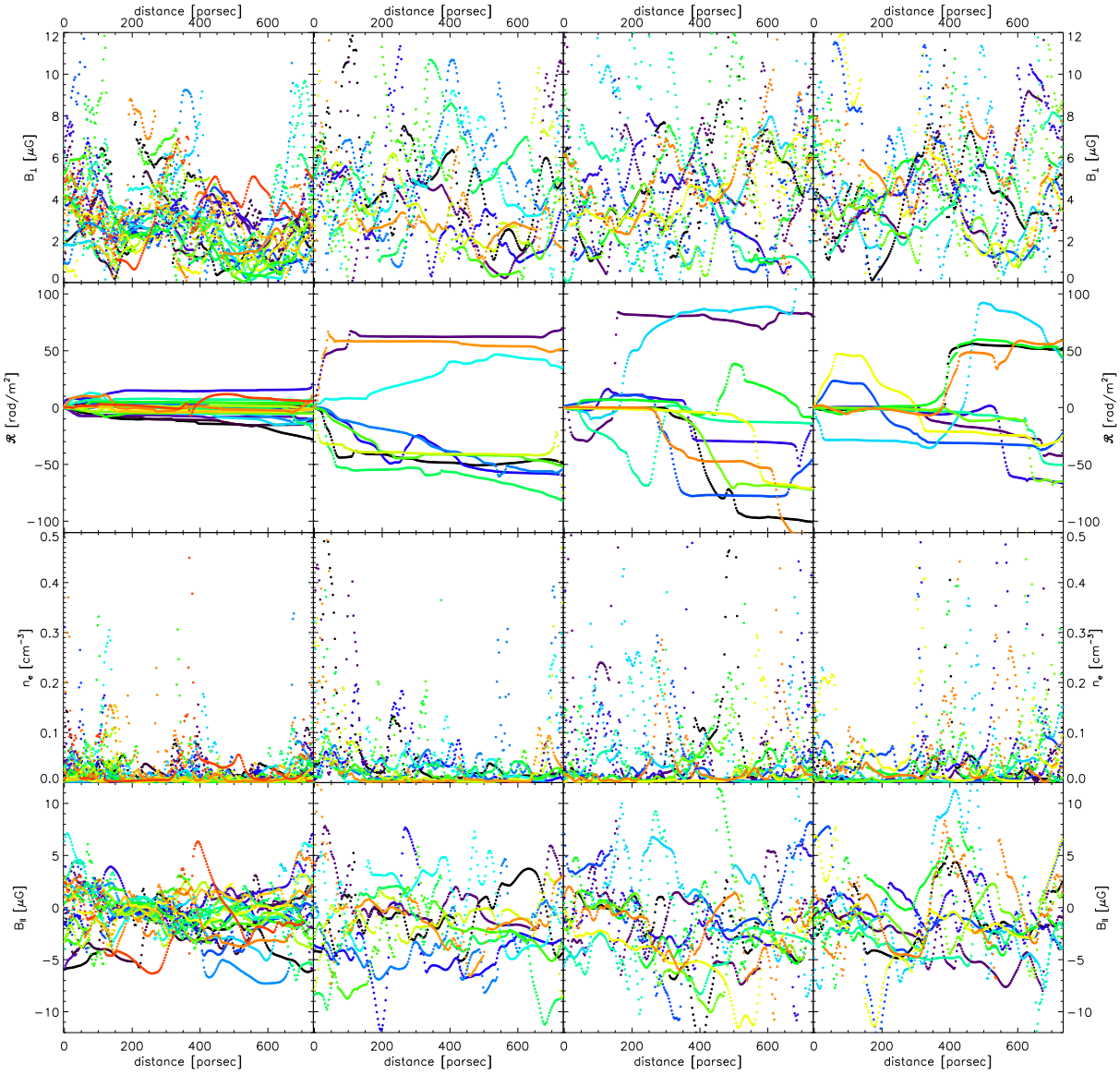

Figure 7.9 — Distribution of synchrotron emission and Faraday rotation along the line-of-sight, for different groups of $P(\mathcal{R})$ spectra. From left to right: the first column shows the variation of the different physical quantities for 20 lines-of-sight with a single narrow peak in the $P(\mathcal{R})$ spectrum with $|\mathcal{R}| \lesssim 15$ rad/m^2. In the second column we plotted the properties of 10 lines-of-sight with a single narrow peak at large $|\mathcal{R}| \gtrsim 40$ rad/m^2. The third and fourth columns both show the properties of lines-of-sight with two narrow peaks in the $P(\mathcal{R})$ spectrum, that are separated by more than 40 rad/m^2. To avoid confusion we only plotted 10 lines-of-sight in each of these two columns. The first row of panels shows how the magnetic field component perpendicular to the line-of-sight varies along the line-of-sight. Since we assume a uniform cosmic ray distribution, the magnitude of this magnetic field component directly translates into the magnitude of the synchrotron emission. It is clear that synchrotron emission occurs in more than one region along the line-of-sight. The second row of panels shows how $\mathcal{R}$ builds up along the line-of-sight. In the third and fourth rows we show how the thermal electron density and line-of-sight magnetic field strength, that determine how the Faraday depth is built up along the line-of-sight, vary. On page 197 we show a colour version of this figure.

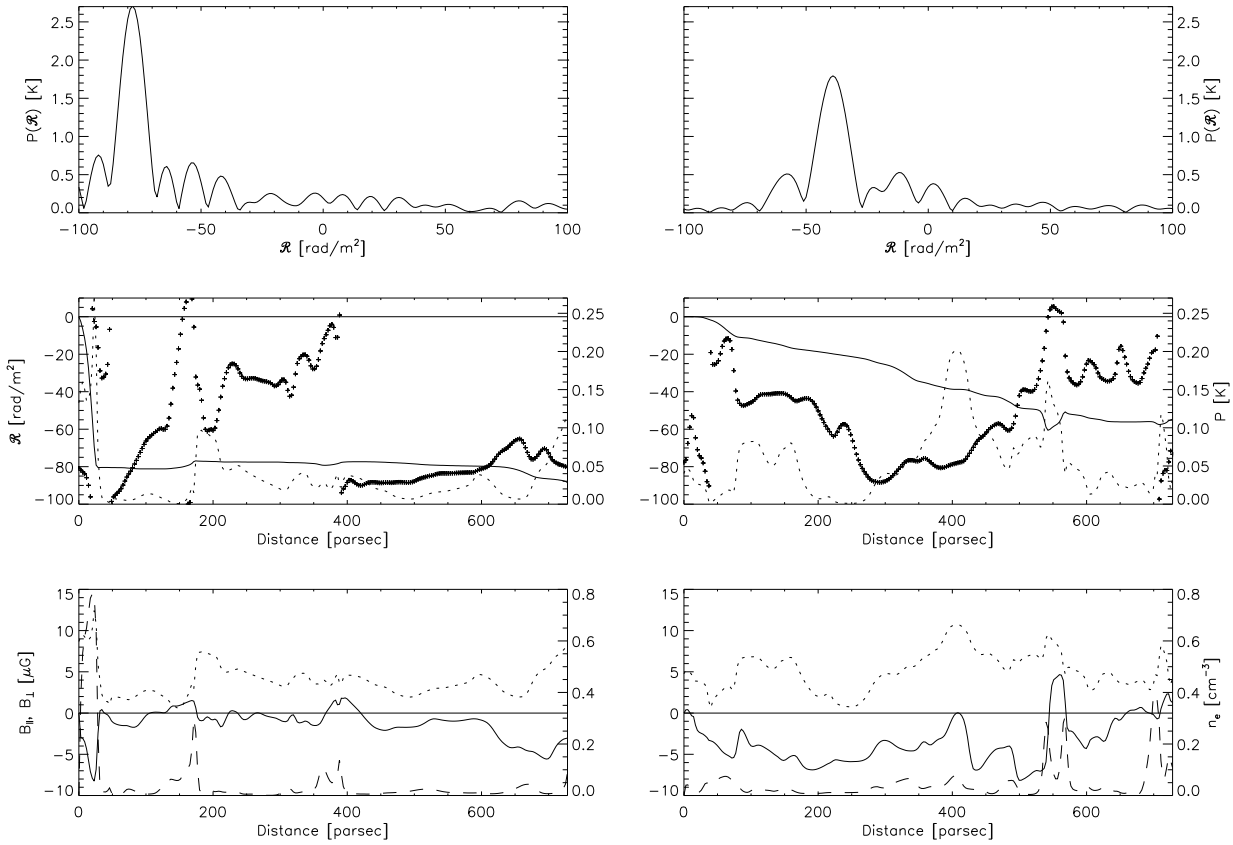

Figure 7.10 — Top row of panels: $P(\mathcal{R})$ spectra for 2 lines-of-sight with a single strong peak at large $|\mathcal{R}|$. The x-axis shows Faraday depths between -100 rad/m^2 and +100 rad/m^2, and the y-axis polarized intensities in Kelven. In the middle panel we plot the line-of-sight distribution of Faraday depth (solid line), emitted synchrotron brightness temperature per pixel at 345 MHz (dotted line; the 345 MHz corresponds to the average λ^2 of the usable frequency channels in GEM. We also assumed that the synchrotron emission generated in each pixel is 70% polarized), and position angle of the emitted radiation (crosses). The position angles vary between -90 $^\circ$ (bottom edge of the panel) and +90° (top edge), and due to their periodicity they can wrap around the bottom and top edges of the panel. The left line-of-sight quickly builds up a large $\mathcal{R}$ close to the observer, whereas the line-of-sight on the right builds up $\mathcal{R}$ more gradually. In the bottom panel we plot the distribution of the line-of-sight component of the magnetic field (solid line), electron density (dashed line), and magnetic field component perpendicular to the line-of-sight (dotted line). The magnetic field component along the line-of-sight, combined with the electron density, are responsible for the variation in $\mathcal{R}$ from the middle panel. The magnetic field component perpendicular to the line-of-sight directly translates into a synchrotron brightness temperature, since we assumed a uniform cosmic ray distribution.

this plot. Also the RMSF of our observations makes it impossible to study the $\Delta\mathcal{R}$ of individual pixels, that are in general small. The number of pixels that we average over is determined by the $\Delta\mathcal{R}$ that is built up over that interval, stronger Faraday gradients/pixel require shorter intervals. We indicated the $\Delta\mathcal{R}$ that we want to build up in the upper left corner of each panel in the left column. If the $\mathcal{R}$ gradient per pixel is larger than the $\Delta\mathcal{R}$ that we want to build up over an interval of pixels, we plot the $\Delta\mathcal{R}$ built up in that pixel versus the electron density or magnetic field strength in that pixel. This explains why there are in these figures also points at $|\nabla\mathcal{R}|$ that are larger than the $\Delta\mathcal{R}$ that we want to build up over an interval of pixels.

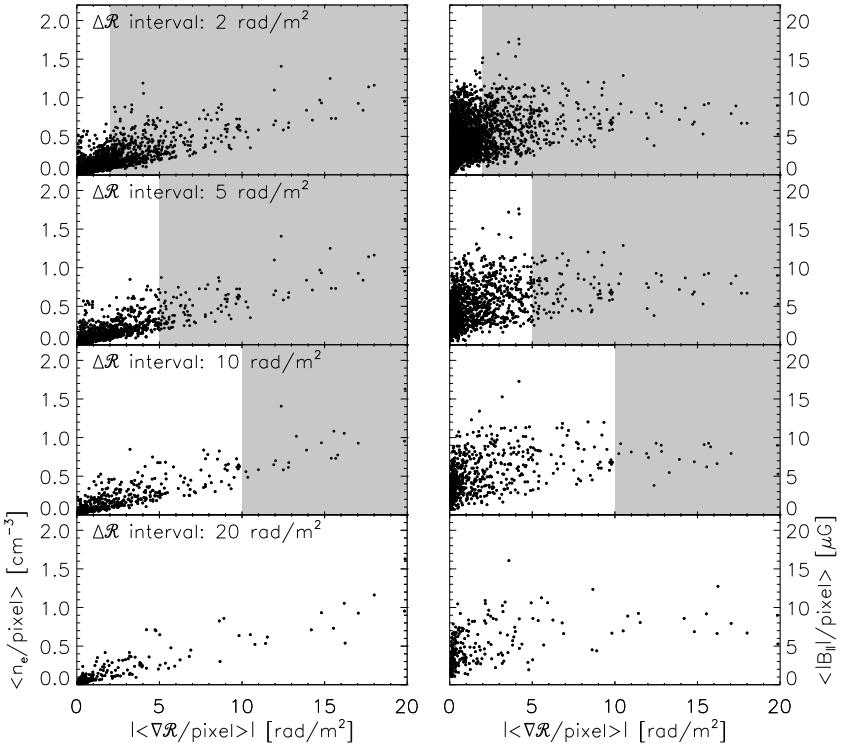

Figure 7.11 — Correlation between the average electron density per pixel and the average Faraday depth per pixel (left column) and the average absolute value of the line-of-sight magnetic field component per pixel and the average Faraday depth per pixel (right column). We averaged over intervals of pixels that build up the Faraday depth indicated in the top of the panels in the left column. Points that lie in the grey region correspond to individual pixels that build up a larger Faraday depth than the Faraday depth indicated in the upper right of each panel. We used lines-of-sight on a 13×13 grid to calculate these averages; we did not select particular lines-of-sight.

Fig. 7.11 shows that the average electron density per pixel is much stronger correlated with the average Faraday depth gradient per pixel than the average magnetic field strength along the line-of-sight, and this is independent of the $\Delta\mathcal{R}$ that we build up over an interval. This supports our idea that strong spikes in electron density are primarily responsible for large Faraday depth gradients. However, strong magnetic fields will in some cases also produce gradients in $\mathcal{R}$ when the electron densities are low. From Fig. 7.11 strong magnetic fields along the line-of-sight appear to be a less important source of large $\mathcal{R}$ gradients than spikes in electron density.

From the distribution of synchrotron emission and Faraday rotation for a few selected lines-of-sight in the middle panels of Figs. 7.10 and 7.12 it is clear that synchrotron emission and Faraday rotation can occur in the same pixels, which inevitably leads to broad lines in the $P(\mathcal{R})$ spectra. However, broad $P(\mathcal{R})$ spectra can also be produced by two nearby narrow $P(\mathcal{R})$ peaks, as is clear from the second line-of-sight in Fig. 7.12. To investigate how often mixing occurs between synchrotron emission and Faraday rotation, we plotted in Fig. 7.13 the correlation between the average amount of synchrotron emission per pixel and the average Faraday depth that is built up over a pixel, identical to how we plotted in Fig. 7.11 the average electron density or line-of-sight magnetic field strength per pixel and the average $\Delta\mathcal{R}$ per pixel. If the $\Delta\mathcal{R}$ in

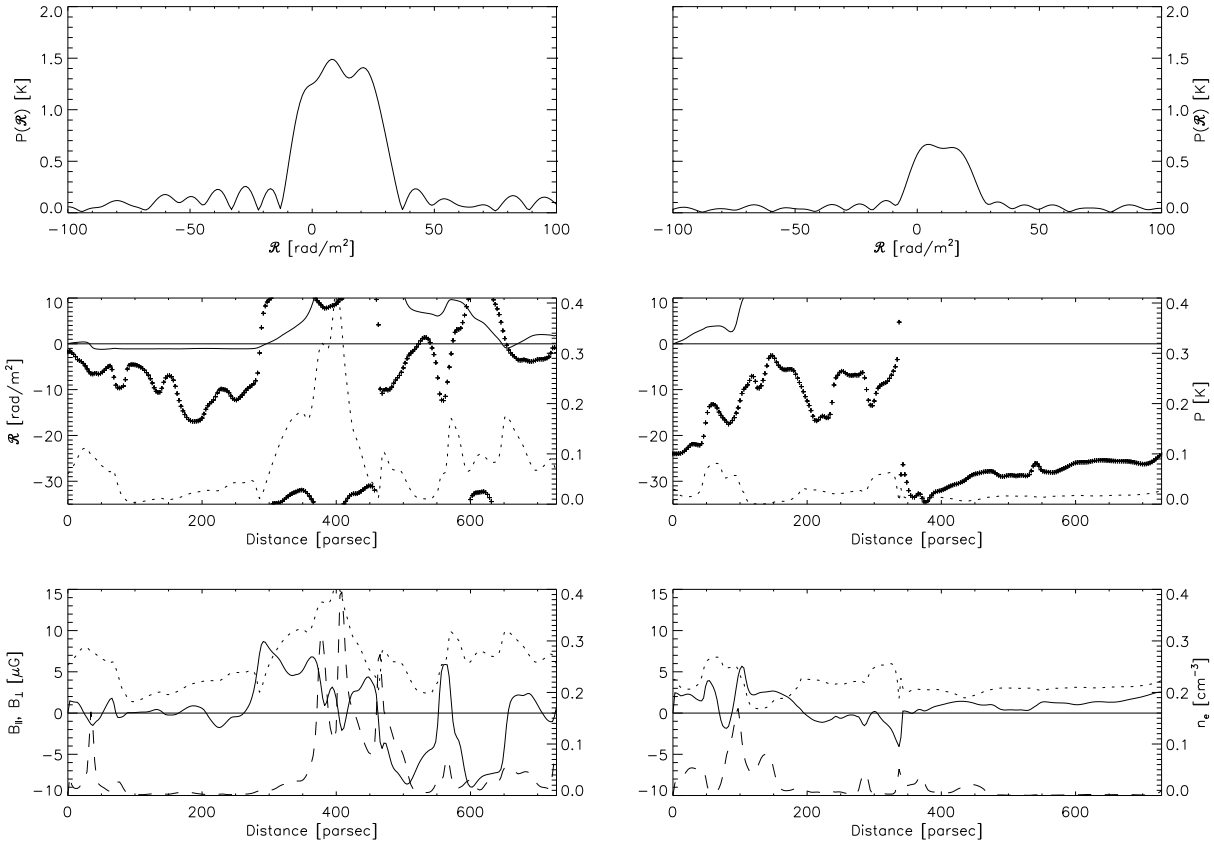

Figure 7.12 — Identical to Fig. 7.10, but for 2 lines-of-sight with a single strong broad $P(\mathcal{R})$ peak. For the line-of-sight on the left this broad peak is produced by synchrotron emission and Faraday rotation occurring in the same parts of the line-of-sight, whereas the broad peak in the $P(\mathcal{R})$ spectrum in the column on the right synchrotron emission and Faraday rotation occur in different parts of the line-of-sight, and the broad peak is the result of the merging of two narrow peaks.

a pixel is larger than the $\Delta\mathcal{R}$ that we want to build up over an interval, we plotted the synchrotron brightness temperature and $\Delta\mathcal{R}$ of that pixel. If synchrotron emission and Faraday rotation occur in the same pixels, we would expect many points to lie far from the coordinate axes. Most of the data points in these figures however lie close to the coordinate axes, and seem to avoid the region with large synchrotron emission/pixel and large Faraday depth/pixel, and this result does not depend on the $\Delta\mathcal{R}$ we want to build up over each pixel interval. We therefore conclude that in most cases Faraday rotation and synchrotron emission do not occur in the same pixels along the line-of-sight. We reached a similar conclusion when we first encountered unresolved peaks in the $P(\mathcal{R})$ spectrum (chapter 2). Future instruments that can observe lower frequencies, like LOFAR and the MWA, will have a better resolving power in Faraday depth. It will then be easier to identify lines-of-sight with broad $P(\mathcal{R})$ features that are produced when synchrotron emission occurs in pixels that also Faraday-rotate.

When we considered the structure in the $P(\mathcal{R})$ spectra that we observed in our 4 data sets, we could not rule out that these could be produced by missing extended features on the sky, since our interferometer observations did not include information on short baselines. Now that we find similar $P(\mathcal{R})$ spectra in our MHD cube that

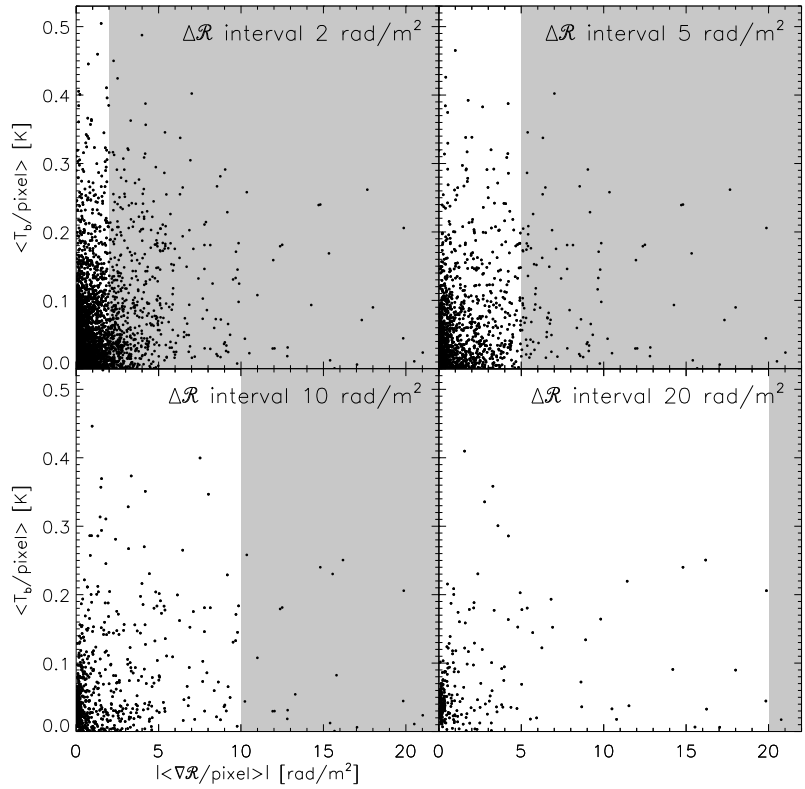

Figure 7.13 — Correlation between the average synchrotron brightness temperature (T_b) per pixel and the average Faraday depth gradient per pixel. We calculated the synchrotron emissivity at 345 MHz, which corresponds to the average λ^2 of the usable frequency channels in GEM. These averages were calculated using pixel intervals that build up the $\Delta\mathcal{R}$ indicated in the top of the panels. Points that lie in the grey region correspond to individual pixels that build up a larger Faraday depth than the Faraday depth indicated in the upper right of each panel. The lines-of-sight that we used to make these figures lie on a 13×13 rectangular grid.

does include all angular scales (we scaled the MHD electron densities, cell sizes and magnetic field strengths using only single-dish radio observations), we can be more confident that what the features we see in the $P(\mathcal{R})$ spectra are related to structure in the ISM rather than to artefacts of the instrument.

One caveat in our analysis is that the Mach number of our simulations is larger than is expected for the warm ISM. A smaller Mach number will probably smooth the thermal electron density distribution, which also means that the gradients due to spikes in the electron density will be smaller, and peaks in the $P(\mathcal{R})$ spectrum will then lie closer to each other. A smoother electron density distribution would also show a flatter EM/DM ratio, which might fit the BMM results better. Furthermore, the line-of-sight would have to become longer to generate all observed EM within the MHD cube, which reduces the difference in length between the line-of-sight that produces all observed EM and the line-of-sight that produces all observed synchrotron radiation.

Finally, from our simulations it is clear that the physical depth cannot be easily extracted from the measured Faraday depth. However, in the near future we want to explore the angular correlation on the sky of features in the $P(\mathcal{R})$ spectrum. If there is a certain degree of isotropy of the features in the $P(\mathcal{R})$ spectra along the line-of-sight

and perpendicular to it, in the plane of the sky, this can help us address the problematic mapping from physical depth to Faraday depth.

7.6 Summary and conclusions

In this chapter we presented a Faraday tomography analysis of an MHD simulation of the Galactic ISM. Our goal was to reach general conclusions on how to interpret the Faraday depth spectra by comparing the Faraday depth spectra from our simulations to the distribution of synchrotron emission and Faraday rotation along the line-of-sight. We scaled the dimensionless electron densities and physical cell sizes by using WHAM emission measures observed towards our 4 WSRT data sets. This approach also requires dispersion measure data, but since we do not have this data available, we used the relation between emission measure and dispersion measure that Berkhuijsen et al. (2006) determined for a sample of 157 Galactic pulsars. To find the correct scaling for our magnetic field strengths, we require that the MHD cube should produce the same amount of synchrotron brightness temperature as the model by Beuermann et al. (1985) in the vicinity of the sun. Since the synchrotron emissivity depends on the distribution of cosmic rays, we used both a uniform distribution and a distribution that is in energy equipartition with the magnetic fields. For these two distributions we calculated the Faraday depths through the entire MHD cube, and the distribution of synchrotron brightness temperatures over the cube faces. Since our results did not strongly depend on which cosmic ray distribution we used, we continued our analysis with the uniform density distribution. One clear problem with our scaling approach is that the length of the line-of-sight required to build up the observed emission measures is shorter by a factor of three than the length of the line-of-sight that is required to produce the observed Galactic synchrotron brightness temperature. This could be an indication that the MHD simulations are more structured that the Galactic ISM; a smoother electron density distribution would need a much longer line-of-sight to build up the observed emission measures. However, the Faraday depth spectra look similar to the ones that we calculated for our WSRT observations (chapters 2 – 6).

The main conclusions of this chapter are twofold. First, features in $P(\mathcal{R})$ spectra at large Faraday depths are in most cases produced by strong Faraday depth gradients over short physical distances. These Faraday depth gradients are often produced by large, but localized, enhancements in the electron density, and to a lesser extent by strong line-of-sight magnetic field components. Second, over most of the lines-of-sight that we investigated, intense Faraday rotation and synchrotron emission do not occur at the same location. Resolved features in the Faraday depth spectra are therefore in most cases produced by merging of 2 or more narrow features, and they are not often produced by regions with both synchrotron emission and Faraday rotation.

Acknowledgements

The Westerbork Synthesis Radio Telescope is operated by the Netherlands Foundation for Research in Astronomy (NFRA) with financial support from the Netherlands Organization for Scientific Research (NWO). The Wisconsin H-Alpha Mapper is funded by the National Science Foundation.

Chapter 8

The WENSS & Dwingeloo surveys and the Galactic magnetic field

Abstract. We investigate the structure of the Galactic magnetic field in the 2nd Galactic quadrant using radio continuum polarization data from the 325 MHz WENSS (*WE*sterbork *N*orthern *S*ky *S*urvey) survey in combination with earlier single-dish observations. We study gradients in polarization angle along Galactic longitude and latitude in the region $130^\circ \lesssim l \lesssim 173^\circ$and $-5^\circ \lesssim b \lesssim 31^\circ$. These gradients were determined with a new method that we developed to efficiently and reliably fit linear gradients to periodic data like polarization angles. Since the WENSS data were obtained with a synthesis array they suffer from the 'missing short spacing' problem. We have tried to repair this by adding an estimate of the large-scale emission based on the single-dish (Dwingeloo) data obtained by Brouw and Spoelstra. Combining all available data we derive a rotation measure (RM) map of the area, from which we estimate all 3 components of the magnetic field vector. In the part of WENSS where large-scale structure in polarized intensity is relatively unimportant, we find that the magnetic field is predominantly perpendicular to the line-of-sight, and parallel to the Galactic plane. The magnetic field components along the line-of-sight and along Galactic latitude have comparable values, and the strength of these components is much smaller than the strength of the total magnetic field. Our observations also cover part of the so-called 'fan' region, an area of strong polarized intensity, where large-scale structure is missing from our WENSS data. We tentatively show that Faraday rotation occurring in front of the Perseus arm is causing both the WENSS RMs and the RMs towards the fan region observed in previous single-dish surveys, and we suggest that the fan is formed by local emission that originates in front of the emission we see in WENSS.

D. H. F. M. Schnitzeler, P. Katgert, M. Haverkorn, and A. G. de Bruyn
Astronomy & Astrophysics, **461**, 963 (2007)

8.1 Introduction

THE diffuse radio emission from our Galaxy provides a powerful tool for studying the various components of the interstellar medium. For example, the well-known all-sky survey by Haslam et al. (1981) at 408 MHz was used by Beuermann et al. (1985) to construct a two-component model of the synchrotron emissivity of our Galaxy. Large parts of the Milky Way have been studied also at other frequencies both in total intensity and in polarized intensity, e.g. Berkhuijsen (1971), Reich et al. (1997), Uyaniker et al. (2003), Bingham & Shakeshaft (1976), Brouw & Spoelstra (1976).

High-resolution polarization studies came about with the work by Junkes et al. (1987), and an aperture synthesis array was first used by Wieringa et al. (1993). Haverkorn et al. (2000) were to the authors' knowledge the first to use an interferometer to derive information on the magnetic field structure in detail using the diffuse emission of our Galaxy. Presently, the International Galactic Plane Survey (IGPS) project is studying a major part of the Galactic plane up to a couple of degrees on either side and at several frequencies (the polarization data from the IGPS are discussed in Taylor et al. (2003) for the Canadian Galactic Plane Survey and by Haverkorn et al. (2006b) for the Southern Galactic Plane Survey).

Equipartition arguments have been used to estimate the strength of the magnetic field (Beck et al. 2003). To study the topology of the field various groups are using different techniques. In particular pulsars and extragalactic sources have provided a large amount of information on the large-scale field and on possible reversals in the direction of the field (see e.g. Han et al. 2004, 2006, and Brown et al. 2003). Extragalactic sources sample the entire line-of-sight through the Galaxy, whereas pulsars can tell us about variations along the line-of-sight if we know their position in the Galaxy. Most pulsars are however confined to the Galactic plane, a drawback extragalactic sources do not have.

One major problem with both extragalactic sources and pulsars is that except in parts of the Galactic plane (Brown et al. 2003, Haverkorn et al. 2006a) the surface density of extragalactic sources and pulsars is low, leaving large gaps between the sampled lines-of-sight. As a result only large-scale structure (LSS) in the magnetic field can be inferred. Extragalactic sources can also have an intrinsic rotation measure (RM), which makes it more difficult to extract the Galactic contribution from the observed RM.

Pulsars have previously been used to provide information on the small-scale magnetic field (Rand & Kulkarni 1989, Han et al. 2004). The polarized diffuse Galactic radio background can also be used for this purpose, as shown by Haverkorn et al. (2004a), who derived the strength of the magnetic field components along the line-of-sight and perpendicular to it, making it possible to study both the small-scale and the large-scale magnetic field. One problem with this method is that the diffuse emission is not very strong, and it can be severely depolarized along the line-of-sight. Correcting for this is complicated by the fact that the amount of emission and depolarization can vary along the line-of-sight. Furthermore the diffuse emission fills the entire telescope beam, which makes modelling more involved than for pulsars and extragalactic sources which are bright point sources.

In this chapter we study the large-scale properties of the polarized diffuse Galactic background at 325 MHz using the WENSS survey (Rengelink et al. 1997). We selected a region spanning about 1000 square degrees between $130^\circ \lesssim l \lesssim 173^\circ$ and $-5^\circ \lesssim b \lesssim 31^\circ$. This area encompasses the Auriga and Horologium regions studied by Haverkorn et al. (2003a, 2003b) using multi-frequency data, as well as a large part of the so-called 'fan' region, an area bright in polarized intensity, where the magnetic field component in the plane of the sky is very regular (Brouw & Spoelstra 1976; Spoelstra 1984).

In Sect. 8.2 we describe the WENSS dataset that we use and the reduction of this dataset. Since this dataset was obtained with an interferometer, LSS will be missing from our observations. In Sect. 8.3 we estimate the contribution of LSS, and we add this estimate to WENSS. We present the results from the original WENSS dataset and that including the LSS estimate in Sect. 8.4. In Sect. 8.5 we describe how we analyse the polarization angle data. We also discuss the robustness of our LSS reconstruction. In Sect. 8.6 we present the results of our analysis in terms of large-scale gradients along Galactic longitude and latitude. In Sect. 8.7 we compare the gradients in polarization angle that we obtain in areas where no LSS is missing from the interferometer observations to gradients in the RMs derived by Spoelstra (1984). This enables us to estimate how reliably gradients in polarization angle can be translated into gradients in RM. In Sect. 8.8 we discuss the physical picture we can draw from our observations; in particular we attempt to reconstruct all components of the 3D magnetic field vector. In this section we also consider some of the implications of our observations for the nature of the the fan region.

8.2 Description of the data

8.2.1 WENSS

WENSS, the Westerbork Northern Sky Survey, is a low-frequency radio survey of extragalactic sources at 325 MHz above $\delta = 30^\circ$ that also contains a wealth of diffuse polarization data (Rengelink et al. 1997). WENSS has a 5 MHz bandwidth divided over 7 channels, and its sensitivity is 18 mJy (5σ) at 325 MHz. The survey was carried out using the Westerbork Synthesis Radio Telescope (WSRT). The WSRT consists of 14 25m dishes, 10 of these are fixed and 4 can be moved along a track, which improves (u,v) coverage.

To map large parts of the sky in a reasonable amount of time WENSS uses the mosaicking technique in which the telescope cycles through 78 or 80 pointings (depending of the declination of the mosaic), integrating each pointing for 20 seconds, and then moving on to the next. If the pointing centers are on a square grid with a separation of 1.5° the off-axis instrumental polarization is very effectively suppressed (down to the 1% level - Wieringa et al. 1993). In this way each mosaic covers roughly 200 square degrees, and in every night each pointing can be observed about 12 times, yielding visibility data along 12 'spokes' in the (u,v) plane.

Each WENSS mosaic is formed by combining six 12 hr observing runs. In each run the telescopes sample the (u,v) plane with a 72 meter baseline increment, and different runs have a different shortest baseline ranging from 3 – 96 meters in 12 meter inter-

vals. This results in baselines from 36 meters to 2760 meters. At 325 MHz this gives a maximum resolution of $54'' \times 54'' \csc \delta$ (FWHM). In the analysis of the data we used a Gaussian taper with a value of 0.25 at a baseline length of 250 meters to increase the signal-to-noise ratio for more extended structures. This degrades the resolution to $6.7' \times 6.7' \csc \delta$. By adding six 12hr observing runs the first grating ring is at 4.4° i.e. outside the $3^\circ \times 3^\circ$ area that we mapped in the individual pointings from which we construct the mosaics.

The 6 mosaics we selected were mostly observed at night. Observing at night limits solar interference, and strong ionospheric RM variations are considerably smaller when the observations are not taking place during twilight. Information on the mosaics can be found in Table 8.1. For the observations that started in the afternoon ionospheric effects are probably small since polarized point sources are still point-like in the data. After the polarization calibration described in the next section we regridded the Stokes Q and U maps from the equatorial to the Galactic coordinate system using the `AIPS` task `REGRD`, after which we calculated the polarized intensity and polarization angle. Polarization angles were corrected for the (local) parallactic angle between the equatorial and Galactic north poles.

8.2.2 Polarization calibration

Rengelink et al. (1997) carried out the total intensity calibration as part of the WENSS survey. For details about this part of the data reduction we refer the reader to their paper. Polarization calibration requires additional reduction steps that we carried out using the `NEWSTAR` data reduction package, and we will briefly describe these here. For a proper (mathematical) treatment of the different steps involved in the polarization calibration we refer the reader to the articles by Hamaker et al. (1996) and Sault et al. (1996).

Corrections for deviations in the alignment and the ellipticity of the antenna dipoles, which cause total intensity I to leak into Stokes U and V, were found using the unpolarized calibrator sources 3C48 and 3C147. The flux scales of these sources is set by the calibrated flux of 3C286 (26.93 Jy at 325 MHz), determined by Baars et al. (1977).

Due to an a-priori unknown phase offset between the responses of the X and Y dipoles there is cross-talk between Stokes U and V. In principle this phase difference can be calibrated with a polarized calibrator source, but since such a source was not available for the WENSS observations we determined the correction by assuming that Stokes V contains only noise, and minimizing the amount of signal in V. For the 5 mosaics observed in January 1992 the correction we found in this way was -9°, a demonstration of the stability of the WSRT on timescales of weeks, whereas for the WN66_045 mosaic, which was observed almost 2 years later, it was +26°.

Finally we have to correct for the different amounts of ionospheric Faraday rotation during the different nights in each mosaic and between mosaics. In each mosaic we found 2 – 3 bright intrinsically polarized extragalactic sources, and we used the variations in the polarization angle of these sources over the different nights to align the polarization vectors. We did not correct for variations in ionospheric Faraday rotation within each individual 12 hr observing run; we only took the average polarization angle over each night. To correct for polarization angle offsets between mosaics we

Table 8.1 — Summary of the observations. For each mosaic the dates (yy/mm/dd) and starting times (UT) are shown of the individual 12 hour observing runs that make up the mosaic. Each run is indicated by the length of its shortest baseline. For each mosaic we also show the central coordinates (both equatorial and Galactic), as well as the resolution (FWHM) after applying a Gaussian taper. We used this resolution in further analysis of the data.

Mosaic	WN50_074	WN50_090	WN66_045	WN66_064	WN66_083	WN66_102
$(\alpha, \delta)_{1950.0}$	(74°,50°)	(90°,50°)	(45°,66°)	(64°,66°)	(83°,66°)	(102°,66°)
(l, b)	(157°,6°)	(163°,14°)	(136°,8°)	(142°,12°)	(146°,19°)	(149°,26°)
Resolution	$6.9' \times 9.0'$	$6.9' \times 9.0'$	$6.9' \times 7.6'$	$6.9' \times 7.6'$	$6.9' \times 7.6'$	$6.9' \times 7.6'$
36 m	92/01/07	92/01/13	93/10/18	92/01/12	92/01/09	92/01/08
	15:24	16:06	18:45	14:26	17:36	17:14
48 m	91/12/31	92/01/06	93/10/24	92/01/05	92/01/02	92/01/01
	15:52	16:33	18:22	14:53	16:21	17:41
60 m	91/12/24	91/12/30	93/10/28	93/01/10	91/12/26	91/12/25
	16:20	17:01	18:06	14:31	16:49	18:09
72 m	91/12/06	91/12/02	93/11/01	91/12/01	91/12/05	91/12/04
	17:41	18:51	17:50	17:11	18:12	19:32
84 m	91/12/10	91/12/16	93/11/07	91/12/15	91/12/21	91/12/11
	17:48	17:56	17:27	16:16	17:44	19:04
96 m	91/12/17	91/12/23	94/10/09	91/12/22	91/12/19	91/12/18
	16:47	17:28	19:22	15:48	17:16	18:37

compared polarization angles in the area of overlap between mosaics. The corrections we found gave a closure error of about 1° when going from WN50_090 to WN50_074, WN66_064, WN66_083 and back to WN50_090. The WN66_045 and WN66_102 mosaics only have one neighbouring mosaic, which means that closure errors cannot be investigated for these mosaics. We assume that the alignment of these mosaics is of the same quality, even though the width of the distribution of polarization angle differences between the WN66_045 and WN66_064 mosaics is almost a factor of 2 larger compared to other mosaics.

8.3 Estimating large-scale polarization structure missing from WENSS

If an interferometer does not provide visibilities for the central part in the (u,v) plane LSS in the sky will be missing from the observations. For the WENSS data structure larger than about 1.5°– 2° is missing. We estimated the importance of structure on these scales from single-dish data from Brouw & Spoelstra (1976), 'BS') and Spoelstra (1984). This (linear) polarization dataset was obtained with the Dwingeloo 25m telescope at frequencies of 1411, 820, 610, 465 and 408 MHz, beam sizes (FWHM) range from 0.6° at 1411 MHz to 2.3° at 408 MHz. These data were however sampled on an irregular grid, with an average pointing distance of about 2°– 3° below a Galactic latitude of 20°, and about 5° above a latitude of 20°.

Before we can combine the BS and WENSS datasets we have to resample the BS data onto the WENSS grid, and we have to extrapolate the BS data from 408 MHz to the WENSS observing frequency of 325 MHz. These issues will be addressed in

the next two subsections. In the third subsection we discuss how we added the two datasets. In Sect. 8.5.2 we will discuss the robustness of the maps we made of the WENSS data including our estimates of the missing LSS.

8.3.1 Interpolating the Brouw & Spoelstra measurements

We addressed the problem of the irregular BS sampling by convolving the BS datapoints with a Gaussian kernel. The severe undersampling of the BS data sets a lower limit to the kernel width, and a reasonable upper limit can be found by requiring that the interpolated data should not be too smeared out. We used 5 different kernels, with FWHM ranging from 3.1° to 8.7°, to interpolate the BS measurements of Stokes Q and U and polarization percentages at their 5 observing frequencies. In addition we interpolated their maps of the intrinsic polarization angle of the emitted radiation and the RM maps they derived.

8.3.2 Extrapolating from 408 MHz to 325 MHz

The second problem is how to get from the BS measurements, with a lowest observing frequency of 408 MHz, to the 325 MHz of the WENSS data. To predict the polarized intensity at 325 MHz, $P_{\rm pred,325}$, we start with the observed polarized intensity at 408 MHz, $P_{\rm obs,408}$, convert it to total intensity and scale it up to 325 MHz using a power-law, and finally convert this back to polarized intensity at 325 MHz:

$$P_{\rm pred,325} \;=\; P_{\rm obs,408} \times (408/325)^{0.7} \times pp_{\rm frac} \tag{8.1}$$

where $pp_{\rm frac}$ is defined as

$$pp_{\rm frac} \equiv \frac{\text{polarization \% at 325 MHz}}{\text{polarization \% at 408 MHz}} \tag{8.2}$$

For the polarization angle at 325 MHz, $\phi_{\rm pred,325}$, we calculate the amount of Faraday rotation from:

$$\phi_{\rm pred,325} \;=\; \phi_{0,\rm BS} + {\rm RM_{BS}}\lambda^2_{\rm (325MHz)} \tag{8.3}$$

where $\lambda_{\rm (325MHz)}$ is the observing wavelength corresponding to 325 MHz. The $\phi_{\rm pred}$ are wrapped back to [$-90°$,$90°$]. For these predictions we use the intrinsic polarization angle of the emitted radiation ϕ_0 and RM as derived in Spoelstra (1984) ('$\phi_{0,\rm BS}$' and '$\rm RM_{BS}$'), together with the power-law index they adopt for the brightness temperature, 2.7 (which gives the 0.7 in Eqn. 8.1 since the 2.7 is used for scaling brightness temperatures, and we convert total intensities), and the polarization fractions they derive using this power-law at the different frequencies. Eqn. 8.3 requires an interpolated map of polarization angles, but interpolation cannot take the periodicity of the data into account. We tried to minimize this effect by interpolating $\phi_{0,\rm BS}$ data, which showed less $\pm\,90°$ transitions than other polarization angle data.

For the actual prediction of the large-scale Stokes Q and U at 325 MHz from the 408 MHz observations we must assume a polarization percentage at 325 MHz. From Fig. 6 in Brouw & Spoelstra (1976) it is clear that the average polarization percentages decrease slightly between 610 MHz and 408 MHz for $b = 0^\circ \rightarrow +20^\circ$. By using the same polarization percentage at 325 MHz and 408 MHz (at each frequency one value for the entire mosaic) we can be sure that we are not underestimating the predicted polarized intensity of the BS data at 325 MHz or, equivalently, the importance of LSS missing from WENSS.

We checked how well this scheme works by using the BS polarization data and interpolated $pp_{\rm frac}$ maps at 1411, 820 and 610 MHz to predict the observed polarized intensity at 820, 610 and 408 MHz respectively. If we do not use a pixel-to-pixel correction for the variation in polarization percentage but just one correction factor for the entire mosaic, we predict on average a polarized intensity that is about the same as the observed intensity. The spread (standard deviation) in the ratio of the predicted vs. the observed polarized intensities (about 0.2) is very similar to that obtained with a pixel-to-pixel correction for variations in polarization fraction, except at 408 MHz where it is 0.5. The equivalent width at 408 MHz when the pixel-to-pixel correction is used is still about 0.3. This increased spread can be explained by varying amounts of Faraday rotation between pixels, which becomes more important at lower frequencies. If part of the emission is actually thermal Bremsstrahlung, we would be overestimating the amount of emission at lower frequencies by using a synchrotron power-law with spectral index 2.7. Apparently this problem is not very important, given the results of our comparison between the predicted and observed polarized intensities.

From these results we conclude that our recipe to predict polarized intensity works sufficiently well that we can attempt to predict polarization data at 325 MHz from the BS 408 MHz data.

8.3.3 Adding the LSS estimate to WENSS

For an excellent review of different methods to add missing LSS to interferometer observations see Stanimirović (2002). We used the 'linear combination approach', where the Stokes Q and U maps from WENSS are added to the reconstructions of Stokes Q and U from the BS data. However, as we could not cross-calibrate the WENSS and BS data the intensity scales are not guaranteed to be identical. A potentially more serious problem is that the polarization vectors in WENSS and BS may have different zero-points. In Sect. 8.5.2 we will investigate the effects of such errors.

In the remainder of this chapter we will us the term 'WENSS LSS' when we refer to the WENSS dataset complemented by a BS reconstruction of the missing large-scale structure in Stokes Q and U at 325 MHz.

8.4 Discussion of the maps

In Fig. 8.1 we show the polarized intensity (in Kelvin) and polarization angle for WENSS and WENSS LSS respectively. Two of the brightest features in both WENSS and WENSS LSS, viz. the V-shaped feature at $(l, b) = (161^\circ, 16^\circ)$ and the ring-like structure at (137°, 7°), were analysed in detail by Haverkorn et al. (2003a, 2003b) using

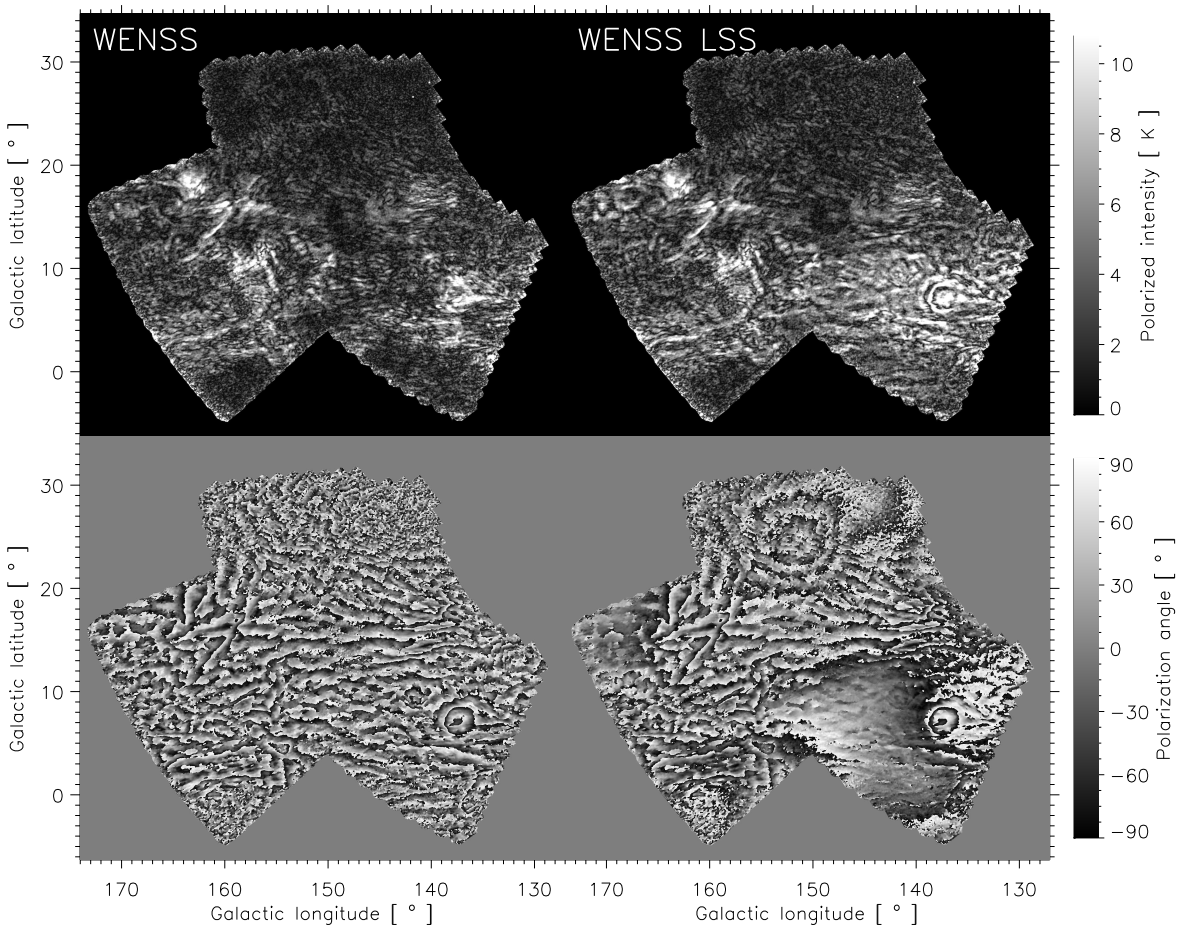

Figure 8.1 — Polarized intensity (top row) and polarization angle (bottom row) mosaics for WENSS (left column) and WENSS including our reconstruction of the missing LSS ('WENSS LSS'; right column). The beamsize of the observations (not indicated) is $6.7' \times 6.7' \csc \delta$ (FWHM). Properties of the reconstruction (see the text): width of the convolution kernel is 5.7° FWHM, $pp_{\rm frac} = 1$, $\Delta\phi = 0°$. The polarized intensity scale in both mosaics is the same. The nested rings in polarization angle in WENSS LSS at Galactic latitudes $b > 20°$ is an artefact due to a single large RM in the BS data surrounded by much smaller RM.

multi-frequency observations. The most striking feature in Fig. 8.1 is the clear stratification of polarization angles in Galactic latitude. In polarized intensity there are also linear features aligned with the Galactic plane, but these are not as clear as the structures in polarization angle. After adding the BS data to WENSS the ring-like structure that was already clearly visible in polarization angle now also becomes more conspicuously ring-like in polarized intensity.

In WENSS LSS there is an area between $136° \lesssim l \lesssim 152°$ and $-3° \lesssim b \lesssim 13°$ where the polarization angles apparently show no clear stratification with Galactic latitude. This region is part of what has previously been referred to by some as the 'fan' region, a large area of high polarized intensity with a strongly aligned projected magnetic field (see e.g. Figs. 6a to 6e in Brouw & Spoelstra 1976 and Fig. 3a in Spoelstra 1984). Where the BS signal is strong (in the upper left and lower right of the maps) there are clear differences between WENSS and WENSS LSS. In some parts this structure in BS seems

to erase the stratification of polarization angle we noted in the previous paragraph, but in large parts of WENSS LSS the stratification is still very clear. We will return to this point in Sect. 8.8. The nested imprint in polarization angle in WENSS LSS above $b = 20^\circ$ is caused by a single line-of-sight in the BS data that has a large RM, surrounded by much smaller RM. This creates steep gradients in RM which by Eqn. 8.4 are translated into steep polarization angle gradients in the reconstructed BS data. There also appears to be a general change in scale of the polarization features above $b = 20^\circ$ in WENSS. In the WN66_102 mosaic, which is the main source of data above $b \gtrsim 20^\circ$, an unusually large fraction of the (u,v) datapoints at the shortest baselines had to be flagged. This could be partly responsible for the observed change in structure. However, flagging of these data in other mosaics did not significantly alter the maps.

8.5 Quantifying the large-scale stratification of polarization angle: technique

The striking stratification of polarization angle in Fig. 8.1 suggests that there is a clear gradient in the direction of Galactic latitude, with only a relatively small variation in Galactic longitude, on which small-scale structure is superimposed. In order to quantify this large-scale gradient it is necessary to filter out these small-scale modulations, and also to correctly handle the 180° ambiguity of the polarization angle.

Resolving the 180° ambiguity by minimizing the difference in polarization angles of consecutive datapoints is sensitive to small-scale structure and noise. By using longer intervals in longitude or latitude we can fit the large-scale behaviour in polarization angle without being influenced too much by small-scale structure, and at the same time resolve the 180°ambiguity for all fitted datapoints together.

8.5.1 Determination

The different steps in our analysis of the polarization angle data are illustrated in Fig. 8.2. To determine the large-scale gradients we first calculate a weighted average of the polarization angles over an area of a fixed size ('bin', the average itself is indicated by '$\phi_{\rm bin}$' in Fig. 8.2). For strips along Galactic latitude these bins are $28' \times 7'$ in size (about 4×1 WENSS beams, taking into account the orientation of the beam in the Galactic coordinate frame) and for strips along Galactic longitude $14' \times 13'$ (or about 2×2 WENSS beams). In this way all bins contain about the same amount of beams, and the different shapes of the bins reflect the difference in steepness between gradients along Galactic longitude and latitude. If the spread of the polarization angles within the bin is larger than 20° the bin is discarded. Furthermore if a cut is placed on e.g. the signal-to-noise ratio of the pixels in a bin, at least 50% of the pixels should be usable (not flagged), otherwise the bin will also be discarded.

We then make a linear fit to all usable $\phi_{\rm bin}$ in an interval of a specified length, as shown in the second row of Fig. 8.2. We only made fits to intervals that contain at least 6 usable bins.

The fits were made using a standard χ^2 minimization. Instead of determining for every possible combination of gradient and offset which 180° 'flips' of the datapoints

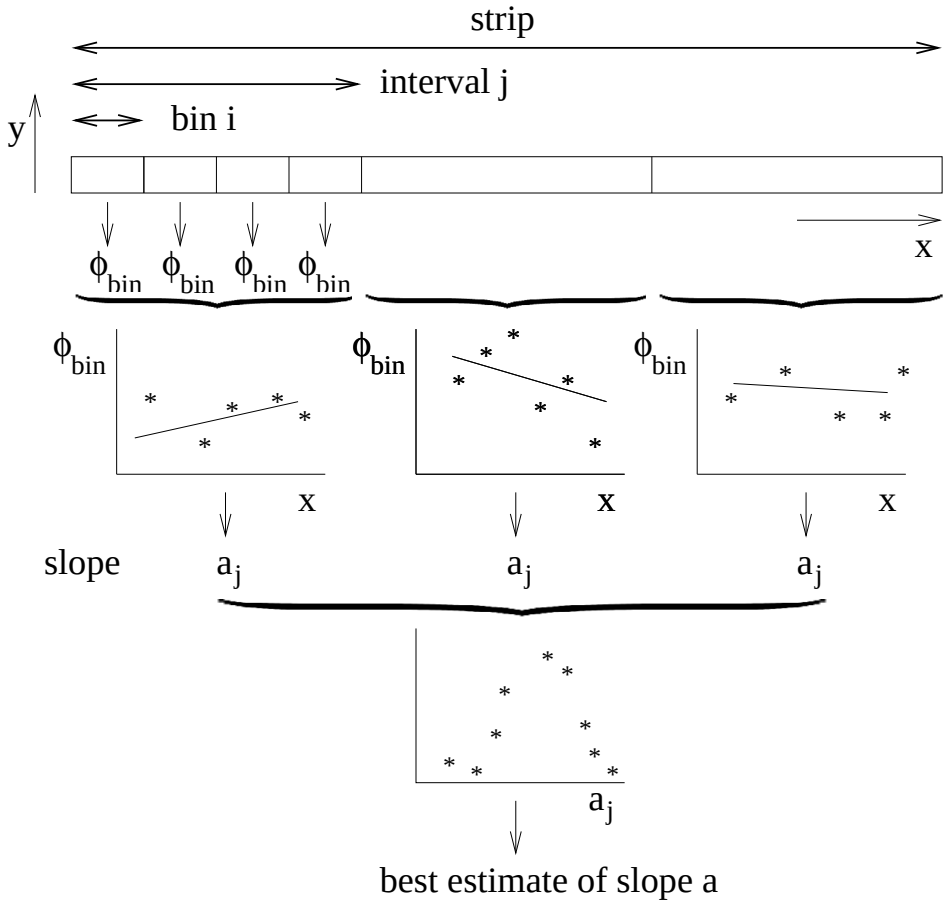

Figure 8.2 — Overview of how we analyse our polarization data. First we derive the average polarization angle in each bin (polarized intensity weighted), $\phi_{\rm bin}$. Bins are aligned with the 'x' and 'y' Galactic coordinates. We then fit a gradient to all $\phi_{\rm bin}$ in an interval, taking into account the periodic nature of the polarization angles, and we repeat this for all intervals in a strip along Galactic longitude or latitude. The gradients can then be used to investigate the average gradient per strip, as shown in the third row.

minimize the χ^2 for that combination it is also possible to determine which configurations of 'flips' are allowed by the data. The best fit to each configuration can then be found using a standard χ^2 minimization, and the configuration with the lowest χ^2 value will give the overall best fit. This method can be shown to be more reliable and time-efficient than an approach that 'probes' which gradient fits the data best. See appendix A for details. This technique can also be extended to situations where the horizontal distance between datapoints varies, as is the case when polarization angle observations at different wavelengths are used to derive RM.

For every strip we also fitted gradients that are shifted by half an interval length to prevent losing information (Nyquist sampling). In the remainder we include the gradients in these shifted intervals in our analysis.

8.5.2 Robustness of the gradients including the LSS estimate

When combining WENSS with our reconstruction of the large-scale structure there are several free parameters that needed to be chosen: the FWHM of the convolution kernel

for the BS data, the possible misalignment between the WENSS and BS polarization vectors ($\Delta\phi$) and differences in the amplitude scales of the WENSS and the BS data (which can be absorbed into differences in $pp_{\rm frac}$). We have investigated the effect of varying these parameters by comparing histograms of polarization angle gradients. In the remainder of this section we will consider only gradients along Galactic latitude and we test for only one interval length of 1.4°. As there is much more structure in the polarization angle gradients along Galactic latitude as compared to gradients along Galactic longitude, gradients along Galactic latitude are more sensitive to changes in the parameters we are investigating. An interval length of 1.4° gives the largest number of usable gradients in our dataset. Since at least 6 bins per interval must be usable to fit a gradient, the number of gradients fitted over short interval lengths will be limited. On the other hand for an area of a given size the number of intervals that can be fitted in that area decreases when the interval length goes up.

Note that we only investigate the *statistical* properties of the polarization angles that we find after adding the large-scale structure. We do not claim that individual pixels will have the correct polarized intensity or polarization angle.

Taking $\Delta\phi = 0°$ we found no significant differences in the distributions of the polarization angle gradients for all widths of the convolution kernel $\gtrsim 5°$ (FWHM). Smaller widths are simply too narrow to smoothly interpolate the undersampled BS datapoints, leading to artifacts. As there are hardly any differences for the different widths of the interpolation kernel we will be using the reconstruction made using the FWHM = 5.7° kernel for further analysis. Since the WENSS data is missing information on scales $\gtrsim$ 1.5°– 2° this means that we do not have information on scales from about 1.5° to about 5° after adding the BS reconstruction.

Since the WENSS and BS datasets do not overlap in the (u,v) plane it is not possible to determine if there is a misalignment between the WENSS and BS polarization vectors. We applied polarization angle offsets of 30°, 60°, 90°, 120° and 150° to the BS reconstruction with a kernel width of 5.7° before adding it to WENSS, and found no significant change in the gradient distribution. We therefore keep $\Delta\phi$ fixed at 0°.

Finally we considered the effects of differences in the intensity scales between WENSS and the reconstructed BS data. These consist of two contributions, the assumed polarization percentage at 325 MHz, which is important for $pp_{\rm frac}$ (cf. Eqn. 8.1), and differences in the flux scales between the WENSS and BS datasets (mentioned in Sect. 8.3.3).

In our reconstruction of the LSS missing from WENSS we assumed that the ratio of the polarization fractions at 325 MHz and 408 MHz (Eqn. 8.2) was 1. This ratio is more likely less than 1, maybe as low as 2/3, which would imply that there is less LSS missing from WENSS than we assumed. In the top two panels of Fig. 8.3 we show the gradient distributions for these two values of $pp_{\rm frac}$. The only major difference between the histograms is the fraction of gradients that are in the peak around 0 radians/deg. The second peak around -2.3 radians/deg hardly changes. In Sect. 8.5.3 we identify these peaks and explain the difference for the two values of $pp_{\rm frac}$. For now it suffices to say that this difference does not influence our results.

Since the influence of calibration differences between the WENSS and BS flux scales is probably smaller than the range of the two values of $pp_{\rm frac}$ we probed, we did not

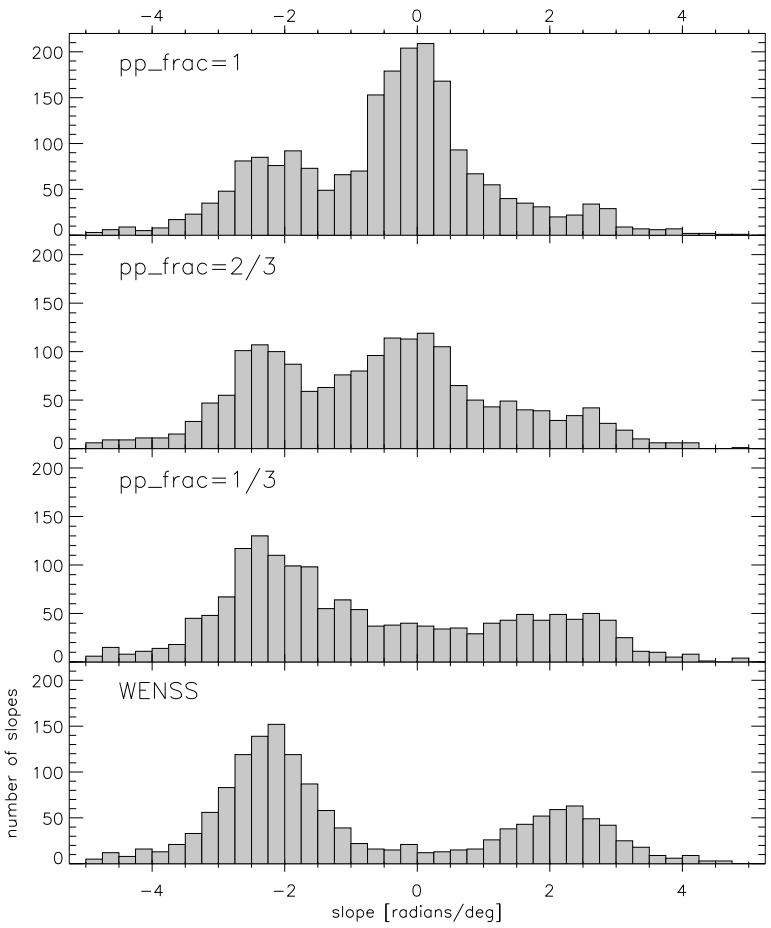

Figure 8.3 — Histograms of gradients fitted to the WENSS LSS data and to WENSS. The top panels show the result for a reconstruction of WENSS LSS using a $pp_{\rm frac}$ (defined in Eqn. 8.2) of 1, 2/3 and 1/3 respectively. In the bottom panel we plot the distribution of the gradients fitted to the WENSS data without the LSS reconstruction. In all cases the width of the convolution kernel used to reconstruct the LSS is 5.7° (FWHM), $\Delta\phi = 0°$, and the interval length over which the gradients were fitted is 1.4°.

consider this difference in flux scale as a separate issue.

8.5.3 Dependence on the value of $pp_{\rm frac}$

In Fig. 8.3 we plotted the distributions of the gradients fitted to the WENSS LSS dataset for $pp_{\rm frac}$ = 1, 2/3, 1/3 and for the original WENSS distribution ($pp_{\rm frac}$ = 0). Gradients in WENSS are found in two peaks at +2.3 radians/deg and −2.3 radians/deg. Since WENSS LSS is constructed as the vector sum of the WENSS and BS datasets, the relative strength of the BS and WENSS polarization vectors determines if the gradients in WENSS LSS show the clear bimodal behaviour of the original WENSS dataset. In this way the negative mode and tentative positive mode in the distribution of gradients in WENSS LSS in Fig. 8.3 can be identified as the two modes of the bimodal WENSS distribution shown in the bottom panel of Fig. 8.3.

When $pp_{\rm frac}$ increases, the BS signal becomes stronger compared to the WENSS signal, and the area where the BS signal is significantly stronger than the WENSS signal also increases. Both factors will 'convert' gradients from the steep gradients in the

peaks in the bimodal WENSS distribution to flatter BS gradients that are found in the peak around 0 radians/deg.

8.5.4 Dependence on interval length

In Sect. 8.5.2 we discussed the distribution of the fitted gradients along Galactic latitude $\partial\phi_{\rm pol}/\partial b$ for an interval length of 1.4°. The distributions in the top panels of Fig. 8.3 are clearly bimodal, with a central dominant peak around 0 radians/deg and a second clear peak at about −2.3 radians/deg. Furthermore there is tentative evidence for a plateau or small peak at around +2.5 radians/deg. For the shortest 2 interval lengths we probed (0.7° and 1.1°) only the central peak is visible, with a plateau extending to about −2.3°/bin. This plateau turns into a clear peak for intervals longer than 1.4°. At longer intervals (2.1°, 2.8°, 4.2° and 5.6°) the width of the central peak decreases and the positive peak at +2.5 radians/deg becomes more prominent. For interval lengths of 4.2° and 5.6° the number of gradients in the central peak decreases rapidly.

The decreasing width of the peak of gradients around 0 radians/deg when going to longer intervals can be explained by the fact that longer intervals will span positive and negative gradients on shorter length scales, and these 'subgradients' will partially cancel each other. At the same time the bimodal WENSS distribution is found for all interval lengths in the WENSS-only data. These effects combined account for the positive WENSS mode becoming more pronounced when going to longer intervals.

The average $\chi^2_{\rm red}$ of the fitted gradients increases when we use longer intervals, going from $\lesssim 4$ for interval lengths of 0.7° to > 20 for intervals of 5.6°. This is due to structure in polarization angle on scales smaller than the length of the fitted gradient.

8.6 Quantifying the large-scale stratification of polarization angle: results

8.6.1 Gradients along Galactic latitude

Fig. 8.4 shows the average polarization angle gradients along Galactic latitude $\partial\phi_{\rm pol}/\partial b$ for each Galactic longitude in our sample, where we separately fitted gradients to datapoints where the ratio of polarized intensities $P_{\rm WENSS}$:$P_{\rm BS}$ is < 3 or > 3 (top and bottom panels respectively).This neatly separates the two distributions of slopes. In the bottom panel of Fig. 8.4 we furthermore calculate the average gradient per strip separately for the positive and negative modes of gradients. Gradients in the top panel do not show this bimodal distribution. The solid line shows the weighted average over all Galactic longitudes; in the bottom panel the weighted average was calculated for the positive and negative modes separately. In both figures we only considered strips that have at least 4 usable gradients, a minimum number for an average gradient per strip to be statistically reasonable.

From Fig. 8.4 it is clear that the gradients in the areas in WENSS LSS where WENSS is relatively bright or faint have very different distributions: whereas the WENSS faint areas show no clear gradients, the WENSS bright areas show a clear bimodal distribution of gradients at about +2 radians/deg and about −2 radians/deg over a wide range of Galactic longitudes. Furthermore this bimodal distribution is present for all the in-

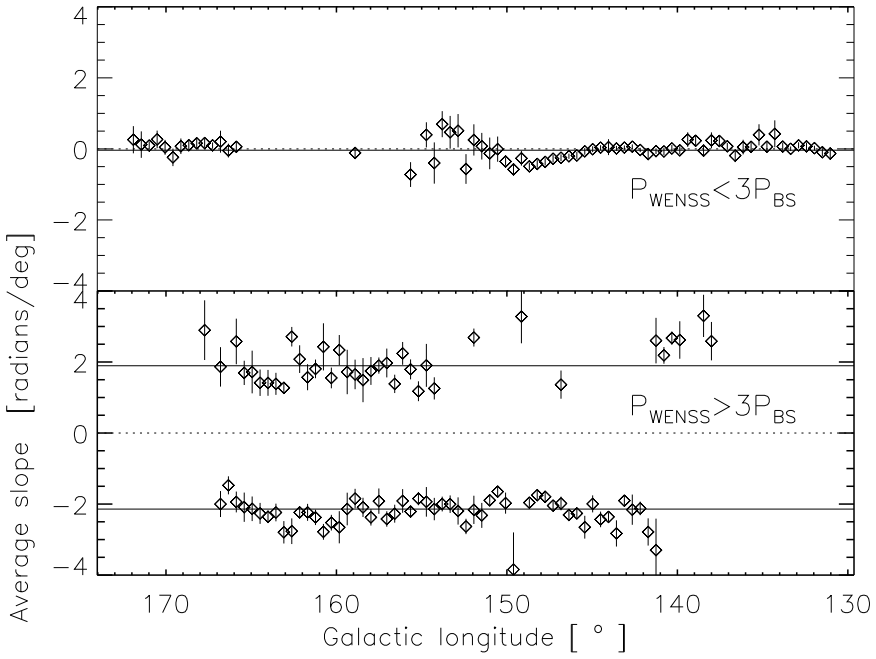

Figure 8.4 — Average gradient per strip along Galactic latitude as a function of Galactic longitude. In the top panel we plotted gradients fitted to datapoints where the polarized intensity from WENSS is less than 3 times the polarized intensity in BS, in the bottom panel we plotted gradients fitted to the remaining datapoints. In the lower panel we show the average gradient per strip for the positive and negative modes separately. We only plotted strips that had at least 4 usable gradients, in the bottom panel each mode has at least 4 usable gradients. The error bars are calculated from the spread (standard deviation) of the gradients in a strip, and are at the 1σ level. The weighted average of the datapoints is indicated by a solid line, and in the bottom panel the weighted average was calculated for the positive and negative modes separately. The width of the interpolation kernel was 5.7° FWHM, $pp_{\rm frac}$ = 1, and the interval length of the fitted gradients is 1.4°.

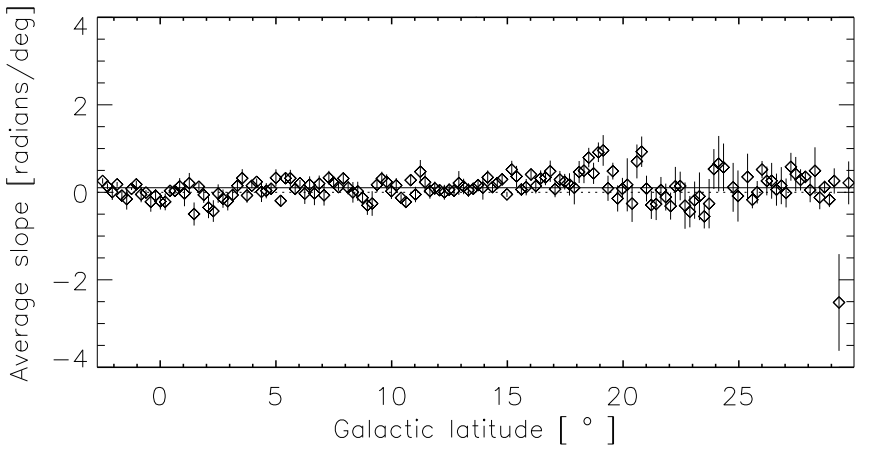

Figure 8.5 — Average gradient per strip along Galactic longitude, as a function of Galactic latitude, plotted on the same vertical scale as in Fig. 8.4. We only considered strips that have a least 4 usable gradients. The error bars are calculated from the spread (standard deviation) of the gradients in a strip, and are at the 1σ level. FWHM of the kernel used in the reconstruction is 5.7°, $pp_{\rm frac}$ = 1, interval length over which the intervals are fitted is 2.8°.

terval lengths we probed (from 0.7° to 5.6°). This last fact leads us to conclude that polarization angle structure on scales that are small compared to the interval length do not dominate our gradient-fitting analysis (these structures only increase the χ^2 of the fit), and that we are indeed sampling an underlying large-scale distribution.

8.6.2 Gradients along Galactic longitude

Gradients along Galactic longitude $\partial\phi_{\rm pol}/\partial l$ behave different from gradients along Galactic latitude. In Fig. 8.5 we show the average gradient per strip along Galactic longitude. We only plotted strips that contain at least 4 usable gradients. The weighted average of the datapoints is indicated by a solid line. Since there is no bimodal distribution of the gradients we did not have to separate the fitted gradients as we did for gradients along Galactic latitude. From this figure it is clear that the average gradient per strip is not significantly different from 0 radians/deg. In the original WENSS dataset we found the same result for gradients along Galactic longitude. The increased spread of the average gradient per strip and also the increased errors per data point above a Galactic latitude of $\approx 18°$ coincides with a change in scale of the structure in polarization angle, which we noted earlier in the WENSS LSS mosaic in Fig. 8.1, and/or a decrease in signal-to-noise ratio.

For the different interval lengths that we probed for strips along Galactic longitude (1.4°, 2.1°, 2.8°, 4.2° and 5.6°) the distribution of the gradients remains single-peaked, and the average gradient along Galactic longitude is always close to 0 radians/deg, but the average $\chi^2_{\rm red}$ per gradient increases as the interval length increases from < 5 to about 10 for the longest intervals.

8.7 Comparison to previous results

We assume that the amount of Faraday rotation is given by $\phi - \phi_0 = {\rm RM}\lambda^2$. This means that if there are no gradients in the intrinsic polarization angle of the emitted radiation ϕ_0, the gradients in polarization angle $\partial\phi_{\rm pol}/\partial x$ (where 'x' is either Galactic longitude or latitude) can be directly translated into RM gradients with:

$$\frac{\partial {\rm RM}}{\partial x} = \frac{1}{\lambda^2}\frac{\partial \phi_{\rm pol}}{\partial x} \tag{8.4}$$

ϕ_0 varies very slowly with position in the region we are considering (see the directions of $\vec{B}_\perp$ plotted in Fig. 8.6), which means that the contribution of $\partial\phi_0/\partial x$ to ∂ RM$/\partial x$ is small. When we include the measured variations in ϕ_0 in our analysis we find identical results.

To test the reliability of our 'translation' of polarization angle gradients as RM gradients we calculated gradients in RM based on the BS dataset. We rederived the RMs from the BS polarization angle measurements to get also a $\chi^2_{\rm red}$ measure of the quality of the fitted RMs, using the 1/signal-to-noise estimate of the error in the measured polarization angle described in Brouw & Spoelstra (1976). In calculating RM gradients we only considered RMs with $\chi^2_{\rm red} < 5$, based on polarization angles for at least 4 of the 5 observing frequencies. In Fig. 8.6 we show these RMs. The RM gradients we

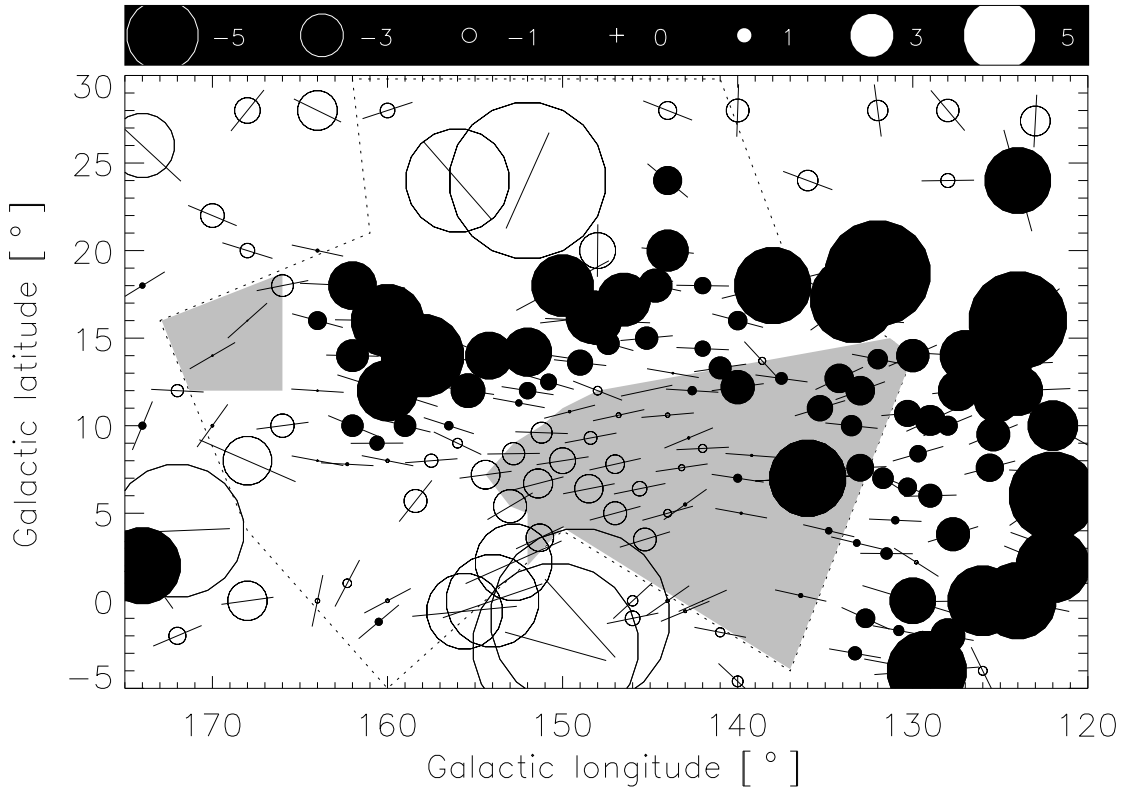

Figure 8.6 — RM and direction of $\vec{B}_\perp$ derived from BS polarization-angle measurements in the area covered by WENSS (enclosed by the dotted line) and its surroundings. The BS bright areas are shown as grey filled polygons. RM are shown when the fit to the observed polarization angles has $\chi^2_{\rm red} < 5$, and polarization angles should be available for at least 4 of the 5 wavelengths. The scale of the plotted symbols is linear and is illustrated in the top panel, units are radians/m^2.

calculated from the BS data use pairs of RM for which the separation in Galactic longitude was smaller than 0.2 times the separation in Galactic latitude to constrain the orientation of the gradients fitted to the RMs. We only fitted gradients to lines-of-sight that were less than 5° apart, which is slightly larger than the average distance between the datapoints shown in Fig. 8.6.

Spoelstra (1984) points out that for a given sampling of λ^2 space the smallest λ^2 distance between two consecutive datapoints will set a maximum to both the RMs that can be determined and to the $B_\parallel$ that is derived from these RMs. Spoelstra's argument is however based on only 2 datapoints, and the other available datapoints will make this criterion less strict. The RMs that were calculated by Haverkorn et al. (2003a) are comparable in size to the RMs found by BS in the same region, but are derived from 5 MHz wide bands around about 350 MHz. An additional 180° difference in polarization angles between two such consecutive bands would require a RM that is about 150 radians/m^2 larger than they derive. In the direction we are considering such large RMs are only observed in pulsars that lie in or beyond the Perseus arm, and since depolarization effects will limit the line-of-sight, we do not believe that such large RMs should be observable in these data. Therefore we think that also the BS RMs are correct and do not suffer from 'aliasing' due to the poor λ^2 sampling.

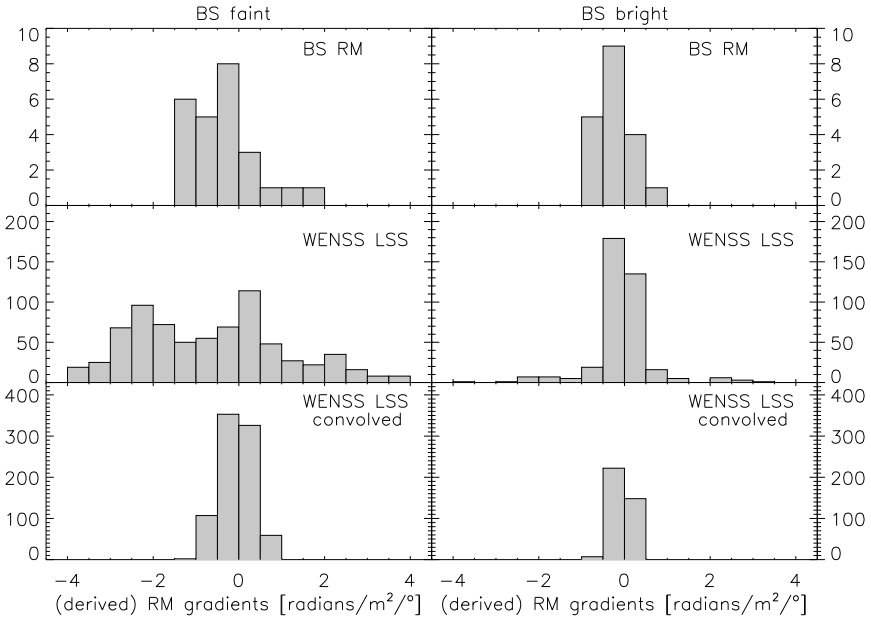

Figure 8.7 — Histograms of the gradients fitted to the RMs that we derived from the BS polarization-angle measurements (top row), and the gradients $(1/\lambda^2) \times \partial\phi_{\rm pol}/\partial b$ derived from WENSS LSS (bottom two rows). The RM gradients we derive only use RMs with $\chi^2_{\rm red} < 5$, and polarization angles should be available for at least 4 of the 5 wavelengths. The bottom row shows gradients in the WENSS LSS data after we convolved it with a 2.3° beam. Gradients in the left column were fitted to the BS faint data, gradients in the right column were fitted to the BS bright data. The gradients fitted to the BS RMs were at most 5° long, the gradients fitted to the WENSS LSS data were 4.2° long. See the text for details.

In Fig. 8.7 we show the gradients we fitted to the BS RMs separately for the BS faint and bright areas. If we found a significant difference between the polarization angle distribution in WENSS LSS and the original distribution in WENSS such an area is identified as BS bright. In Fig. 8.6 we indicated the BS bright areas by a grey shading.

In the second row of Fig. 8.7 we show the distribution of the gradients we fitted to the polarization angle data, scaled to gradients in RM by the factor of $1/\lambda^2$ in Eqn. 8.4. These gradients were fitted over an interval of 4.2°.

To see if the distribution of the BS RM gradients can be scaled up to the gradients we derived from WENSS LSS we used a Kolmogorov-Smirnov two sample test using Eqn. 8.4 as a description for the mapping of the BS gradients onto the WENSS gradients, where we apply a scale factor to the BS RMs. At the 5% confidence level for rejection scale factors between 1.7 and about 3.1 are permitted, with an average value of about 2.4. The KS probability has a maximum of 0.7 for a scale factor of 2.2.

In the BS faint region the RM gradients we derived are about a factor of 2.4 smaller than the RM gradients implied by the WENSS data. To simulate the effects of the difference in size between the WENSS and BS beams we convolved the WENSS LSS map with the 2.3° beam of the BS data at 408 MHz. The results for the convolved data are shown in the bottom row of Fig. 8.7. Clearly the larger telescope beam of the BS data can account for the narrowing of the distribution and the apparent disappearance of the negative mode.

8.8 Physical picture

In this section we will interpret our data in terms of a simple model of the ISM. In Sects. 8.8.1 and 8.8.2 we will derive information on the magnetic field component along the line-of-sight and on the component perpendicular to the Galactic plane. In Sect. 8.8.3 we will discuss what we infer from our data about the so-called 'fan' region.

In our model we simulate a single line-of-sight through a volume of ISM with synchrotron emission and/or Faraday rotation. This volume contains both a regular and a random magnetic field. The regular field has a constant strength and direction, and the random field has a constant strength, but it changes direction on a scale that is (much) smaller than the size of the simulated volume. This ensures that there are enough draws of the orientation of the random field component along the line-of-sight that its statistical properties can be calculated analytically. The amount of emission only depends on the length of the total magnetic field vector (the sum of the regular and random components) projected perpendicular to the line-of-sight, as indicated in Appendix A of Haverkorn et al. (2004). Similarly, the total magnetic field projected along the line-of-sight sets the amount of Faraday rotation. However, only a fraction of the line-of-sight is filled with cells that contain Faraday rotating electrons; in each of these cells the electron density is constant. The simulated volume of ISM is illuminated from the back by polarized synchrotron radiation; this background is assumed to have no internal Faraday rotation.

One important ingredient in this model is the dispersion measure DM, the line-of-sight integral of the electron density, $\mathrm{DM}[\mathrm{cm}^{-3}\mathrm{pc}] = \int_{l.o.s.} n_e \mathrm{d}l$, which we cannot determine from our observations. To estimate DM we integrated the NE2001 electron density model by Cordes and Lazio (2003) out to 500 pc ('local') and 2 kpc (about the distance of the Perseus arm for these lines-of-sight). Since pulsars in the second Galactic quadrant that lie beyond the Perseus arm have RMs that are typically 100 radians/m^2, at least an order of magnitude larger than RMs of pulsars that lie in front of the arm (see the Galactic distribution of pulsars in e.g. Weisberg et al. 2004), we argue that the magnitude of the BS RMs, typically less than 10 radians/m^2, puts the Faraday-rotating electrons that produce these RMs between us and the Perseus arm, which means that the 2 kpc we use is a reasonable upper limit to the length of the line-of-sight. Note that for the 2 kpc line-of-sight and a Galactic latitude of 18° (the maximum latitude that we will probe - see Table 8.2), the line-of-sight reaches a maximum height above the Galactic plane of about 600 pc, which means that we do not reach out into the Galactic halo.

8.8.1 Deriving the line-of-sight magnetic field component

In this section we will derive strengths for the magnetic field component along the line-of-sight for a number of Galactic latitudes. We will use the RMs determined from the BS data and the DM we calculated from the NE2001 model for the 2 assumed lengths of the line-of-sight.

Following Sokoloff et al. (1998) we introduce the Faraday depth $\mathcal{R}$ defined as the line-of-sight integral of the product of the magnetic field and the electron density

$\mathcal{R} = 0.81 \int_{l.o.s.} n_e \vec{B} \cdot \mathrm{d}\vec{l}$, $[B] = \mu$G, $[n_e] = \mathrm{cm}^{-3}$, $[|\vec{l}|] = \mathrm{pc}$, and $[\mathcal{R}] = \mathrm{radians/m}^2$. As is customary the length of a vector will be denoted by $B = |\vec{B}|$. Since it is an integral along the line-of-sight it will not depend on the 'clumpiness' of the distribution of the Faraday rotating electrons.

If the line-of-sight is long enough, or if the average is taken over a number of lines-of-sight that are short, the contribution of the random magnetic field to $\mathcal{R}$ will cancel out in our model, and $\mathcal{R} \propto \mathrm{DM} B_{\mathrm{reg},\parallel}$. This means that we can calculate $B_{\mathrm{reg},\parallel}$ from $\mathcal{R}$ and DM using

$$B_{\mathrm{reg},\parallel} = \frac{\mathcal{R}}{0.81\mathrm{DM}} = \frac{\int_{l.o.s.}^{observer} n_e \vec{B} \cdot \mathrm{d}\vec{l}}{\int_{l.o.s.} n_e \mathrm{d}l} \equiv \langle B_{\mathrm{reg},\parallel} \rangle_{n_e} \tag{8.5}$$

where the magnetic field strength is in μG. The ratio of integrals on the r.h.s. of Eqn. 8.5 defines the electron density weighted average $B_{\mathrm{reg},\parallel}$, or $\langle B_{\mathrm{reg},\parallel} \rangle_{n_e}$. Since the $B_{\mathrm{reg},\parallel}$ we calculate from Eqn. 8.5 is defined to be constant throughout our model, $\langle B_{\mathrm{reg},\parallel} \rangle_{n_e}$ will be equal to $B_{\mathrm{reg},\parallel}$ in this case.

The rotation measure RM is defined as the derivative of polarization angle with respect to wavelength squared and, contrary to $\mathcal{R}$, it does depend on the exact distribution of emitting and Faraday rotating regions along the line-of-sight. This has been shown for example in Sokoloff et al. (1998). Therefore the ratio of RM to $\mathcal{R}$ will be different for different configurations of synchrotron-emitting and Faraday-rotating regions.

We use BS polarization angle measurements with Galactic longitudes between about 150° and 160° and Galactic latitudes between 5° and 20°, excluding the Auriga region between $156° \lesssim l \lesssim 165°$ and $12° \lesssim b \lesssim 18°$ where the RMs might be affected by local structure. Most of the BS data we consider thus lie in an area of WENSS LSS where LSS does not dominate. We estimated RMs and the intrinsic polarization angle of the emitted radiation ϕ_0 from neighbouring (measured) lines-of-sight along 6 Galactic latitudes at a Galactic longitude of 152°, as shown in the first 3 columns of Table 8.2, and the errors given in the headings of these columns reflect our estimate of the spread around these averages. ϕ_0 can be derived by extrapolating the BS polarization angles to $\lambda = 0$ meters. Note that in the 3rd column of Table 8.2 we indicate the direction of the magnetic field perpendicular to the line-of-sight, $\hat{\mathbf{B}}_\perp$, which is perpendicular to the direction indicated by ϕ_0. At other Galactic longitudes the number of reliable RMs is either much lower, or LSS is missing from the interferometer observations. To correct the RMs in Table 8.2 for beam effects these values had to be multiplied by a factor of 2.4 ± 0.7 as discussed in Sect. 8.7.

In columns 4 and 6 of Table 8.2 we show the values for $B_{\mathrm{reg},\parallel}$ we calculated from Eqn. 8.5 for the two assumed lengths of the line-of-sight. The error in $B_{\mathrm{reg},\parallel}$ is based on the range in Galactic latitude of the position of the line-of-sight (which gives a range in allowed DM), the error in the estimated RMs, and the uncertainty in the scale factor between the WENSS and BS RM gradients. We compared the $B_{\mathrm{reg},\parallel}$ found using Eqn.

8.5 to the $B_{\mathrm{reg},\parallel}$ from the model by Haverkorn et al. (2004a), in the remainder referred to as 'H04a'. In their model Faraday rotation occurs in the synchrotron-emitting thin disc in cells filled with thermal electrons. Cell sizes range between 1 and 60 pc. These cells have a constant electron density of 0.08 cm^{-3}, and the filling factor assumed in this model is 0.2 (values based on Reynolds 1991). The height of the synchrotron emitting thin disc is 180 pc (Beuermann et al. 1985). The H04 model contains both a regular magnetic field, with constant strength and direction, and a random field, with constant strength, but a direction that is randomly drawn in each cell. The thin disc is illuminated from the back by a synchrotron-emitting halo. Emission and Faraday rotation in this halo are assumed to occur on such large angular scales that the emission from the halo has a uniform total and polarized intensity and direction of the plane of polarization.

The H04 model simulates a large number of lines-of-sight that each have their own distribution of Faraday rotating cells. By specifying the strength and the direction of $\vec{B_{\mathrm{reg},\parallel}}$ and $\vec{B_{\mathrm{reg},\perp}}$, the strength of $\vec{B_{\mathrm{ran}}}$, and the total and polarized intensities of the background illuminating the thin disc, the H04 model predicts by numerical radiative transfer the observables Stokes I, RM, Stokes Q and U and their standard deviations (the spread of the observables being created by the different configurations of Faraday rotating cells along the line-of-sight). By comparing these output parameters to their observations, H04 constrain the range of allowed input parameters.

One major advantage of the H04 model over our own analytical model is that the numerical treatment in the H04 model can predict RMs. The RM is difficult to calculate analytically, since every configuration of Faraday rotating cells will have a different amount of depolarization, which means that the behaviour of the polarization angles with wavelength squared will be different. Therefore our model depends on a relation between RM and $\mathcal{R}$ as input, which we inferred by comparing our results to the ones from the H04 model.

H04 find a $B_{\mathrm{reg},\parallel}$ of -0.42 μG in the direction of their Auriga field. When we use Eqn. 8.5 we find a value of -0.40 μG if we use the same input DM as in the H04 model, and by setting $\mathcal{R}$ = RM. From this we conclude that setting $\mathcal{R}$ = RM works well in this case. The DM used in the H04 model in this direction is 10 cm^{-3}pc, lower than the 31 cm^{-3}pc we determine from the NE2001 model by integrating it out to the same distance. In part this difference in DM is due the filling factor that is used in the H04 model. For the clumpy disc they model, where all cells have the same electron density, a filling factor of 0.4 instead of the 0.2 used in the H04 model would agree better with the Reynolds data. This doubles the DM in the H04 model, bringing it closer to the value predicted from the NE2001 model.

8.8.2 Reconstructing the 3D magnetic field vector. The magnetic field strength perpendicular to the Galactic plane

In this section we will derive information on the magnetic field component perpendicular to the Galactic plane $\vec{B_{\mathrm{z}}}$. Since our derivation will only apply to the regular magnetic field we will drop the 'reg' subscript when we indicate field components. The relations between the different magnetic field components are illustrated in the

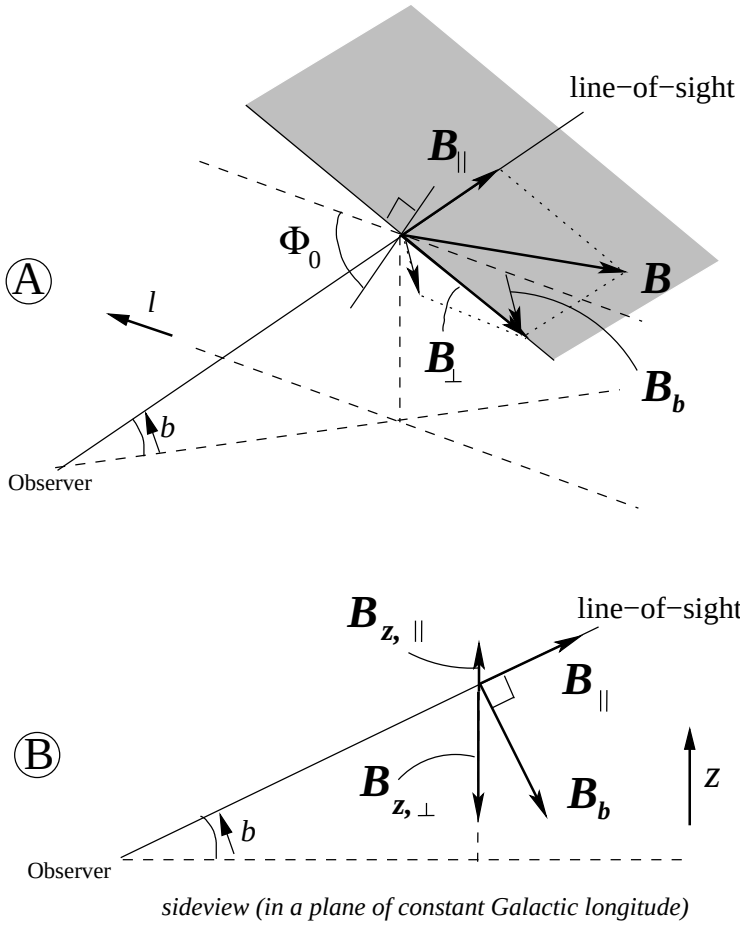

Figure 8.8 — Relations the different magnetic field components that are discussed in the text. Panel B shows panel A from the side in a plane of constant Galactic longitude. The magnetic field components along and perpendicular to the line-of-sight are $\vec{B_\parallel}$, resp. $\vec{B_\perp}$. The plane spanned by $\vec{B_\parallel}$ and $\vec{B_\perp}$ is indicated in grey. $\vec{B_\perp}$ is directed perpendicular to ϕ_0, both being defined in the plane perpendicular to the line-of-sight. $\vec{B_b}$ is the component of $\vec{B_\perp}$ along Galactic latitude. We indicated the directions of increasing Galactic longitude l and latitude b and height above the Galactic plane z, and defined B_b and B_z to increase when moving away from the Galactic plane.

top panel of Fig. 8.8. First we will derive the strength of the magnetic field component perpendicular to the line-of-sight $\vec{B_\perp}$ and its orientation. $\vec{B_\perp}$ can be decomposed into a component along Galactic longitude and a component along Galactic latitude $\vec{B_\mathrm{b}}$. The component of $\vec{B_\perp}$ along Galactic longitude does not contribute to $\vec{B_\mathrm{z}}$. $\vec{B_\mathrm{z}}$ can then be calculated from the projected $\vec{B_\mathrm{b}}$ and $\vec{B_\parallel}$: $B_z = B_{z,\perp} + B_{z,\parallel} = B_b \cos(b) - B_\parallel \sin(|b|)$, as illustrated in the bottom panel in Fig. 8.8. The sign of B_z is such that a positive B_z points away from the Galactic plane both for positive and negative Galactic latitudes. The sign of B_b should be chosen accordingly.

The strength of $\vec{B_\perp}$ cannot be determined from our data. However, if we interpret the different $B_\parallel$ that we determine in Table 8.2 as the result of different orientations of $\vec{B}$ with respect to the line-of-sight (assuming that $\vec{B}$ has a constant length for these lines-

Table 8.2 — Estimated average RM and direction of $\vec{B}_\perp$ ('$\hat{\mathbf{B}}_\perp$') from the BS data at a longitude of about 152° for different Galactic latitudes. Estimates of the uncertainties in the parameters are given in the fourth row and in the columns for $B_{\mathrm{reg},\parallel}$, and are based on the range in Galactic latitude of the position of the line-of-sight, the spread of both RM and direction of $\hat{\mathbf{B}}_\perp$, the uncertainty in the scale factor between the WENSS and BS RM gradients, and the modeling uncertainties in the H04 model. Using Eqn. 8.5 the measured RM (after being corrected for beam effects as described in Sect. 8.7) together with DM calculated from the NE2001 model out to 500 pc and 2 kpc, can be used to calculate the magnetic field component along the line-of-sight, $B_{\mathrm{reg},\parallel}$. B_z can then be calculated by projecting $\vec{B}_\parallel$ and the component of $\vec{B}_\perp$ along Galactic latitude, as is illustrated in the bottom panel of Fig. 8.8.

			500 pc line-of-sight		*2 kpc line-of-sight*	
b	$\langle \mathrm{RM}_{BS} \rangle$	$\hat{\mathbf{B}}_\perp$	$B_{\mathrm{reg},\parallel}$	B_z	$B_{\mathrm{reg},\parallel}$	B_z
[°]	[rad/m^2]	[°]	[μG]	[μG]	[μG]	[μG]
0.5	0.3	6°		0.32		0.20
7[a]	2.0	10	0.24 ± 0.08	0.51	0.07 ± 0.02	0.33
9	1.5	0	0.18 ± 0.06	-0.03	0.06 ± 0.02	-0.01
10.5[b]	0	-	0 ± 0.04	-	0 ± 0.01	-
12	-1.2	-12	-0.14 ± 0.05	-0.61	-0.05 ± 0.02	-0.39
14	-3.4	-14	-0.41 ± 0.12	-0.64	-0.14 ± 0.04	-0.43
18[b]	0	-	0 ± 0.03	-	0 ± 0.01	-

[a] The $b = 7°$ datapoint lies in a part where the BS data is 'intermediate' in brightness, whereas all other datapoints are in BS faint areas. B could therefore be different compared to other datapoints.

[b] At these latitudes ϕ_0 could not be reliably estimated, which means that B_z could not be determined.

of-sight), $B_\perp$ can be calculated as a projection of $\vec{B}$. To do this B has to be known. In the vicinity of the sun pulsar RMs give a B that is typically about 2 μG, and equipartition arguments indicate for the total magnetic field (regular+random) a strength of about 6.5 μG (Beck et al. 1996). In H04 both $B_\parallel$ and $B_\perp$ are derived, which give a $B \approx 3.3$ μG. If we assume that B in the direction of H04's Auriga field is the same as in our data, we only have to rescale their B to the lengths of the lines-of-sight we use. The scaling of $B_\parallel$ depends only on DM, and we can use our analytical model to derive the scaling properties of $B_\perp$ from Stokes I and σ_I, in a similar way as was used in H04. In this way we find $B = 3.2 \pm 0.5$ and 2.0 ± 0.4 μG for our 500 pc and 2 kpc lines-of-sight.

B_b can be derived from $B_b = B_\perp \sin(2(\phi_0 + \pi/2))$. Note that since ϕ_0 follows from $1/2 \arctan(U/Q)$, where U and Q refer to Stokes U and Q respectiely, it has a period of 180°, which is why there is a factor of 2 in this equation. The plane of polarization (and therefore also the direction of $\vec{B}_\perp$) is perpendicular to ϕ_0, which accounts for the $\pi/2$ in the expression for B_b. Once the orientation of the plane of polarization is known, $\vec{B}_\perp$ can still point in 2 directions. The global geometry of the magnetic field can be used to determine in which of the two possible directions $\vec{B}_\perp$ is pointing: Brown et al. (2003) and Johnston-Hollitt et al. (2004) derive from RMs of extragalactic radio sources that the field points towards smaller Galactic longitudes. We will assume that the features we observe in WENSS LSS follow the same global field direction.

The errors we quote for $B_\parallel$ and B_z are based on the range in Galactic latitude for

the position of the line-of-sight, the spread in RM and the orientation of $\hat{\mathbf{B}}_\perp$ and (in the case of B_z) also uncertainties in the parameters modeled by H04. Even though our estimates of B_z are 2σ values at best, B_z is between $1/2$ to 4 times $B_\parallel$, for both lengths of the line-of-sight that we use. Since in all these cases the $B_\parallel$ and B_b components are small compared to the total B, most of $\vec{B}$ should be oriented along Galactic longitude, and therefore the magnetic field must be azimuthal, and directed towards smaller Galactic longitudes. Using pulsar observations Han and Qiao (1994) estimate that $B_z \approx 0.2 - 0.3\ \mu$G, similar to our results.

To reach these conclusions we made a number of assumptions that, though reasonable, are hard to prove using our current data. We did not take into account the intrinsic difficulty of constraining the NE2001 model in the second Galactic quadrant which is the result of the small number of known pulsars in this direction. Since this only influences DM and therefore $B_\parallel$, but does not influence $B_\perp$, we think it unlikely that the error in DM is so large that it influences our conclusion of an azimuthal field. With better datasets, of the type described in Haverkorn et al. (2003a, 2003b), some of these assumptions could be tested for their validity, and the errors in $B_\parallel$ and B_z could also be reduced. We have obtained several of such datasets recently.

To investigate if the results we present here can be considered 'typical' for this quadrant we can look at the BS RMs that lie outside the area covered by WENSS, since we showed in Sect. 8.7 that the BS RMs can be considered as scaled-down versions of WENSS RMs (at least in the BS faint part of WENSS LSS). Outside WENSS the BS sampling however becomes much poorer, and also the RMs seem to become much less correlated (which is probably in part due to the poorer sampling). Therefore it is at the moment not possible to investigate whether the results we present here apply only to a local feature or are more general.

8.8.3 Implications for the fan region

The region between $136^\circ \lesssim l \lesssim 152^\circ$ and $-3^\circ \lesssim b \lesssim 13^\circ$ is part of the so-called 'fan' region that we already mentioned in Sect. 8.4. In the original WENSS dataset (without the single-dish information) the polarization angle gradients in this area are bimodally distributed like in the rest of WENSS, as is also clear from the bottom panel in Fig. 8.3, where there is a lack of gradients around 0 radians/m^2/deg even though this figure includes polarization angle gradients in the fan region. One difference between the fan and the region outside the fan is that the ratio of positive to negative polarization angle gradients in WENSS inside the fan is about 1:1, whereas this ratio is more 1:3 for WENSS as a whole.

We suggest that the fan is a region of enhanced emission that lies in front of the emission we see in WENSS. Due to the short lines-of-sight to the fan in this model, Faraday rotation effects, in particular variations in the amount of Faraday rotation across the fan surface, will be small. The polarized signal emitted by the fan will then be modulated by the foreground Faraday screen on angular scales that are too large to be detected by an interferometer due to its missing short spacings. The longer lines-of-sight to the background emission would make Faraday rotation effects strong enough that the background *can* be detected by the interferometer. We therefore identify struc-

ture we see in WENSS as resulting from the Faraday modulation of this background emission. If the fan would lie at the same distance as the WENSS emission it should also be visible in the interferometer data. In the large single-dish beam the background emission, which is highly structured in polarization angle due to Faraday rotation, will get beam depolarized. If the fan would lie at the same distance as the background it too would get beam depolarized in the single-dish data, contrary to what we observe.

In this model the separation along the line-of-sight between the fan and the background emission is determined by the amount of small-scale structure in polarization angle. If the amount of structure on small angular scales is smaller than what we derive from WENSS (e.g. due to missing short baselines) the separation in distance becomes less. However the similarity of BS RMs inside and outside the fan, supplemented by the presence of a bimodal WENSS distributed in both these regions, suggests that we are not grossly overestimating the variation of polarization angles on small scales.

Spoelstra (1984) concludes from a comparison between the polarization angles of starlight emitted by stars at known distances and ϕ_0 that the Faraday rotating medium responsible for the RMs observed towards the fan should lie within a few hundred parsecs. RMs derived from the diffuse ISM in the direction of the fan are small compared to RMs derived for pulsars that, in this part of the Galaxy, lie beyond the Perseus arm, which would also indicate that most of the Faraday rotating medium seen towards the fan lies in front of the Perseus arm. Wolleben (2005) suggests that the source of the emission seen towards the fan region forms a single physical structure that extends both above and below the Galactic plane. He tentatively identifies the low polarized intensities near the Galactic plane that appear to separate the parts of the fan region above and below the Galactic plane as depolarization occurring in HII complexes. This puts the source of the emission observed towards the fan beyond these complexes. One of the furthest of these complexes (with a moderate correlation with polarized intensity) is the IC1795/1805 complex around $(l, b) = (135^\circ, 1^\circ)$ at 2.1 kpc. The observations by Wolleben et al. were carried out at 1.4 GHz, whereas Spoelstra uses also data at much lower frequencies. Since depolarization (both line-of-sight and beam) will be more important at lower frequencies, the bulk of the observed signal will be coming from closer to the observer than at higher frequencies, which makes comparing data at such different frequencies more difficult.

The fan region can clearly be seen in the RMs in Fig. 8.6. One striking feature appears to be a (smooth) change in RM from positive at around $(l, b) = (150^\circ, 6^\circ)$, to about 0 at $l = 142^\circ$ to negative at around $(l, b) = (130^\circ, 11^\circ)$. Furthermore the negative and positive RMs are of about the same magnitude. A physical model of this structure would require knowledge of the strength of the magnetic field component in the plane of the sky. The observations and modelling by Haverkorn et al. (2003b) imply a strong (≈ 3.2 μG) field in the plane of the sky, but their modelling includes also the 'ring' feature at $(l, b) = (137^\circ, 7^\circ)$. There are a number of indications that this ring structure could be a different type of object than its surroundings: the single large RM in Fig. 8.6 lies at the position of the ring, whereas the other RMs in its vicinity are smaller, and furthermore the single-dish data show a local depression at the position of the ring in the generally high polarized intensities seen towards the fan region.

8.9 Summary & Conclusions

We have studied the polarization properties of the diffuse Galactic radio background at 325 MHz in the region $130^\circ \lesssim l \lesssim 173^\circ$, $-5^\circ \lesssim b \lesssim 31^\circ$ using the WENSS dataset. We determined gradients in polarization angle (which can be translated into gradients in RM), taking into account the periodic nature of the polarization angle data. The WENSS data show gradients that are coherent over large areas. We find a bimodal distribution of gradients along Galactic latitude, with peaks at +2.1 radians/deg and -2.1 radians/deg, with about three times as many gradients in the negative mode as there are in the positive mode, and with hardly any gradients in between the two modes. Along Galactic longitude the gradients are in general nearly zero.

We investigated the importance of LSS missing in our data from the higher frequency single-dish data obtained by Brouw&Spoelstra (1976). We first interpolated between the lines-of-sight of the single-dish data, followed by an extrapolation to 325 MHz, the observing frequency of WENSS. We ran several consistency tests between the different frequencies present in the single-dish observations which show that the data allow this handling in a robust way, independent of the exact parameters we use. Our reconstruction of the LSS missing from WENSS is only statistical in nature, we do not claim to reconstruct the correct observables for individual pixels. We refer to the combined WENSS/BS datasets as 'WENSS LSS'. We estimate that the combined dataset is still insensitive to structure on spatial scales between $\approx 1.5^\circ$ and $\approx 5^\circ$.

After adding our estimate of missing LSS to the WENSS data, many polarization angle gradients are 'converted' from the steep bimodal WENSS distribution into a peak around zero radians/deg. The negative mode of WENSS gradients remains clearly visible. Since we constructed WENSS LSS as the (polarization) vector sum of WENSS and BS, the original WENSS or BS data will dominate if its polarization vectors are much longer than the vectors in the other dataset. Therefore in regions where the BS signal is strong the slowly-varying (nearly zero radians/deg) BS gradients will dominate WENSS LSS.

By using a Kolmogorov-Smirnov (KS) test to compare the polarization angle gradients from the BS faint part of WENSS LSS to scaled-up gradients from the BS RMs. We found that these distributions are similar, and we set limits to the scale factor using this KS test. We illustrated the importance of the difference in size between the WENSS and BS beams by convolving the WENSS LSS data with the BS 408 MHz single-dish beam, which made the clear bimodal distribution of polarization angle gradients in WENSS LSS look more like the distribution of BS RM gradients.

We proceeded by deriving the strength of the magnetic field component along the line-of-sight using these scaled-up RMs together with dispersion measures from the NE2001 thermal electron density model by Cordes & Lazio (2003), see Table 8.2 where we show the values derived for lines-of-sight of lengths 0.5 and 2 kpc. By comparing the magnitude of the scaled-up RMs to RMs measured for pulsars in front of and beyond the Perseus arm we conclude that the Faraday rotation effects we are observing in the BS faint part of our data should be occurring between us and the Perseus arm.

We used the estimate of the strength of the total (regular) magnetic field by Haverkorn et al. (2004a) to derive the strength of the magnetic field in the plane of

the sky $\vec{B_\perp}$, and even though our results are about $1-3\sigma$ at best, we showed that the component of $\vec{B_\perp}$ along Galactic longitude is much stronger than both the component of $\vec{B_\perp}$ along Galactic latitude and $\vec{B_\parallel}$. We also determined the strength of the magnetic field component perpendicular to the Galactic plane, B_z, shown in Table 8.2.

Part of the area covered by WENSS LSS includes the 'fan' region, an area bright in polarized intensity, but at the same time extended on large angular scales, which meant that it could not be detected by the WSRT. We note that the large-scale emission that is detected by the single-dish does not vary on the same angular scales as the WENSS data, and we suggest that the large-scale emission seen towards the fan lies in front of the emission we see in WENSS. The magnitude of the RMs observed towards the fan are small, indicating that they are caused by Faraday rotation occurring between us and the Perseus arm.

Acknowledgements

We would like to thank Titus Spoelstra and Wolfgang Reich for supplying us with the Brouw & Spoelstra '76 dataset. We would also like to thank Maik Wolleben for useful discussion on the nature of the fan region. Finally we would like to thank the anonymous referee for constructive remarks that helped to improve the manuscript. The Westerbork Synthesis Radio Telescope is operated by the Netherlands Foundation for Research in Astronomy (NFRA) with financial support from the Netherlands Organization for Scientific Research (NWO). MH acknowledges support from the National Radio Astronomy Observatory, which is operated by Associated Universities, Inc., under cooperative agreement with the National Science Foundation.

8.10 Appendix A: A new method for fitting linear gradients to periodic data

The main problem when fitting functions to periodic data like polarization angles is the correct handling of the 180° ambiguity. Finding the best-fitting slope and offset requires at the same time finding the number of times 180° has to be added to each datapoint to minimize the distance between the line fitted to the data and the datapoint. This means that for n datapoints $n+2$ degrees of freedom have to be solved, 1 degree of freedom per datapoint to determine the number of 180° 'wraps' (N_i; i=1,...,n), and 2 degrees to determine slope and offset. The only solution to this problem is that at least 2 of the N_i are known a priori. The best-fitting slope and offset will however only depend on the (small number of) datapoints for which the N_i are known, which can be shown by working out the equations that minimize χ^2.

An alternative approach which takes the behaviour of all datapoints into account when determining slope and offset can be formulated as follows. When making a linear fit one can pick a combination of slope and offset and then bring each datapoint to within 90° of the imposed linear fit, which will minimize the χ^2 for that fit. By comparing the χ^2 for all possible combinations of slope and offset one then finds the best fit to the data.

Instead of considering all possible slopes and offsets generally only combinations

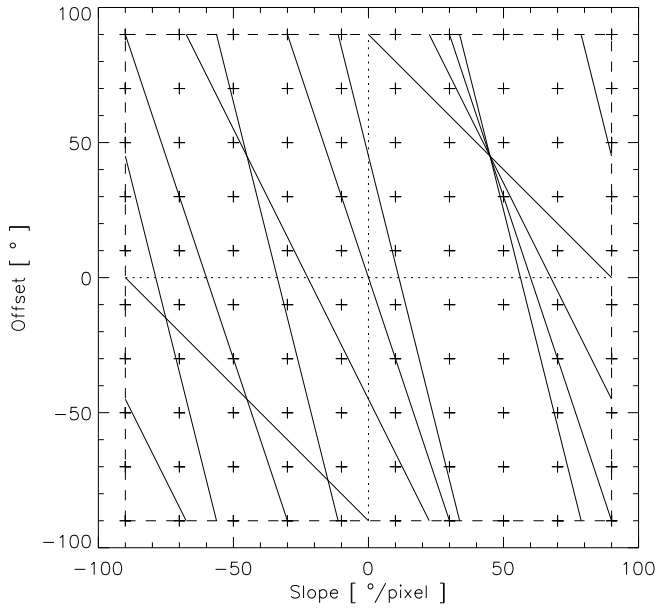

Figure 8.9 — Illustration of which domains and configurations are allowed by a simple example distribution of 4 pixels with coordinates (pixel,polarization angle) = (1,0°), (2,45°), (3,−90°) and (4,−45°). All domain boundaries that belong to a single data point run parallel to each other, and the boundaries are steeper if the data point is further from the origin of the fitted line, which is at pixel coordinate 0 in this example. For comparison we also show a grid that probes (slope,offset) combinations (indicated as crosses) with grid spacing 20°/pixel × 20°.

are considered that lie on a finite grid. For a periodic function only the central part of the complete (slope,offset) space has to be investigated. For polarization angle gradients this means that only slopes between −90°/pixel and +90°/pixel and offsets between −90° and +90° have to be investigated since other slopes and offsets are indistinguishable from slopes and offsets in this central space.

In this appendix we discuss an alternative method which is not based on a grid of slopes and offsets. Instead it maps areas in (slope,offset) space ('domains') which share the same configurations (N_1,..., N_n) of 180° wraps. For a given (slope,offset) combination the lowest χ^2 is found when all datapoints are within 90° of the fitted line formed by that (slope,offset) combination. Each domain boundary is thus formed by (slope,offset) combinations for which one datapoint is at exactly 90° from the fitted line. Crossing this boundary means going to (slope,offset) combinations for which the datapoint will be further than 90° from the fitted line, and it can be brought to within 90° by adding an extra ±180° to the datapoint, which changes the configuration. Each datapoint thus defines a set of domain boundaries, and the ensemble of the domain boundaries of the individual datapoints will define the domains.

For each of these domains the best-fitting combination of slope and offset is found by a χ^2 fit. Since all combinations of slopes and offsets in the domain share the same best fit, it becomes possible to cover the entire solution space by mapping the domains.

One possible cause of concern could be that the least-squares solution falls outside its domain. However the χ^2 of this solution will always be higher than the minimum χ^2

of the best fit in the domain the solution has crossed into: If the best-fitting (slope,offset) combination lies outside the domain it is supposed to be in, by definition of the domain borders at least one of the datapoints is further than 90° from the line formed by that (slope,offset) combination. For that (slope,offset) combination it is however always possible to find a configuration where all datapoints are within 90° of the line formed by that (slope,offset) combination, and this configuration will therefore give a better fit. This furthermore guarantees that the lowest χ^2 in (slope,offset) space will always lie inside the domain it is supposed to be, and that by mapping the domains and using a χ^2 fit in every domain we will find this best-fitting solution.

The boundaries of the domains are set by the noise realization of the observations. Since the same distance between the datapoint and the linear fit is used to find the position of the domain borders and in the definition of χ^2, the domain mapping approach will be no more sensitive to the influence of noise than a standard χ^2 fit applied to a non-periodic dataset.

The configuration-mapping approach covers all solutions in (slope,offset) space and is therefore much more reliable than the grid-based approach which only probes the quality of certain (slope,offset) combinations. But furthermore it is very easy to figure out where the boundaries of the domains are, and therefore this method is also much faster. In one example of 4 datapoints at (pixel,polarization angle) = (1,0°), (2,45°), (3,−90°) and (4,−45°) the grid-based approach using a coarse grid of 20°/pixel×20° already requires 100 gridpoints, whereas there were only 21 domains in this configuration that needed to be investigated (see Fig. 8.9).

Sarala and Jain (2001) discuss a different method to find the best-fitting gradient for a periodic dataset. Their analysis includes all wraps of the individual datapoints and using the appropriate statistics they derive a maximum-likelihood criterion. By bringing the datapoints to within 90° of the fitted gradient our method can use the standard non-periodic statistics.

The method we describe here can also be used for fitting RMs to polarization angle observations at different wavelengths, since this would mean solving $\phi = a\lambda^2 + b$ for the parameters 'a' and 'b', which is identical to the $\phi = ax + b$ we solved for the spatial RM gradients. One important difference however is that the regular spacing of the pixels we fitted RM gradients to limits the range of slopes that give unique fits to the data: slopes steeper than 90°/pixel are indiscernible from slopes that are flatter. If the polarization angles are irregularly sampled in λ^2 space there are no such limits, which means that there are no boundaries that limit the range of RMs that have to be investigated. The regular spacing of datapoints also causes the degeneracy that steeper gradients can be fitted with the same quality by adding π radians to the second datapoint, 2π to the third etc. For an irregular spacing this degeneracy is (at least partially) lifted.

Chapter 9

The large-scale magnetic field in the second Galactic quadrant

Abstract. In this chapter we study the properties of the large-scale magnetic field in the second Galactic quadrant. To this end we combine the rotation measures of polarized extragalactic sources, pulsars, and the Faraday depths and rotation measures if the diffuse emission with the dispersion measures that we calculate from the WHAM Hα intensities (at $|b| > 5^\circ$) and the NE2001 model by Cordes & Lazio (at $|b| < 5^\circ$). The electron-density weighted average magnetic field strength $\langle B_\parallel \rangle$ in general agrees well for pulsars and extragalactic sources in this part of the Galaxy. This means that the average magnetic field strength in front of the pulsar is very similar to the average magnetic field strength along the rest of the line-of-sight through the Galaxy beyond the pulsar. The $\langle B_\parallel \rangle$ that we derive for the diffuse emission only agree with the $\langle B_\parallel \rangle$ of the point sources at positive Galactic latitudes. At negative Galactic latitudes the $|\langle B_\parallel \rangle|$ that we find for the diffuse emission are smaller than the $|\langle B_\parallel \rangle|$ of the point sources by a factor of 2 – 4. Since we used the dispersion measure for the entire line-of-sight through the Galaxy to calculate $\langle B_\parallel \rangle$ for the diffuse emission, this implies that the diffuse emission that we observe originates within 1/4 – 1/2 of the length of the complete line-of-sight. From our data we find no evidence that there is a reversal of the magnetic field with respect to the Galactic plane, at least in the second Galactic quadrant. We modeled the large-scale magnetic field using a logarithmic spiral. The model predicts much stronger gradients with Galactic longitude in $\langle B_\parallel \rangle$ than are observed, and we argue that large-scale reversals in the magnetic field along the line-of-sight can reduce the magnitude of the $\langle B_\parallel \rangle$ gradient in the model. The $\langle B_\parallel \rangle$ in our data show structure on scales larger than $\sim 10^\circ$ -20° which is in between the angular scales on which $\langle B_\parallel \rangle$ varies in our model of the large-scale field, and the angular scales of the small-scale turbulent field.

D. H. F. M. Schnitzeler, P. Katgert and A. G. de Bruyn

9.1 Introduction

In this chapter we study the large-scale magnetic field of our Galaxy in in the second Galactic quadrant, i.e. in the Galactic longitude range $80^\circ \lesssim l \lesssim 200^\circ$ with Galactic latitudes from -40° $\lesssim$ b $\lesssim$ 40°. To this end we combine information from polarized extragalactic sources, pulsars, and the diffuse emission. Brown et al. (2003 and 2007) studied the properties of the large-scale magnetic field within a couple of degrees of the Galactic plane, in the fourth Galactic quadrant and for Galactic longitudes between $105^\circ \lesssim l \lesssim 135^\circ$ respectively. From the rotation measures of extragalactic sources and the rotation measures and inferred distances of pulsars, Han et al. (1997) found evidence for an A0 type Galactic dynamo, which has a reversed field direction above and below the Galactic plane, with many field reversals between the Galactic spiral arms.

We combine the information that extragalactic sources, pulsars and the diffuse emission give us about the large-scale magnetic field. To this end we calculate for every source the electron-density weighted magnetic field component along the line-of-sight, $\langle B_\parallel \rangle$:

$$\langle B_\parallel \rangle \equiv \frac{\int\limits_{\text{line-of-sight}}^{\text{observer}} n_\mathrm{e} \vec{B} \cdot \mathrm{d}\vec{l}}{\int\limits_{\text{line-of-sight}} n_\mathrm{e} \mathrm{d}l} = \frac{\mathcal{R}}{0.81 \text{ DM}} \tag{9.1}$$

where the electron density n_e is in cm^{-3}, the magnetic field B is in μG, and the distance along the line-of-sight l is measured in parsec. The Faraday depth of a point 'x' along the line-of-sight $\mathcal{R}(x)$[rad/m^2] $= 0.81 \int_{\text{source at 'x'}}^{\text{observer}} n_e$ [cm^{-3}] $\vec{B}$ [μG] $\cdot \mathrm{d}\vec{l}$ [pc]. We distinguish between Faraday depth and rotation measure RM = $\partial\, \Phi(\lambda^2)/\partial\, \lambda^2$, the derivative of the observed polarization angle Φ with respect to λ^2. In Sect. 9.2 we describe which data sets we use to compile the Faraday depths and rotation measures that we will be using in the rest of this chapter. The dispersion measure DM is the line-of-sight integral of the electron density, DM[cm^{-3}pc] = $\int_0^\infty n_\mathrm{e} \mathrm{d}l$. The length of the line-of-sight that produces the Faraday depth and DM differs between extragalactic sources, pulsars and the diffuse emission that we observe. However, all three sources trace $\langle B_\parallel \rangle$; it therefore makes more sense to compare $\langle B_\parallel \rangle$ between these different types of sources than their Faraday depth or DM separately. To our knowledge this is the first time that information from these different sources has been combined in this way to study the large-scale magnetic field.

Since DM can only be observed directly for pulsars, we need DM sampled on a fine grid for the region that we are interested in to calculate $\langle B_\parallel \rangle$ for the extragalactic sources and the diffuse emission. We describe how we determined DM for the present area in Sect. 9.3. We can get a reasonable estimate for the DMs of lines-of-sight through the entire Galaxy in two steps: first we calculate emission measures
EM[cm^{-6}pc] = $\int_0^\infty n_\mathrm{e}^2 \mathrm{d}l$ from measured WHAM Hα intensities (Haffner et al. 2003). In the second step we use the relation between EM and DM that Berkhuijsen et al. (2006) derived to translate the EM we calculated from the WHAM data to DM. This process is described in more detail in Sect. 9.3.1. The WHAM survey samples the region of the

second Galactic quadrant that we are interested in much finer than the pulsars that are used to constrain the NE2001 electron density model by Cordes & Lazio (2003) in this part of the Galaxy. We return to this point in Sect. 9.3.2, where we compare the DM we calculate from WHAM to the DM from the NE2001 model and to the DM that are observed for pulsars in these regions.

In Sect. 9.4 we derive $\langle B_{\parallel} \rangle$ by combining the WHAM/NE2001 DM with the RM and Faraday depths of the extragalactic sources, pulsars, and diffuse emission. To make the global structure in $\langle B_{\parallel} \rangle$ stand out more clearly, we average the $\langle B_{\parallel} \rangle$ over cells of $10^{\circ} \times 10^{\circ}$ and $20^{\circ} \times 20^{\circ}$. Finally, we construct in Sect. 9.5 a model of what $\langle B_{\parallel} \rangle$ the large-scale field produces by combining what is known about the large-scale Galactic magnetic field from different sources, and we compare our model to the observations.

9.2 Compilation of Faraday depths and rotation measures

9.2.1 Extragalactic sources

A recent compilation of RMs for extragalactic sources was kindly provided by Peter Frick and Rodion Stepanov. Their catalogue (Frick et al. 2001) combines the older catalogues of Simard-Normandin & Kronberg (1980) and Broten (1988; updated in 1991) with a number of smaller catalogues. Their catalogue lists 290 sources in the region that we are interested, and these are plotted as circles in Figs. 9.1 and 9.2.

Jo-Anne Brown kindly provided us with rotation measures for 555 extragalactic sources from the Canadian Galactic Plane Survey (CGPS; Taylor et al. 2003) in the Galactic longitude range $80^{\circ} \lesssim$ l $\lesssim 145^{\circ}$ with Galactic latitudes -3° $\lesssim$ b $\lesssim 5^{\circ}$. Since these CGPS sources have a very large source density of about 1 source/square degree, we only plotted RM averages in Figs. 9.1 and 9.2, and left out previously known sources in the same area to avoid confusion.

Finally, we also included the rotation measures and Faraday depths of extragalactic sources that were observed with the WSRT. These were discussed by Haverkorn et al. in the direction of (l, b) = (161°,16°) and (l, b) = (137°,7°) (2003a and 2003b), as well as by us in chapters 2 to 6. In Table 9.1 we provide characteristics for these data sets. Extragalactic sources from these data sets are plotted onto a grey background in Fig. 9.1 that indicates the boundaries of the individual WSRT data sets.

One drawback of using RMs of extragalactic sources is that extragalactic sources can also have an intrinsic RM, that is different for different sources. To compensate for this RMs of nearby extragalactic sources are often averaged, leaving only the Milky Way contribution to the RM.

9.2.2 Pulsars

The ATNF pulsar catalogue[1] is an updated master list of pulsars and their DMs and RMs (when known) (Manchester et al. 2005). The 57 known pulsars in our area of interest are plotted in Figs. 9.1 and 9.2 as squares.

[1] `http://www.atnf.csiro.au/research/pulsar/psrcat/`

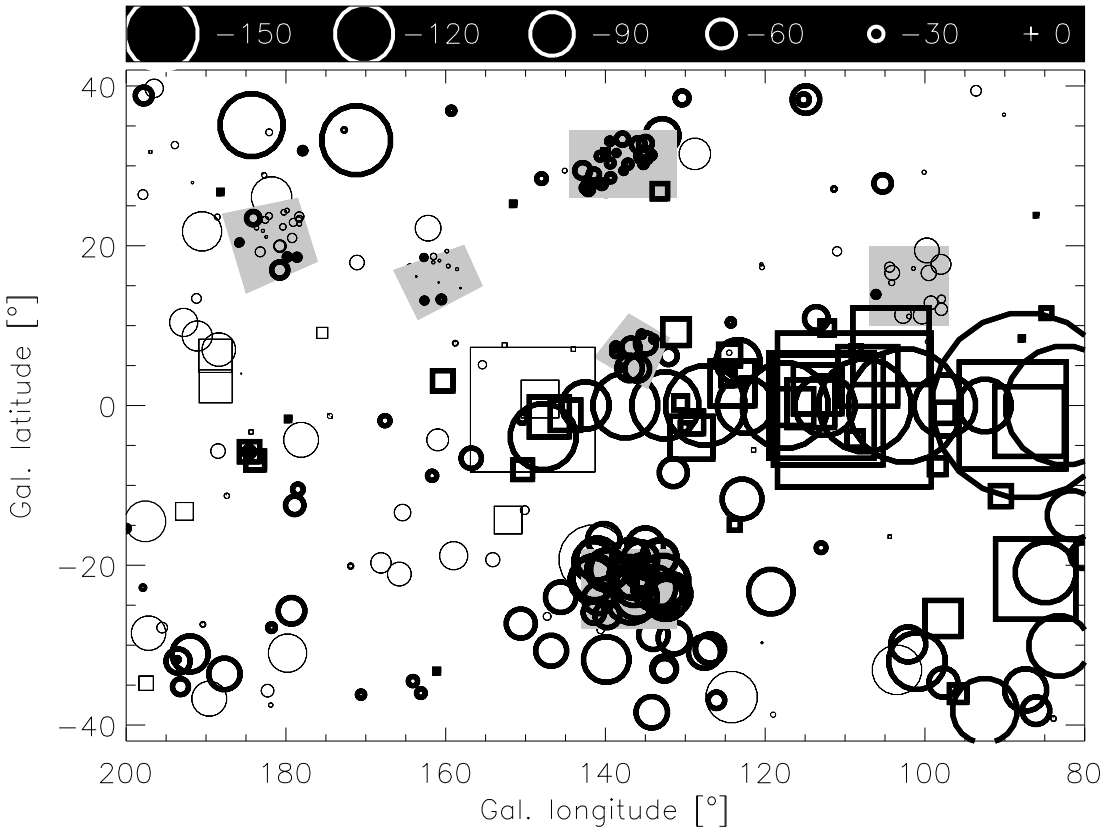

Figure 9.1 — Rotation measures and Faraday depths of extragalactic sources (circles) and pulsars (squares). This figure only shows sources for which |RM| or $|\mathcal{R}| < 150$ rad/m^2, Fig. 9.2 shows the other sources. Sources with negative RM and $\mathcal{R}$ are indicated by symbols with thick lines. The six regions indicated in grey contain point sources from Haverkorn et al. (2003a and 2003b) and from chapters 2 – 6. We averaged CGPS RM in the region $80° \lesssim l \lesssim 145°$ and $-3° \lesssim b \lesssim 5°$ in the areas indicated by the rectangles in Fig. 9.2, and plotted only the average RM. In this region we left out extragalactic sources from other catalogues.

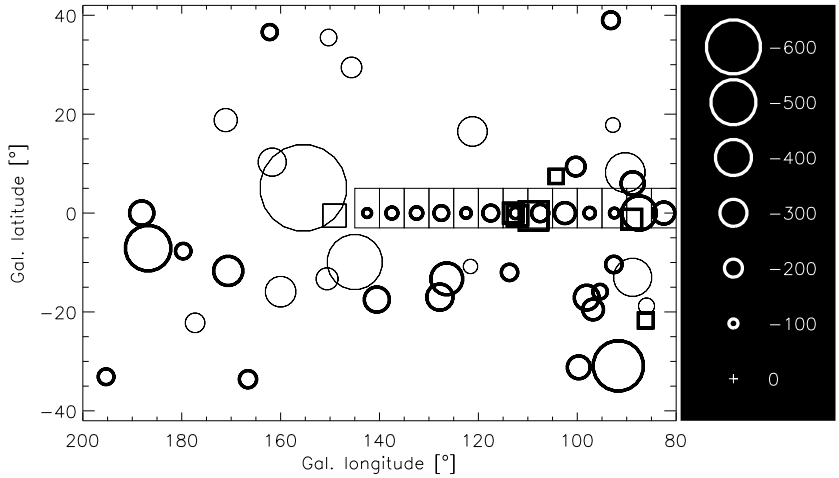

Figure 9.2 — Similar to Fig. 9.1 but for sources with |RM| or $|\mathcal{R}| > 150$ rad/m^2. We also indicated the regions over which we average the CGPS RM.

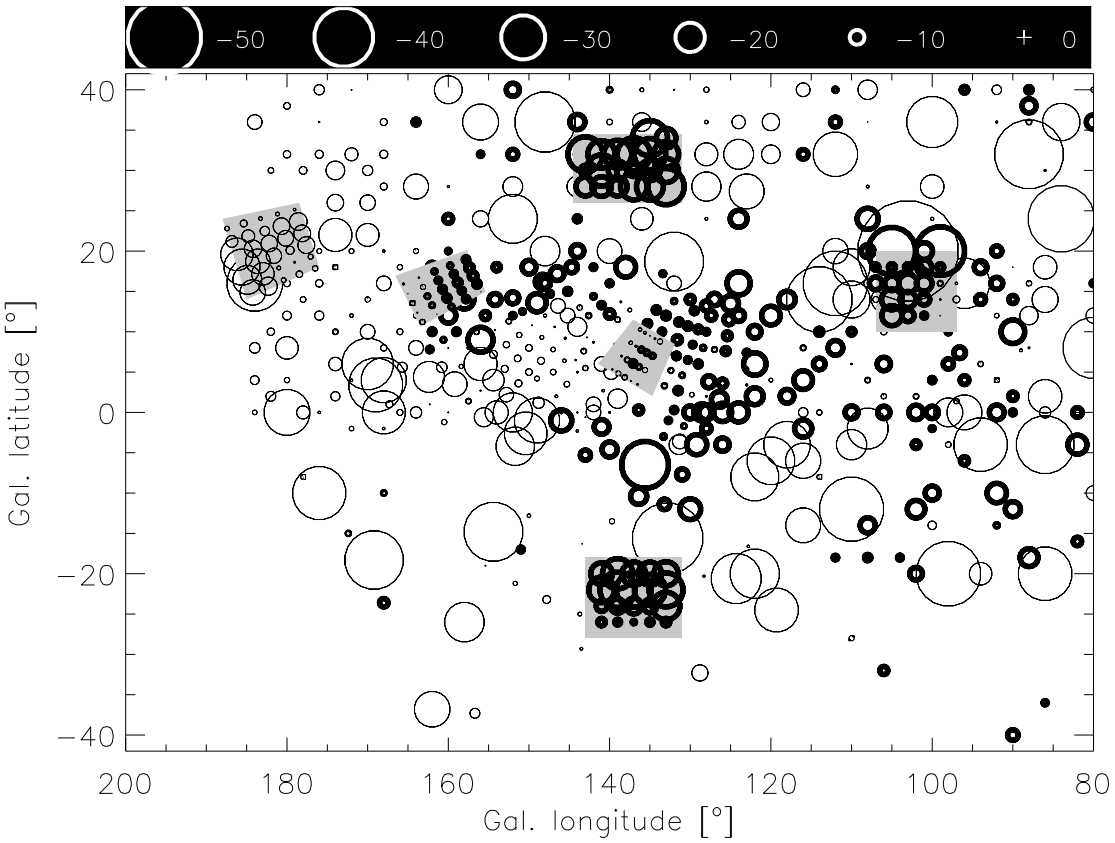

Figure 9.3 — Rotation measures from Spoelstra (1984) and Haverkorn et al. (2003a and 2003b), and Faraday depths of the strongest diffuse emission for the data sets from chapters 2 – 6. The Haverkorn et al. data and our data lie in the grey regions. We multiplied Spoelstra's RMs by a factor of 2.4, to make the RM gradients fit the observed WENSS polarization angle gradients from chapter 8. Both the Haverkorn et al. rotation measures and our Faraday depths are plotted on a $2^\circ \times 2^\circ$ grid, and are averages over all measures lines-of-sight within 1° from a grid point. Note the difference in RM scale compared to Fig. 9.1!

Table 9.1 — Characteristics of the 4 WSRT data sets that we analysed using Faraday tomography in chapters 2 – 6, and the 2 data sets ('AUR' and 'HOR') that were analysed by Haverkorn et al. (2003a, 2003b). These data sets lie in the grey regions indicated in Figs. 9.1 and 9.3.

Mosaic	l,b	$\langle \mathcal{R} \rangle_{\rm DIM,EGS}$ [μG]	$\langle B_\parallel \rangle_{\rm DIM,EGS}$ [μG]	$B_{\parallel,\rm reg}$
GEM	(181°, 20°)	8, 6	0.3, 0.2	0.6
CEP	(102°, 15°)	-10, 22	-0.1, 0.3	-3.6
TRI	(137°,-23°)	-20,-78	0.6,-2.4	-2.1
CAM	(138°, 30°)	-28,-19	-2.2,-1.5	-1.9
AUR	(161°, 16°)	-3, 2		
HOR	(137°, 7°)	-1,-21		

9.2.3 Diffuse emission

Brouw & Spoelstra (1976) surveyed a large part of the second Galactic quadrant in the 1970s with the Dwingeloo radio telescope at 408, 465, 610, 820, and 1411 MHz. Spoelstra (1984) calculated RMs for this data set, and 450 of his lines-of-sight lie in the region of the second Galactic quadrant that we are interested in. In chapter 8 we compared the gradients in Spoelstra's RMs to the polarization angle gradients in the WENSS polarization data between $130^\circ \lesssim$ l $\lesssim 173^\circ$ and $-5^\circ \lesssim$ b $\lesssim 31^\circ$. WENSS, the Westerbork Northern Sky Survey, is a low-frequency radio survey of extragalactic sources at 325 MHz above $\delta = 30^\circ$ that also contains a wealth of diffuse polarization data (Rengelink et al. 1997). The WENSS polarization angle gradients are significantly larger than Spoelstra's RMs would produce at the WENSS observing frequency of 325 MHz, and we concluded that Spoelstra's RMs should be increased by a factor of 2.4. This difference in steepness between the WENSS gradients and the RM gradients is likely due to the difference in beamsize between the high-resolution WSRT WENSS data and the low-resolution Dwingeloo dish data that Spoelstra used to calculate his RMs. We applied this correction factor to Spoelstra's RM that we plotted in Fig. 9.3, and in the rest of this chapter.

In our analysis we also include the rotation measures that Haverkorn et al. (2003a and 2003b) derived for the diffuse emission, and the Faraday depths of the strongest polarized emission from chapters 2 – 6. We plotted the Spoelstra rotation measures together with Haverkorn et al.'s rotation measures and our Faraday depths in Fig. 9.3. To make this plot we sampled both Haverkorn et al.'s rotation measures and our Faraday depths on a $2^\circ \times 2^\circ$ grid, and averaged all lines-of-sight within 1° from a grid point.

9.3 Dispersion measures

9.3.1 Calculating DM from measured WHAM Hα intensities

The WHAM survey has measured Hα intensities in Rayleigh for the region we are interested in on a regular $\sim 1^\circ \times 1^\circ$ grid. To convert the Hα intensities to emission measures, we can use Eqn. 1 from Haffner et al. (1998):

$$\mathrm{EM} \;=\; 2.75 T_4^{0.9}\; I_{\mathrm{H}\alpha}(\mathrm{R})\; \mathrm{e}^{2.2\ \mathrm{E(B-V)}} \tag{9.2}$$

where T_4 is the temperature of the warm interstellar medium in units of 10^4 K, which is typically 0.8 (Reynolds 1985), and $I_{\mathrm{H}\alpha}$ is the Hα intensity in Rayleigh. For each WHAM line-of-sight we calculated the interstellar E(B-V) reddening values from Schlegel et al. (1998) and the programs available on[2].

Finally, with the emission measures that we derived we can calculate dispersion measures using the relation that Berkhuijsen et al. (2006) established from their sample of 157 Galactic pulsars with Galactic latitudes $|b| > 5^\circ$:

$$\mathrm{EM} \;=\; 0.042 \pm 0.014\ \mathrm{DM}^{1.47 \pm 0.09} \tag{9.3}$$

[2] `http://astro.berkeley.edu/~marc/dust/data/data.html`

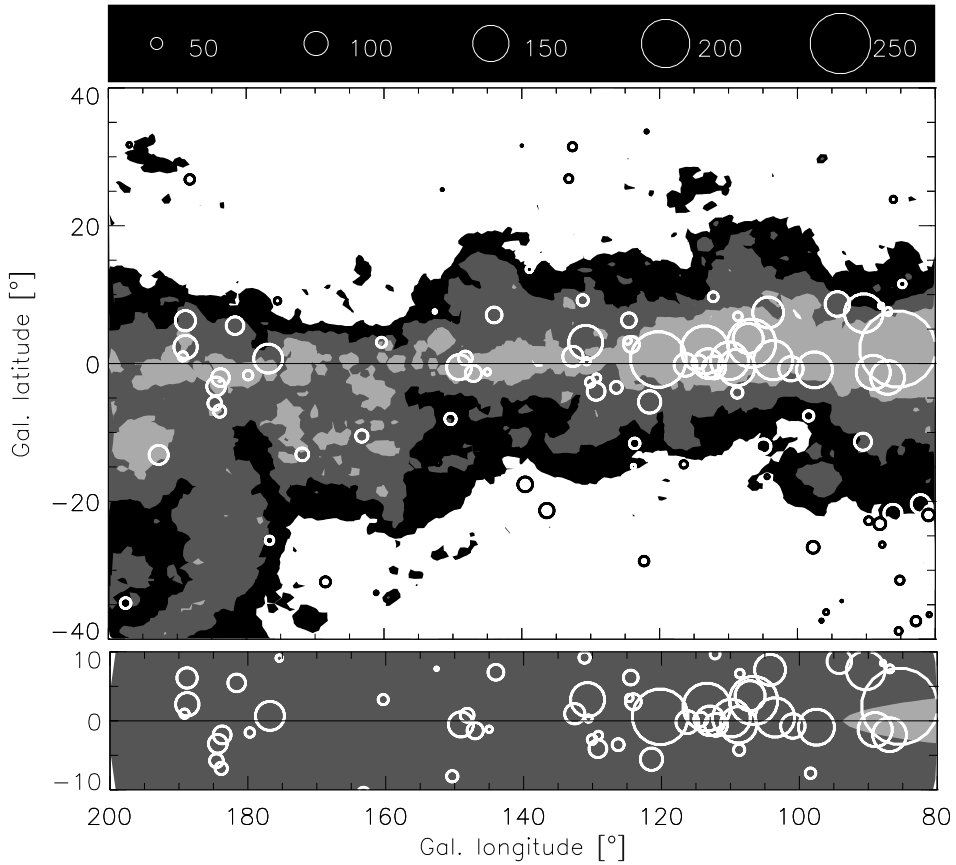

Figure 9.4 — *Top panel:* distribution of the DM that we calculated from the WHAM Hα intensities. The different grey shadings indicate different DM; white corresponds to DM < 50 cm^{-3}pc, and the next contours are at DMs of 100 and 400 cm^{-3}pc. We overplotted the DM measured for pulsars from the ATNF pulsar catalogue, the linear scale for the pulsar DM is shown at the top, units are cm^{-3}pc.
Bottom panel: DM for lines-of-sight through the entire Milky Way that we calculated from the NE2001 model by Cordes & Lazio (2003). Also in this panel we overplotted the measured pulsar DM. Clearly the NE2001 model produces much smoother DM than our method that uses the WHAM Hα intensities.

For a given EM their data show a 1σ spread of about 30% in DM (see their Fig. 7). In the top panel of Fig. 9.4 we plot contour levels for DM = 50, 100 and 400 cm^{-3}pc for the DM we calculated from WHAM Hα intensities. In the rest of the text we will use 'WHAM DM' as a shorthand for 'DM calculated from the WHAM Hα intensities'.

Free electrons in the hot intercloud phase (HIM) of the ISM will also contribute to the measured rotation measures and Faraday depths, yet they are not detected in WHAM. Snowden et al. (1997) modeled the free electron density in the HIM in the Galactic plane from ROSAT diffuse X-ray emission maps, and they found that this electron density is smaller by a factor of 10 compared to the electron density in the warm ionized medium that WHAM can detect. We therefore neglect the HIM contribution to the rotation measures and Faraday depths.

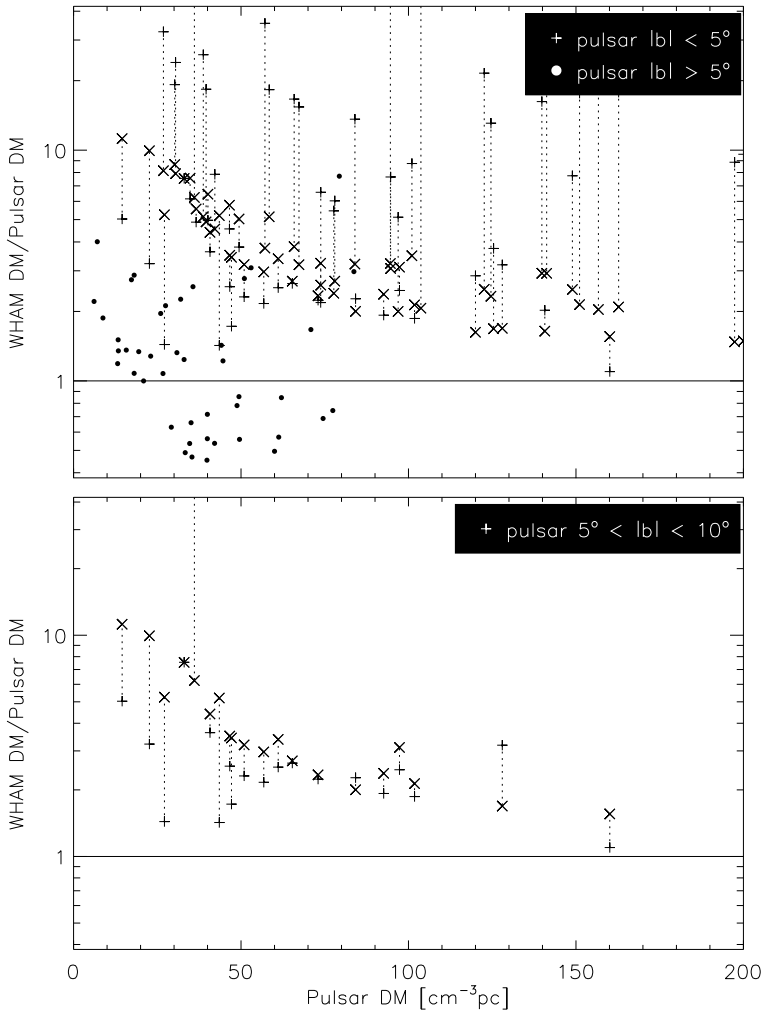

Figure 9.5 — *Top panel:* Comparison between the DM that were measured for pulsars from the ATNF pulsar catalogue, and the ratio between the DM that we calculated from the WHAM Hα intensities (pluses and dots to indicate pulsars that lie within or further than 5° from the Galactic plane resp.) and the measured pulsar DM. For pulsars within 5° from the Galactic plane we also plot the ratio between the NE2001 DM for a line-of-sight through the entire Galaxy and the measured pulsar DM (crosses). We calculate DM from the WHAM DM by using a statistical relation between EM and DM; therefore we can expect that in some cases the WHAM DM/pulsar DM ratio can be smaller than 1. Since the NE2001 model is very smooth, the spread in the DM that we calculated from this model is relatively small (bottom panel of Fig. 9.4, which explains why the crosses appear to fall on one line. 6 pulsar lines-of-sight are missing from this plot since they fall outside the plot range. We averaged the WHAM DM and NE2001 DM(∞) over lines-of-sight within $\sqrt{2}$ degrees from the pulsar, $\sqrt{2}$ degrees being the diagonal distance between the WHAM lines-of-sight that lie on a $\sim 1^\circ \times 1^\circ$ grid.
Bottom panel: Similar to the top panel, but showing only pulsars with Galactic latitudes $5^\circ \lesssim$ b $\lesssim 10^\circ$. The WHAM DM are no longer systematically larger than the NE2001 DM(∞), as was the case in the top panel for pulsars with $|b| < 5^\circ$. From this we conclude that we can use the WHAM DM for Galactic latitudes $|b| > 5^\circ$.

9.3.2 Comparison between WHAM DM, NE2001 DM, and measured pulsar DM

Schlegel et al. (1998) note that their reddening values for Galactic latitudes lower than $|b| < 5^\circ$ are unreliable since they did not remove contaminating sources of interstellar reddening from their data at these low latitudes. In this section we compare the WHAM DM we calculated using the Schlegel et al. reddening values at these low Galactic latitudes to the DM calculated from the NE2001 electron density model by Cordes & Lazio, for a line-of-sight that extends out to 17.5 kpc from the location of the sun (where the electron densities from the NE2001 model become negligible), and to distances up to 3.5 kpc from the Galactic plane (where a line-of-sight at a Galactic latitude of 10° covers a horizontal distance of 17.5 kpc). We will indicate the DMs that we calculate with the NE2001 model for lines-of-sight through the entire Galaxy by 'NE2001 DM(∞)'. As a more absolute gauge of the quality of the DM that we calculate from WHAM and the NE2001 DM(∞) we compare both to the DM measured for pulsars at these latitudes. Since the WHAM DM and NE2001 DM(∞) were calculated for the entire line-of-sight through the Galaxy, and pulsars lie much more nearby, the WHAM DM and NE2001 DM(∞) should on average be larger than the measured pulsar DM. Statistical scatter in for example's Berkhuijsen et al.'s EM/DM relation, or scarcity of pulsars in certain regions that make the NE2001 model less well constrained can of course produce modeled DM that are smaller than the measured pulsar DM.

In the top panel of Fig. 9.4 we plot contours for the DM that we calculated from WHAM Hα intensities at DM of 100 and 400 cm^{-3}pc. We overplot the DM measured for pulsars in the same region as pulsars; the linear scale for the pulsar DM is shown on top of this figure. In the bottom panel we plot contours at the same levels as for the WHAM DM for the NE2001 DM(∞) that we calculated for lines-of-sight in the same direction as the WHAM lines-of-sight. Clearly the NE2001 DM(∞) are much smoother than the WHAM DM.

To investigate what effects using the wrong E(B-V) can have on the WHAM DM, we plot in Fig. 9.5 the ratio of the calculated WHAM DM to the measured pulsar DM as a function of pulsar DM. To calculate the WHAM DM at the position of the pulsar, we averaged the WHAM DM that we calculated over all WHAM lines-of-sight that lie within $\sqrt{2}$ degrees from the position of the pulsar. $\sqrt{2}$ degrees is the diagonal distance between WHAM grid points that lie on a $\approx 1^\circ \times 1^\circ$ grid. Pluses indicate pulsars lying within 5° from the Galactic plane, and filled circles indicate pulsars that lie further than 5° from the plane. For pulsars with $|b| < 5^\circ$ we plotted as crosses the NE2001 DM(∞) that we calculated for the pulsar line-of-sight.

The top panel of this plot clearly shows that the WHAM DM for pulsars at latitudes $|b| < 5^\circ$ are systematically (much) larger than the NE2001 DM(∞). This could be due to using wrong E(B-V) reddening values, since Schlegel (1998) already cautions when using his reddening values at so close to the Galactic plane. For lines-of-sight further than 5° from the Galactic plane, the WHAM DM are much more consistent with the pulsar DM, even though the pulsar line-of-sight is only a fraction of the line-of-sight that produces the WHAM DM. The average WHAM DM/pulsar DM for these data points is 1.9, and their standard deviation is 1.4 (we left out one line-of-sight where the WHAM DM/pulsar DM ratio was about 50). Due to the spread in the EM/DM con-

version of Eqn. 9.3 we would expect a standard deviation of 0.6. We did not correct for the DM that is built up in the part of the line-of-sight beyond the pulsar, which likely explains the large average and spread of the WHAM DM/pulsar DM. In the bottom panel of Fig. 9.5 we show the WHAM DM/pulsar DM and NE2001 DM(∞)/pulsar DM ratios for pulsars between 5° and 10° from the Galactic plane. The WHAM DM are for these pulsars no longer systematically larger than the NE2001 DM(∞), as was the case for pulsars with $|b| < 5°$. From this we conclude that we can use the WHAM DM for Galactic latitudes $|b| > 5°$ and that we should use the NE2001 DM(∞) closer to the Galactic plane, to reduce the systematical effects that the WHAM DM suffer from at these low latitudes.

9.4 The n_e-weighted magnetic field strength $\langle B_\parallel \rangle$

In this section we calculate $\langle B_\parallel \rangle$ from Eqn. 9.1 by combining the rotation measures and Faraday depths that we compiled in Sect. 9.2 with the dispersion measures that we calculated from the WHAM Hα intensities and (at Galactic latitudes $|b| \lesssim 5°$) the NE2001 DM(∞). We only use pulsars for which both RM and DM are known. For the extragalactic sources we can estimate DM in the way described in Sect. 9.3. However, the distance at which the bulk of the polarized emission that we observe originates is still a big unknown. There are indications that the bulk of the diffuse emission that we observe is emitted in the nearer parts of the line-of-sight. In our CEPHEUS data set (chapter 4) for example we found that most of the extragalactic sources have a Faraday depth with opposite sign from the Faraday depths of the strongest diffuse emission, and in our TRIANGULUM data set (chapter 5) the Faraday depths of the extragalactic sources were more negative than the Faraday depths of the strongest diffuse emission by a factor of 4! Since we cannot accurately establish a distance from which the observed diffuse emission is coming, we will use the DM for the entire line-of-sight through the Galaxy, and the $|\langle B_\parallel \rangle|$ we derive for the diffuse emission are then lower limits to the actual $\langle B_\parallel \rangle$.

In Fig. 9.6 we plot the $\langle B_\parallel \rangle$ that we found for the point sources (top panel; pulsars, for which we can measure DM directly and therefore determine $\langle B_\parallel \rangle$ exactly, and extragalactic sources, for which we have to model DM, which introduces errors in $\langle B_\parallel \rangle$) and for the diffuse emission (bottom panel), for which we can determine only lower limits to $|\langle B_\parallel \rangle|$. Away from the Galactic plane, the $\langle B_\parallel \rangle$ that we derive from pulsars and extragalactic sources are very similar. The $\langle B_\parallel \rangle$ that we derive from pulsars and extragalactic sources are similar, except maybe within a few degrees from the Galactic plane (as is clear from comparing the pulsar $\langle B_\parallel \rangle$ to the CGPS $\langle B_\parallel \rangle$). This implies that $\langle B_\parallel \rangle$ must be roughly constant along the line-of-sight in front of the pulsar and beyond. This is a trivial result if all the Faraday-rotating electrons lie in front of the pulsars. Fig. 9.5 however shows that since the WHAM DM (for $|b| > 5°$) or NE2001 DM(∞) (for $|b| < 5°$) are in general larger than the measured pulsar DM, which means that Faraday rotation also occurs beyond the pulsar, and we can rule out our trivial explanation for the similarity between the $\langle B_\parallel \rangle$ of the pulsars and the extragalactic sources.

On the other hand, for Galactic longitudes $\lesssim 140°$ and negative Galactic latitudes, the $\langle B_\parallel \rangle$ that we derived for the diffuse emission appear to be smaller than the $\langle B_\parallel \rangle$

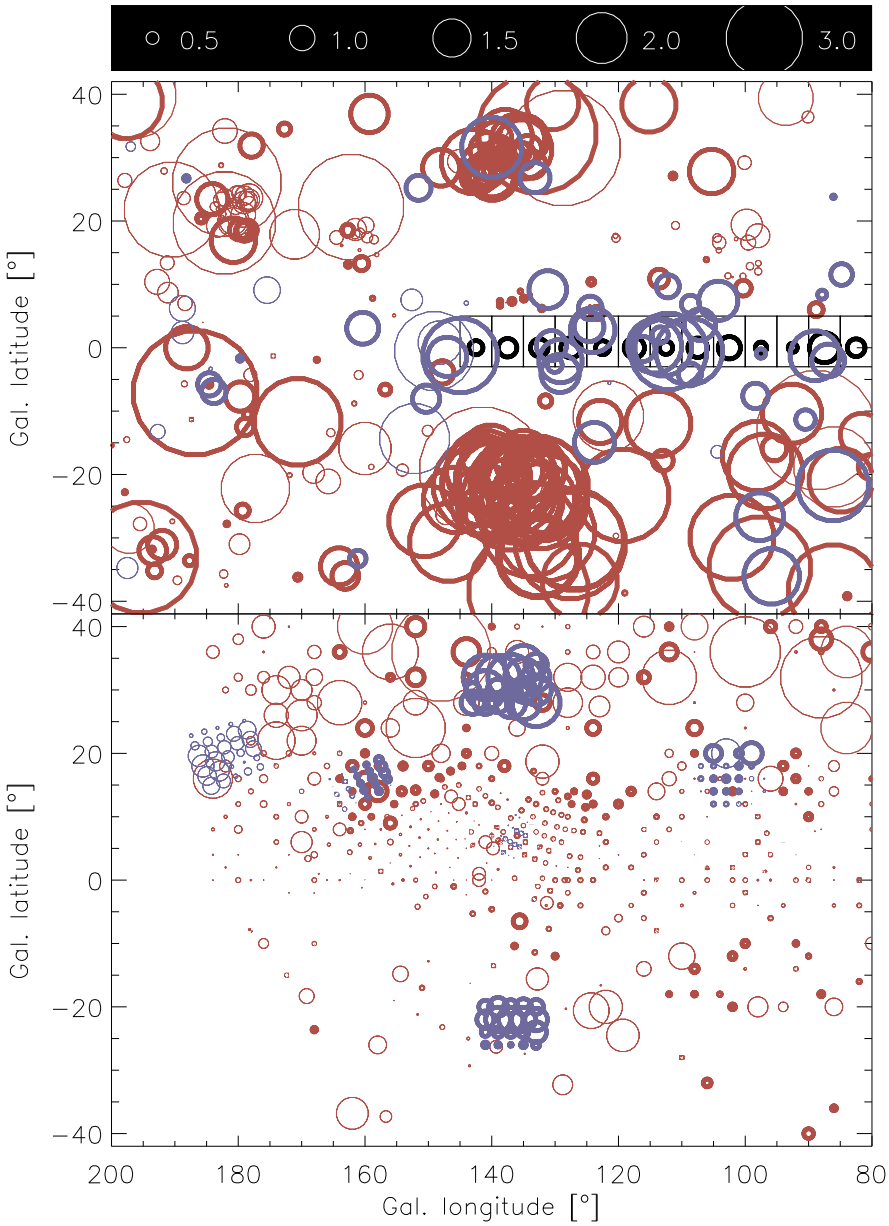

Figure 9.6 — $\langle B_\parallel \rangle$ derived from extragalactic sources and pulsars (top panel; red and blue circles resp.) and from the diffuse Galactic emission (bottom panel; red circles are $\langle B_\parallel \rangle$ based on rotation measures from Spoelstra (1984), blue circles are $\langle B_\parallel \rangle$ based on rotation measures from Haverkorn et al. (2003a, 2003b) and from the Faraday depths with the strongest diffuse polarized emission, chapters 2 – 6). Circles with thin edges show positive $\langle B_\parallel \rangle$, and circles with thick edges negative $\langle B_\parallel \rangle$. Black circles indicate the $\langle B_\parallel \rangle$ that we calculate by averaging rotation measures of CGPS sources in the black boxes. To avoid confusion we removed sources from the Frick et al. catalogue that lie in the region that is also covered by the CGPS. 28 lines-of-sight from the top plot were excluded because they had $|\langle B_\parallel \rangle| > 5$ μG. The $\langle B_\parallel \rangle$ for the Haverkorn et al. data and for our data were calculated on a $2^\circ \times 2^\circ$ grid, where we averaged rotation measures and Faraday depths over all lines-of-sight within 1° from a grid point. In this averaging we only included rotation measure fits from Haverkorn et al. that have $\chi^2_{\rm red} < 2$. On page 198 we show a colour version of this figure.

that we derived for the point sources. The data are not sufficient to make a similar statement for Galactic longitudes $> 140^\circ$. At positive Galactic latitudes the $\langle B_\parallel \rangle$ that we derived from point sources and from the diffuse emission are much more similar. Also the $|\langle B_\parallel \rangle|$ of the diffuse emission seem to increase further away from the Galactic plane.

The observationally established fact that the $|\langle B_\parallel \rangle|$ that we determine for polarized extragalactic sources and the diffuse emission increase for larger absolute Galactic latitudes, whereas the $|\langle B_\parallel \rangle|$ that we derived for the pulsars don't, could have three different causes. First, the pulsars that we use have measured DM, whereas to calculate the $\langle B_\parallel \rangle$ for extragalactic sources and the diffuse emission we had to model DM. The models we use, even though they are the best available, could overproduce DM close to the Galactic plane. The alternative to this, that the models produce too little DM further from the Galactic plane, can be ruled out since the pulsar $\langle B_\parallel \rangle$, for which we exactly know the DM, become more similar to the $\langle B_\parallel \rangle$ of the extragalactic sources and the diffuse emission further from the Galactic plane. Second, the effect that we see smaller $|\langle B_\parallel \rangle|$ close to the Galactic plane is real, and the pulsar $\langle B_\parallel \rangle$ disagrees with the $\langle B_\parallel \rangle$ of the extragalactic sources because there is a large-scale field reversal beyond the pulsar. But then this field reversal should also lie in front of the region where the diffuse emission is generated, which puts this region at many kpc from the observer, whereas it is generally thought that most of the diffuse emission originates close to the sun. Third, the magnetic field could have a substantial poloidal component. This poloidal component becomes more aligned with lines-of-sight at large $|b|$. This interpretation however requires a poloidal magnetic field with a strength of a couple of μG, a considerable fraction of the total magnetic field that is thought to be only 6 μG strong (2001).

Since we calculate $\langle B_\parallel \rangle$ for the diffuse emission by using the DM for an entire line-of-sight through the Galaxy, we expect the $|\langle B_\parallel \rangle|$ derived from the diffuse emission to be smaller than the $|\langle B_\parallel \rangle|$ that we derived from point sources. Above the Galactic mid-plane the $\langle B_\parallel \rangle$ of the diffuse emission and the point sources seem to agree, which means that the WHAM DM are appropriate to calculate $\langle B_\parallel \rangle$ for the diffuse emission. At negative latitudes the difference in $\langle B_\parallel \rangle$ by a factor of 2 – 4 between the diffuse emission and the extragalactic sources would indicate that in order to produce the same $\langle B_\parallel \rangle$ as the extragalactic sources, the DM should cover only 1/2 – 1/4 of the line-of-sight through the entire Galaxy. The electron density in the NE2001 model terminates at about 15 kpc from the sun in the NE2001 model in the second Galactic quadrant, which implies that the diffuse emission that we observe originates from within about 4 – 8 kpc of the sun. Since the electron density distribution decreases away from the Galactic plane and further from the Galactic centre, these values are actually upper limits.

Simard-Normandin & Kronberg (1980) were the first to identify the large negative rotation measures of extragalactic sources at $60^\circ < l < 140^\circ$ and $-40^\circ < b < 10^\circ$ as a special feature that they refer to as 'Region A'. They modeled this region as a magnetic bubble, and found that it is likely to be very big (with a diameter of order 3 kpc) with an enhanced electron density (~ 0.03 cm^{-3}). Fig. 9.4 however shows that the DM in this region are similar above and below the Galactic plane. The increased rotation measures of extragalactic sources seen through Region A must therefore be produced by an enhanced $\langle B_\parallel \rangle$ as well, as is clear from Fig. 9.6.

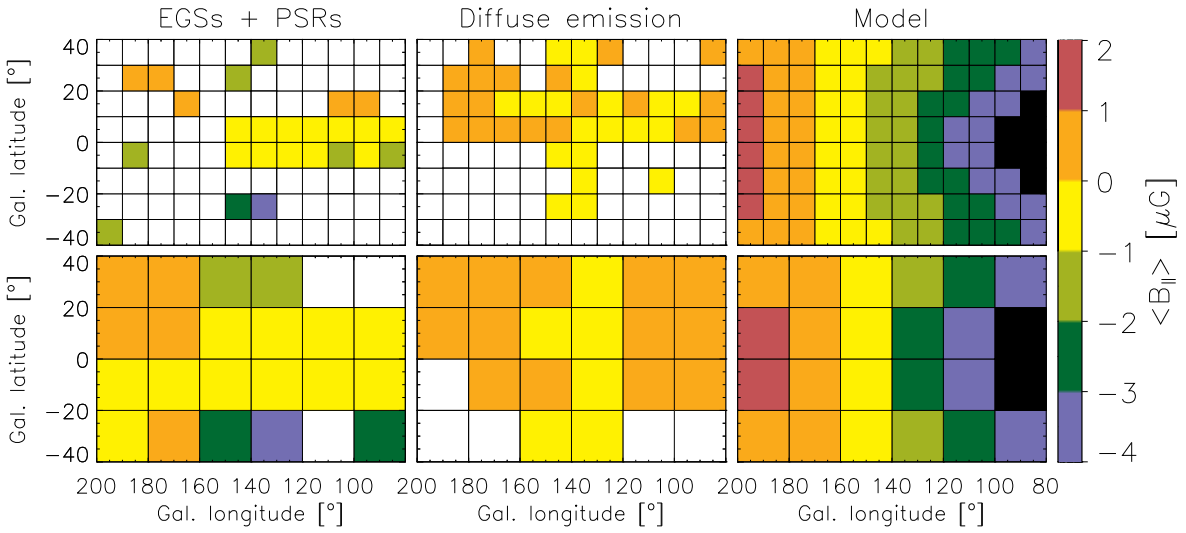

Figure 9.7 — $\langle B_\parallel \rangle$ from Fig. 9.6 averaged over cells of $10^\circ \times 10^\circ$ (top row of panels) and $20^\circ \times 20^\circ$ (bottom row of panels). To construct this figure we calculated $\langle B_\parallel \rangle$ for each CGPS source individually. Empty (white) cells have less than 5 lines-of-sight in them. Black cells have $\langle B_\parallel \rangle <$ -4μG. The first two columns show the averaged $\langle B_\parallel \rangle$ that we calculated from the $\langle B_\parallel \rangle$ of extragalactic sources and pulsars, the second column shows the averaged $\langle B_\parallel \rangle$ that we calculated from the $\langle B_\parallel \rangle$ of the diffuse emission. In the third column we plot the $\langle B_\parallel \rangle$ that we calculate for the model of the large-scale Galactic magnetic field that we describe in Sect. 9.5. On page 199 we show a colour version of this figure.

There is still much small-scale structure in the $\langle B_\parallel \rangle$ in Fig. 9.6. To better bring out the large-scale structure, we average the $\langle B_\parallel \rangle$ over cells of $10^\circ \times 10^\circ$ (top row of panels from Fig. 9.7) and $20^\circ \times 20^\circ$ (bottom row of panels from Fig. 9.7). These figures clearly show that on average there is also a difference in sign between the $\langle B_\parallel \rangle$ that we derive from the point sources and the diffuse emission. This is important to note, since even though we cannot exactly predict DM for each individual line-of-sight, a difference in sign of the $\langle B_\parallel \rangle$ can only be produced by structure in the magnetic field.

9.5 A model of the large-scale Galactic magnetic field

In this section we model $\langle B_\parallel \rangle$ using a logarithmic spiral arm model for the magnetic field, and we compare the modeled $\langle B_\parallel \rangle$ to the $\langle B_\parallel \rangle$ that we derived in the previous section. Starlight polarization observations and pulsar RM data indicate that the pitch angle p of the magnetic field spiral arms should be about -8° (see references in Beck 2007a). We let the strength of the total magnetic field $B_{\rm total}$ vary with Galactocentric radius $\mathrm{R_{GC}}$ according to:

$$B_{\rm total}(R_{\rm GC})[\mu{\rm G}] = \begin{cases} 11 - 0.5\,\mathrm{R_{GC}}\ [\mathrm{kpc}] & (\mathrm{R_{GC}} \leq 22\ \mathrm{kpc}) \\ 0 & (\mathrm{R_{GC}} > 22\ \mathrm{kpc}) \end{cases}$$

This relation roughly fits the data from Fig. 1 in Beck (2001; based on results by Berkhuijsen et al.) for 3 kpc $\lesssim \mathrm{R_{GC}} \lesssim$ 17 kpc, we extended this fit to the range from 0 kpc to 22 kpc, where $B_{\rm total}$ becomes 0 μG. To keep our model as simple as possible,

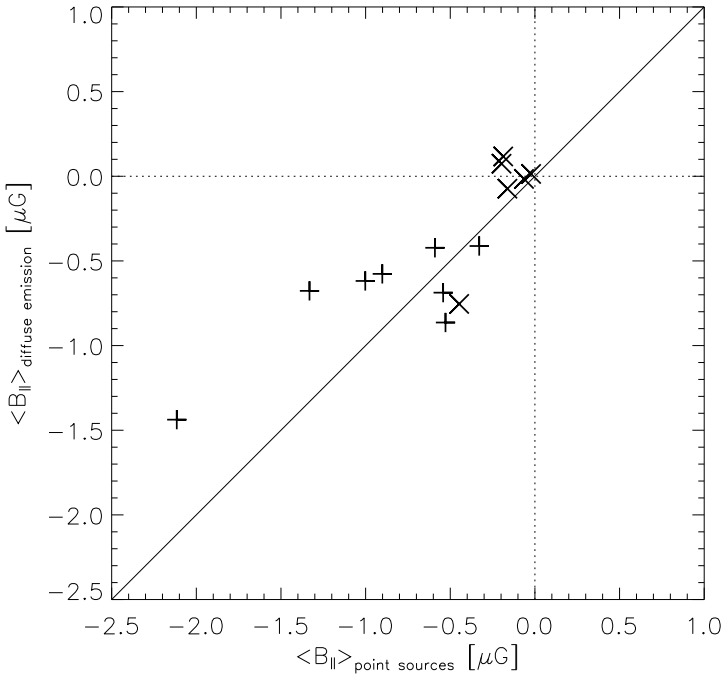

Figure 9.8 — Comparison between the $\langle B_{\parallel} \rangle$ that we derive for point sources (pluses) and the diffuse emission (crosses) for cells that have a counterparts at opposite Galactic latitudes. We averaged the $\langle B_{\parallel} \rangle$ of individual lines-of-sight over $10^{\circ} \times 10^{\circ}$ cells to make this plot. The majority of cell pairs support a magnetic field model that is symmetric above and below the Galactic plane, even though we could not use most of the cells from the top row of Fig. 9.7 since they contain less than 5 lines-of-sight.

we simply set $B_{\rm regular} = B_{\rm total}$, without modeling the contribution from the turbulent magnetic field.

For lines-of-sight outside the Galactic plane we need to know the symmetry of the magnetic field direction with respect to the Galactic plane. Han (2007) argues that in the inner Galaxy the magnetic field has opposite directions above and below the Galactic plane. In Fig. 9.8 we compare the magnetic field strengths of pairs of $10^{\circ} \times 10^{\circ}$ cells from the top row of panels from Fig. 9.7 on opposite sides of the Galactic plane. Even though for many cells we do not have data available, the data we have indicate a magnetic field direction that is symmetric above and below the Galactic plane, and this is how we will model the large-scale magnetic field of our Galaxy in our region of interest.

We modeled the z-dependence of the magnetic field as

$$B_{\rm total}({\rm z}, R_{\rm GC}) = \begin{cases} B_{\rm total}({\rm z}=0, R_{\rm GC})\, {\rm e}^{-{\rm z\ [kpc]}/7.2\ {\rm kpc}} & ({\rm z} \leq 5\ {\rm kpc}) \\ 0 & ({\rm z} > 5{\rm kpc}) \end{cases}$$

The dependence of $B_{\rm total}$ on z includes 2 effects. Within 5 kpc from the Galactic plane we model the z-dependence of the magnetic field as an exponential with a scale height of 7.2 kpc. Beck (2007c) argues that the magnetic field has in the case of energy equipartition between the magnetic field and the cosmic rays a scale height that is 4 times the scale height of the synchrotron-emitting thick disk, which is about 1.8 kpc (Beuermann

et al. 1985). The magnetic field scale height in the Milky Way therefore is 7.2 kpc. We include a cut-off in the magnetic field strength at 5 kpc, since our observations tell us the electron-density weighted magnetic field strength, and Fig. 12 from Berkhuijsen et al. (2006) indicates that most of the electrons lie within 3 – 4 kpc from the Galactic plane. To be on the safe side we placed the cut-off at 5 kpc.

The orientation of the magnetic field vector changes along the line-of-sight. We checked that the variation of the magnetic field orientation along a given line-of-sight is always a small fraction of the average magnetic field strength (a factor of about 1/2 – 1/3). It is therefore reasonable to use the average magnetic field strength along the line-of-sight to compare to our observations.

In the right columns of Fig. 9.7 we plot the $\langle B_{\parallel} \rangle$ that we modeled. The pitch angle of our model should be OK within 5 – 10°, since the model predicts the change in sign of $\langle B_{\parallel} \rangle$ at approximately the right location. Clearly our model predicts much stronger gradients in $\langle B_{\parallel} \rangle$ than we observe; our observations seem to indicate structure on angular scales between the scales of the large-scale magnetic field that we modeled, and the turbulent magnetic field that we averaged out over the cells. Also the $\langle B_{\parallel} \rangle$ of our WSRT mosaics show structure on scales from 1° – 10°, that are not predicted by our model of the large-scale field. These are important indications that it is not sufficient to model observations with only the large-scale field and a small-scale (turbulent) field. One could argue that the diffuse emission and pulsars probe only the nearby ISM, but the extragalactic sources should still more closely follow the modeled $\langle B_{\parallel} \rangle$. Reversals in the magnetic field direction can produce a smaller modeled $\langle B_{\parallel} \rangle$ gradient: the fanning out of the logarithmic spiral arms produces a longer line-of-sight through the regions with reversed field at $l = 180°$ than at $l = 90°$ which partially cancels the $\langle B_{\parallel} \rangle$ gradient that we modeled so far. However, Brown et al. (2003) dispute the existence of such a large-scale reversal in the second Galactic quadrant. That field reversals are possible over large angular scales is seen in our CEPHEUS mosaic (chapter 4), where the diffuse emission and polarized extragalactic sources have Faraday depths of opposite sign.

As a future project it will be interesting to compare our results to what large-scale fields $\alpha - \Omega$ dynamo theory predicts to exist (see e.g. Ferrière 2000).

9.6 Conclusions

In this chapter we compared the $\langle B_{\parallel} \rangle$ (defined in Eqn. 9.1) that we calculated for pulsars, extragalactic sources and lines-of-sight with diffuse emission in the area $80° \lesssim l \lesssim 200°$ and $-40° \lesssim b \lesssim 40°$. Since dispersion measures (DMs) can only be directly observed for pulsars, we need to model DM for the other two types of sources. For both the extragalactic sources and the diffuse emission we calculate DM for the entire line-of-sight through the Galaxy, which, in the case of the diffuse emission, gives only a lower limit to $|\langle B_{\parallel} \rangle|$. For lines-of-sight at Galactic latitudes $|b| > 5°$ we model DM by first deriving emission measures EM from the observed WHAM Hα intensities, and then converting these EM to DM by using the EM/DM relation that Berkhuijsen et al. (2006) established for a sample of 157 pulsars. At Galactic latitudes below $|b| = 5°$ the required interstellar E(B-V) reddening corrections are very uncertain, and for these

lines-of-sight we integrated the NE2001 model by Cordes & Lazio (2003) through the entire Galaxy.
The $\langle B_{\parallel} \rangle$ that we calculate for point sources (pulsars and extragalactic sources) agree very well outside the Galactic plane; close to the Galactic plane the $\langle B_{\parallel} \rangle$ of pulsars are somewhat larger than the $\langle B_{\parallel} \rangle$ of the extragalactic sources. For the pulsars at higher Galactic latitudes this result implies that the $\langle B_{\parallel} \rangle$ in front of the pulsar is the same as the $\langle B_{\parallel} \rangle$ beyond the pulsar. The $\langle B_{\parallel} \rangle$ of the diffuse emission on the other hand only agrees with the $\langle B_{\parallel} \rangle$ of the point sources at positive Galactic latitudes. At negative Galactic latitudes and for Galactic longitudes $\lesssim 140^{\circ}$, the $\langle B_{\parallel} \rangle$ of the diffuse emission are smaller than the $\langle B_{\parallel} \rangle$ of the point sources by a factor of 2 – 4. The data that we compiled does not contain enough lines-of-sight to extend this result to larger longitudes.
We calculated the DM for lines-of-sight with diffuse emission for the entire line-of-sight through the Galaxy. Therefore, if there is a difference between the $\langle B_{\parallel} \rangle$ of the diffuse emission and the $\langle B_{\parallel} \rangle$ of the extragalactic sources, this implies that the diffuse emission that we observe is emitted within 1/2 – 1/4 of the line-of-sight to the extragalactic sources. Since the electron density in the NE2001 model becomes negligible at about 15 kpc from the sun in the second Galactic quadrant, which in this case indicates the 'edge' of the Galaxy, the diffuse emission should originate within 4 – 8 kpc of the sun. In some regions however the $\langle B_{\parallel} \rangle$ of the diffuse emission even has a different sign from the $\langle B_{\parallel} \rangle$ of the pulsars and extragalactic sources, which cannot be explained by errors in the modeling of DM, but instead is a clear indication that the diffuse emission does not sample the same line-of-sight as the pulsars and extragalactic sources.
To better bring out the large-scale structure in $\langle B_{\parallel} \rangle$ we averaged the $\langle B_{\parallel} \rangle$ of individual lines-of-sight over cells of $10^{\circ} \times 10^{\circ}$ and $20^{\circ} \times 20^{\circ}$. We do not find evidence for a reversals in the magnetic field direction above and below the Galactic plane, in the relatively small number of regions with a high surface density of usable lines-of-sight. We modeled the large-scale field as a logarithmic spiral to compare to our observations. The observations show much more structure on angular scales between the angular scales of the large-scale field that we modeled and the turbulent (small-scale) field that we averaged out over the $10^{\circ} \times 10^{\circ}$ and $20^{\circ} \times 20^{\circ}$cells. Our observations do not show the large-scale gradients in $\langle B_{\parallel} \rangle$ that we would expect from our model of the large-scale Galactic magnetic field. Large-scale reversals in the magnetic field direction can reduce the $\langle B_{\parallel} \rangle$ gradient that we modeled, but Brown et al. (2003) argue against such a reversal in the outer Galaxy. Our CEPHEUS mosaic (chapter 4) however shows that field reversals on scales $\gtrsim 10^{\circ}$can exist.

Acknowledgements

We would like to thank Rodion Stepanov and Jo-Anne Brown for providing us with their rotation measure catalogues. The Westerbork Synthesis Radio Telescope is operated by the Netherlands Foundation for Research in Astronomy (NFRA) with financial support from the Netherlands Organization for Scientific Research (NWO). The Wisconsin H-Alpha Mapper is funded by the National Science Foundation.

Bibliography

Axon, D.J., & Ellis, R.S. 1976, MNRAS, 177, 499

Baars, J.W.M., Genzel, R., Pauliny-Toth, I.I.K., Witzel, A. 1977, A&A, 61, 99

Beck, R., Brandenburg, A, Moss, D., et al. 1996, ARA&A, 34, 155

Beck, R., 2001, Space Science Reviews, 99, 243

Beck, R., Shukurov, A., Sokoloff, D., Wielebinski, R. 2003, A&A, 411, 99

Beck, R., in *How Does the Galaxy Work?*, 2004,
eds. Alfaro, E.J., Perez, E., Franco, J., ASSL Vol. 315, 277

Beck, R., Fletcher, A., Shukurov, A., et al. 2005, A&A, 444,739

Beck, R. 2007a, in *Sky Polarisation at Far-Infrared to Radio Wavelengths*,
eds. Miville-Deschênes, M.-A., & Boulanger, F., EAS Publication series, Vol. 23, 19

Beck, R. 2007b, A&A, 470, 539

Beck, R. 2007c, `http://arxiv.org/abs/0711.4700`

Berkhuijsen, E.M. 1971, A&A, 14, 359

Berkhuijsen, E.M., Horellou, C., Krause, M., et al. 1997, A&A, 318, 700

Berkhuijsen, E.M., Mitra, D., Mueller, P. 2006, AN, 327, 82

Beuermann, K., Kanbach, G., Berkhuijsen, E.M. 1985, A&A, 153, 17

Bingham, R.G., & Shakeshaft, J.R. 1961, MNRAS, 136, 347

Bower, J.C., et al. 1999, ApJ, 521, 582

Bowman, J.D., Barnes, D.G., Briggs, F.H., et al. 2006, AJ, 133, Issue 4, 1505

Brentjens, M.A., & De Bruyn, A.G. 2005, A&A, 441, 1217

Bridle, A.H., Davis, M.M., Fomalont, E.B., Lequeux, J. 1972, Nature Physical Science,
235, 123

Broten, N.W., MacLeod, J.M., Vallee, J.P. 1988, Ap&SS, 141, 303

Brouw, W.N., & Spoelstra, T.A.Th. 1976, A&A, 26, 129

Brown, J.C., Taylor, A.R., Wielebinski, R., Mueller, P. 2003, ApJ, 592, L29

Brown, J.C., Haverkorn, M., Gaensler, B.M., Taylor, A.R. et al. 2007, ApJ, 663, 258

Burn, B.J. 1966, MNRAS, 133, 67

Cesarsky, C.J. 1980, ARAA, 18, 289

Cho, J., Lazarian, A., Vishniac, E.T. 2003, ApJ, 595, 812

Clegg, A.W., Cordes, J.M., Simonetti, J.M., Kulkarni, S.R. 1992, ApJ, 386, 143

Cordes, J.M., & Lazio, T.J.W. 2002,
`http://xxx.lanl.gov/abs/astro-ph/0207156`, and
`http://astrosun2.astro.cornell.edu/~cordes/NE2001`

Davis, L. Jr., & Greenstein, J.L. 1951, ApJ, 114, 206

De Bruyn, A.G., & Brentjens, M.A. 2005, A&A, 441, 931

De Bruyn, A.G., Katgert, P., Haverkorn, M., Schnitzeler, D.H.F.M. 2006, AN, 327, 487

De Zeeuw, P.T., Hoogerwerf, R., De Bruijne, J.H.J. et al. 1999, ApJ, 117, 354

Dumke, M., Krause, M., Wielebinski, R., Klein, U. 1995, A&A, 302, 691

Elliott, K.H. 1970, Nature, 226, 1236E

Ferrière, K., & Schmitt, D. 2000, A&A, 358, 125

Ferrière, K.M. 2001, Reviews of Modern Physics, Vol. 73, Issue 4, 1031

Field, G.B., Goldsmith, D.W., Habing, H.J. 1969, ApJ, 155, 149

Fletcher, A., Berkhuijsen, E.M., Beck, R., Shukurov, A. 2004, A&A, 414, 53

Fletcher, A., Beck, R., Berkhuijsen, E., et al. 2004b, in *How does the Galaxy work?*, eds. Alfaro, E.J., Perez, E., Franco, J., ASSL Vol. 315, 299

Frick, P., Stepanov, R., Shukurov, A., Sokoloff, D. 2001, MNRAS 325, 649

Gaensler, B.M., Haverkorn, M., Staveley-Smith, L., et al. 2005, Science, 307, 1610

Groenewegen, M.A.T., Udalski, A., Bono, G. 2008,
`http://arxiv.org/abs/0801.2652`

Haffner, L.M., Reynolds, R.J., Tufte, S.L. 1998, ApJ, 501, L83

Haffner, L.M., Reynolds, R.J., Tufte, S.L., et al. 2003, ApJS, 149, 405H

Hamaker, J.P., Bregman, J.D., Sault, R.J. 1996, A&AS, 117, 137

Han, J.L., & Qiao, G.J. 1994, A&A, 288, 759

Han, J.L., Manchester, R.N., Berkhuijsen, E.M., Beck, R. 1997, A&A 322, 98

Han, J.L., Beck, R., Berkhuijsen, E.M. 1998, A&A, 335, 1117

Han, J.L., Ferriere, K., Manchester, R.N. 2004, ApJ, 610, 820

Han, J.L., Manchester, R.N., Lyne, A.G., et al. 2006, ApJ, 642, 868

Han, J.L. 2007, in *Astrophysical Masers and their Environments*, eds. Chapman, J.M., & Baan, W.A., IAU symposium 242, and `http://arxiv.org/abs/0705.4175`

Haslam, C.G.T., Klein, U., Salter, C.J., et al. 1981, A&A, 100, 209

Haslam, C.G.T., Stoffel, H., Salter, C.J., Wilson, W.E. 1982, A&A, 47, 1

Haverkorn, M., Katgert, P., De Bruyn, A.G. 2000, A&A, 356, L13

Haverkorn, M., Katgert, P., De Bruyn, A.G. 2003a, A&A, 403, 1031

Haverkorn, M., Katgert, P., De Bruyn, A.G. 2003b, A&A, 404, 233

Haverkorn, M., Katgert, P., De Bruyn, A.G. 2004a, A&A, 427, 169

Haverkorn, M., Gaensler, B.M., McClure-Griffiths, N.M., et al. 2004b, ApJ, 609, 776

Haverkorn, M., Katgert, P., De Bruyn, A.G. 2004c, A&A, 403, 1031

Haverkorn, M., Katgert, P., De Bruyn, A.G. 2004d, A&A, 404, 233

Haverkorn, M., Gaensler, B.M., Brown, J.C., et al. 2006a, ApJ, 637, L33

Haverkorn, M., Gaensler, B.M., McClure-Griffiths, N.M., et al. 2006b, ApJS, 167, 230

Heesen, V., Krause, M., Beck, R., Dettmar, R.-J. 2007, AN, 328, 637

Heiles, C., & Kulkarni, S.R. 1987, in *Physical processes in interstellar clouds*, eds. Morfill, G.E. & Scholer, M., 13

Heiles, C. 1996, in *Polarimetry of the interstellar medium*, eds. Roberge W.G., & Whittet, D.C.B., ASP Conference Series vol. 97, 457

Heiles, C. 2001, in *Tetons 4: Galactic structure, Stars & The interstellar medium*, eds. Woodward, C.E., Bicay, M.D., Shull, J.M., ASP conference series Vol. 231, 294

Heitsch, F., Zweibel. E.G., Mac Low, M.-M., et al. 2001, ApJ, 561, 800

Houde, M., Bastien, P., Dotson, J.L. et al. 2002, ApJ, 569, 803

Humphreys, R.M. 1978, ApJSS, 38, 309

Indrani, C., & Deshpande, A.A. 1998, New Astronomy, 4, 33

Israel, F.P., Mahoney, M.J., Howarth, N. 1992, A&A, 261, 47

Jones, T.J., Klebe, D., Dickey, J. M. 1992, ApJ, 389, 602

Johnston-Hollitt, M., Hollitt, C.P., Ekers, R.D. 2004,
Statistical Analysis of Extragalactic Rotation Measures.
In *The Magnetized Interstellar Medium, Proceedings of the conference*,
eds. Uyaniker, B., Reich, W., Wielebinski, R., p. 13

Jones, T.J., Klebe, D., Dickey, J. M. 1992, ApJ, 389, 602

Junkes, N., Fürst, E., and Reich, W. 1987, A&AS, 69,451

Krause, M., Wielebinski, R., Dumke, M. 2006, A&A, 448, 133

Longair, M.S. 1981, *High Energy Astrophysics: Volume 2, Stars, the Galaxy and the Interstellar Medium* (Cambridge University Press)

Mac Low, M.-M. 1999, ApJ, 524, 169

Manchester, R.N., Hobbs, G.B., Teoh, A., Hobbs, M. 1993-2006 (2005), AJ, 129

Mathewson, D.S., & Ford, V.L. 1970, MmRAS, 74, 139

McKee, C.F., & Ostriker, J.P. 1977, ApJ, 218, 148

Minter, A.H., Spangler, S.R. 1996, ApJ, 458, 194

Mitra, D., Wielebinski, R., Kramer, M., Jessner, A. 2003, A&A, 398, 993

Niklas, S., Ph.D. thesis, University of Bonn, 1995

Ohno, H. & Shibata, S. 1993, MNRAS, 262, 953

Patrikeev, I., Fletcher, A., Stepanov, R. et al. 2006, A&A, 458, 441

Phillipps, S., et al. 1981, A&A, 103, 405

Rand, R.J., & Kulkarni, S.R. 1989, ApJ, 343, 760

Rand, R.J., & Lyne, A.G. 1994, MNRAS, 268, 497

Reich, P., Reich, W., Fürst, E. 1997, A&AS, 126, 413

Rengelink, R., Tang, Y., De Bruyn, A.G., et al. 1997, A&AS, 124, 259

Reynolds, R.J. 1985, ApJ, 294, 256

Reynolds, R.J. 1991, ApJ, 372, L17

Reynolds, R.J., Sterling, N.C., Haffner L.M. 2001, ApJ, 558, 101

Röttgering, H.J.A., Braun, R., Barthel, P.D. et al. 2006,
`http://arxiv.org/abs/astro-ph/0610596`

Sarala, S., & Jain, P. 2001, MNRAS, 328, 623

Sault, R.J., Hamaker, J.P. Bregman, J.D. 1996, A&AS, 117, 149

Schlegel, D.J., Finkbeiner, D.P., Davis, M. 1998, ApJ, 500, 525

Shukurov, A., & Berkhuijsen, E.M. 2003, MNRAS, 342, 496

Simard-Normandin, M., & Kronberg, P.P. 1980, ApJ, 242, 74

Snowden, S.L., Egger, R., Freyberg, M.J., et al. 1997, ApJ, 485, 125

Sokoloff, D.D., Bykov, A.A., Shukurov, A., et al. 1998, MNRAS, 299, 189

Spoelstra, T.A.T. 1984, A&A, 135, 238

Stanimirović, S. 2002, Short-Spacings Correction from the Single-Dish Perspective. In *Single-Dish Radio Astronomy: Techniques and Applications*, eds. S. Stanimirovic, D. Altschuler, P. Goldsmith, Salter, C.J., ASP Conference Proceedings, vol. 278, 375

Stepanov, R., Frick, P., Shukurov, A., Sokoloff, D. 2002, A&A, 391, 361

Strong, A.W., Moskalenko, I.V., Reimer, O. 2000, ApJ, 537, 763

Tabataei, F.S., Krause, M., Beck, R. 2007, A&A, 472, 785

Taylor, A.R., Gibson, S.J., Peracaula, M., et al. 2003, AJ, 125, 3145

Taylor, A.R. 2004, AAS meeting 205, #78.05; Bulletin of the American Astronomical Society, Vol. 36. See also `http://www.ras.ucalgary.ca/GALFACTS/`

Taylor, J.H., Manchester, R.N., Lyne, A.G. 1993, ApJS, 88, 529

Tickle, J. 2006, in *Brainiac*, Sky One TV series. See also `http://www.skyone.co.uk/programme/pgefeature.aspx?pid=15&fid=149`

Tielens, A. 2005, in *The physics and chemistry of the interstellar medium*, Cambridge University Press, ISBN 0-521-82634-9

Uyaniker, B., Landecker, T., Gray, A.D., Kothes, R. 2003, ApJ, 585, 785

Vallée, J.P. 1995, ApJ, 454, 119

Vallée, J.P. 2002, ApJ, 566, 261

Weisberg, J. M., Cordes, J. M., Kuan, B., et al. 2004, ApJS, 150, 317

Wieringa, M., De Bruyn, A.G., Jansen, D. et al. 1993, A&A, 268, 215

Wolleben, M., Ph.D. thesis, University of Bonn, 2005

Wolleben, M., Landecker, T.L., Reich, W., Wielebinski, R. 2006, A&A ,448, 411

Colour figures

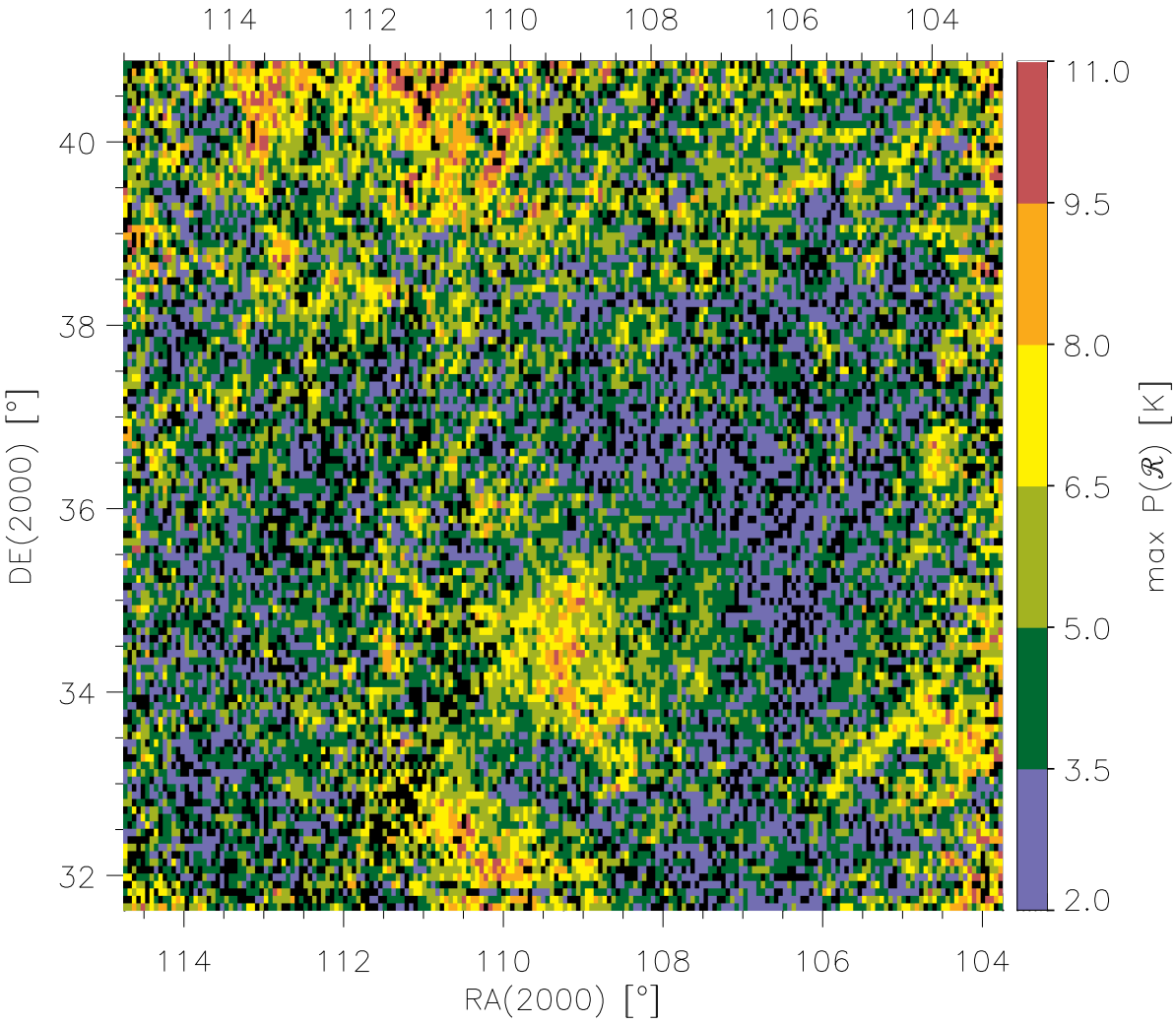

Figure 10.1 — [GEMINI] $P(\mathcal{R})$ of the highest peak in the $\mathcal{R}$ spectrum. Each pixel represents one telescope beam, and the pixel size is $2.8' \times 4.9'$. The lines-of-sight that are shown in this plot have a second peak in the $P(\mathcal{R})$ spectrum that is at most half the strength of the main peak. Out of a total of 22.800, lines-of-sight 2720 do not obey this selection criterium, and they are shown in black, as are the 769 lines-of-sight that have $P(\mathcal{R}) < 2$ K. The 1σ noise level in the $P(\mathcal{R})$ maps is 0.14 K.

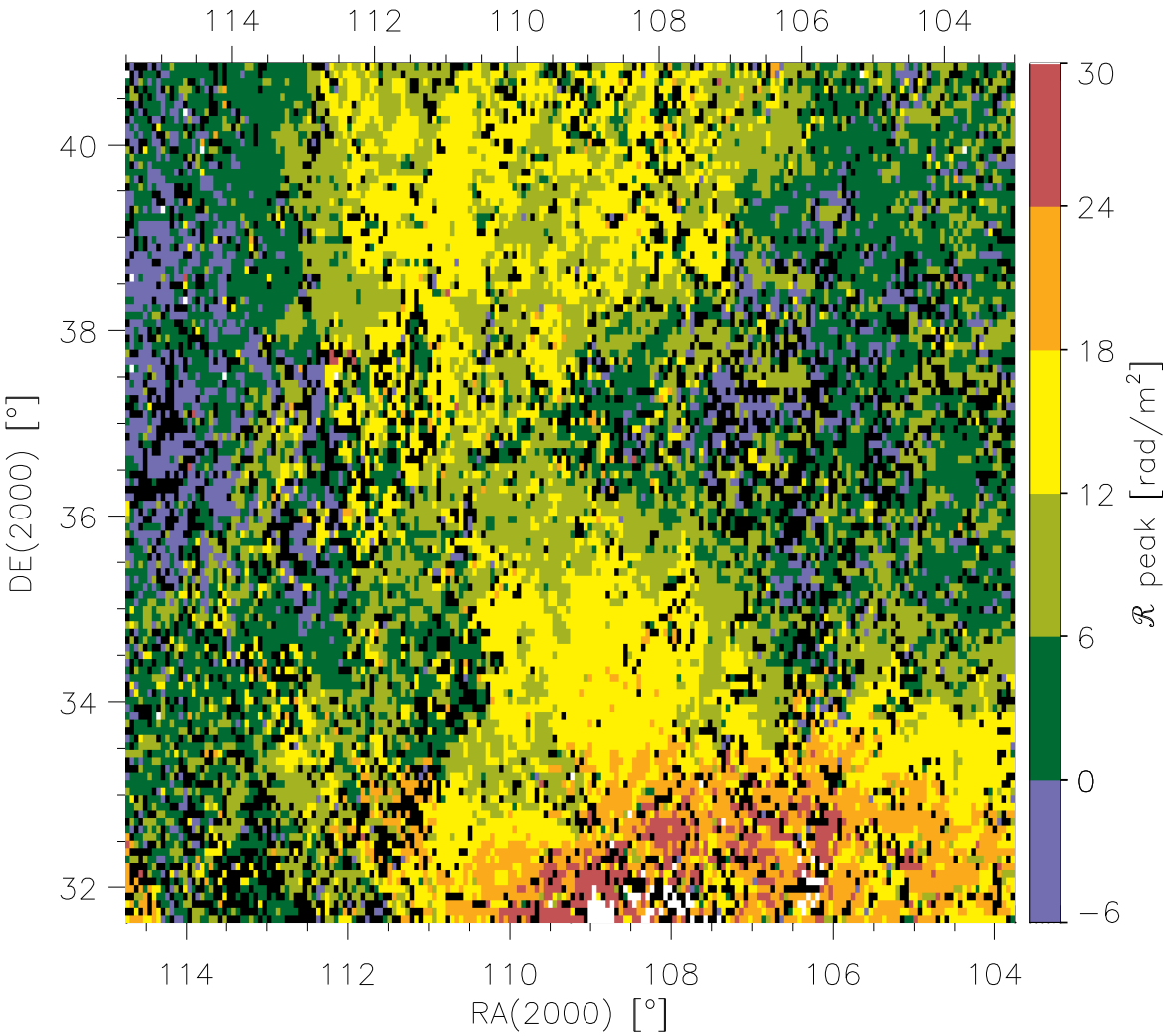

Figure 10.2 — [GEMINI] $\mathcal{R}$ corresponding to the $P(\mathcal{R})$ plotted in Fig. 10.1. The lines-of-sight plotted in these figures are selected by using the same criterium. Lines-of-sight indicated in white have $\mathcal{R} > 30$ rad/m^2. Lines-of-sight indicated in black either did not pass the selection criterium or have $\mathcal{R} <$ -6 rad/m^2 (2720 and 727 lines-of-sight resp.).

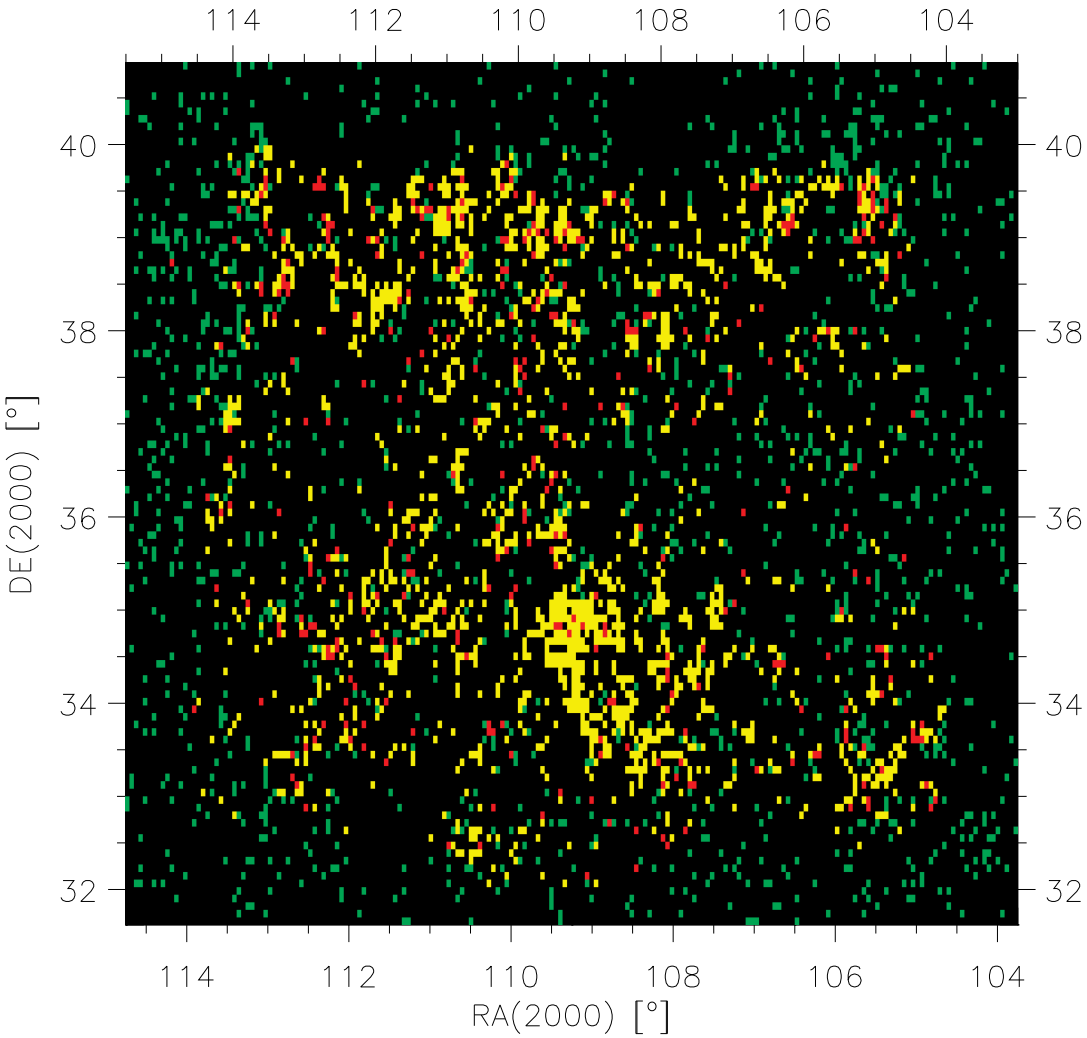

Figure 10.3 — [GEMINI] Distribution of independent lines-of-sight with a main peak that satisfies the Δ criterion (green pixels), or with $\chi^2_{\rm red} < 2$ and $\max(P(\mathcal{R})) > 2$ K (yellow pixels), or that satisfy all three criteria (red pixels). Lines-of-sight that did not pass these criteria are shown as black pixels. The outer edges of the mosaic show an increase in $\chi^2_{\rm red}$, which explains the absence of yellow pixels.

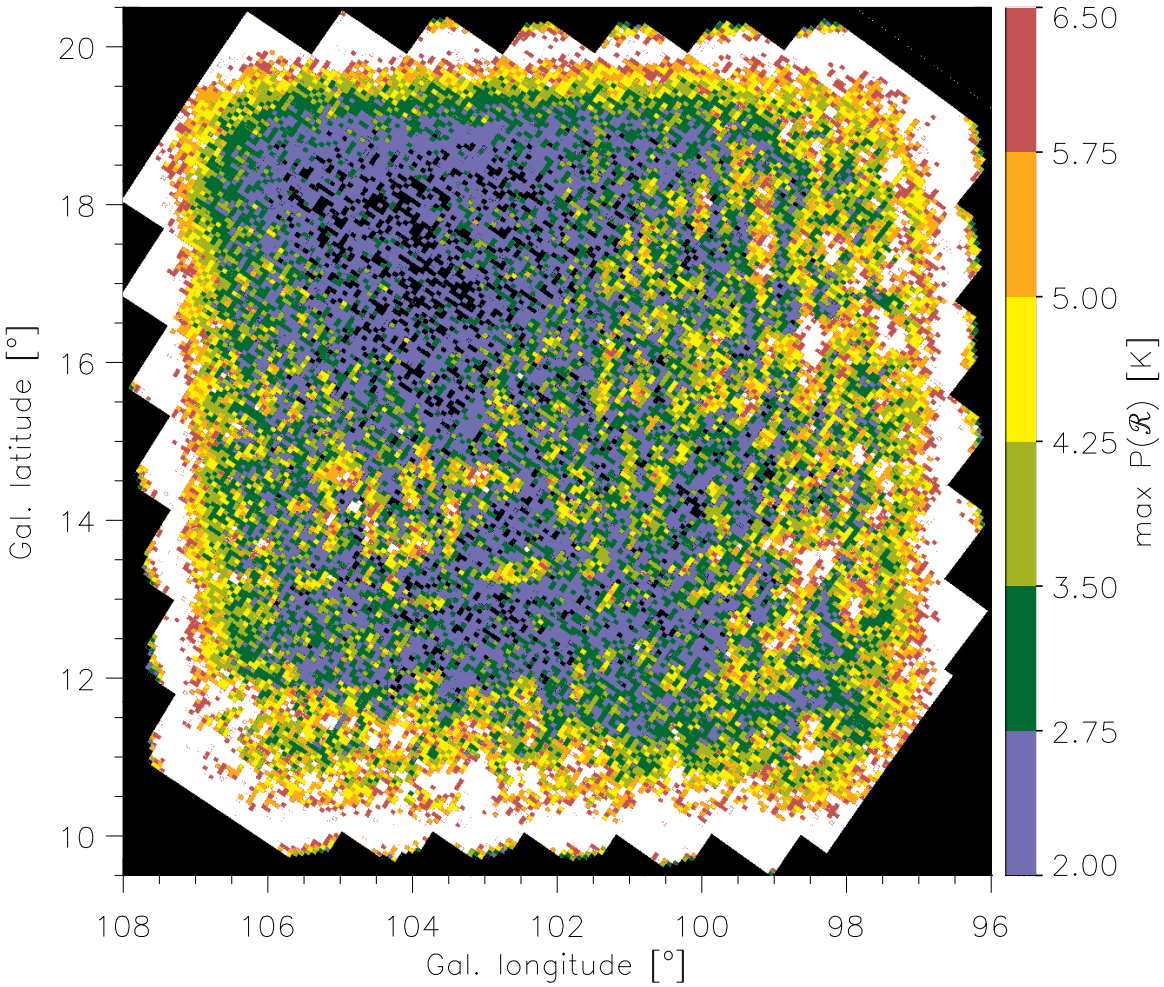

Figure 10.4 — [CEPHEUS] $P(\mathcal{R})$ of the highest peak in the $\mathcal{R}$ spectrum. Each pixel represents one telescope beam, and the pixel size is $3.0' \times 3.3'$. Out of a total of about 28.000 lines-of-sight, 1287 lines-of-sight have $P(\mathcal{R}) < 2$ K, shown in black, and 3894 lines-of-sight have $P(\mathcal{R}) > 6.5$ K, which are shown in white. The 1σ noise level is 0.13 K.

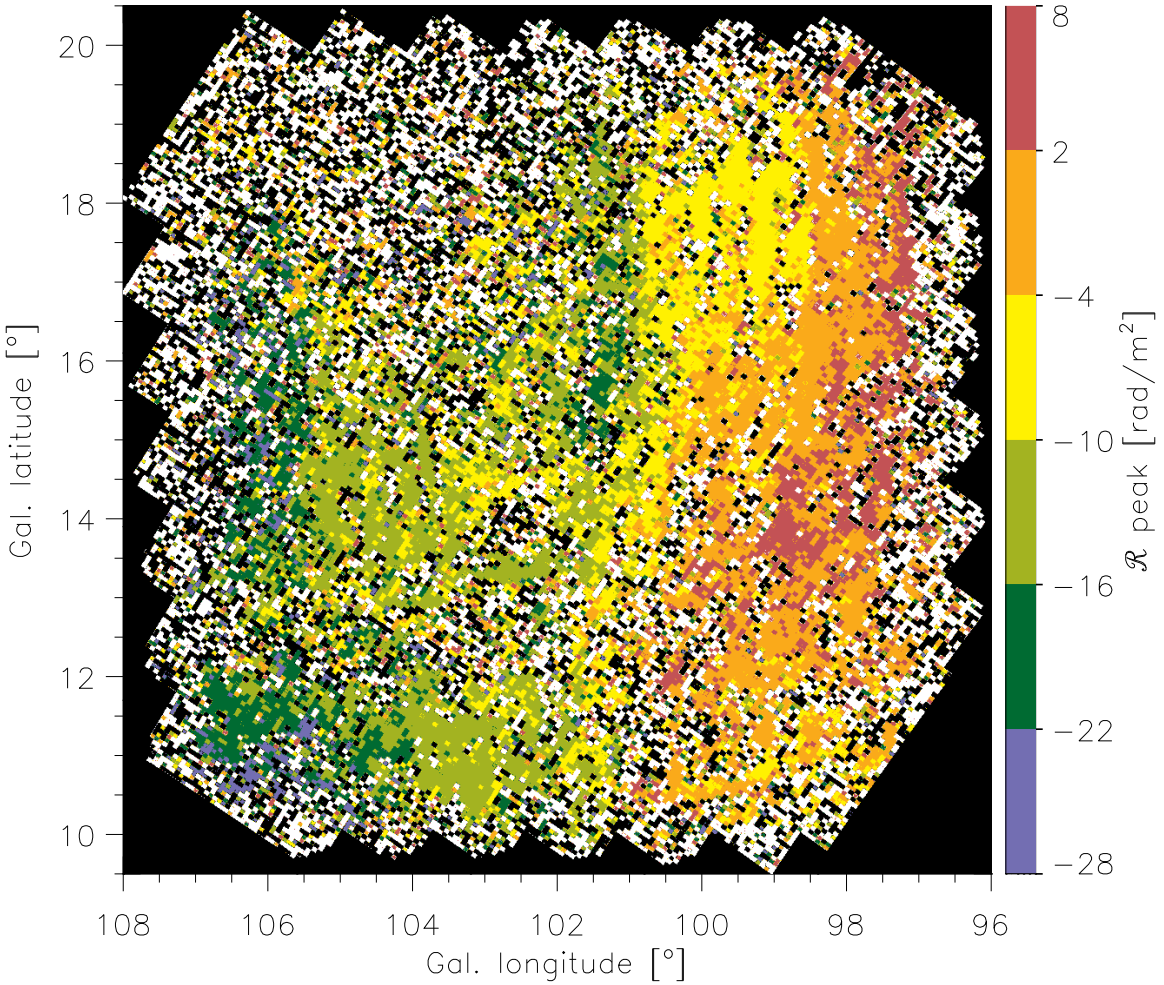

Figure 10.5 — [CEPHEUS] $\mathcal{R}$ corresponding to the $P(\mathcal{R})$ plotted in Fig. 4.2. Lines-of-sight with $\mathcal{R}$ < -28 rad/m^2 are shown in white, lines-of-sight indicated in black have $\mathcal{R} > 8$ rad/m^2 (5009 and 5670 lines-of-sight respectively). Most of the discarded lines-of-sight fall either on the edge of the mosaic, or in the upper left region with low signal strength.

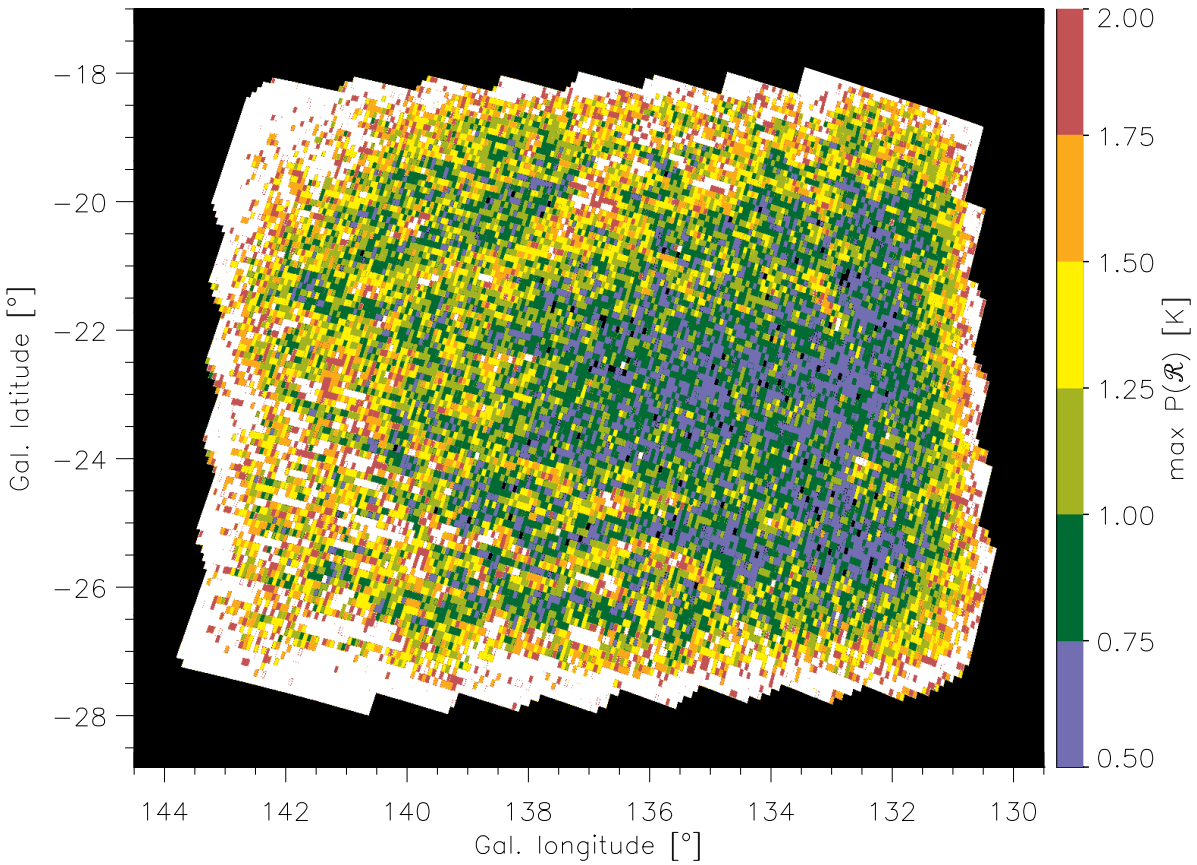

Figure 10.6 — [TRIANGULUM] $P(\mathcal{R})$ of the highest peak in the $\mathcal{R}$ spectrum. Each pixel represents one telescope beam, and the pixel size is $3.4' \times 5.6'$. Out of a total of about 18.500 lines-of-sight, 111 lines-of-sight have $P(\mathcal{R}) < 0.5$ K, shown in black, and 3402 lines-of-sight have $P(\mathcal{R}) > 2.0$ K, that are shown in white. The 1σ noise level is 0.06 K.

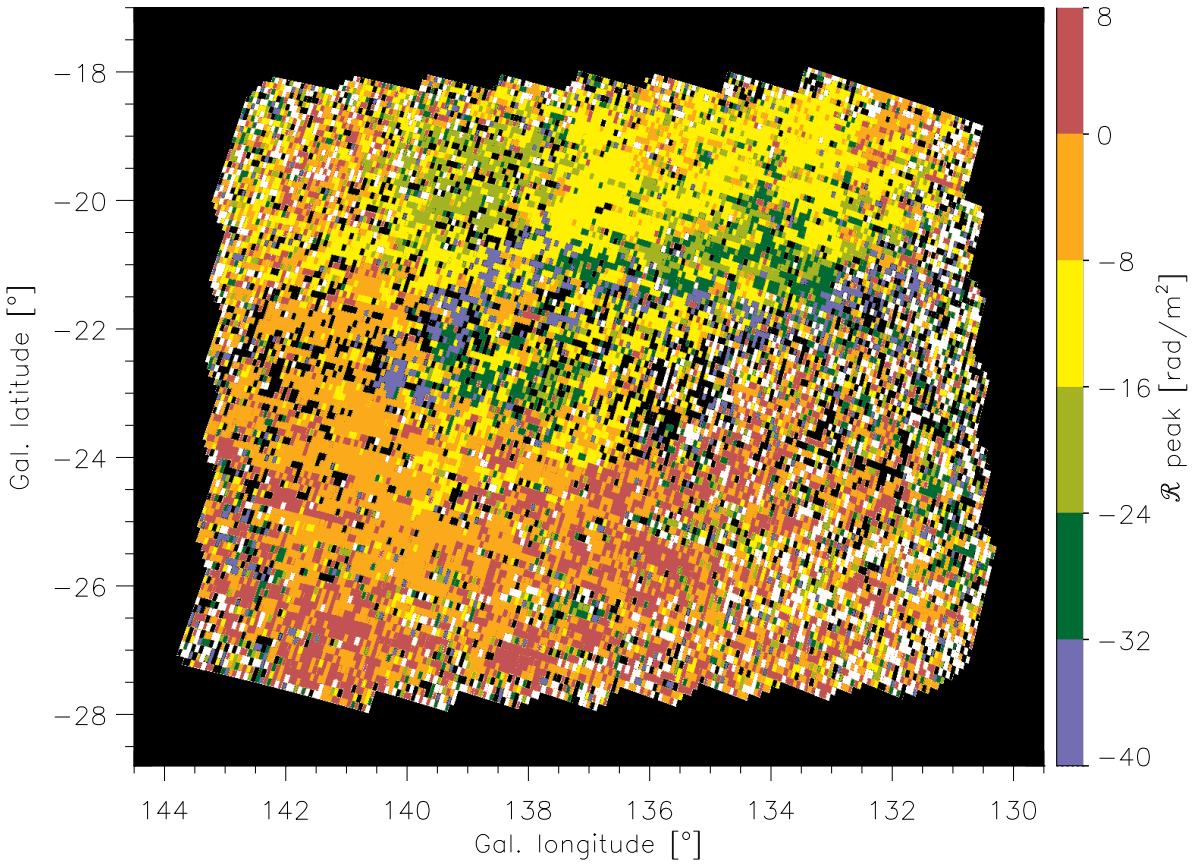

Figure 10.7 — [TRIANGULUM] $\mathcal{R}$ corresponding to the $P(\mathcal{R})$ plotted in Fig. 5.2. The 2233 lines-of-sight indicated in white have $\mathcal{R} > 8$ rad/m^2, and the 1698 black lines-of-sight that fall inside the mosaic have $\mathcal{R} < -40$ rad/m^2.

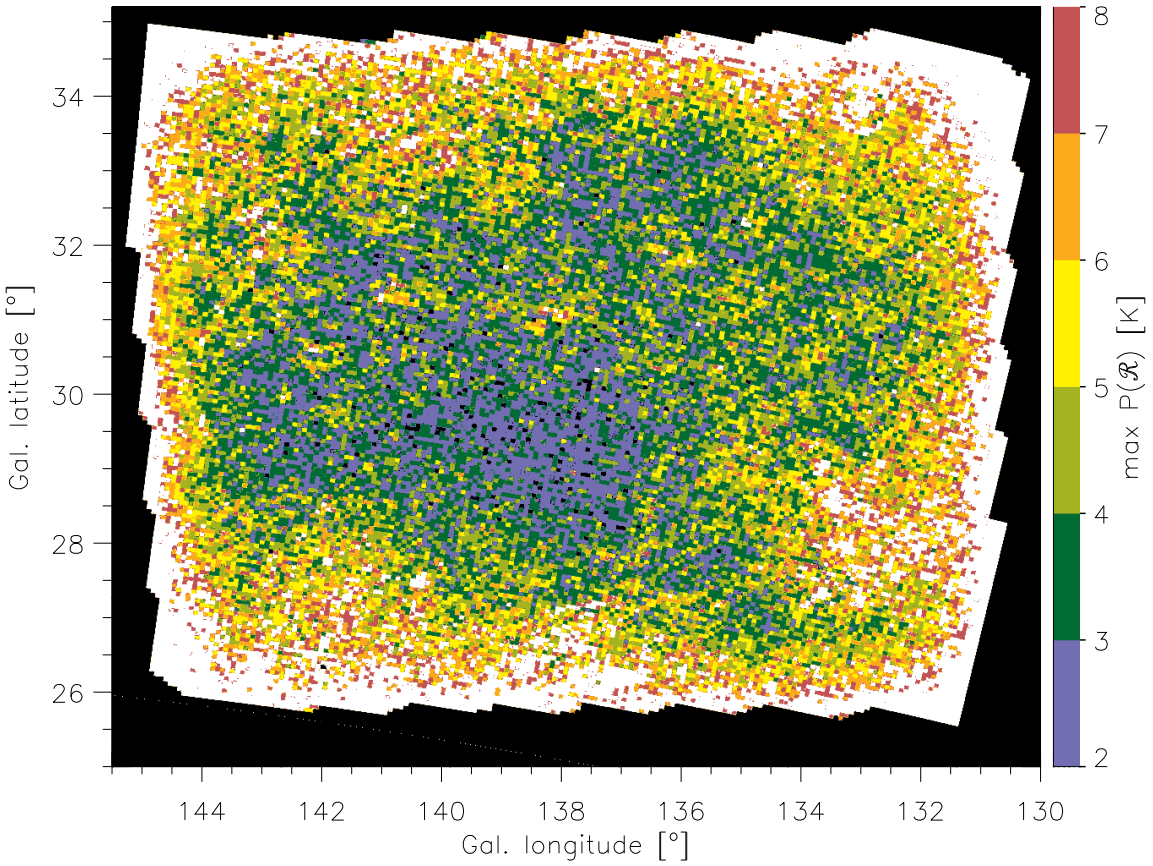

Figure 10.8 — [CAMELOPARDALIS] $P(\mathcal{R})$ of the highest peak in the $\mathcal{R}$ spectrum. Each pixel represents one telescope beam, and the pixel size is $2.9' \times 3.0'$. Out of a total of 26.000 lines-of-sight, 5314 lines-of-sight have $P(\mathcal{R}) > 8$ K, and these are shown in white. The 1σ noise level is 0.16 K.

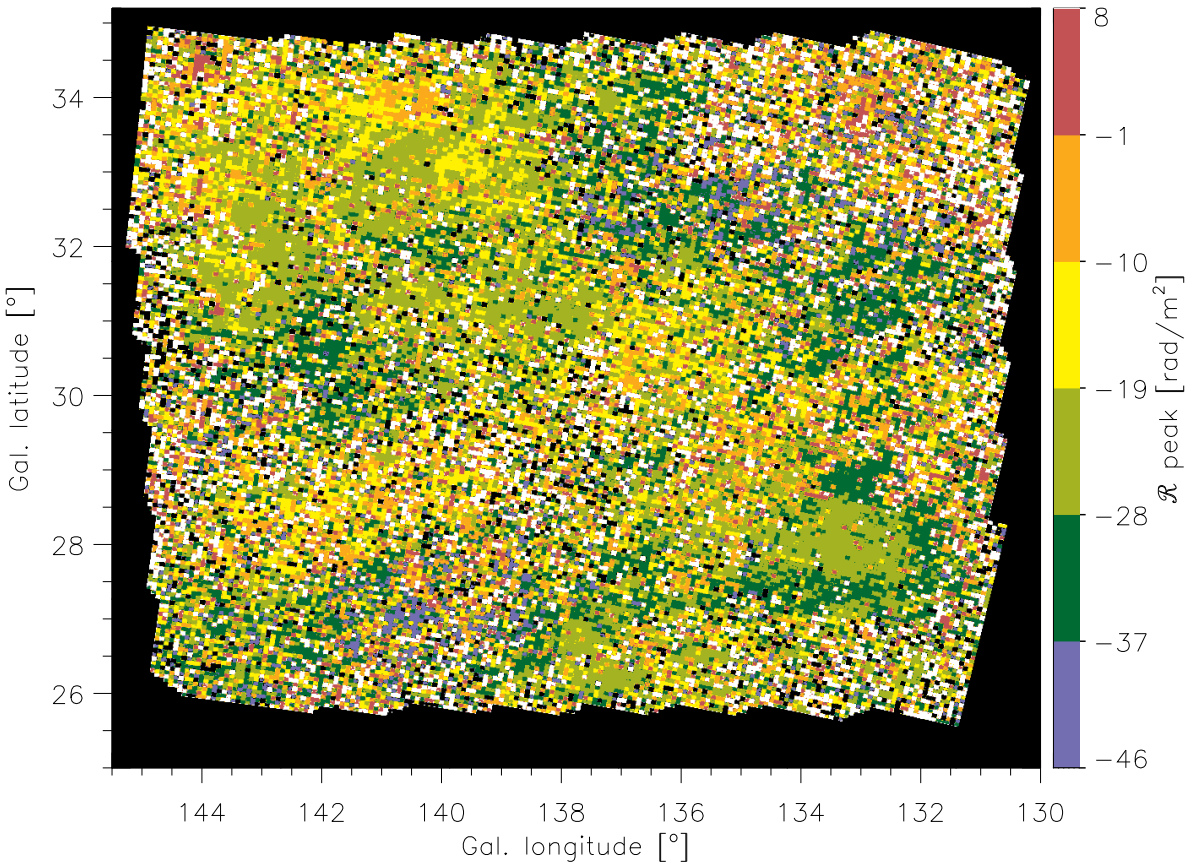

Figure 10.9 — [CAMELOPARDALIS] $\mathcal{R}$ corresponding to the $P(\mathcal{R})$ plotted in Fig. 6.2. The 3713 lines-of-sight indicated in white have $\mathcal{R} > +8$ rad/m^2, and the 1482 black lines-of-sight that fall inside the mosaic have $\mathcal{R} < -46$ rad/m^2.

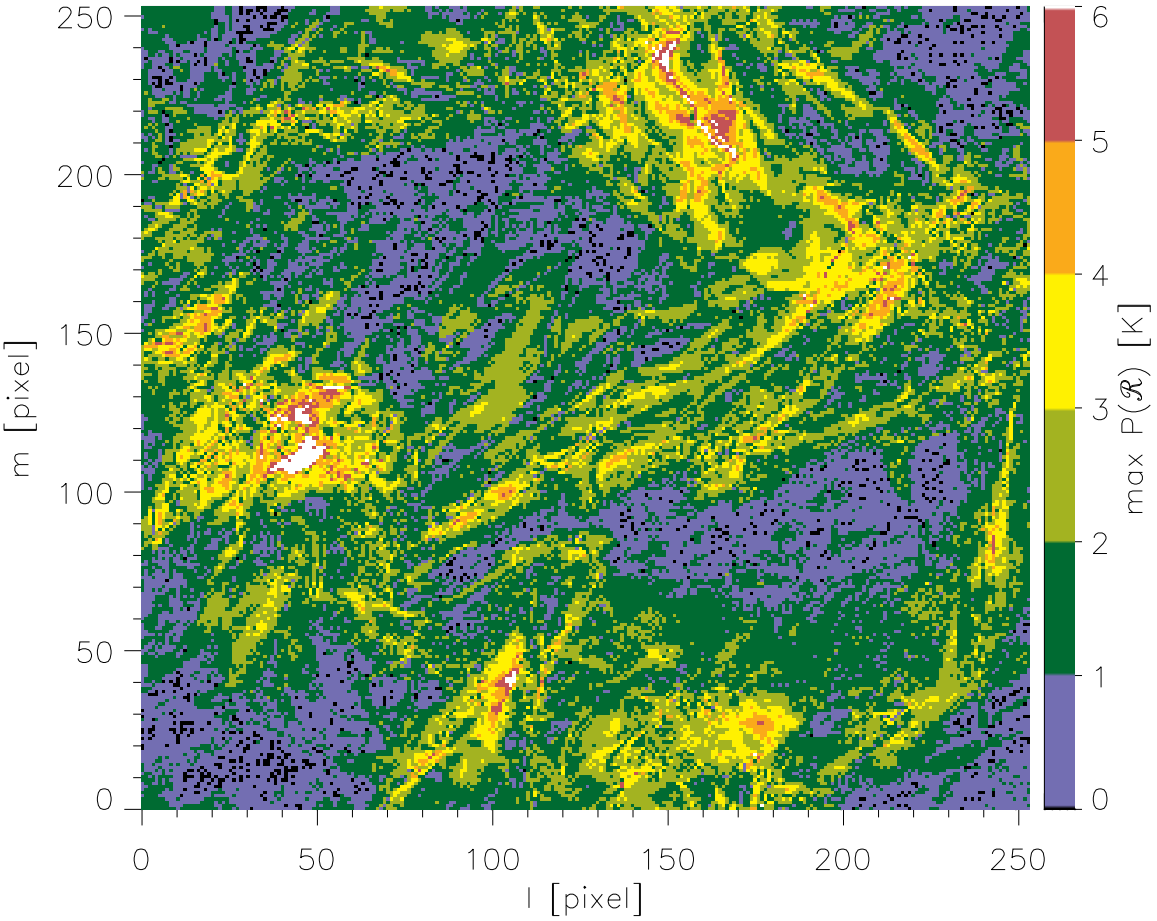

Figure 10.10 — [SIMULATION] Polarized brightness temperature (in Kelvin) of the highest peak in the $P(\mathcal{R})$ spectrum in our MHD cube. We used lines-of-sight parallel to the Z-axis of our cube. To calculate the synchrotron emissivities we used a uniform cosmic ray density distribution. Each pixel represents one line-of-sight. The 176 lines-of-sight indicated in white have $P(\mathcal{R}) > 6$K. Since we added the noise levels of our GEMINI data set to calculate the $P(\mathcal{R})$ spectra from our MHD cube, the 1σ noise level is the same as the 1σ noise level of the GEMINI $P(\mathcal{R})$ spectra = 0.14 K.

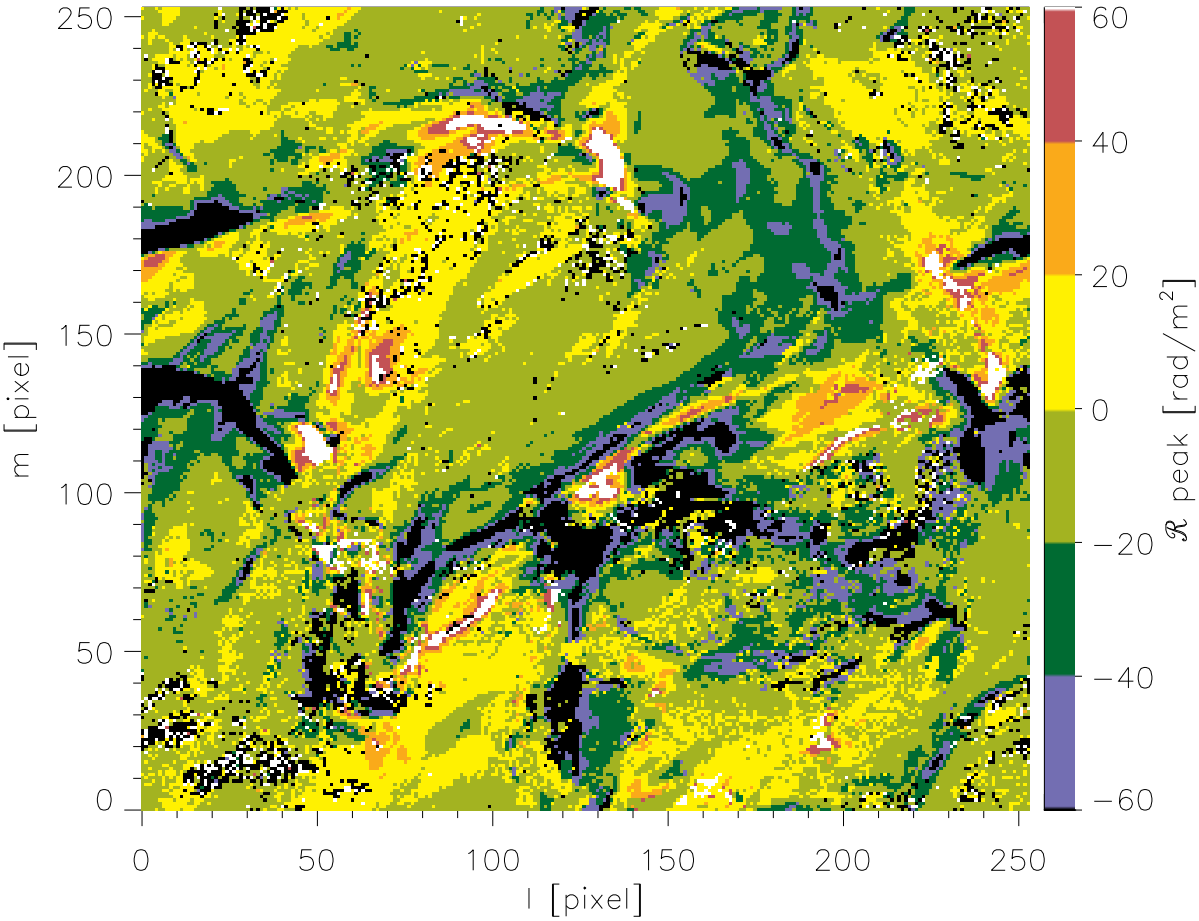

Figure 10.11 — [SIMULATION] Identical to Fig. 7.6, but for the Faraday depth $\mathcal{R}$ of the highest peak in the $P(\mathcal{R})$ spectrum. The 4910 lines-of-sight indicated in black have $\mathcal{R}$ < -60 rad/m^2, and the 1724 lines-of-sight indicated in white have $\mathcal{R} > 60$ rad/m^2.

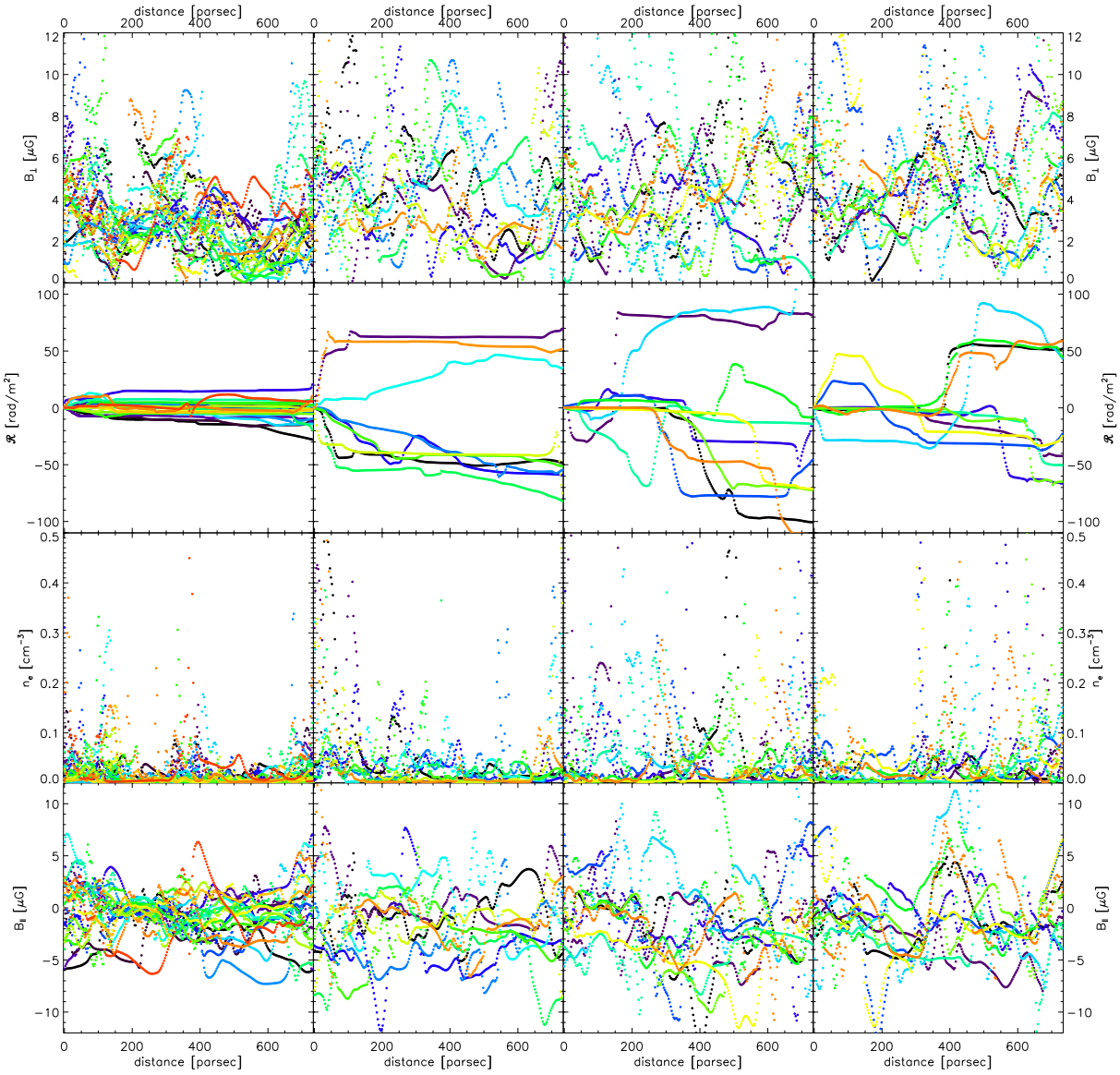

Figure 10.12 — Distribution of synchrotron emission and Faraday rotation along the line-of-sight, for different groups of $P(\mathcal{R})$ spectra. From left to right: the first column shows the variation of the different physical quantities for 20 lines-of-sight with a single narrow peak in the $P(\mathcal{R})$ spectrum with $|\mathcal{R}| \lesssim 15$ rad/m^2. In the second column we plotted the properties of 10 lines-of-sight with a single narrow peak at large $|\mathcal{R}| \gtrsim 40$ rad/m^2. The third and fourth columns both show the properties of lines-of-sight with two narrow peaks in the $P(\mathcal{R})$ spectrum, that are separated by more than 40 rad/m^2. To avoid confusion we only plotted 10 lines-of-sight in each of these two columns. The first row of panels shows how the magnetic field component perpendicular to the line-of-sight varies along the line-of-sight. Since we assume a uniform cosmic ray distribution, the magnitude of this magnetic field component directly translates into the magnitude of the synchrotron emission. It is clear that synchrotron emission occurs in more than one region along the line-of-sight. The second row of panels shows how $\mathcal{R}$ builds up along the line-of-sight. In the third and fourth rows we show how the thermal electron density and line-of-sight magnetic field strength, that determine how the Faraday depth is built up along the line-of-sight, vary.

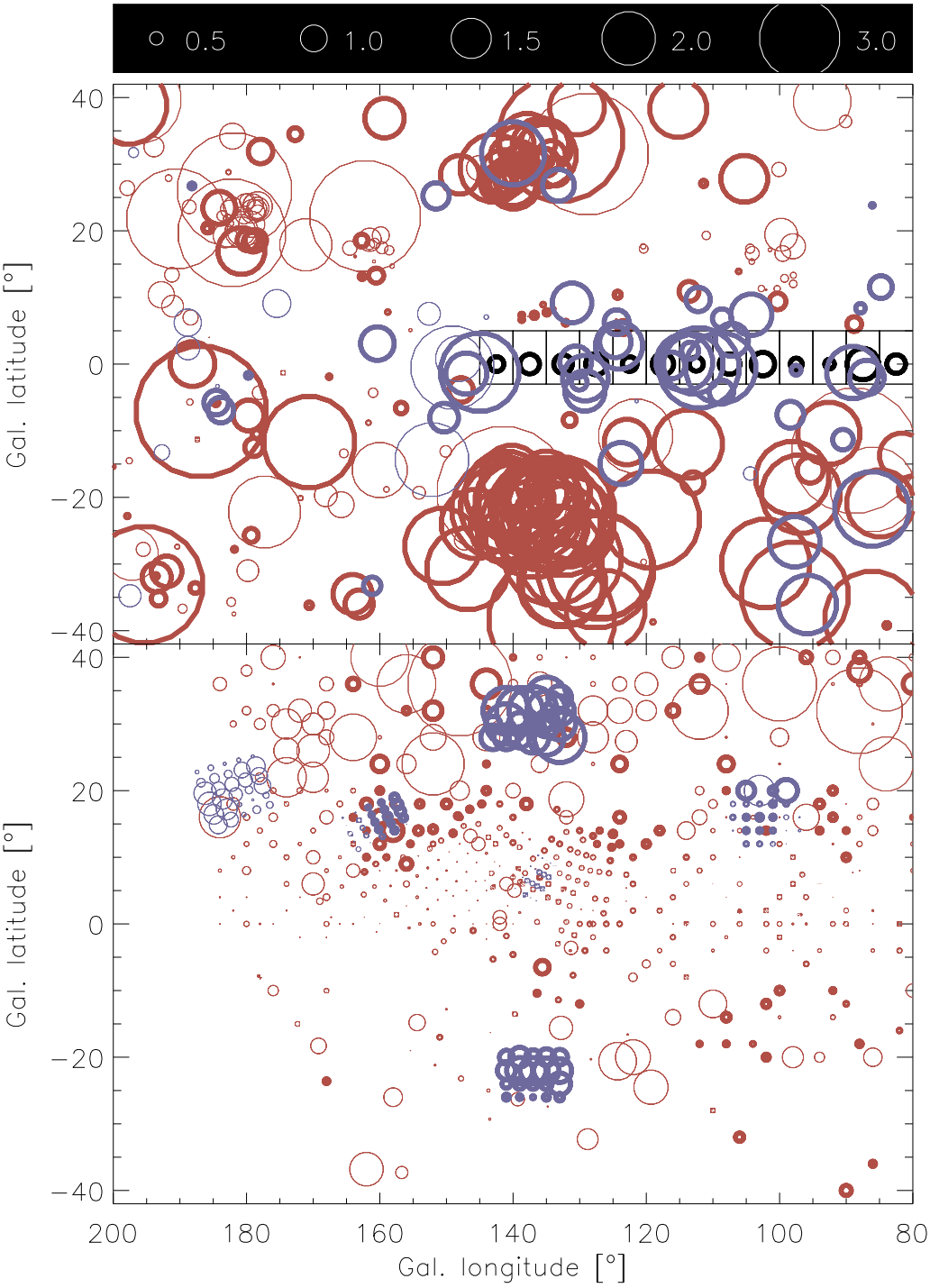

Figure 10.13 — $\langle B_\parallel \rangle$ derived from extragalactic sources and pulsars (top panel; red and blue circles resp.) and from the diffuse Galactic emission (bottom panel; red circles are $\langle B_\parallel \rangle$ based on rotation measures from Spoelstra (1984), blue circles are $\langle B_\parallel \rangle$ based on rotation measures from Haverkorn et al. (2003a, 2003b) and from the Faraday depths with the strongest diffuse polarized emission, chapters 2–6). Circles with thin edges show positive $\langle B_\parallel \rangle$, and circles with thick edges negative $\langle B_\parallel \rangle$. Black circles indicate the $\langle B_\parallel \rangle$ that we calculate by averaging rotation measures of CGPS sources in the black boxes. To avoid confusion we removed sources from the Frick et al. catalogue that lie in the region that is also covered by the CGPS. 28 lines-of-sight from the top plot were excluded because they had $|\langle B_\parallel \rangle| > 5\ \mu$G. The $\langle B_\parallel \rangle$ for the Haverkorn et al. data and for our data were calculated on a $2^\circ \times 2^\circ$ grid, where we averaged rotation measures and Faraday depths over all lines-of-sight within 1° from a grid point. In this averaging we only included rotation measure fits from Haverkorn et al. that have $\chi^2_{\rm red} < 2$.

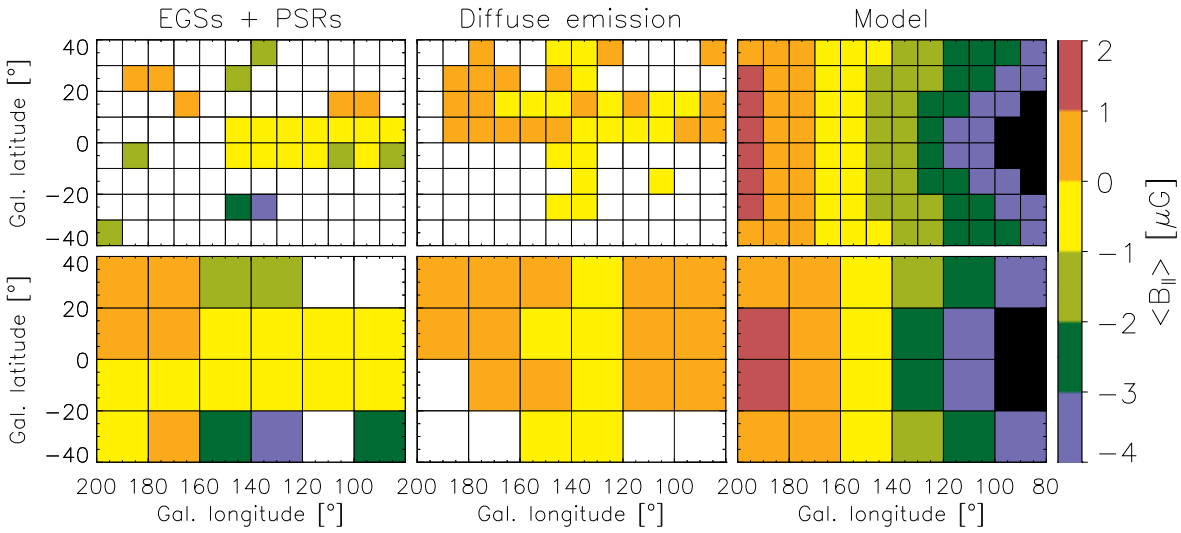

Figure 10.14 — $\langle B_\parallel \rangle$ from Fig. 9.6 averaged over cells of $10^\circ \times 10^\circ$ (top row of panels) and $20^\circ \times 20^\circ$ (bottom row of panels). To construct this figure we calculated $\langle B_\parallel \rangle$ for each CGPS source individually. Empty (white) cells have less than 5 lines-of-sight in them. Black cells have $\langle B_\parallel \rangle <$ -4 μG. The first two columns show the averaged $\langle B_\parallel \rangle$ that we calculated from the $\langle B_\parallel \rangle$ of extragalactic sources and pulsars, the second column shows the averaged $\langle B_\parallel \rangle$ that we calculated from the $\langle B_\parallel \rangle$ of the diffuse emission. In the third column we plot the $\langle B_\parallel \rangle$ that we calculate for the model of the large-scale Galactic magnetic field that we describe in Sect. 9.5.

Nederlandse samenvatting

Magnetische velden in de Melkweg

De afstanden tussen sterren zijn ontzettend groot: de dichtstbijzijnde ster (Proxima Centauri) ligt op 4.2 lichtjaar, oftewel ruim een kwart miljoen keer de afstand van de aarde tot de zon. De zon staat op haar beurt op zo'n 26 duizend lichtjaar van het centrum van de Melkweg, en de Melkweg zelf is weer 200 duizend lichtjaar groot. Toch is de ruimte tussen de sterren niet helemaal leeg: iedere kubieke centimeter bevat een paar atomen atomair waterstof, het meest voorkomende element in het heelal, verder wat helium, en een heel klein beetje zwaardere atomen. Maar omdat de Melkweg zo groot is, is al dat gas ongeveer samen toch nog zo'n paar procent van de totale geschatte massa aan sterren in de Melkweg. Een paar procent van het gas is bovendien geïoniseerd. Dit lijkt misschien vreemd omdat het buiten de aardse dampkring zo koud is. Hete sterren en sterren die op het eind van hun leven exploderen zenden echter veel fotonen uit die voldoende energie hebben om een elektron uit een waterstof atoom te slaan. De vrije elektronen in dit kleine deel geïoniseerd gas spelen een belangrijke rol in mijn onderzoek, zoals verderop zal blijken.

Tussen de sterren bevindt zich ook een magnetisch veld. Dit magnetisch veld is erg zwak vergeleken met dat van de aarde (ongeveer een miljoen keer zo zwak) of dat van een koelkastmagneetje (ongeveer een miljard keer zo zwak). Stromen van geladen deeltjes in het gas tussen de sterren wekken dit magnetisch veld op, en houden het in stand. Een bewegende lading wekt een magnetisch veld op, en als een groep geladen deeltjes in dezelfde richting bewegen, zullen de (zwakke) magnetische velden van de afzonderlijke deeltjes elkaar versterken en op die manier een sterker magnetisch veld produceren. Als echter alle geladen deeltjes door elkaar bewegen, zal hun gecombineerde magnetische veld niet heel sterk zijn. Een belangrijke (en op dit moment nog grotendeels onopgeloste) vraag is hoe je van deze velden op betrekkelijk kleine schaal uitkomt bij de magnetische velden op grote schaal die we in sterrenstelsels zien (zie bijvoorbeeld figuur 10.15), en waarvoor ook in de Melkweg aanwijzingen te vinden zijn.

Bewegende ladingen zullen door een magnetisch veld worden afgebogen, waardoor ze ook rond de magnetische veldlijnen gaan draaien. Dit is bijvoorbeeld ook gebeurd met de geladen deeltjes op de omslag van mijn proefschrift. Omdat de geladen deeltjes op een kleine afstand rond het magnetisch veld draaien, is het lastig voor ze om tussen de magnetische veldlijnen te bewegen. Dit betekent dat de ronddraaiende ladingen en de magnetische velden sterk aan elkaar gekoppeld zijn, en dat ze niet onafhankelijk van elkaar kunnen bewegen. Een gaswolk die zwaar genoeg is, zal onder haar eigen gewicht instorten en daarmee sterren vormen. Als die gaswolk echter een magnetisch veld bevat, zal de instortende wolk ook het magnetisch veld meesleuren, maar dit verzet zich tegen de instorting, waardoor de wolk minder snel in zal storten

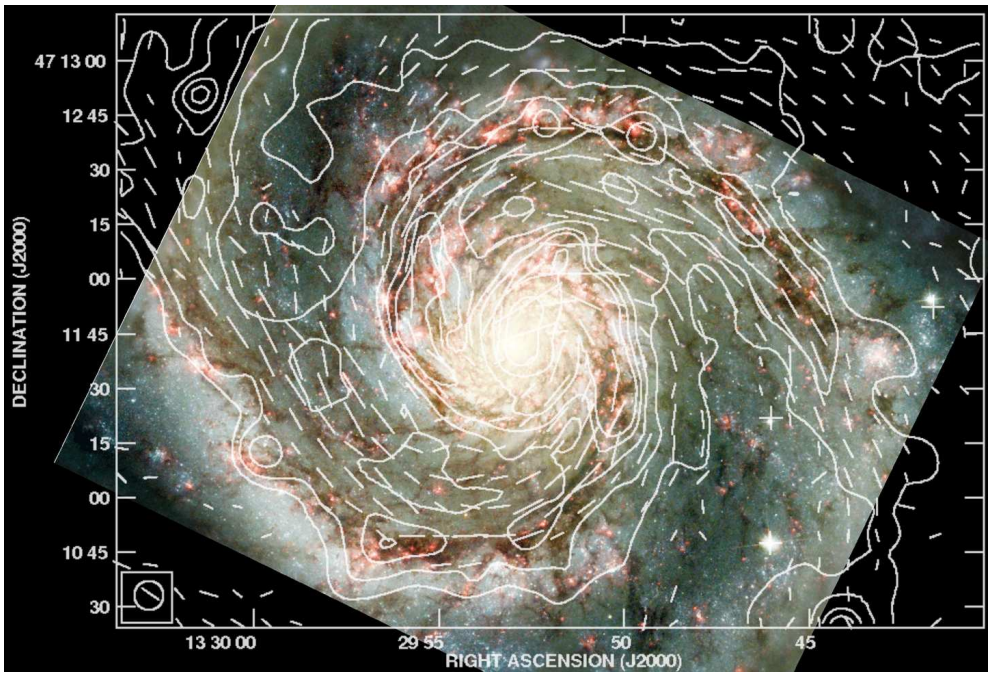

Figuur 10.15 — Het magnetisch veld in de binnendelen van het sterrenstelsel M51. De streepjes geven de richting van het magnetisch veld aan; hun lengte is een maat voor de helderheid van de gepolariseerde radiogolven die we op die plek meten. Op de achtergrond zijn de binnenste delen van M51 zelf te zien, zoals we ze ook met het blote oog zouden waarnemen. (Met dank aan Andrew Fletcher, NASA en het Hubble heritage team (STScI/AURA)).

dan een wolk zonder magnetisch veld. Op een vergelijkbare manier zal ook het gas in de spiraalarmen van een sterrenstelsel zoals de Melkweg anders bewegen als er ook een magnetisch veld aanwezig is.

Faraday draaiing

Het is onmogelijk om magnetische velden rechtstreeks waar te nemen, we zien alleen het effect dat ze hebben op geladen deeltjes. De spiraalbanen die sommige deeltjes op de omslag van mijn proefschrift beschrijven zijn hier een goed voorbeeld van. In dit proefschrift bestudeer ik het magnetisch veld in de Melkweg door te kijken naar een natuurkundig verschijnsel dat Faraday draaiing heet, en dat als volgt werkt. Het licht dat we zien met onze ogen of de radiogolven die ik bestudeer in dit proefschrift bestaan uit golven van een elektrisch veld en een magnetisch veld. De golf in het elektrisch veld ligt in 1 vlak, het polarisatievlak, en de golf in het magnetisch veld ligt in een vlak loodrecht daarop. De golven in beide vlakken planten zich in dezelfde richting voort, en dat is de richting waarin de lichtstraal beweegt. Als een lichtstraal een elektron tegenkomt, zal de golf in het elektrisch veld een kracht uitoefenen op het elektron, waardoor het elektron samen met die golf op en neer gaat bewegen. Het magnetisch veld kan geen ladingen versnellen, maar alleen afbuigen. Ik zal het herhaaldelijk hebben over 'elektronen', terwijl andere geladen deeltjes net zo goed worden versneld door de golf in het elektrisch veld. (Vrije) elektronen komen echter verreweg het meest

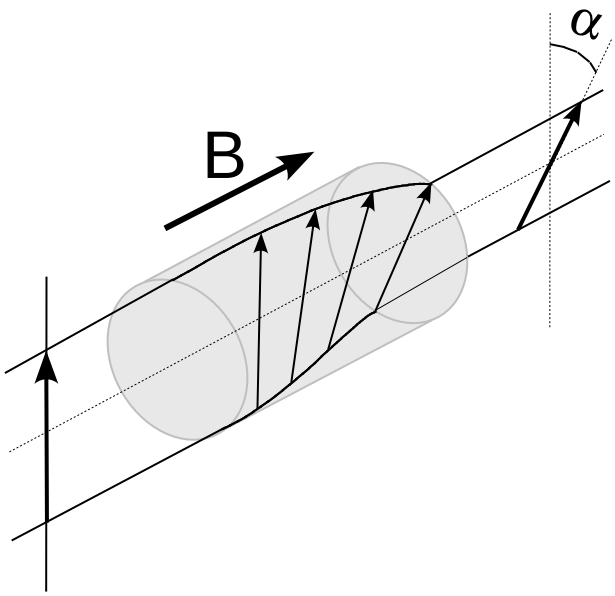

Figuur 10.16 — Faraday draaiing grafisch uitgelegd. Een radiogolf beweegt van links beneden naar rechts boven door een cylinder met vrije elektronen en een magnetisch veld B (grijs). Het polarisatievlak van de radiogolf (aangegeven met pijltjes), dat voordat de golf door de cylinder beweegt nog verticaal stond, wordt door Faraday draaiing in de cylinder over een kleine hoek α verdraaid. De hoek waarover het polarisatievlak wordt verdraaid wordt snel groter als je op lange (radio)golflengten kijkt. Daarom heb ik Faraday draaiing op radiogolflengten bestudeerd.

voor, en omdat ze zo licht zijn, worden ze het sterkst versneld door het elektrisch veld in de lichtgolf.

Voor Faraday draaiing is het cruciaal dat er niet alleen elektronen (of andere geladen deeltjes) zijn, maar ook een extern magnetisch veld. De elektronen draaien dan rond dit magnetisch veld, en hun draairichting wordt bepaald door de richting van het magnetisch veld. Als er dan een lichtgolf op die elektronen valt, zullen de elektronen niet alleen rond het externe magneetveld blijven draaien, maar tegelijkertijd zullen ze ook een kracht ondervinden ten gevolge van het elektrisch veld van de lichtgolf. Deze kracht koppelt de ronddraaiende elektronen aan de lichtgolf, waardoor het polarisatievlak van de lichtgolf een beetje mee gaat draaien met de elektronen (zie figuur 10.16). Dit effect heet Faraday draaiing. Hoe sterk dit effect is, hangt af van de sterkte van het magnetisch veld, de dichtheid van vrije elektronen, en de afstand die de lichtgolf aflegt door het gebied met magnetisch veld en elektronen. Magnetische velden in de Melkweg zijn zwak, maar de enorme afstanden tussen de sterren maken Faraday draaiing toch meetbaar.

Een andere eigenschap van Faraday draaiing is dat de hoek waarover het polarisatievlak draait sterk toeneemt met de golflengte waarop je waarneemt. Daarom worden vooral lange (radio) golflengtes gebruikt om Faraday draaiing waar te nemen.

Het is belangrijk om te realiseren dat je met Faraday draaiing alleen maar iets te weten kunt komen over de component van het magnetisch veld die langs je gezichtslijn staat. Als je de volledige magnetisch veld vector wil weten, moet je ook informatie hebben over de component van het magnetisch veld die loodrecht op je gezichtslijn

Figuur 10.17 — Enkele van de 14 schotels van de radiotelescoop in Westerbork, die ik heb gebruikt voor mijn promotie onderzoek. (Met dank aan Harm-Jan Stiepel)

staat.

Synchrotron straling

Lichtbronnen zoals een kachel of de zon zenden lichtgolven uit omdat ze heet zijn. De radiogolven die we op lange golflengtes waarnemen (orde grootte 10 cm – 1 m) worden echter uitgezonden door geladen deeltjes die bijna met de snelheid van het licht rond de magnetische veldlijnen van de Melkweg bewegen. Deze snelle geladen deeltjes veranderen in hun spiraalbeweging rond het magnetisch veld de hele tijd van richting, en de energie die ze daardoor verliezen zenden ze uit in de vorm van radiogolven. Dit soort straling heet synchrotron straling. Geladen deeltjes die niet zulke hoge snelheden hebben, zenden geen synchrotron straling uit als ze rond het magnetisch veld draaien. Eigenlijk is dit de omgekeerde situatie van wat ik in de paragraaf over Faraday draaiing beschreef: daar versnelde het elektrisch veld in een (radio)golf een lading, nu zenden ladingen juist radiogolven uit vanwege hun cirkelbeweging (een cirkelbeweging is een versnelde beweging).

Er zijn 2 goede redenen te noemen waarom ik Faraday draaiing van juist synchrotron straling heb onderzocht. Het licht dat hete objecten zoals de zon uitzenden, ontstaat doordat afzonderlijke atomen elk één lichtgolf uitzenden. De polarisatievlakken van die lichtgolven staan verschillende kanten op, zodat de straling die we zien maar een heel lage netto polarisatie heeft, meestal maar 1% van het totale vermogen van de

lichtbundel, of nog minder. Synchrotron straling kan echter sterk gepolariseerd zijn, zelfs tot 70%. Dat heeft ermee te maken dat de ladingen die synchrotron straling uitzenden zo snel bewegen, en dat die ladingen ten gevolge van het magnetisch veld ongeveer dezelfde banen afleggen. De tweede reden om synchrotron straling te bestuderen, is dat synchrotron straling vergeleken met andere vormen van straling heel helder is op lange (radio) golflengtes. Omdat de hoeken waarover het Faraday effect het polarisatievlak draait ook groter worden op langere golflengtes, is synchrotron straling een geschikte keus om het magnetisch veld van de Melkweg te bestuderen. Een bonus daarbij is dat zowat overal in de Melkweg synchrotron straling wordt opgewekt, waardoor we in onze waarnemingen niet beperkt zijn tot bepaalde objecten zoals pulsars (de overgebleven kernen van zware sterren) of radiobronnen in ver weg gelegen sterrenstelsels. Omdat we de radiogolven uit de Melkweg niet alleen maar langs bepaalde gezichtslijnen zien, zoals wel het geval is voor bijvoorbeeld pulsars en andere sterrenstelsels, noemen we de Melkweg straling ook wel 'diffuse' straling.

Ik heb in dit proefschrift onderzoek gedaan met de radiotelescoop in Westerbork, in Drenthe (zie figuur 10.17). Door de signalen van de afzonderlijke telescoopschotels op een slimme manier te combineren, kan de Westerbork telescoop een veel gedetailleerdere afbeelding maken dan met één van de afzonderlijke telescoopschotels mogelijk is.

Voor Faraday draaiing heb je een magnetisch veld nodig, en geladen deeltjes die rond dat veld draaien. De snelle geladen deeltjes die synchrotron straling uitzenden, draaien ook rond de magnetische veldlijnen, en daarom zullen ook zij via het Faraday effect het polarisatievlak van radiogolven draaien. De dichtheid van deze snelle geladen deeltjes is echter zoveel lager dan die van normale (vrije) elektronen dat we hun bijdrage aan Faraday draaiing kunnen verwaarlozen. Je kunt dus spreken over een tweedeling tussen enerzijds de geladen deeltjes die verantwoordelijk zijn voor Faraday draaiing, maar die geen synchrotron straling uitzenden omdat ze daarvoor te traag bewegen, en anderzijds de snelle geladen deeltjes die synchrotron straling uitzenden, maar waarvan de dichtheid te laag is om een bijdrage te leveren aan Faraday draaiing.

Faraday tomografie

Faraday tomografie is een slim wiskundig trucje waarmee je voor een gemeten radiosignaal kunt bepalen wat de bijdragen zijn van verschillende delen van de gezichtslijn. De hoeveelheid Faraday draaiing hangt af van de padlengte door het gebied met vrije elektronen en magnetisch veld. Als het magnetisch veld overal langs je gezichtslijn dezelfde richting op staat, zal het Faraday effect daarom het polarisatievlak van radiogolven die ver van de aarde worden opgewekt meer draaien dan radiogolven die dichterbij ontstaan. Je moet dan wel een manier hebben om je gemeten radiosignaal op te splitsen in 'veel draaiing', 'weinig draaiing', en alles wat daar tussenin ligt, en daar helpt de wiskunde achter Faraday tomografie je bij. De hoeveelheid Faraday draaiing kun je wiskundig namelijk op dezelfde manier beschrijven als de toonhoogte van muziek: lage tonen (weinig draaiing) komen van dichtbij de aarde, hoge tonen (veel draaiing) van verder weg. Net als dat je met je oren hoge tonen van lage tonen kunt

onderscheiden, kun je met Faraday tomografie 'veel draaiing' onderscheiden van 'weinig draaiing', en daarmee kun je dus iets zeggen over de structuur van het magnetisch veld langs de gezichtslijn, en de hoeveelheid radiovermogen die wordt opgewekt op een zekere afstand van de aarde.

Uit de data die ik heb geanalyseerd blijkt dat het magnetisch veld niet altijd in dezelfde richting staat langs de gezichtslijn. Omdat de richting waarin het Faraday effect het polarisatievlak draait afhangt van welke kant het magnetisch veld op staat langs je gezichtslijn, zal een verandering in de richting van het magnetisch veld betekenen dat in het ene deel van je gezichtslijn het Faraday effect het polarisatievlak de ene kant op draait, en in het andere deel van de gezichtslijn juist de andere kant op. De tegenovergestelde draairichtingen van het Faraday effect zullen elkaar gedeeltelijk opheffen als je een radiosignaal meet dat ontstaat voorbij het punt waar het magnetisch veld van richting verandert. Als je radiogolven met een lage hoeveelheid Faraday draaiing meet, kun je dus in die situatie niet langer zeggen of die radiogolven dichtbij de zon ontstaan, of juist ver weg, voorbij het punt waar het magnetisch veld van richting verandert. Wel kun je nog steeds iets zeggen over de variatie in Faraday draaiing en opgewekt radiovermogen langs de gezichtslijn.

Voor Faraday tomografie heb je waarnemingen nodig op veel verschillende golflengtes. Zo heb ik voor de verschillende datasets uit hoofdstukken 2–6 waarnemingen op zo'n 150–200 golflengtes gebruikt in mijn Faraday tomografie analyse. Radio telscopen konden tot enkele jaren geleden niet zoveel golflengtes tegelijkertijd waarnemen. Met de 5–10 kanalen die je toen kon waarnemen, kon je alleen iets zeggen over de gemiddelde sterkte van het magnetisch veld langs de hele gezichtslijn, terwijl je tegenwoordig met Faraday tomografie ook iets kunt zeggen over afzonderlijke delen van je gezichtslijn.

Mijn onderzoek

Voor mijn promotie heb ik onderzocht hoe het magnetisch veld van de Melkweg eruit ziet. Ik heb 4 gebieden aan de hemel waargenomen met de radiotelescoop in Westerbork (hoofdstuk 2–6) en ik heb radio data van een ouder onderzoeksproject bestudeerd voor een groot gebied aan de hemel (hoofdstuk 8). Al deze data liggen in het deel van de Melkweg dat, als je met de rug naar het Melkweg centrum staat, tussen je uitgestrekte rechter arm en je kijkrichting recht vooruit ligt, het zogenaamde tweede Galactische kwadrant. Het doel van mijn onderzoek was om het magnetisch veld op kleine schalen te bestuderen, voor elk van mijn datasets afzonderlijk, maar ook om de informatie in mijn datasets te combineren met gegevens uit de literatuur, om zo iets te kunnen zeggen over het grote-schaal magneetveld in het tweede Galactische kwadrant (hoofdstuk 9). Ook heb ik gewerkt aan een computersimulatie van het magnetisch veld en de elektronen dichtheden in het gas tussen de sterren, zodat we beter kunnen begrijpen hoe we onze waarnemingen moeten interpreteren (hoofdstuk 7).

Elk van mijn 4 datasets is naar een sterrenbeeld genoemd: GEMINI (Tweelingen), CEPHEUS (Cepheus was volgens de Griekse mythologie koning van Aethiopia, een koninkrijk tussen Syrië en de Rode Zee), TRIANGULUM (Driehoek) en CAMELOPARDALIS (Giraffe). Ik heb meegeholpen met het plannen van de waarnemingen met

de Westerbork telescoop voor 3 van de 4 datasets. Nadat deze gebieden aan de hemel waren waargenomen, heb ik de data geijkt en heb ik stoorsignalen verwijderd. Voor elk van mijn datasets bepaalde ik voor de diffuse synchrotron straling en ook voor puntbronnen (pulsars en de kernen van sterrenstelsels buiten de Melkweg) de sterkte van het deel van het magnetisch veld dat langs de gezichtslijn staat. Deze 3 typen bronnen geven namelijk informatie over verschillende delen van de gezichtslijn. Faraday draaiing van radiostraling uit sterrenstelsels buiten de Melkweg vertelt je iets over het magnetisch veld langs de gezichtslijn door de hele Melkweg (tussen de Melkweg en het andere sterrenstelsel is er nauwelijks Faraday draaiing omdat de elektronen dichtheden en magnetisch veld sterktes daar erg klein zijn). Een pulsar ligt in de Melkweg op een bekende afstand. Je kunt voor een pulsar bepalen hoeveel Faraday draaiing er is tussen ons en de pulsar. Door de hoeveelheid Faraday draaiing van het pulsar signaal te vergelijken met de hoeveelheid Faraday draaiing van de signalen van sterrenstelsels buiten de Melkweg, kun je iets zeggen over de hoeveelheid Faraday draaiing tussen de pulsar en de sterrenstelsels. Omdat de elektronen dichtheden en magnetische velden tussen de Melkweg en andere sterrenstelsels zo klein zijn, komt dit erop neer dat je vooral meet hoeveel Faraday draaiing er is in het deel van de gezichtslijn dat vanuit ons gezien achter de pulsar ligt. Tenslotte kun je door de hoeveelheid Faraday draaiing in de diffuse synchrotron straling te vergelijken met de hoeveelheid Faraday draaiing in het signaal van de pulsars of de extragalactische bronnen iets te weten komen over waar de diffuse synchrotron straling vandaan komt. Dat is namelijk nog altijd een onopgelost probleem. De analyse van elk van mijn datasets afzonderlijk staat in hoofdstuk 2 t/m 6.

Een eerste resultaat van mijn analyse was dat in elk van mijn 4 datasets interessante structuren te vinden waren aan de hemel. **Hoofdstuk 2** is een kort artikel over de GEMINI dataset waarin we laten zien dat er in deze dataset gebieden zitten waar synchrotron straling en Faraday draaiing niet in hetzelfde stukje gezichtslijn plaatsvindt. Dit is een onverwacht resultaat, omdat we verwachtten dat de geladen deeltjes die synchrotron straling uitzenden zo snel bewegen dat ze overal langs de gezichtslijn wel te vinden zouden zijn.

In **hoofdstuk 3** bespreken we de GEMINI dataset uitgebreid. Deze dataset laat structuur zien op schalen van graden (de volle maan heeft een diameter van 1/2 graad; een vuist aan het eind van een uitgestrekte arm is ongeveer 10 graden breed). In dit hoofdstuk geven we ook een verklaring voor wat we rapporteerden in hoofdstuk 2. Synchrotron straling wordt (vrijwel) alleen uitgezonden loodrecht op de richting van het magnetisch veld waar de snelle geladen deeltjes omheen draaien. Als het magnetisch veld langs de gezichtslijn staat, zien we geen synchrotron straling uit dat stukje gezichtslijn. We zien dan wel Faraday draaiing, en op die manier kun je verklaren waarom synchrotron radiogolven en Faraday draaiing niet altijd uit hetzelfde stukje gezichtslijn hoeven te komen. In GEMINI lijkt de structuur in het magnetisch veld langs de gezichtslijn bovendien redelijk eenvoudig te zijn. Dit kan ermee te maken hebben dat we met onze GEMINI dataset zowat loodrecht op de magnetische veldlijnen in de Melkweg kijken, waardoor Faraday draaiing (dat afhangt van de sterkte van het magnetisch veld langs de gezichtslijn) in deze richting niet heel sterk is.

De CEPHEUS dataset uit **hoofdstuk 4** is om verschillende redenen interessant. Ten

eerste zien we een gelaagdheid in de hoeveelheid Faraday draaiing die loodrecht op het Melkweg vlak staat (zie figuur 10.5 op bladzijde 190) over hoekafstanden van 5° – 10°. We hadden niet verwacht een zulke mooie gelaagdheid in Faraday draaiing tegen te komen, laat staan een gelaagdheid die zo duidelijk is over zulke grote afstanden. Een tweede opvallende eigenschap van de CEPHEUS dataset is dat het radiosignaal van pulsars en sterrenstelsels buiten de Melkweg door Faraday draaiing de andere kant op wordt gedraaid dan het diffuse signaal van de Melkweg. Dit betekent dat het magnetisch veld ergens langs de gezichtslijn van teken verandert (zoals ik beschreef in het stukje over Faraday tomografie), over een gebied dat ten minste zo groot is als de oppervlakte van de CEPHEUS dataset (10 vierkante graden). Ook betekent dit dat de meeste diffuse synchrotron straling dichtbij de zon wordt opgewekt, omdat we anders voor de diffuse straling dezelfde hoeveelheid Faraday draaiing zouden meten als voor de pulsars en de sterrenstelsels buiten de Melkweg. Met 'dichtbij' bedoel ik dan 'dichtbij' op Melkweg schaal, en dat betekent dat de diffuse synchrotron straling wordt uitgezonden ergens tussen ons en de dichtstbijzijnde spiraalarm van de Melkweg, die op zo'n 6000 lichtjaar ligt (afhankelijk van welke richting je kijkt ligt hij zelfs nog verder weg).

De TRIANGULUM dataset die ik bespreek in **hoofdstuk 5** ligt in tegenstelling tot de andere 4 datasets beneden het Melkweg vlak. Net als in de CEPHEUS dataset vinden we een groot verschil in de hoeveelheid Faraday draaiing van de diffuse synchrotron straling van onze Melkweg enerzijds en van de pulsars en extragalactische bronnen anderzijds. In tegenstelling tot CEPHEUS laten de laatste 2 soorten bronnen in TRIANGULUM juist veel meer Faraday draaiing zien dan de diffuse synchrotron straling in TRIANGULUM, en we weten nog niet goed waardoor dit komt.

In CAMELOPARDALIS (**hoofdstuk 6**) hebben de signalen van de diffuse synchrotron straling van onze Melkweg en van pulsars en extragalactische bronnen ongeveer dezelfde hoeveelheid Faraday draaiing (net als in GEMINI). Het bijzondere aan CAMELOPARDALIS is dat de totale hoeveelheid elektronen langs de gezichtslijn in dit deel van de Melkweg heel laag is vergeleken met mijn andere datasets. Om de hoeveelheid Faraday draaiing te verklaren die we in CAMELOPARDALIS zien, moet het magnetisch veld er dus redelijk sterk zijn.

Naast mijn waarnemingen met de Westerbork telescoop heb ik ook computersimulaties van Fabian Heitsch gebruikt om meer te weten te komen over hoe we onze data kunnen interpreteren (**hoofdstuk 7**). Het voordeel van de simulaties is namelijk dat je weet hoe sterk de magnetische velden zijn, wat de elektronen dichtheden zijn etc. Je kunt dan uitrekenen hoe je die simulaties zou waarnemen met de Westerbork telescoop, en als je dan de gesimuleerde waarnemingen vergelijkt met de werkelijke waarnemingen, kun je iets zeggen over hoe de magnetische velden en elektronen dichtheden er in het echt uit moeten zien. De snelheden van het gesimuleerde gas zijn een stuk hoger dan de gemiddelde snelheid in het echte gas van de Melkweg. Ik heb toch deze simulaties gebruikt in mijn onderzoek, omdat het heel lastig is om de lage snelheden in het echte gas goed te simuleren. Uit dit onderzoek kwamen 2 belangrijke conclusies. Ten eerste lijken de simulaties aan te tonen dat als we synchrotron straling met veel Faraday draaiing zien, dit vaak ontstaat in stukjes gezichtslijn met een heel hoge elektronendichtheid, en dat dit niet zo vaak het gevolg is van structuur in het

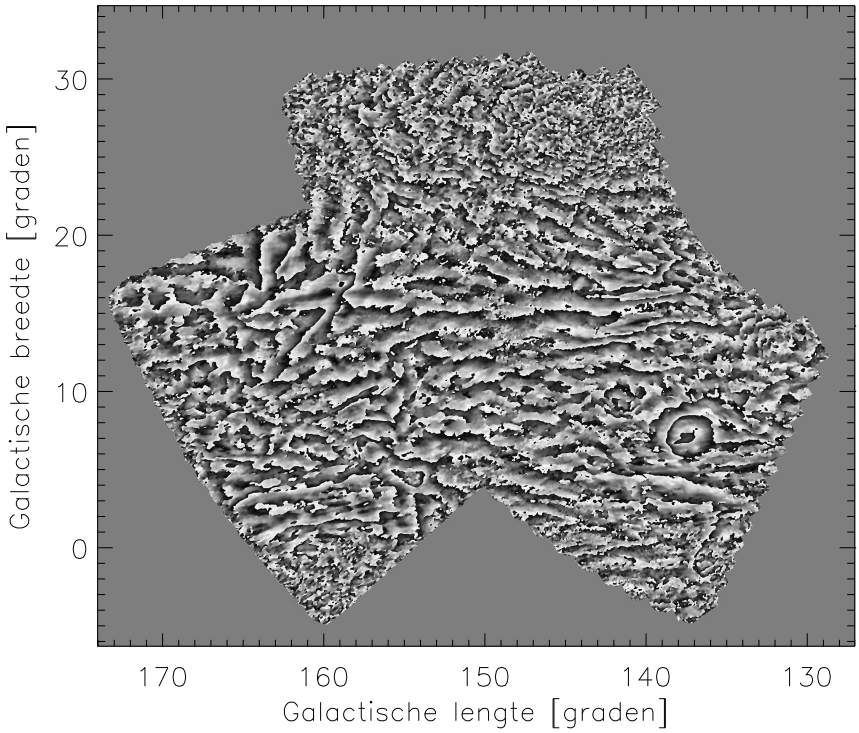

Figuur 10.18 — Faraday draaiing in werking in de Melkweg. Ik laat hier de hoeken van het polarisatievlak zien, zoals we deze maten met WENSS. Polarisatiehoeken zijn periodiek, en lopen van -90° tot +90°, waarna ze weer -90° worden. Een hoek van -90° is in deze figuur zwart, en een hoek van +90° is wit. De periodiciteit van de polarisatiehoeken maakt dat je vaak zwarte pixels naast witte pixels ziet liggen. Langs de assen van deze figuur heb ik Galactische coordinaten uitgezet. Galactische coordinaten zijn vergelijkbaar met de geografische coordinaten op de aardbol, met dit verschil dat Galactische coordinaten het Melkweg vlak als referentie hebben (op een Galactische breedte van 0°), en geografische coordinaten hebben de aardequator als referentievlak. Het gebied boven een Galactische breedte van 20° bevat nauwelijks signaal, de structuren die je hier ziet worden door ruis geproduceerd, en hebben niks te maken met de Melkweg.

magnetisch veld. Een tweede belangrijke conclusie is dat er niet vaak synchrotron radiogolven worden uitgezonden op dezelfde plekken langs de gezichtslijn waar je ook Faraday draaiing hebt. Het mooie is dat we iets dergelijks al hadden afgeleid op grond van onze GEMINI waarnemingen in hoofdstuk 2 en 3.

Hoofdstuk 8 gaat over WENSS, de *We*sterbork *N*orthern *S*ky *S*urvey. Dit was een onderzoek uit de jaren '90 dat oorspronkelijk was bedoeld om radiobronnen voor een groot deel van de hemel te catalogiseren. WENSS bleek ook prima geschikt om Faraday draaiing in de diffuse synchrotron straling van de Melkweg mee te onderzoeken. Jammer genoeg bevat WENSS gegevens voor maar 1 golflengte, zodat we niet direct de hoeveelheid Faraday draaiing kunnen afleiden. Daarom interpreteren we de variatie in polarisatiehoek die we meten in WENSS als een variatie in Faraday draaiing tussen gezichtslijnen, en op die manier kunnen we toch nog iets zeggen over structuur in het magnetisch veld van de Melkweg. Wat we niet hadden verwacht te zien is de mooie gelaagdheid van de WENSS polarisatiehoeken evenwijdig aan het Melkweg vlak weg over zo'n groot deel van het gebied dat we onderzochten (zie figuur 10.18).

Zoiets kan wijzen op netjes geordende magnetische velden en elektronen dichtheden, of dat we vooral naar een dichtbij deel van de Melkweg kijken waar het magnetisch veld en de elektronen dichtheden heel gestructureerd zijn. In de CEPHEUS dataset zien we trouwens juist een gelaagdheid die loodrecht op de richting van de gelaagdheid in WENSS staat, en dat is misschien wel een net zo vreemd resultaat (zie figuur 10.5 op bladzijde 190. Ook al laat ik een andere grootheid zien in deze figuur dan in fig. 10.18, de variatie van beide grootheden met positie aan de hemel kun je wel met elkaar vergelijken.). In hoofdstuk 8 laten we ook zien dat je met wat vereenvoudigende aannames de volledige 3D magnetisch veld vector kunt reconstrueren, zie figuur 8.8 uit hoofdstuk 8. Faraday draaiing alleen levert je namelijk alleen de magnetisch veld component langs je gezichtslijn op. Om de 3D magnetisch veld vector te reconstrueren moet je dan ook nog de sterkte van het magnetisch veld loodrecht op de gezichtslijn weten (die we bepaalden uit de sterkte van de synchrotron straling), en de richting van de magnetisch veld vector loodrecht op de gezichtslijn (die je kunt bepalen als je weet hoeveel Faraday draaiing er is).

Tenslotte heb ik wat ik heb geleerd over het magnetisch veld uit mijn eigen datasets en uit WENSS gecombineerd met gegevens van andere onderzoekers om zo iets te weten te komen over het magnetisch veld van de Melkweg op grote schaal (**hoofdstuk 9**). Ik heb me geconcentreerd op het tweede Galactisch kwadrant. Toen ik al deze gegevens combineerde, bleken ze helemaal niet goed te passen met het model voor het grote-schaal magnetisch veld van de Melkweg. Dit model voorspelt namelijk een veel te sterk verloop in het magnetisch veld over het gebied waarvoor ik data verzamelde. Een mogelijke verklaring hiervoor zou kunnen zijn dat het magnetisch veld van richting omkeert ergens langs de gezichtslijn. Iets dergelijks heb ik geconcludeerd voor mijn CEPHEUS dataset (zie hoofdstuk 4), maar in mijn model zou het magnetisch veld een andere richting moeten hebben op een veel grotere schaal, en wetenschappers zijn het er nog niet over eens of er in dit deel van de Melkweg een omkering van het magnetisch veld op zulke grote schaal bestaat. De data die ik verzamelde laten bovendien zien dat er ook structuur in het magnetisch veld is op schalen tussen de allergrootste schalen (die ik heb gemodelleerd) en de kleinste schalen die ik met mijn data kon bestuderen. Er zit dus veel meer structuur in het magnetisch veld dan in de modellen die alleen maar deze grote en kleine schalen bevatten, en weinig schalen daartussenin.

Curriculum vitae

Op 17 september 1979 ben ik geboren in het Zuid-Limburgse Heerlen. Na een omzwerving in Eindhoven, doorliep ik tussen 1991 en 1997 het Katholiek Gymnasium Rolduc in Kerkrade, thans College Rolduc. Al vroeg had ik interesse om sterrenkunde te gaan studeren, maar of dat wat voor mij zou zijn was nog maar de vraag. Gelukkig waren er de vrijdagavonden waarop mijn vader me naar de Sterrewacht Schrieversheide reed, zodat ik meer kon leren over sterren, planeten en sterrenstelsels. In mijn vijfde leerjaar kreeg ik ook de gelegenheid om gedurende 3 weken van mijn zomervakantie te leren over zwarte gaten. Die zomerschool werd georganiseerd door de Sterrewacht Leiden.

In september 1997 begon ik aan mijn studie sterrenkunde in Leiden. Tijdens mijn studie heb ik onder begeleiding van Prof. dr. H.J. Habing en Dr. M. Messineo onderzoek gedaan naar AGB sterren in 47 Tucanae. Mijn afstudeerproject, onder begeleiding van Dr. M. Haverkorn en Dr. P. Katgert, ging over hoe we met polarisatie data uit de Westerbork Northern Sky Survey het interstellaire medium van onze Melkweg konden bestuderen. En dat smaakte naar meer. Ik studeerde af in juni 2003.

In september van datzelfde jaar begon ik met mijn promotie-onderzoek naar het Galactische interstellaire medium. Hetzelfde onderwerp als mijn afstudeerproject, maar deze keer had ik niet 6 maanden, maar 4 jaar de tijd. Ger de Bruyn en Michiel Brentjens hadden een nieuwe idee genaamd rotatiemaat synthese uitgewerkt, en voor mijn promotie-onderzoek zou ik die techniek gaan gebruiken. Het resultaat van mijn onderzoek onder begeleiding van Dr. P. Katgert en Prof. dr. A.G. de Bruyn kunt u in dit proefschrift lezen. Tijdens mijn promotie heb ik ook heel wat reizen gemaakt. Ik nam deel aan conferenties in Leiden, Puerto Rico, Parijs, Calgary en Perm (Rusland), waar ik resultaten van mijn onderzoek heb gepresenteerd. Ook bracht ik werkbezoeken aan Dwingeloo, Cambridge (Verenigde Staten), Calgary en Penticton (Canada). Ik heb deelgenomen aan de NOVA herfstschool in Dwingeloo, en aan de VLA Summer School in Socorro (Verenigde Staten). Ik begeleidde Eveline Helder bij haar klein onderzoek op de Sterrewacht, ik assisteerde bij het vak Sterevolutie, en verschillende jaren heb ik meegeholpen met het LappTop project voor middelbare scholieren.

Na mijn promotie zal ik als postdoc mijn onderzoek naar het magnetisch veld van onze Melkweg en het interstellaire medium voortzetten aan de andere kant van de wereld, in Sydney, Australië, in de groep van Dr. Naomi McClure-Griffiths.

Nawoord

De eerste en laatste bladzijde van elk boek zijn altijd heel belangrijk, en ik wil de laatste gebruiken om een aantal mensen te bedanken die op hun manier een bijdrage hebben geleverd aan niet alleen dit proefschrift, maar ook aan de afgelopen jaren op de Sterrewacht en daarbuiten.

Tim, Thom en Patrick, bedankt voor goede herinneringen aan vele jaren. Roderik, Isa, Stijn, Liesbeth en Jan-Pieter, bedankt voor al die pauzes/lunches/avondetens/keren dat we zijn uitgeweest. Simon, Evelyn, Maria, Andrew and Sergio, my fellow roommates of 527: thanks for the great atmosphere, and for enduring the music that I play. Carolina, I thank you for sharing your stories (and tea) with me. Pascal, keep making music! Melanie and Leonie: I thank you for stirring up the Sterrewacht. Simone, Marc, Marinda en Remco, cenare insieme sarà più difficile tra qualche mese, ma grazie per tutte le sere che eravamo insieme. Tim en Evelyne, en Simon en Hilke, bedankt ook voor jullie gastvrijheid (de staf bij Eazie moet ons nu toch zo onderhand wel kennen). Emily en Marcus, aan jullie heb ik mijn liefde voor lange-afstanden wandelen te danken. Ik wil ook allen danken op de andere Sterrewacht, Sterrewacht Schrieversheide (thans Explorion), voor al die vrijdagavond lezingen en de waarneemavonden met de Celestron C8 in de kleine koepel... in het bijzonder bedankt Bert en Wilma!

I would also like to thank the many colleagues that I met at several conferences and summer schools, for making these such enjoyable events. I hope to see many of you again in the near future!

David, Tycho, Erik en Aart: zonder jullie zou het hele computer netwerk binnen de kortste keren in de soep lopen. De zaterdag voor ik m'n proefschrift naar de drukker zou sturen, liep mijn computer helemaal vast, maar dit hadden jullie snel weer opgelost. Kirsten, Jeanne, Liesbeth, Anita en Marja: jullie zijn de tandwielen in het mechaniek van de Sterrewacht.

One of the things that I like the most of the Sterrewacht is its diversity. I enjoyed the many discussions that I had with members of other research groups, ranging from astrochemistry, to high-z galaxies, instrumentation, and universe awareness. This is for sure one of the things that I will miss the most after I've left the Sterrewacht, and I would like to thank everyone who has contributed in his or her own way.